New magnetic nanocomposite materials

A thesis submitted to the University of Dublin in application for the degree of Doctor of Philosophy

Serena Corr

School of Chemistry
University of Dublin
Trinity College

DECLARATION

This thesis has not been submitted as an exercise for a degree at any other university. Except where stated, the work described therein was carried out by me alone.

I give permission for the Library to lend or copy this thesis upon request.

Signed: Serena Cork.

Declaration

This thesis is submitted by the undersigned to the University of Dublin, Trinity College for the examination of Doctorate of Philosophy. Except as otherwise indicated, the author carried out the work described herein alone and has not submitted as an exercise for a degree to any other university

Serena Corr

Abbreviations

AC	alternating current
AFM	Atomic Force Microscopy
B_{hf}	Hyperfine magnetic field
^{t}Bu	*tert*-butyl
BBB	Blood brain barrier
BM	Bohr magnetons
ccp	cubic close packed
Cltx	Chlorotoxin
conc	concentration
DLS	Dynamic Light Scattering
DMSO	Dimethyl sulfoxide
DNA	Deoxyribonucleic acid
DTPA	diethylenetriamine pentaacetic acid
EDC	*N*-(3-Dimethylaminopropyl)-*N'*-ethylcarbodiimide
EDX	Energy Dispersive X-Ray analysis
emu	Electromagnetic unit
FTIR	Fourier Transform Infrared
H	Applied magnetic field
HBSS	Hanks' Balanced Salt Solution
HRTEM	High Resolution Transmission Electron Microscopy
IS	Isomer shift
JCPDS	Joint Committee on Powder Diffraction Studies
LD_{50}	Lethal Dose, 50%
M	Magnetisation
MHz	Megahertz
MR	Magnetic Resonance
MRI	Magnetic Resonance Imaging
nm	nanometres
NMR	Nuclear Magnetic Resonance
NMRD	Nuclear Magnetic Resonance Dispersion

PMA	Phorbol 12-myristate 13-acetate
PCS	Photon correlation spectroscopy
PDI	Polydispersity index
PEG	Polyethylene glycol
PSS	Polysodium-4-styrene sulfonate
PVA	Poly vinyl alcohol
QD	quantum dots
R_1	Spin-lattice relaxation rate
R_2	Spin-spin relaxation rate
r_1	relaxivity
Rpm	rotations per minute
RT	Room temperature
SEM	Scanning Electron Microscopy
SPIO	Superparamagnetic iron oxide
SQUID	superconducting quantum interference device
τ	Relaxation time
T	Tesla
T_1	Longitudinal relaxation time (or spin-lattice relaxation time)
T_2	Transverse relaxation time (or spin-spin relaxation time)
T_B	Blocking temperature
T_C	Curie temperature
TCD	Trinity College Dublin
TEM	Transmission Electron Microscopy
TGA	Thermogravimetric analysis
THF	Tetrahydrofuran
THP-1	Human acute monocytic leukemia cell line
UV	ultraviolet
XRD	X-Ray diffraction

Summary

The main aim of this project is to develop new iron oxide based nanomaterials with potential biomedical applications. This work involves the synthesis of various magnetite, maghemite and cobalt ferrite nanocomposites, the study of these materials using different instrumental techniques and the evaluation of their potential biomedical applications.

Chapter 1 gives a background to the area of nanotechnology and explains why magnetic nanoparticles are of such technological importance. A review of the use of magnetic nanoparticles and nanocomposites in targeted drug delivery, magnetic resonance imaging (MRI) and hyperthermia treatment is given. Also discussed are the current techniques for preparing magnetic iron oxide nanoparticles.

The various experimental procedures and techniques which are used to characterise the synthesised materials are discussed in Chapter 2. Some of these include FTIR and Raman spectroscopy, X-Ray diffraction (XRD) patterns, magnetisation measurements, Mössbauer spectroscopy, Nuclear Magnetic Resonance dispersion (NMRD) techniques and Electron Microscopy (EM).

In Chapter 3, an organometallic approach to synthesising magnetite nanocrystals is developed. The heterometallic Fe(II) alkoxide $[(THF)NaFe(O^tBu)_3]_2$ was employed as an iron source for the preparation of magnetic nanocrystals, which were produced using hydrolysis and ultrasonic treatment. In order to determine the best experimental conditions for the preparation of these nanocrystals, a statistical analysis called a 2^2 factorial study was carried out. This allows the variation of two experimental parameters at two different levels (e.g. low or high temperature as one parameter and short or long ultrasound times as the other). The resulting nanocrystals have been characterized and a 3-D contour plot generated, which gives a quick guide to the conditions necessary to produce particles of a required size.

The use of a metallorganic precursor is again described in Chapter 4, but this time in order to produce new silica iron oxide nanocomposite materials. Because silica coated materials are biocompatible and allow for further modification, these materials could have useful applications in biomedicine. In this work new silica-maghemite nanorods

have been produced and investigated, whose formation is dependant on the concentration of silica employed in the preparation.

Chapter 5 deals with the preparation of magnetic-fluorescent nanocomposite materials. These are of great interest in biological imaging, as these materials could provide a two-in-one diagnostic tool, whereby cell imaging is possible using confocal microscopy and, if the particles form a stable suspension, they could also be useful as MR contrast agents. Here, magnetic-fluorescent nanocomposites were prepared by two different methods; one where a porphyrin molecule is ionically linked to a stabilizer on the nanoparticle and another where the porphyrin is covalently bound to silica coated magnetic nanoparticles. These nanocomposites have been characterized by FTIR and Raman spectroscopy, TEM and NMRD analysis and UV-vis and fluorescence spectroscopy. Human THP-1 cells are exposed to the particles and live cell confocal imaging is used to locate any internalized nanoparticles.

Investigation of DNA-stabilised magnetic nanowires is presented in Chapter 6. Double and single stranded Herring and Salmon DNA are used as stabilizers for magnetic nanoparticles during the growth process. The resulting stable suspensions are studied by NMRD analysis to determine their viability as MR contrast agents. As part of this work, a magnetic fluid has been synthesized which has an unprecedented high relaxivity at low field. This could be a potential candidate for low field contrast agent imaging. Intercalation studies are also carried out to check if fluorescent magnetic nanocomposites can be made by the interaction of the intercalator acridine orange with the DNA particle stabilizer.

The use of synthetic polyelectrolytes as stabilizers for magnetite and cobalt ferrite nanoparticles is the subject of Chapter 7. A systematic study was carried out, varying the metal and polyelectrolyte concentrations, to generate a new family of iron oxide based contrast agents with tunable relaxivity. The formation of magnetic nanowires and their alignment using an external magnetic field has been demonstrated. These new composites are of great interest as, depending on the initial concentrations chosen, a contrast agent can be synthesized which has the required r_{1max} at a certain frequency.

Chapter 8 details the conclusions of this work and also further studies to be carried out with some of the materials synthesised. In summary, a number of interesting

new magnetic materials, including nanocrystals, nanocomposites, and nanowires have been synthesised and characterised. Some of these could have exciting potential applications in the field of biomedicine.

Acknowledgements

Firstly, I would like to thank my supervisor, Dr. Yurii Gun'ko, who gave me this great opportunity to work in such an interesting and exciting area of materials chemistry. The past four years spent as a postgraduate in his group have been my best yet and I have really enjoyed working as part of his research group. Thank you for all your encouragement, guidance and help over the past few years.

Thank you to Professor John Kelly for all his help and advice throughout my studies, in particular with the DNA experiments.

Thank you to Professor John Corish for allowing me to work in the School of Chemistry. I would like to thank all the staff of the School of Chemistry for all their help over the past few years. It is a great pleasure and a privilege to work with so many wonderful people. Whenever I have needed any help – be that research or teaching – nobody was ever too busy.

Thank you to Dr. Dermot Brougham and his research team in DCU – Eoin, Carla, Sarah and Swapan. All NMRD profiles and PCS measurements were carrid out in Dr. Brougham's lab. NMRD analysis for the DNA work was carried out by Dr. Swapan Ghosh and some iron determinations for the PSS functionalized magnetite samples were carried out by Carla Meledandri.

Thank you to Dr. Alexious Douvalis (formerly of TCD, now at the University of Ioannina, Greece) who carried out all Mössbauer measurements in this thesis and also thanks to Robbie Gunning and Dr. Munuswamy Venkatesan from the School of Physics, TCD who ran all magnetization measurements. Thank you to the staff of the Centre for Microscopy and Analysis in TCD for use of the TEM and SEM facilities and for all their help and encouragement, in particular David John, Neal Leddy and Colin Reid. Thank you also to Dr. Peter Nellist from the Department of Materials at the University of Oxford for carrying out high resolution TEM studies on the iron oxide-silica nanocomposites.

Confocal imaging was carried out by Jennifer Conroy and Dr. Adriele Prina_Mello. Thank you to Dr. Yurii Volkov for use of these facilities and also for his helpful discussions on the fluorescent-magnetic nanocomposites. Lifetime measurements

were carried out by Dr. Yury Rakovich in the Physics Department. Thank you also to Dr. Tanya Perova for use of the Raman machine.

I have been very lucky during my PhD to work with a fantastic group of postgrads and postdocs. To all members of Yurii's group, past and present, thank you so much for welcoming me into the group and for putting up with me when there was another chapter to read – Steve, Gemma, Rowan, Ian, Michelle, Joe, Renata, Anna, Mick, Maciej, Aine and Arunas. Getting to work with you guys makes Monday mornings a little easier ☺

I would like to thank my family who has been so supportive of me through everything. To my mum and dad who are always at the end of a phoneline or waiting at the bus station, to my sister Marianne and my brothers Patrick and Eoghan – I love you all so much. Without you I would never have come this far. Also, thank you to Anna, Michael, Marie Claire and Elma, who have always been so good to me. Those breakfasts have fueled this work!

To all my friends who have been there for me when I was excited about new results or complaining about experiments – I can't wait to see you all again! – especially Terry, Carlos, Liam, Ger, Gary, Graham, Belle, Orla, Ann Marie, Michelle, Emma and all the gang.

Finally, I'd like to thank Ian. You're the one who has had to put up with me the most!! I'm so lucky to have someone so supportive, patient, caring and, of course, handsome, in my life. I couldn't have done this without you.

Table of Contents

Figures, Schemes and Tables

Chapter 1 Introduction

Chapter 2 Experimental

Chapter 3 Magnetite nanocrystals from metallorganic precursors

Chapter 6 DNA-magnetite nanocomposites and their interactions with fluorescent dyes

Chapter 7 Polyelectrolyte stabilised magnetite and cobalt ferrite nanoparticles

Chapter 8: Conclusions and Future Work

9. Appendices

Chapter 1: Introduction

"A chemist comes to us and says, ``Look, I want a molecule that has the atoms arranged thus and so; make me that molecule.'' The chemist does a mysterious thing when he wants to make a molecule. He sees that it has got that ring, so he mixes this and that, and he shakes it, and he fiddles around. And, at the end of a difficult process, he usually does succeed in synthesizing what he wants. By the time I get my devices working, so that we can do it by physics, he will have figured out how to synthesize absolutely anything, so that this will really be useless." *Richard Feynman, There's Plenty of Room at the Bottom*

1.1 Small is good – why nanotechnology is vital for technological advances

Advances in nanotechnology allow researchers to work at cellular and molecular levels, thereby advancing our understanding of processes in a host of areas which up to now had not been possible to study, in particular biotechnology. With their controllable sizes, nanoparticles and nanocomposites can be tuned to the dimensions of cells (10-100 μm), viruses (20-450 μm), proteins (5-50 μm) or even genes (2 nm wide and 10-100 nm long).[1] Because their properties differ from those of their bulk counterparts, nanoparticles offer a range of potential applications based on their unique characteristics.

The term "nanotechnology" is traditionally used to describe materials with a size less than 100 nm. To give an idea of the dimensions in question, a nanometre is one billionth of a meter, or about ten atoms wide. Although the nano prefix has been used to provide a new host of buzzwords, chemists have been dealing in the nanoscale since the first chemical synthesis. In practise, nanotechnology combines chemistry, materials science, engineering and physics to provide new materials which have potential applications in medicine, information technology and environmental science.

However, nanotechnology is not without its controversy. In 1986, Eric Drexler speculated in his novel, Engines of Creation, that self-replicating robots with molecular-scale dimensions could be used to build everyday goods cheaply and efficiently. He noted that if such robots were ever to escape they could be potentially dangerous: "We cannot afford certain kinds of accidents."[2] These ideas have been the fodder for many science fiction novels and films, where the term "grey goo" has been used to describe the ensuing havoc wreaked by these "nanobots". Unfortunately, this term has been used to play on the publics fears of this new technology. Nanoscience and its applications have the potential to provide tremendous benefits to mankind. It is true that, while the outcomes given by Drexler, who has since

expressed regret at the coining of the phrase, are rather fanciful, there are genuine concerns regarding health and safety issues of such small material entering the human body.

Examples of nanotechnology employed in industry and commercial pursuits abound. For example, the company Invitrogen manufacture quantum dots (QDs) (nanocrystals of semiconducting materials) which can be used in biological imaging. Once excited, quantum dots will emit light of a distinct colour and wavelength, as the colour depends on the size of the dot. If coated, the dots may be made specific for certain parts of a cell. These nanocrystals are advantageous over conventional dyes as they are extremely stable and can be repeatedly excited for hours at a time while ordinary dyes last a matter of minutes.[3] Figure 1.1 shows cadmium telluride quantum dots which have been ingested by macrophage cells and are located in the cytoplasm of the cell.[4]

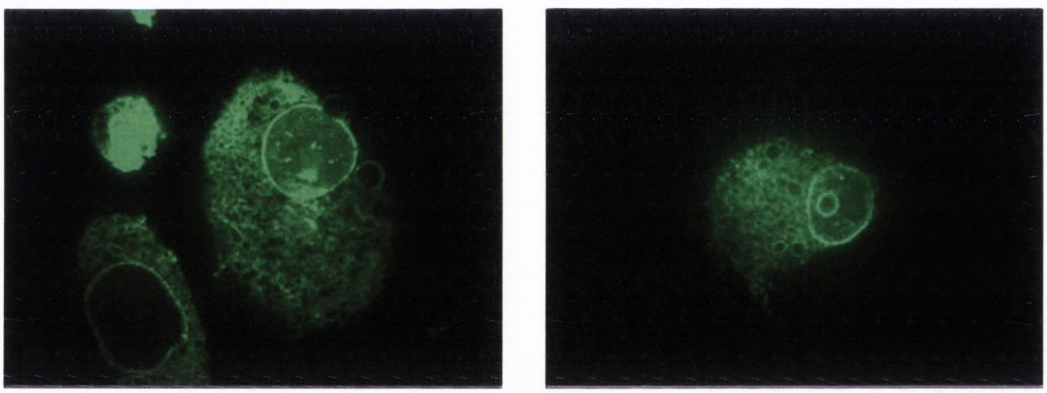

Figure 1.1 Thioglycolic acid-stabilised CdTe QDs showing intracellular localisation following a 10 minute incubation time in THP-1 cells.

1.2 The attractiveness of magnetic materials

The focus of this thesis is the investigation of new magnetic materials for potential materials science and biomedical use, including as MRI contrast agents, drug delivery systems and cell labellers. Magnetic nanomaterials represent one of the most exciting prospects in current nanotechnology. The reason magnetic nanoparticles are the focus of this research is mainly for their great potential for biological uses. Magnetic particles may be used as contrast agents in MR imaging. External magnetic fields could bring particles which are internalised in the body to a site of interest. Magnetic nanoparticles also heat up once subjected to an external magnetic AC field, which

opens up possibilities in hyperthermic cancer treatment. The area of magnetic nanoparticles is therefore not only attractive in terms of applications, but it also represents an exciting and fast growing field to be a part of.

The magnetic particles used in this project are mainly magnetite (Fe_3O_4), with some work done with maghemite (γ-Fe_2O_3) and cobalt ferrite ($CoFe_2O_4$). Some of the physical properties of these materials are listed in Table 1.1. These properties are discussed in more detail in the magnetism section of this thesis. One of the attractive possibilities of these magnetic nanoparticles is the fact that they can be relatively easily functionalised with molecules which will bestow new properties on the particles. These include drug molecules, fluorescent compounds and hydrophobic and hydrophilic coatings. Functionalised nanoparticles will be referred to as nanocomposites throughout this thesis.

Table 1.1 Physical properties of several iron oxide based materials[5]

Ferrite	Saturation Magnetisation ($J\ T^{-1}\ kg^{-1}$)[6]	Magnetocrystalline anisotropy constant ($kJ\ m^{-3}$)	Density ($t\ m^{-3}$)
γ-Fe_2O_3	73.5	-5	4.87
Fe_3O_4	92	-11	5.18
$CoFe_2O_4$	80.8	200	5.2

1.3 The properties of iron oxide magnetic materials

1.3.1 Structure.

Magnetite (Fe_3O_4) and maghemite (γ-Fe_2O_3) are both members of the ferrite family (see Section 1.3.2 for further discussion). Ferrimagnetic oxides (or ferrites) exist as ionic compounds, consisting of arrays of positively charged iron ions and negatively charged oxide ions. Ferrites adopt a spinel structure based on a cubic close packed (ccp) array of oxide ions. The ccp structure (ABCABC...) consists of three layers, each geometrically distinct from each other. The third layer (C) is placed in the octahedral holes created from the stacking of layers A and B. In this way, the octahedral and tetrahedral holes alternate throughout the structure. If the divalent ions occupy only tetrahedral sites, then the spinel is called direct, while if they occupy only octahedral sites, the spinel is said to be inverse.

Magnetite (Fe_3O_4) is a black mineral which contains both Fe^{2+} and Fe^{3+} ions. It has an inverse spinel structure (Figure 1.2). It is responsible, along with titanomagnetite, for the magnetic properties of rocks.[7] The divalent ions (Fe^{2+}) occupy two thirds of the octahedral (B) sites and the trivalent ions (Fe^{3+}) occupy the remaining B sites and all tetrahedral (A) sites. This particular framework is adopted because the larger divalent Fe^{2+} ions will occupy the roomier octahedral positions.

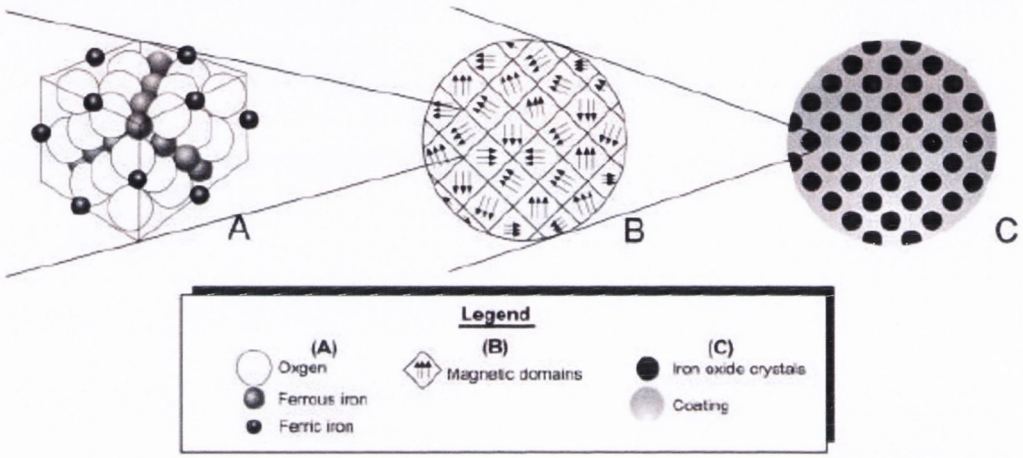

Figure 1.2 (A) Inverse spinel structure of the magnetite lattice, **(B)** magnetic domains and **(C)** magnetic nanoparticles[8]

Maghemite (γ-Fe_2O_3) is a red-brown material, similar in structure to magnetite, but it contains cation deficient sites. In maghemite, only 5/6 of the total available positions are filled and only by Fe^{3+}, with the remainder vacant. Maghemite can be thought of as a completely oxidised form of magnetite.[9] Cobalt ferrite is a black ferrimagnetic material with an inverse spinel structure.

1.3.2 Magnetic properties

1.3.2.1 Magnetism

Magnetism has been a subject of interest from as early as the 6th century, when the Greek philosopher Thales of Miletus noticed the attraction of iron to lodestone (magnetite).[10] Magnetism arises because of the spin property of electrons and may be thought of as the process by which materials exert an attractive or repulsive force on other materials. Hans Christian Oersted, in 1919, discovered that a magnetic field was generated by a moving electric current.[11] He found that a nearby compass

needle was moved by a flowing current. This type of magnetism (produced by the movement of electrons in an electric current) is called electromagnetism. A magnetic field may also be produced by a permanent magnet from the quantum-mechanical spin and orbital motion of electrons.

1.3.2.2 Classification of magnetic materials

Materials may be classified by their response to an applied external magnetic field as diamagnetic (opposes magnetic fields), paramagnetic (magnetised in the direction of and proportional to the applied field) or ferromagnetic (the largest effect which may be magnetised by orders of magnitude greater than the applied field).

Paramagnetic substances possess unpaired electrons which may be randomly orientated. The distinction between dia- and paramagnetic substances was first recognised by Faraday in 1845 but the interpretation of the differences in behaviour was first explained by Paul Langevin.[12] Langevin realised that the overall magnetic behaviour of a substance depends on the magnetic moments of the individual atoms. Each electron in an atom possesses a spin magnetic moment which, in turn, possesses an orbital magnetic moment. The combined spin and orbital magnetic moments give rise to the overall magnetic moment of the atom. However, the atom will only show an overall resultant magnetic moment (i.e. display paramagnetic behaviour) if there are unpaired electrons present in its valence shell. Because paired electrons within orbitals must have an equal and opposite magnetic moment, the overall magnetic moment would equal zero if there is an even number of valence electrons (i.e. diamagnetic behaviour).

Below a certain characteristic temperature (the Néel or Curie temperature), iron oxides may undergo a transition to a magnetically ordered state and become ferromagnetic, antiferromagnetic, or ferrimagnetic (Figure 1.3).[7] The Curie temperature describes ferromagnetic and ferrimagnetic substances, while the Néel temperature deals with antiferromagnetic substances. In ferro- and ferrimagnetic materials, a long-range atomic level ordering of the unpaired electrons exists. There is a parallel alignment of spins in ferromagnetic species which gives rise to an overall net magnetic moment. This parallel alignment of spins is the result of an interaction between magnetic moments termed exchange. The origin of the exchange interaction comes from the expression for the energy of interaction between neighbouring atoms. An extra electrostatic term appears here and is denoted by an exchange integral J

which may be positive or negative.[13] The positive sign denotes parallel alignment of the spins, while a negative sign denotes antiparallel alignment. The exchange integral is therefore thought of as the difference in energy between these two states.

When the temperature is raised, this ordering decreases due to thermal fluctuations of the individual magnetic moments. Antiferromagnetic species, on the other hand, have no overall net magnetic moment because the spins are of equal magnitude but are aligned in an antiparallel fashion.

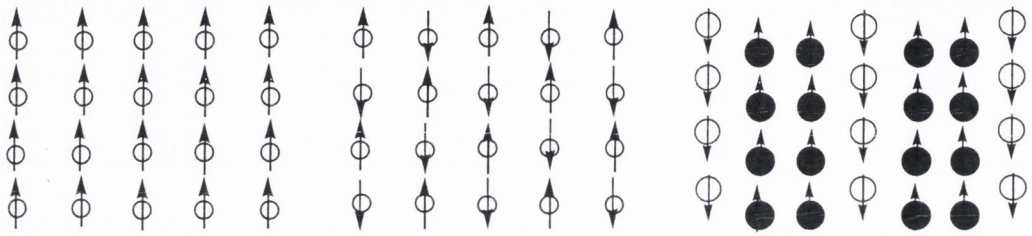

Figure 1.3 Ferromagnetism, antiferromagnetism and ferrimagnetism

There are interpenetrating sublattices within a ferrimagnet where there are regions aligned in an antiparallel fashion thereby causing a partial cancelling of the magnetic moment. However, the magnitude of the moments is unequal giving a ferrimagnet an overall magnetic moment. Because of the inverse spinel structure of magnetite, each molecule consists of one Fe^{3+} ion on an A site and one Fe^{2+} and one Fe^{3+} ion on a B site. Because of this atomic arrangement, magnetite exists as a ferrimagnet. The magnetic moment of Fe^{2+} and Fe^{3+} ions are known to be 4 BM and 5 BM respectively. If all spins become aligned in an applied magnetic field, we expect a resultant magnetic moment of 14 BM. However, the observed magnetic moment for magnetite is 4.08 BM. In 1948, Néel proposed that the Fe^{3+} ions in the A and B sites align antiparallel to each other, thereby cancelling out their magnetic moments.[12] Therefore, the resultant magnetic moment of 4.08 BM arises from the contribution of the Fe^{2+} ions on the B sites only.

1.3.2.3 Magnetic domains

Each of these substances (ferro-, antiferro- and ferrimagnets) are arranged in a domain structure. A domain is a region where the spins are aligned in the same direction. Neighbouring domains have different spin orientations. If a large enough external magnetic field is applied, all domains become aligned in the same direction. This is the point of saturation magnetisation.

The magnetic field is strong within a domain, but the bulk material will usually not be magnetised as the domains will be randomly orientated with respect to one another. However, these domains may be forced to align in one direction by the application of an external magnetic field. At the Curie temperature for ferromagnets, the ferromagnetic property disappears as a result of thermal agitation. As the temperature is increased, thermal fluctuations can destroy the parallel alignment of spins. This continues until T_c is reached where, without the magnetic ordering, there are no longer internal magnetic fields and the material is described as paramagnetic.

The alignment of spins becomes important when the spontaneous magnetisation (the magnetic moment per unit volume) of the substance is studied. The magnetic material is placed in a magnetic field of known strength, H. This gives rise to a characteristic sigmoidal shape of the M-H curve, with M approaching saturation at large values of H. Often for ferro- and ferrimagnetic materials, a hysteresis is observed in magnetisation curves (Figure 1.4).

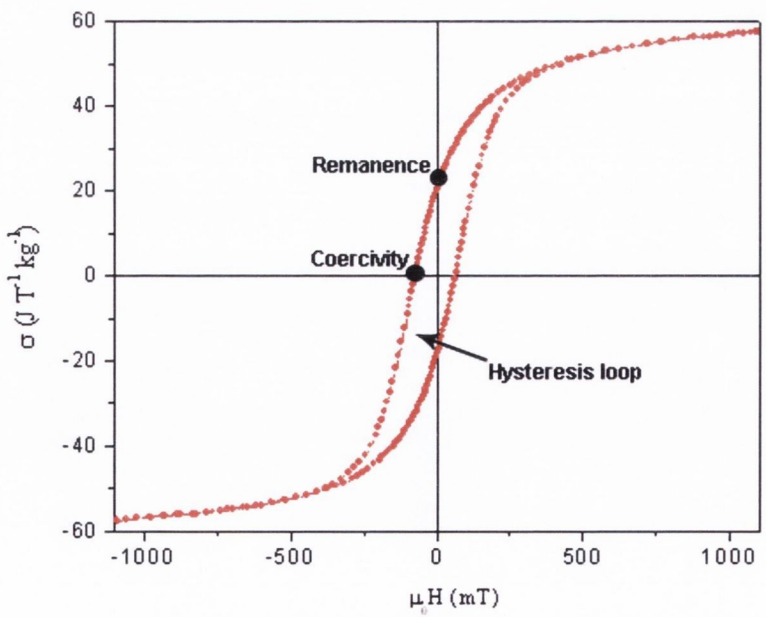

Figure 1.4 Magnetisation curve for magnetic nanoparticles of cobalt ferrite

The shapes of these open hysteresis loops are determined by the particle size. If particles are of a large size (1 μm) a narrow hysteresis is seen, while for smaller sizes (of the order of 10 nm) there is no hysteresis observed due to a phenomenon called superparamagnetism.[14] Superparamagnetic particles consist of a single magnetic domain where the particle is in a state of uniform magnetisation at any field.

Magnetisation changes are associated with the movement of boundary walls between domains, where the magnetisation is in different directions. The relaxation time of the magnetisation of small ferro- and ferrimagnetic materials is found to decrease with decreasing particle size.[15] Superparamagnetism arises as a result of magnetic anisotropy, i.e. the spins are aligned along a preferred crystallographic direction. When the energy is increased, the magnetisation may be reversed along this direction. If the relaxation time of the particle at a given temperature is short, the direction of the particles magnetisation changes spontaneously and the particle may be said to be superparamagnetic.[16] The blocking temperature, T_B, is defined as the temperature for which the relaxation time, τ, is equal to the characteristic time of the technique. For magnetisation measurements and Mössbauer spectroscopy, these times are 100 and 10^{-8} s respectively.[15] If the sample is made up of smaller particles, the total magnetisation decreases with decreasing particle size because of increased dispersion in the exchange integral. Finally, the superparamagnetic state is reached where each particle acts as a spin which suppresses the exchange interaction between the particles.[14]

1.3.2.4 Superparamagnetism

A phenomenon known as superparamagnetism may exist for particles with a size of 10 nm or less where the material may display properties similar to paramagnetism below T_c. For superparamagnetic material below T_c, the thermal energy is sufficient to change the magnetisation of the whole particle. In this case, instead of each individual atom independently influenced by an external magnetic field, the magnetic moment of the entire particle is aligned with the magnetic field. Even though the temperature is below the Curie temperature and the thermal energy is not sufficient to overcome the coupling forces between neighbouring atoms, the thermal energy is enough to change the direction of magnetisation of the entire crystallite. The resulting fluctuations in the direction of magnetisation cause the

magnetic field to average to zero. The material behaves in a manner similar to paramagnetism, except that instead of each individual atom being independently influenced by an external magnetic field, the magnetic moment of the entire crystallite tends to align with the magnetic field.

1.4 Potential applications of iron oxide nanoparticles

1.4.1 Biological applications

Because of their size, magnetic nanoparticles offer some attractive possibilities in biomedical applications as they can "get close" to a biological entity of interest. Also, because they are magnetic, they open up the possibility of target directed applications.[1] This is of great importance, as one major disadvantage of nanoparticle therapy is the problem of getting the particle to the site of interest. Using magnetic nanoparticles, an external magnetic field could be used to attract the particles to the desired area, to hold them there until the treatment is complete and finally to remove them. Obviously, toxicity is of major concern when advocating particles for biomedical use. The important factors which determine the biocompatibility and toxicity of magnetic materials are the nature of the magnetically responsive component (e.g. magnetite) and the final size of the particles and their composites. Iron oxide nanoparticles of magnetite or maghemite are by far the most commonly employed for biomedical applications, as there is no risk of further oxidation, which is possible with some other magnetic materials.[17] Magnetite nanoparticles have been found to be physiologically well tolerated, with dextran-magnetite showing no measurable toxicity index LD_{50}.[18]

1.4.1.1 Iron on the brain

The normal adult body contains between three and five grams of iron and about two thirds of this is present as haemoglobin in the blood.[19] The remaining iron is believed to act as a store of the proteins ferritin and hemosiderin. Ferritin molecules contain small iron oxide particles surrounded by a protein shell. It is believed that, with the increase of 3 T MRI scanners available, this brain iron may be used to detect several neurodegenerative diseases. For example, the involvement of iron has been reported in Alzheimer's, Parkinson's and Huntington's diseases. Although MRI is not currently used to detect these diseases, high-field imaging, in conjunction with biomarkers, may be a way forward in their detection.

Magnetic nanoparticles have been proposed for use as biomedical agents for many years. Their potential is far-ranging with applications including targeted drug delivery systems, hyperthermia agents and MRI contrast agents. Because nanoparticles exist in the same size domain as biological entities, they are suitable for bio-tagging or labelling. The size and shape of the nanoparticles becomes important when considering cell membrane penetration. In order to interact with a biological target, a biocompatible shell or coating is required around the nanoparticle surface. The choice of shell type may also include fluorescent molecules, thereby conferring fluorescent abilities to the magnetic nanocomposites. Detection techniques must also be considered in nanoparticle design. In order to fully utilise magnetic nanoparticles in biomedicine, it is vital to first investigate the biological tissues in question. For the most part, these tissues are cancerous.

Neoplastic (or tumour) tissue is heterogeneous in nature, with haemorrhaged areas as well as densely vascularised regions present in order to supply the tissue with blood, nutrients and oxygen to sustain angiogenesis (tumour growth).[20] Tumour blood vessels possess several abnormalities including a high proportion of proliferating endothelial cells (responsible for controlling blood pressure, blood clotting, new blood vessel formation and controlled passage of materials),[21] and an increased tortuosity.[22] The combination of abnormalities results in an increase in the permeability of tumour cells. The reported pore cutoff size for transport across tumour membranes is in the region of 380-780 nm.[20] The transport of a drug across the tumour interstitial space is controlled by a number of factors, including the physiological and physicochemical properties of the membrane and by the physicochemical properties of the drug itself (e.g. size, configuration, charge, hydrophobicity). In order to effectively deliver anti-cancer drugs, it is therefore important to overcome drug resistance at both a cellular and non-cellular level and to control the distribution, biotransformation and clearance of the drug from the body. Non-cellular drug resistance may be due to the poorly vascularised areas of the tumour tissue restricting drug access to the tumour and thereby protecting the tumour from cytotoxicity. Also, as tumour cells contain an acidic environment, basic drugs may be ionized and prevented from crossing the cell membrane.[23] Cellular mechanisms impeding anti-cancer drugs involve changes in the biochemistry of the malignant cells, e.g. altered enzyme function. Another factor to consider when employing anti-cancer drugs is the large dosages required for effectiveness. The

efficacy of chemotherapy may be limited by the adverse effects of cancer treatment drugs on normal, healthy cells.

1.4.1.2 Drug delivery

In order to overcome some of the problems associated with tumour treatment, colloidal nanoparticles could be used in conjunction with anti-cancer drugs. By careful design and functionality, these nanocomposites could prevent cellular and non-cellular interference with drug activity and increase the cancer cell-selectivity of the drugs while reducing toxicity to normal cells. Nanoparticles may act as vehicles for drug transport while, at the same time, protecting the drug from premature release. The accumulation of intravenously injected nanoparticles relies on diffusion across the leaky, permeable tumour vasculature. The particles may be injected intravenously and transported to the region of interest by the circulatory system.[17]

One major disadvantage with current chemotherapies is their non-specific nature. This leads to deleterious side-effects as they may cause damage not just to cancerous tissue but to the surrounding healthy tissue. 0The motivation behind magnetic nanoparticles as drug delivery agents is to localise these treatments so that only tissue to be treated is subjected to the drug. It is hoped that magnetic nanoparticles could bear on their surface a pharmaceutical drug which could be driven to the target and then released. For this application to be realised, the size, charge and surface chemistry will play a major role in determining the efficiency of such agents. For example, following administration to the body, larger particles (> 200 nm) are usually sequestered by the spleen as a result of filtration and are eventually removed by the cells of the phagocyte system, which results in shorter blood circulation times. If the particles are too small (> 10 nm), they have been found to be removed rapidly from the body by the renal system. In order to increase the blood circulation time of these particles, some workers have coated them with polymeric surfactants which minimise the protein adsorption to the particle surface.[24]

In order to investigate the uptake of superparamagnetic nanoparticles by human cancer cells, Petri-Fink *et al.*[25] have coated the particles with polyvinyl alcohol (PVA) and some PVA-based copolymers. They have found that cell toxicity is increased for higher polymer concentrations, as with lower concentrations the colloidal stability is sacrified. Of the modified PVA moieties tested, they found that

only the amino derivative was found to interact with the melanoma cells. The authors have postulated that the particles enter the cells by endocytosis.

Bergemann and coworkers[26] have prepared negatively charged magnetic nanoparticles to which they have ionically bound drugs, including the anti-cancer drug Epirubicin. The in vivo release of the drug was monitored in Sprague-Dawley rats. In vitro, a desorption half-life of 30 minutes is reported, while *in vivo* that time is increased to 45 minutes. This may be due to impaired diffusion of Epirubicin through the vascular wall. The first clinical trials of magnetic drug targeting in human patients were reported by Lübbe *et. al.*[27] Here, 100 nm particles were coated with the anti-cancer drug Epirubucine in a similar method to Bergemann *et. al.*[26] A 0.8 T external magnetic field was used to concentrate the drug in the target regions. Patients in the trial had advanced and unsuccessfully pretreated cancers or sarcomas. It was found that the ferrofluid was directed to the tumors in half the patients tested. It was concluded that transfer of parameters from animal to human trials were not sufficient, as significant physiological changes occur between species and sizes.[28]

The efficiency of cobalt ferrite magnetic fluids has also been investigated.[29] In this work, the authors have found that when the particles are coated with polyethylene glycol (PEG) they can remain for longer times in the bloodstreams of Swiss mice than compared to citrate coated particles which are taken up by phagocytic cells. It is interesting to note that the capillaries and parenchyma cells appear normal after subjection to the magnetic fluid. No tissue damage would indicate that these fluids are indeed biocompatible.

1.4.1.3 Magnetic Resonance Imaging (MRI)

Magnetic resonance imaging (MRI) is a noninvasive diagnostic technique that uses paramagnetic species to enhance proton relaxivity. Originally called Nuclear Magnetic Resonance Imaging, the name was changed in the 1970s to avoid the negative connotations implied by the word "nuclear". Beginning as a tomography technique for imaging thin sections of the body, it is now used to give a full 3-D representation of the body. Although the NMR technique was discovered independently by Bloch and Purcell as far back as 1946, it was not until the 1970s that it was employed for the first imaging experiments by Paul Lauterbur and Raymond Damadian. In order to understand MRI, it is necessary to discuss the underlying

principles of NMR. Because each hydrogen atom has an NMR signal, it is possible to image the body using this signal.

The Nuclear Magnetic Resonance (NMR) effect arises from the fact that nuclei have an associated spin. For ^{1}H nuclei, the nuclear spin quantum number, *I*, has a value of ½. After interaction with a magnetic field, a spin-half nucleus gives rise to two energy levels, $m_I = +½$ (the spin up or α state) and $m_I = -½$ (the spin down or β state). The population ratio between the α and β states may be described by the Boltzmann equation:

$$\frac{N_\beta}{N_\alpha} = e^{\frac{-\mu B_0}{kT}}$$

where T is the sample temperature, B_0 is the applied magnetic field strength, and μ is the nuclear magnetic moment. The whole basis for NMR spectroscopy relies on the fact that there is a slight excess of magnetic moments in the α state, i.e. aligned with the applied magnetic field. At equilibrium, due to the population excess, there is a small net sample magnetisation, M_0, pointing along the direction of the applied field (Figure 1.4).

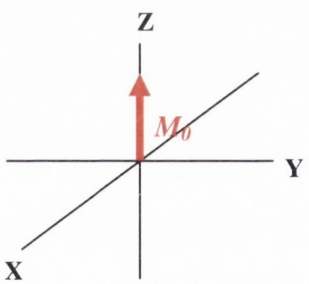

Figure 1.5 The net magnetisation at equilibrium of protons exposed to an external magnetic field. The applied magnetic field B_0 points along the z axis.

Transitions can be stimulated between these states by a pulse of radiofrequency (rf). When a photon of frequency υ is absorbed, the particle can undergo transitions between the α and β states. The frequency υ depends on the gyromagnetic ratio (a characteristic of the individual nucleus) of the particle and is given by:

$$\upsilon_L = \gamma B_0/2\pi$$

where B_0 is the external magnetic field strength (T) and γ is the gyromagnetic ratio (rad T^{-1} s^{-1}). In order to stimulate transitions, the photon must have the same energy as the energy difference between the two states, given by:

$$E = h\nu$$

where E is the energy of the photon, h is Planck's constant (6.626×10^{-34} J s) and ν is the resonance or Larmor frequency. This is in the radio frequency range for typical magnetic fields and for MRI is usually at 80 MHz.

When a pulse of rf radiation is applied to a sample, it affects the sample magnetisation vector. The pulse causes the vector to be rotated from the z-axis into the x-y plane. After the rf pulse, the net magnetisation vector gradually relaxes back along the z-axis. This process is termed relaxation and may be broken into two different mechanisms. T_1 is called the longitudinal relaxation time and refers to the return of the net magnetisation to the z direction (Figure 1.6). T_2 is the transverse relaxation time and refers to the dephasing of the magnetisation in the x-y plane. T_1 and T_2 are the characteristic times for the recovery of the magnetisation to the equilibrium value.

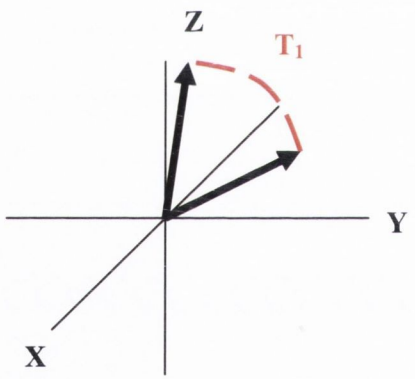

Figure 1.6 Vector models of the T_1 relaxation processes

Because the hydrogen atoms give up their absorbed energy to the surrounding tissue (lattice) in order to realign with B_0, T_1 is also referred to as the spin-lattice relaxation time.[30] On the other hand, the T_2 relaxation process does not involve dissipation of energy into the surrounding tissue or medium. Because this is a result of the exchange of energy of between spinning protons, T_2 is termed the spin-spin relaxation time. T_1 and T_2 relaxation times can vary for different tissues and hence relaxation may be used to provide image contrast. One advantage of MRI is it can

allow the imaging of the soft tissue structure of the musculoskeletal system of whole animals.[18] MRI relies on the fact that, although the magnetic moment on a single proton is extremely small, the large number of protons present in the body provides a measurable effect in the presence of a large magnetic field.[1] In order to obtain the sharpest images, a contrast agent can be employed. These can improve image quality by reducing the relaxation times and hence alter the NMR signal intensity of the water in body tissues containing the agent.[17]

There are three ways in which a contrast agent may act. It may accumulate around cells without actually penetrating or attaching to the cell wall. In this case, the contrast agent may act to image fluid filled areas of the body, e.g. the kneecapsule.[31] In the other two cases, the contrast agent may attach to the cell wall or enter the cell. The method of action strongly depends on the administration route.

The most common contrast agents currently used are paramagnetic gadolinium ion complexes. Gd^{3+} had seven unpaired electrons and has, therefore, an efficient paramagnetic relaxation mechanism. However, free Gd^{3+} is toxic and gadolinium chelates tend to be non-specific and accumulate rapidly in the liver.[18] Such problems may be overcome with the advent of superparamagnetic iron oxide MR contrast agents.[32] It has been suggested that the magnetic particles could be functionalised *via* conjugation to various monoclonal antibodies, peptides, or proteins to achieve target-directed MRI.[33, 34] However, upon conjugation to biomolecules it is important to maintain the efficiency or relaxivity of the agent. Due to restrictions of size in the extracellular space of 50 nm, it is important to produce monodisperse magnetic nanoparticles of a uniform size with a biocompatible coating. The MRI contrast agents used routinely now are non-selective and their relaxivity is strongly dependent on their particle size. Thus, there is an urgent need and demand for novel magnetic fluids with functionalised nanoparticles of an appropriate size.

Because superparamagnetic particles do not retain any residual magnetism after removal of the magnetic field, they are not as susceptible to aggregation as larger multi-domain particles. A dispersion of such small material (ca. 10nm) in the form of a magnetic fluid provides an ideal material for use as magnetic resonance (MR) contrast agents. Magnetic nanoparticles as contrast agents in MR may be used to localise and diagnose brain tumours, cardiac infarcts or liver lesions.[26]

If superparamagnetic nanoparticles can be functionalised with molecules capable of specific recognition of cell types, a localisation of tumour cells may be

possible. Veiseh *et. al.*[35] have prepared magnetite nanoparticles with a polyethylene glycol coating and have subsequently functionalised these with chlorotoxin (Cltx), a glioma tumour-targeting molecule, and the fluorescent molecule Cy5.5. Cltx is a peptide purified from the venom of the giant Israeli scorpion. They have shown that the nanoparticle-Cltx conjugates target glioma tumour cells and that this internalisation into the cells can be visualised by confocal imaging. The reported T_2 relaxation times (5 ms for the Cltx coated particles, 95 ms without) are promising for glioma detection. They have also demonstrated an affinity of these nanocomposites for glioma cells over healthy tissues.

Tumour specific monoclonal antibodies have also been conjugated to iron oxide nanoparticles in an attempt to provide an alternative contrast agent to paramagnetic gadolinium chelates, which must be administered at high concentrations to detect cancerous cells.[33] The mouse antibody L6 has been used since it possesses a surface antigen which is also present in small-cell lung carcinoma, breast carcinoma and colon carcinoma. These authors have found that with osmotic blood brain barrier (BBB) disruption, the particles can cross the BBB and be used to image the brains of rats. The relaxivities of these agents are 16.5 and 34.8 $mmol^{-1}$ s^{-1} for r_1 and r_2 respectively, which is higher than gadopentetate dimeglumine, 4.5 and 5.7 $mmol^{-1}$ s^{-1} for r_1 and r_2 respectively. This higher relaxivity shows the potential use of these antibody conjugated nanoparticles.

Dextran coated magnetic nanoparticles have been used to detect liver lesions as they have been found to be specifically absorbed into the reticuloendothelial system in the liver and the spleen.[36] This results in the shortening of the T_1 of normal liver tissue and any cancerous tissue appears darker in the T_1-weighted image. The reported r_1 value at 20 MHz and 40 °C is 24 L/mmol/s. Superparamagnetic iron oxide (SPIO) MR contrast imaging agents have been reported to have applications in bowel contrast, liver and spleen imaging, lymph node imaging,[37, 38] bone marrow imaging, perfusion imaging and MR angiography.[8] The relaxivities of typical SPIO contrast agents are 30 $mMol^{-1}$ s^{-1} and 100 $mMol^{-1}$ s^{-1} for r_1 and r_2 respectively and are substantially larger than the relaxivity of Gd-DTPA (4 $mMol^{-1}$ s^{-1} and 6 $mMol^{-1}$ s^{-1} for r_1 and r_2 respectively). Oral SPIO contrast agents are coated with a non-biodegradable and insoluble matrix (e.g. siloxanes in contrast agent AMI-121, Advanced Magnetics). This SPIO agent has undergone clinical trials and has reported T_1 and T_2 relaxivities of 3.2 and 72 $mMol^{-1}$ s^{-1} respectively. The primary particle size

is 10 nm, while the hydrodynamic radius is 300 nm. Liver and spleen imaging has been accomplished using AMI-25 (Endorem, Guerbet), which is found to rapidly accumulate there upon intravenous injection. The agent is slowly cleared from both the liver (half-life, 3 days) and spleen (half-life, 4 days).

Targeted cancer imaging has been investigated by Choi *et. al.*[39] using folate treated magnetic nanoparticles. The folate receptor is a protein which is over-expressed in various types of human tumours, where it acts to capture folate to feed rapidly dividing tumour cells. The idea here was to use dextran coated magnetic nanoparticles which were tethered to folic acid and a fluorescent imaging agent (fluorescein thioisocyanate). In this way, once the particles were internalised into the cancer cells, it was possible to obtain a tumour image *in vivo*. The resulting T_2-weighted MR images reveal a 38% decrease in the intensity of the tumour tissue owing to the presence of the folate coated nanoparticles (Figure 1.7a, b). Internalisation was also confirmed using confocal imaging of human carcinoma cells which express the surface receptors for folic acid (Figure 1.7c).

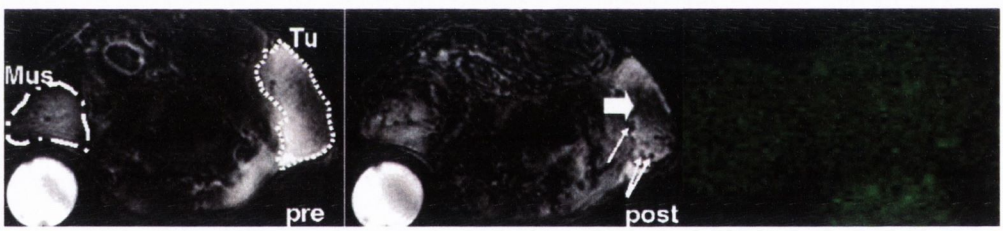

Figure 1.7 (a) (b) T2-weighted MR images of tumour cells before and after magnetic fluid administration and **(c)** confocal imaging of cells with internalised magnetic fluid[39]

MRI has a number of advantages over other instrumental diagnostic methods. First of all, MRI can provide excellent, detailed images of soft tissue *in vivo*. Secondly, MRI is a functional imaging modality, similar to nuclear medicine techniques. For instance, MRI can be used to measure blood flow in vessels or tissue perfusion or changes in blood oxygenation. Thirdly, MRI is a dynamic imaging modality. As it is apparently safe, images can be acquired continuously as with ultrasound. This allows dynamic studies to be performed for instance of the beating of the heart, the movement of joints, or the handling of a meal in the gastrointestinal tract, or the central nervous system response to external stimulus. The enormous

versatility and flexibility of MRI, and its relative safety and non-invasive nature, has led to an enormous increase in demand for scans over the last decade.[40]

1.4.1.4 Hyperthermia

The process of heating certain organs or tissues to temperatures of between 41° and 46°C for cancer treatment is called hyperthermia. Hyperthermia increases the efficiency of radiation and chemotherapy by reducing the viability of cancerous tissues and thereby increasing their sensitivity to treatment. Hyperthermia, however, does not display the more harmful side effects which chemotherapy and radiotherapy do. As far back as 1957, there have been reports of magnetic particles (20 – 100 nm) used in the treatment of lymphatic metastases in dogs by Gilchrist *et. al.*[41] They found that there was an appreciable heating of the tissues under examination and postulated that by using smaller particles with improved magnetic characteristics these particles could be heated to higher temperatures for longer periods of time, thereby increasing the damage imposed on the cancerous tissue. The first reports of using magnetic nanoparticles for intracellular hyperthermia date back to 1979, when Gordon *et. al.* treated Sprague-Dawley rats, which had spontaneous tumours, with ferrofluids.[42] Spontaneous tumours were chosen because they are most difficult to destroy and they are most closely related to human neoplastic tissue. They proved cellular uptake of the nanoparticles had been achieved using electron microscopy and also showed that heating occurred once an AC magnetic field was applied. The general hyperthermia procedure involves the injection of magnetic material into the tissue of interest, followed by the application of an AC magnetic field of the required strength and frequency to cause the particles to heat.[18] The underlying theory supporting the use of magnetic nanoparticles for this purpose is that there will be an induced current flowing through any metallic object once it is subjected to an alternating magnetic field. The amount of current produced depends on the size of the magnetic field and on the size of the object. As the current flows within the material, the metal resists the flow of current and in this way heats up by a process termed inductive heating. If the material is magnetic, this heating effect is even larger. Superparamagnetic or single-domain magnetic particles produce substantially more heat than their bulk counterparts.[43] In order to be effective, the heat generated by the particles must be at least 42°C for 30 minutes.

1.4.2 Recording devices

Data storage in modern hard disk drives is achieved by forming films of cobalt alloys which are made up of 15-20 nm magnetic grains, whose magnetic orientation can be aligned by a recording head positioned above the film. A bit of information may then be stored as a common orientation of hundreds of these grains.[44] The past five decades have seen engineers and scientists working to control the orientation of smaller and smaller magnetic materials in disk drives in order to increase their data storage capacity. Sun *et. al.*[45] have reported the synthesis of 4 nm FePt nanoparticles coated with oleic acid and oleyl amine stabilisers, which they have employed for high-density recording purposes. Once the particles were annealed at 560°C for 30 minutes, they formed a smooth ferromagnetic film. Recording studies carried out showed that the particles could support stable magnetisation reversal transitions (bits) at room temperature.

1.5 Methods of synthesis of magnetic nanoparticles

Owing to the importance of nanosized magnetic materials in a variety of fields including biotechnology, medicine, and magnetic storage and recording devices to name but a few, the preparative methods of these particles have received considerable interest in recent years. For example, if a magnetic fluid is to be employed in ink-jet printing, it must be carried in a solvent which may evaporate quickly (e.g. organic solvents). However, if the particles are required for use in loudspeakers, seals or motors, where they will remain in working gaps, often at high temperatures, a high-molecular lubricating oil must be used.[46] For use in these areas, particular attention must be paid to the synthesis of these particles as, depending on the route employed, it may be possible to tailor-make products with desired properties. Recently, synthetic research has concentrated on the preparation of monodisperse magnetic nanoparticles as, especially in biomedicine, uniformity in shape and size is an important prerequisite for use as diagnostic and treatment tools. Current methods for the preparation of magnetic nanoparticles include synthesis by coprecipitation, sol-gel processing, microemulsions, high temperature decomposition of organic precursors and aerosol/vapour methods, which will be discussed in detail.

1.5.1 Synthesis by coprecipitation

The formation of uniform particles may be achieved *via* a homogeneous precipitation reaction. The coprecipitation process involves the simultaneous occurrence of nucleation, growth, coarsening and/or agglomeration, of which the nucleation and growth processes dictate the final particle size and morphology. A short burst of nucleation occurs when the concentrations of the constituent species in the reaction reach the point of critical supersaturation. Thus, numerous small crystallites will be initially formed (nucleation), but will tend to aggregate to form larger, more thermodynamically stable particles (growth) (Figure 1.8). This growth occurs via the diffusion of solutes from the solution to the particle surface.[47]

In order to produce monodisperse nanoparticles the nucleation process should occur quite quickly and the growth process should be quite slow. These two processes should also occur separately and subsequent nucleation events should be avoided. However, if nucleation occurs during the growth process, monodispersity may still be achieved. The formation and growth of nuclei cause a decrease in the concentration of available solutes present in solution. After the initial nucleation phase, it may be assumed that there are fewer nuclei formed at a later stage, while the nuclei already present will grow at the expense of the remaining solute and smaller particles which may exist.[48] This phenomenon is known as Ostwald ripening, where the smaller particles are essentially consumed by larger ones.[49]

Without the presence of a stabiliser, the particles will tend to agglomerate. Particles may be stabilised in two main ways: (a) surfactants or capping ligands may be bound to the particle surface to create steric repulsions between individual particles and (b) charged species may be employed to generate electrostatic repulsions between particles.

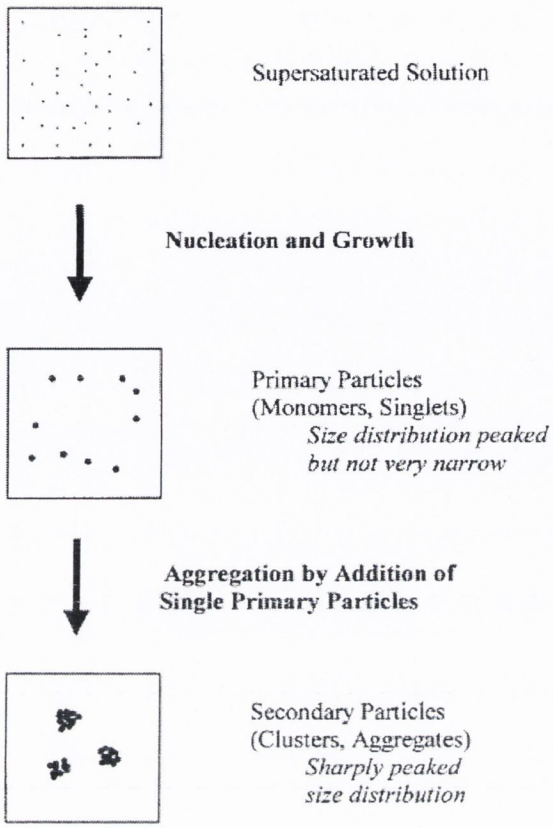

Figure 1.8 Nucleation and growth processes for nanoparticle formation [48].

Precipitation of magnetic nanoparticles from aqueous solution provides an excellent starting point for the formation of biomedical devices. This solution technique also presents a convenient way of modifying the surface of the nanoparticle. The experimental procedure for the preparation of uniform magnetite nanoparticles is a relatively simple one involving the precipitation of iron (II) and iron (III) salts in deoxygenated water by the addition of ammonia[50] or sodium hydroxide[51] solution. It is important to use the iron (II) and iron (III) solutions immediately, as goethite (α-FeOOH) may be formed in aging iron (III) solutions, while iron (II) may oxidise at low pH.[52] The size of these particles may be controlled by varying the ionic strength of the precipitation medium and the temperature. A series of experiments carried out by Qiu[53] have found that magnetite particles with a size of 6.4 nm may be achieved by using a 1.0 M sodium chloride aqueous solution in place of water. Particle size was found to increase upon heating to 70 °C.

Massart and co-workers have carried out extensive work on the preparation of magnetic fluids from nanoparticles.[53-55] Basic and acidic sols of magnetic

nanoparticles, produced *via* the coprecipitation method, have been prepared using tetramethylammonium hydroxide and perchloric acid, respectively, as stabilisers. The sols are found to have negative charges under alkaline conditions due to adsorbed OH^- ions and positive charges under acidic conditions due to H_3O^+ ions. It was found that stable sols cannot be formed in the pH range 5 – 9 due to the neutralisation of charges.

Bee *et. al.*[56] have reported the effects of citrate ions on nanoparticle formation. Citrate ions were chosen as they have been found to interfere with the formation and growth of iron oxide nanoparticles and the aim of this work was to find a correlation between decreased particle size and the presence of citrate ions. This interference is believed to occur in two steps: (a) the citrate ions chelate to the metal ions thereby preventing nucleation and (b) the ions adsorb on the nuclei surface to prevent further growth. Microscopy results indicate that the initial particle size is approximately 8 nm. With the introduction of citrate ions, this size decreases to 2 nm for a molar ratio of citrate to metal of 3%. XRD patterns are in good agreement with these results. Wang and co-workers[57] have also employed citrate ions in a large excess to produce ultrafine magnetic nanoparticles with an average particle size of 5 nm. These particles are found to oxidise at room temperature in the air to maghemite (γ-Fe_2O_3). This work has involved the study of oxygen effects during particle preparation, which leads to the formation of a mixture of iron oxides and the sharp decrease (35 %) in magnetisation values indicates the presence of some completely oxidised materials.

Markovitch *et. al.*[58] have employed the use of a stabiliser prior to particle formation to produce magnetite nanoparticles with an average size of 6 nm or 2 nm, depending on the reaction conditions. Monodisperse nanoparticles, soluble in hexane, were precipitated from a solution containing $FeCl_3$ and $FeCl_2$ in a molar ratio of 2:1, along with oleic acid. In order to achieve monodispersity in their samples, a number of size-selective precipitations were carried out (Figure 1.9).

The surface characteristics of magnetite nanoparticles produced *via* the coprecipitation technique have been studied by Sun *et. al.*[59] They have investigated the properties of magnetite nanoparticles with an average size of 12 nm and have found from zeta potential measurements that the point of zero charge (pH_{PZC}) for magnetite occurs at pH 6. At acidic pH, the zeta potential is positive and decreases with increasing pH. In acidic pH, the dominating species had been assigned as $\equiv Fe(II, III)OH_2^+$. As the pH increases, $\equiv Fe(II, III)OH$ becomes the dominant species

around pH_{PZC}. At alkaline pH, the negative zeta potential is attributed to the surface species, $\equiv Fe(II, III)O^-$.

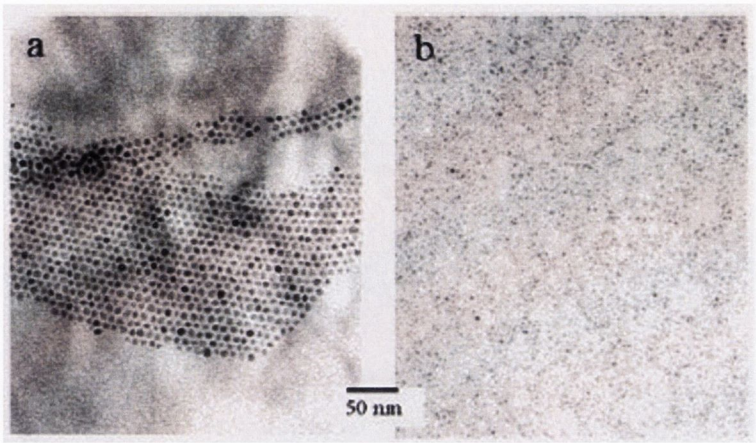

Figure 1.9 TEM images of size selected (a) 6 nm and (b) 2 nm oleic acid coated magnetite nanoparticles deposited from hexane on carbon-coated copper grids[58]

Liu *et. al.*[16] have investigated the magnetic properties of coprecipitated magnetite. They have looked for superparamagnetic behaviour in nanoparticles prepared at different temperatures. Typical superparamagnetic particles display almost immeasurable coercivity and remanence in their magnetisation curves. The authors have found the saturation magnetisation at 300 K is 50.27 emu/g, which is considerably less that that for bulk magnetite, which has a value of 92 emu/g. The decrease in magnetisation is attributed to size effects. The particle size may be calculated from magnetisation measurements from:

$$D_m = \left(\frac{18 \kappa_B T \chi_i}{\pi \rho M_s} \right)$$

where χ_i is the initial magnetic susceptibility ($\chi_i = (dM/dH)_{H \to 0}$), ρ the density of magnetite (5.18 g cm^{-3}) and κ_B the Boltzmann constant. The mean nanoparticle diameter was found to be 10 nm from TEM, but 6 nm from magnetisation measurements. The decrease in size from magnetisation may be attributed to a magnetically "dead" layer on the particle surface, i.e. the surface layer of atoms in the magnetite particles does not contribute to the magnetic properties.

Thus coprecipitation provides a simple, straight-forward method for the preparation of magnetic nanoparticles of uniform size and distribution

1.5.1.1 Mechanism for the growth of iron oxide nanoparticles by coprecipitation

At pHs higher than 8, oxidation of Fe^{2+} proceeds *via* the formation of $Fe(OH)_2$ and produces magnetite as the end product, once the atmosphere is kept oxygen free.[7, 60] In order to predict which is the most likely product to be formed in a reaction, it is often informative to look at the Gibbs Free Energy change, ΔG, for that reaction. The free energy (or chemical potential) is the driving force of the reaction and decreases until the system is at equilibrium. A certain reaction will proceed if the ΔG for the forward reaction is negative, i.e. energy is released and the products are stable with respect to their starting materials. For the reaction

$$3\ Fe(OH)_2 \longrightarrow Fe_3O_4 + H_2 + 2H_2O$$

the ΔG_r° is -33.8 kJ mol^{-1}. This means that at standard temperatures and pressures, $Fe(OH)_2$ is thermodynamically unstable and will decompose to give magnetite, hydrogen gas, and water.

Tamaura *et. al.*[61] have suggested that the formation of magnetite from air oxidation of $Fe(OH)_2$ proceeds *via* three stages: (1) formation of iron (III) oxides and slow formation of Fe_3O_4, (2) rapid formation of Fe_3O_4 and (3) a stationary or linear formation of Fe_3O_4. Infrared spectra correspond to this hypothesis, showing that band intensities for γ-FeO(OH) decrease, while those for α-FeO(OH) and Fe_3O_4 increase in the initial stage, bands for Fe_3O_4 is rapidly formed with consumption of $Fe[OH]_2$ and decrease in iron (III) oxides in the middle stage and finally Fe_3O_4 is preferentially formed in the final stage. Their findings suggest that an iron (III) oxide is formed from the oxidation of $Fe[OH]_2$ and reacts with the remaining Fe^{2+} to form Fe_3O_4. Further growth of the magnetite particles can occur by the formation of an iron (III) oxide layer on the magnetite surface by adsorption and subsequent oxidation of Fe^{2+} on the surface.

Ferric hydroxide is a poorly crystallised hydrated oxyhydroxide, made up of a short-range ordered arrangement of $Fe(O, OH, OH_2)_6$ octahedra. It has been reported that pure ferric hydroxide may be directly converted to goethite.[62] At Fe^{2+}/Fe^{3+}

ratios of greater that 0.1, this transformation is suppressed and a spinel structure is formed. The particles grow *via* a dissolution-reprecipitation process where there is an Fe^{2+}/Fe^{3+} composition of about 1/3 in average and the reprecipitated matter is non-stoichiometric magnetite. These observations are confirmed by TEM and Mössbauer spectroscopy.

1.5.2 Synthesis by thermal decomposition

In 2002, Sun and Zeng[63] reported the preparation of monodisperse magnetite nanoparticles (Figure 1.10 a, b) *via* a high temperature decomposition method. By heating a mixture of iron (III) acetylacetonate, $Fe(acac)_3$, 1,2-hexadecanediol, oleic acid and oleylamine in phenyl ether to 265 °C, they produced magnetic nanoparticles with an average size of 4 nm. To produce larger particles of 20 nm, they used these 4 nm particles as seeds and added more precursor materials. The particles were readily soluble in non-polar solvents and did not require a time-consuming size selection process. Furthermore, haematite (α-Fe_2O_3) and maghemite (γ-Fe_2O_3) nanoparticles could be produced by annealing the magnetite nanoparticles in oxygen. Since then, the reduction of $Fe(acac)_3$ has been used by many groups to produce uniform magnetic nanoparticles and studies have been carried out to investigate the size-tailoring properties by varying reaction conditions (e.g. solvent,[64-66] capping group,[64, 67] temperature,[64] reactant concentrations,[68] etc.).

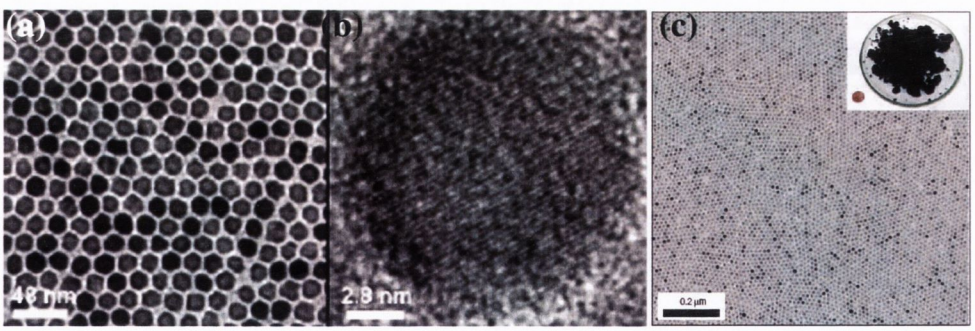

Figure 1.10 TEM images of monodisperse magnetite nanoparticles prepared *via* thermal decomposition of **(a)** **(b)**$Fe(acac)_3$ in phenyl ether in the presence of 1,2-hexadecanediol, oleic acid and oleylamine [69]; and **(c)** iron-oleate complex[70]

Hyeon *et. al.*[70] have reported the synthesis of monodisperse nanoparticles from an iron-oleate complex generated *via* the reaction of iron (III) chloride and

sodium oleate (Figure 1.10 c). This complex was heated to 320 °C in 1-octadecane and aged for 30 minutes. The resulting nanoparticles were then readily dispersible in organic solvents, such as toluene and hexane. Their studies have found that the growth process of these nanoparticles is both time and temperature dependent, e.g. no particles were produced at 240 °C after one day, but when aged for 3 days highly disperse 14 nm particles were formed. Larger particles could be synthesised by increasing the reaction temperature and by increasing the concentration of oleic acid used in the experiment.[71] The nature of the iron oxide was also found to depend on the particle size, with the smallest 5 nm particles present as maghemite (γ-Fe_2O_3) and the larger particles made up of Fe_3O_4.

High temperature decomposition reactions of iron pentacarbonyl ($Fe(CO)_5$) have been used to produce nanoparticles of cobalt, iron, iron-platinum, cobalt-platinum and iron oxide.[72-74] Monodisperse maghemite nanoparticles are found to form after reaction of $Fe(CO)_5$ with dioctyl ether and oleic acid followed by aeration of the samples to further oxidise the iron oxide.[6] This study found that as the molar ratio of stabiliser to iron precursor was increased, smaller particles were formed. The shape evolution of magnetite nanocrystals formed by thermal decomposition of $Fe(CO)_5$ in the presence of dodecylamine has also been studied by Cheon and coworkers.[75] By tuning the capping agent to iron precursor ratio, particles of different shapes and sizes can be synthesised. For example, at a ratio of 1:1 diamond, triangle and spherically shaped nanocrystals were formed.

1.5.3 Metallorganic precursors

Magnetic nanoparticle production from a metallorganic route presents a more difficult challenge, as there is a greater risk of oxidation of the metal precursor prior to particle formation. Iron oxide particles of maghemite and haematite have been prepared by the hydrolysis of iron tri-*n*-butoxide in an octanol/acetonitrile solution.[76] The particle size dependence on temperature has been investigated. It has been reported that the particle size and degree of aggregation increased with increasing temperature. Cobalt particles have been synthesised by the decomposition of the organometallic precursor $Co(\eta_3\text{-}C_8H_{13})(\eta^4\text{-}C_8H_{12})$.[77] Here, 1.5 nm particles were synthesised in the presence of polyvinylpyrrolidone. Some of the work on iron oxide particles from iron metallorganic precursors has been carried out by Gun'ko *et. al.*[78-80] For example, maghemite nanoparticles which display room temperature

superparamagnetic properties have been synthesised by the hydrolysis of the iron (II) precursor $[Fe(OBu^t)_2(THF)]_2$.[78] Further work on the metallorganic route to new magnetic nanoparticles and nanocomposites is one of the aims of this thesis, since it provides a convenient single source precursor approach for the preparation of new materials.

1.5.4 Microemulsion approach

Reverse micelles, or surfactant stabilised water-in-oil emulsions, have been successfully employed as nanoreactors for the preparation of magnetic nanoparticles. Some of the disadvantages of this method of preparation include (i) agglomeration of particles; (ii) poor particle crystallinity; and (iii) a low yield of particles, since a large volume of solvent is generally required to produce a small number of particles.[81] Pileni and coworkers have pioneered the used of water-in-oil or reverse micelles to prepare magnetic nanocrystals.[15] In a typical experiment, divalent iron dodecylsulfate is dissolved in aqueous solution to form mixed oil-in-water micelles. After addition of a base, the suspension is allowed to stir for 2 hours before washing to remove any excess surfactant. The resulting micelles are soluble in water to form an alkaline magnetic fluid or may be brought to neutral *via* the addition of citrate ions. This method is a robust one in terms of the number of materials which may be synthesised, e.g. Fe_3O_4, γ-Fe_2O_3, $Co_xFe_yO_4$ and $Co_xZn_yFe_zO_4$ have been produced.

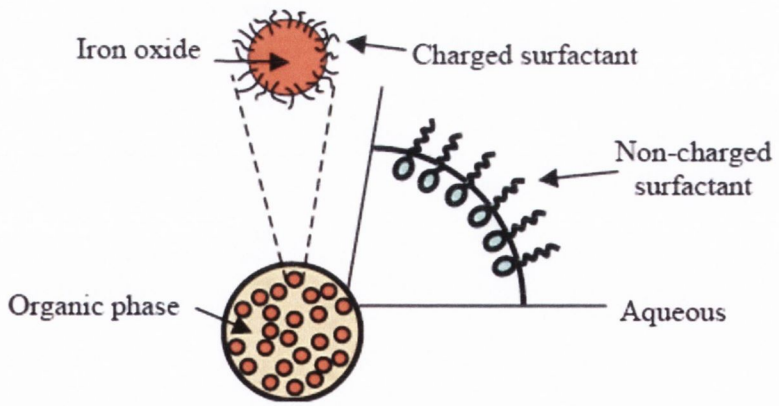

Figure 1.11 Schematic representation of an oil-in-water magnetic emulsion droplet[82]

1.5.5 Other methods of magnetic nanoparticles synthesis

Some other methods for the preparation of magnetic nanoparticles have included spray pyrolysis to produce carbonyl coated iron nanoparticles[83] and microwave synthesis of iron oxide particles from Fe (III) precursors.[84] Both of these methods involve high temperatures (between 500 and 700 °C) and may lead to the production of several iron oxide phases.

1.6 Aims and objectives of this work

The main aim of this project is to develop novel iron oxide based nanocomposites with potential biomedical applications. The major scientific and technical objectives of this work are to:

- Prepare magnetic iron oxide based nanoparticles and nanocomposites from new iron alkoxide precursors.
- Develop and investigate new silica-iron oxide nanocomposites
- Prepare new stable magnetic fluids based on functionalised iron oxide nanoparticles for MRI and other potential biomedical applications.
- Evaluate these magnetic fluids by measuring the effect of magnetic nanocomposites on the water proton spin–lattice relaxation time using the NMRD technique.
- Develop novel "two in one" fluorescent/magnetic nanocomposites for intracellular visualisation, manipulation and diagnostics.
- Characterise the nanoparticles, nanocomposites, and magnetic fluids fully using different instrumental techniques (e.g. FTIR, Raman, UV-vis, and Mössbauer spectroscopy, magnetisation measurements, NMRD).

Because of their controllable size, biocompatibility, and magnetic properties, these nanoparticles and nanocomposites present attractive applications in many fields of biotechnology and medicine. With this in mind, one aim is to prepare stable suspensions of magnetite nanoparticles of a uniform size and to study their potential as MRI contrast agents. The NMRD technique will be applied to study the efficiency of our particles in an aqueous environment. The major obstacle encountered in the preparation of magnetic fluids is the aggregation of particles. In order to overcome this, a variety of stabilisers will be employed, including functionalised siloxanes, polyelectrolytes and DNA, in the synthesis of the particles.

New magnetic composite materials will be prepared and investigated, including iron oxide-silica nanocomposites. These materials may exhibit interesting magnetic behaviour, which may be studied via Mössbauer spectroscopy and magnetisation methods.

It is hoped a new family of magnetic-fluorescent nanocomposite materials will be prepared. To date, there has been very little research in this area. These materials are expected to provide new diagnostic tools for cell labelling and both the optical and magnetic detection of these cells. Magnetic fluorescent nanocomposites might also potentially serve as agents for "two in one" hyperthermia and photodynamic therapy.

Overall, the successful realisation of this project should result in development of new magnetic nanomaterials with a broad range of potential applications.

References

[1] Q. A. Pankhurst, J. Connolly, S. K. Jones, J. Dobson, *Journal of Physics D-Applied Physics* **2003**, *36*, R167.

[2] J. Giles, *Nature* **2004**, *429*, 591.

[3] E. Klarreich, *Nature* **2001**, *413*, 450.

[4] S. J. Byrne, S. A. Corr, T. Y. Rakovich, Y. K. Gun'ko, Y. P. Rakovich, J. F. Donegan, S. Mitchell, Y. Volkov, *Journal of Materials Chemistry* **2006**, *16*, 2896.

[5] T. Rheinlander, T. Priester, M. Thommes, *Journal of Magnetism and Magnetic Materials* **2003**, *256*, 252.

[6] K. Woo, J. Hong, S. Choi, H. W. Lee, J. P. Ahn, C. S. Kim, S. W. Lee, *Chemistry of Materials* **2004**, *16*, 2814.

[7] R. M. Cornell, U. Schwertmann, *The Iron Oxides*, Wiley VCH Verlag GmbH and Co., Weinheim, **1996**.

[8] Y. X. J. Wang, S. M. Hussain, G. P. Krestin, *European Radiology* **2001**, *11*, 2319.

[9] U. Schwertmann, R. M. Cornell, *Iron Oxides in the Laboratory*, WILEY-VCH Verlag GmbH, Weinheim, **2000**.

[10] S. B. Darling, S. D. Bader, *Journal of Materials Chemistry* **2005**, *15*, 4189.

[11] D. Jiles, *Introduction to Magnetism and Magnetic Materials*, Chapman and Hall, London, **1998**.

[12] E. W. Lee, *Magnetism: An Introduction Survey*, Dover Publications Inc., New York, **1970**.

[13] R. Carey, E. D. Isaac, *Magnetic Domains and Techniques for their Observation*, The English Universities Press Limited, London, **1966**.

[14] R. V. Kumar, Y. Koltypin, Y. S. Cohen, Y. Cohen, D. Aurbach, O. Palchik, I. Felner, A. Gedanken, *Journal of Materials Chemistry* **2000**, *10*, 1125.

[15] M. P. Pileni, *Advanced Functional Materials* **2001**, *11*, 323.

[16] Z. L. Liu, Y. J. Liu, K. L. Yao, Z. H. Ding, J. Tao, X. Wang, *Journal of Materials Synthesis and Processing* **2002**, *10*, 83.

[17] P. Tartaj, M. D. Morales, S. Veintemillas-Verdaguer, T. Gonzalez-Carreno, C. J. Serna, *Journal of Physics D-Applied Physics* **2003**, *36*, R182.

[18] C. C. Berry, A. S. G. Curtis, *Journal of Physics D-Applied Physics* **2003**, *36*, R198.

[19] J. F. Schenck, E. A. Zimmerman, *Nmr in Biomedicine* **2004**, *17*, 433.

[20] I. Brigger, C. Dubernet, P. Couvreur, *Advanced Drug Delivery Reviews* **2002**, *54*, 631.

[21] L. C. Shaw, H. Pan, A. Afzal, S. L. Calzi, P. E. Spoerri, S. M. Sullivan, M. B. Grant, *Gene Therapy* **2006**, *13*, 752.

[22] E. Bullitt, D. L. Zeng, G. Gerig, S. Aylward, S. Joshi, J. K. Smith, W. L. Lin, M. G. Ewend, *Academic Radiology* **2005**, *12*, 1232.

[23] M. Stubbs, P. M. J. McSheehy, J. R. Griffiths, C. L. Bashford, *Molecular Medicine Today* **2000**, *6*, 15.

[24] A. K. Gupta, M. Gupta, *Biomaterials* **2005**, *26*, 3995.

[25] A. Petri-Fink, M. Chastellain, L. Juillerat-Jeanneret, A. Ferrari, H. Hofmann, *Biomaterials* **2005**, *26*, 2685.

[26] C. Bergemann, D. Muller-Schulte, J. Oster, L. Brassard, A. S. Lubbe, *Journal of Magnetism and Magnetic Materials* **1999**, *194*, 45.

[27] A. S. Lubbe, C. Alexiou, C. Bergemann, *Journal of Surgical Research* **2001**, *95*, 200.

[28] A. S. Lubbe, C. Bergemann, J. Brock, D. G. McClure, *Journal of Magnetism and Magnetic Materials* **1999**, *194*, 149.

[29] S. Kuckelhaus, S. C. Reis, M. F. Carneiro, A. C. Tedesco, D. M. Oliveira, E. C. D. Lima, P. C. Morais, R. B. Azevedo, Z. G. M. Lacava, *Journal of Magnetism and Magnetic Materials* **2004**, *272-76*, 2402.

[30] S. Mornet, S. Vasseur, F. Grasset, E. Duguet, *Journal of Materials Chemistry* **2004**, *14*, 2161.

[31] S. G. C. Adam, in *Europhysics News, Vol. 34*, **2003**.

[32] C. W. Jung, P. Jacobs, *Magnetic Resonance Imaging* **1995**, *13*, 661.

[33] L. G. Remsen, C. I. McCormick, S. RomanGoldstein, G. Nilaver, R. Weissleder, A. Bogdanov, K. E. Hellstrom, I. Hellstrom, R. A. Kroll, E. A. Neuwelt, *American Journal of Neuroradiology* **1996**, *17*, 411.

[34] D. K. Kim, Y. Zhang, J. Kehr, T. Klason, B. Bjelke, M. Muhammed, *Journal of Magnetism and Magnetic Materials* **2001**, *225*, 256.

[35] O. Veiseh, C. Sun, J. Gunn, N. Kohler, P. Gabikian, D. Lee, N. Bhattarai, R. Ellenbogen, R. Sze, A. Hallahan, J. Olson, M. Q. Zhang, *Nano Letters* **2005**, *5*, 1003.

[36] K. Takahama, Y. Amano, H. Hayashi, T. Kumazaki, *Journal of Nippon Medical School* **2002**, *69*, 571.

[37] R. Weissleder, G. Elizondo, J. Wittenberg, A. S. Lee, L. Josephson, T. J. Brady, *Radiology* **1990**, *175*, 494.

[38] R. Weissleder, G. Elizondo, J. Wittenberg, C. A. Rabito, H. H. Bengele, L. Josephson, *Radiology* **1990**, *175*, 489.

[39] H. Choi, S. R. Choi, R. Zhou, H. F. Kung, I. W. Chen, *Academic Radiology* **2004**, *11*, 996.

[40] P. A. Gowland, *Progress in Biophysics and Molecular Biology* **2005**, *87*, 175.

[41] R. K. Gilchrist, R. Medal, W. D. Shorey, R. C. Hanselman, J. C. Parrott, C. B. Taylor, *Annals of Surgery* **1957**, *146*, 596.

[42] R. T. Gordon, J. R. Hines, D. Gordon, *Medical Hypotheses* **1979**, *5*, 83.

[43] M. Babincova, D. Leszczynska, P. Sourivong, P. Babinec, *Medical Hypotheses* **2000**, *54*, 177.

[44] R. F. Service, *Science* **2000**, *287*, 1902.

[45] S. H. Sun, C. B. Murray, D. Weller, L. Folks, A. Moser, *Science* **2000**, *287*, 1989.

[46] K. Raj, B. Moskowitz, R. Casciari, *Journal of Magnetism and Magnetic Materials* **1995**, *149*, 174.

[47] V. K. Lamer, R. H. Dinegar, *Journal of the American Chemical Society* **1950**, *72*, 4847.

[48] J. Park, V. Privman, E. Matijevic, *Journal of Physical Chemistry B* **2001**, *105*, 11630.

[49] B. L. Cushing, V. L. Kolesnichenko, C. J. O'Connor, *Chemical Reviews* **2004**, *104*, 3893.

[50] S. E. Khalafalla, G. W. Reimers, *IEEE Transactions on Magnetics* **1980**, *16*, 178.

[51] Y. S. Kang, S. Risbud, J. F. Rabolt, P. Stroeve, *Chemistry of Materials* **1996**, *8*, 2209.

[52] A. P. Philipse, M. P. B. Vanbruggen, C. Pathmamanoharan, *Langmuir* **1994**, *10*, 92.

[53] X. P. Qiu, *Chinese Journal of Chemistry* **2000**, *18*, 834.

[54] R. Massart, E. Dubois, V. Cabuil, E. Hasmonay, *Journal of Magnetism and Magnetic Materials* **1995**, *149*, 1.

[55] R. Massart, *IEEE Transactions on Magnetics* **1981**, *17*, 1247.

[56] A. Bee, R. Massart, S. Neveu, *Journal of Magnetism and Magnetic Materials* **1995**, *149*, 6.

[57] Z. L. Liu, H. B. Wang, Q. H. Lu, G. H. Du, L. Peng, Y. Q. Du, S. M. Zhang, K. L. Yao, *Journal of Magnetism and Magnetic Materials* **2004**, *283*, 258.

[58] T. Fried, G. Shemer, G. Markovich, *Advanced Materials* **2001**, *13*, 1158.

[59] Z. X. Sun, F. W. Su, W. Forsling, P. O. Samskog, *Journal of Colloid and Interface Science* **1998**, *197*, 151.

[60] Y. Zhu, Q. Wu, *Journal of Nanoparticle Research* **1999**, *1*, 393.

[61] Y. Tamaura, P. V. Buduan, T. Katsura, *Journal of the Chemical Society-Dalton Transactions* **1981**, 1807.

[62] E. Tronc, P. Belleville, J. P. Jolivet, J. Livage, *Langmuir* **1992**, *8*, 313.

[63] S. Sun, H. Zeng, *J. Am. Chem. Soc.* **2002**, *124*, 8204.

[64] F. X. Redl, C. T. Black, G. C. Papaefthymiou, R. L. Sandstrom, M. Yin, H. Zeng, C. B. Murray, S. P. O'Brien, *Journal of the American Chemical Society* **2004**, *126*, 14583.

[65] N. Pinna, S. Grancharov, P. Beato, P. Bonville, M. Antonietti, M. Niederberger, *Chemistry of Materials* **2005**, *17*, 3044.

[66] Z. Li, H. Chen, H. B. Bao, M. Y. Gao, *Chemistry of Materials* **2004**, *16*, 1391.

[67] Z. Li, L. Wei, M. Y. Gao, H. Lei, *Advanced Materials* **2005**, *17*, 1001.

[68] J. M. Vargas, R. D. Zysler, *Nanotechnology* **2005**, *16*, 1474.

[69] Y. K. Sun, M. Ma, Y. Zhang, N. Gu, *Colloids and Surfaces A-Physicochemical and Engineering Aspects* **2004**, *245*, 15.

[70] J. Park, K. J. An, Y. S. Hwang, J. G. Park, H. J. Noh, J. Y. Kim, J. H. Park, N. M. Hwang, T. Hyeon, *Nature Materials* **2004**, *3*, 891.

[71] T. Hyeon, S. S. Lee, J. Park, Y. Chung, H. Bin Na, *Journal of the American Chemical Society* **2001**, *123*, 12798.

[72] A. Hutten, D. Sudfeld, I. Ennen, G. Reiss, W. Hachmann, U. Heinzmann, K. Wojczykowski, P. Jutzi, W. Saikaly, G. Thomas, *Journal of Biotechnology* **2004**, *112*, 47.

[73] Q. J. Guo, X. W. Teng, S. Rahman, H. Yang, *Journal of the American Chemical Society* **2003**, *125*, 630.

[74] T. Hyeon, *Chemical Communications* **2003**, 927.

[75] J. W. Cheon, N. J. Kang, S. M. Lee, J. H. Lee, J. H. Yoon, S. J. Oh, *Journal of the American Chemical Society* **2004**, *126*, 1950.

[76] M. Kimata, D. Nakagawa, M. Hasegawa, *Powder Technology* **2003**, *132*, 112.

[77] J. Osuna, D. deCaro, C. Amiens, B. Chaudret, E. Snoeck, M. Respaud, J. M. Broto, A. Fert, *Journal of Physical Chemistry* **1996**, *100*, 14571.

[78] G. B. Biddlecombe, Y. K. Gun'ko, J. M. Kelly, S. C. Pillai, J. M. D. Coey, M. Venkatesan, A. P. Douvalis, *Journal of Materials Chemistry* **2001**, *11*, 2937.

[79] Y. K. Gun'ko, U. Cristmann, V. G. Kessler, *European Journal of Inorganic Chemistry* **2002**, 1029.

[80] Y. K. Gun'ko, S. C. Pillai, D. McInerney, *Journal of Materials Science-Materials in Electronics* **2001**, *12*, 299.

[81] Y. Lee, J. Lee, C. J. Bae, J. G. Park, H. J. Noh, J. H. Park, T. Hyeon, *Advanced Functional Materials* **2005**, *15*, 503.

[82] R. Veyret, T. Delair, C. Pichot, A. Elaissari, *Journal of Magnetism and Magnetic Materials* **2005**, *295*, 155.

[83] F. Yu, J. N. Wang, Z. M. Sheng, L. F. Su, *Carbon* **2005**, *43*, 3018.

[84] D. Vollath, D. V. Szabo, R. D. Taylor, J. O. Willis, K. E. Sickafus, *NanoStructured Materials* **1995**, *6*, 941.

Chapter 2: Experimental

2.1. Characterisation techniques

2.1.1. Infrared (IR) spectroscopy

Infrared spectra are obtained from the interaction of solids with electromagnetic radiation (phonons) in the wavelength range approximately 1mm to 1 μm (10 to 10000 cm^{-1}).[1] These interactions result in the excitation of the molecules' vibrational states. A vibrating or rotating atomic group can be associated with the motion of an electric charge, especially when the charges of the atoms in a molecule are asymmetrically distributed or when the vibration of the atoms results in an asymmetry in the charge distribution. Consequently, electromagnetic radiation of a particular frequency can only be absorbed by a molecule if there is a change in the dipole moment associated with the vibrational excitation of the atomic group concerned. Vibrations which show no change in the dipole moment are infrared inactive.[2] A transmission infrared spectrum is a plot of the percentage radiation absorbed versus the frequency of the incident radiation in wavenumbers (cm^{-1}). FTIR spectra (200-4000cm^{-1}) were recorded by diffuse reflectance using a Perkin Elmer Spectrum One FT-IR spectrophotometer. Samples were pressed into KBr disks and spectra were recorded.

2.1.2. Raman spectroscopy

The Nobel Prize in Physics was awarded to the Indian physicist Chandrasekhara Venkata Raman in 1930 "for his work on the scattering of light and for the discovery of the effect named after him". The Raman spectroscopy technique is based on the interaction of electromagnetic radiation with a molecule. The interaction of photons with a molecule can yield three phenomena: absorption, emission and scattering. Absorption and emission occur when the photon involved has the same energy as the difference in energy between two energy levels of the molecule under investigation. Scattering occurs as an immediate effect (~ 10^{-14} s) of the interaction of the photon with the molecule, where the photon does not have the same energy as the difference in two energy levels of the molecule. Photons may be scattered in two ways: elastically (also called Rayleigh scattering) where there is no

net change in energy of the incident photon or with a change in energy (Raman scattering).

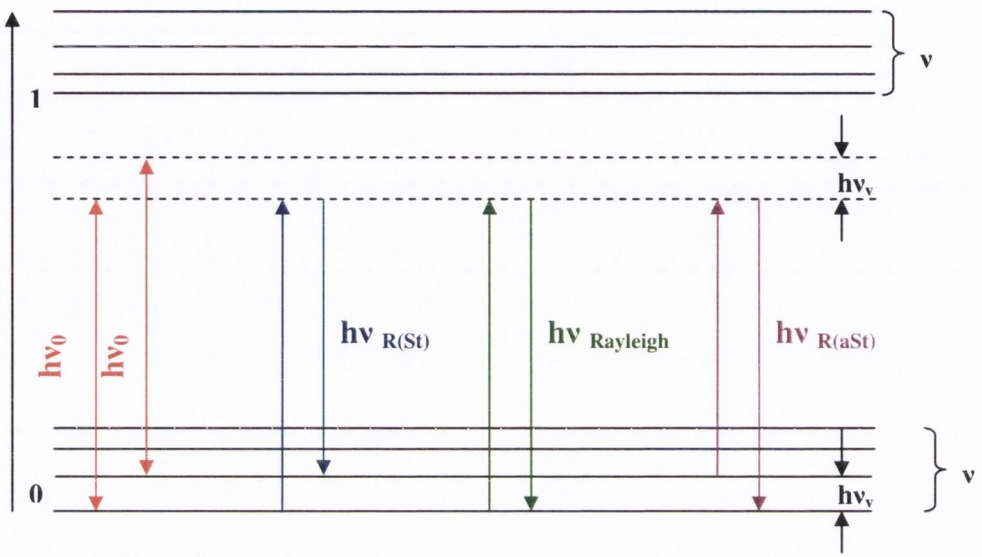

Figure 2.1 Possible scattering events in Raman spectroscopy, 0 is the ground state and 1 is the first excited state. Reproduced from [3]

The solid lines in Figure 2.1 denote vibrational energy states, while the dotted lines are for virtual energy levels in the molecule separated by energy $h\nu_v$ (where ν_v is the frequency of one of the possible normal vibrations of the molecule). When the photon with initial energy $h\nu_0$ interacts with the molecule, it may proceed with a loss of energy $h\nu_{R(St)}$ (Stokes scattering, smaller than ν_0) or with an increase in energy $h\nu_{R(aSt)}$ (anti-Stokes scattering, greater than ν_0). If there is no net change, this results in Rayleigh scattering, $h\nu_{(Rayleigh)}$. Rayleigh scattering results in a line of strong intensity in the resulting Raman spectrum, which can be 10^3-10^4 times great than Stokes and anti-Stokes Raman bands.[3] The energy difference between the frequencies of the incident photon and the scattered photons are the same and equal to the molecular vibration frequency:

$$h\nu_0 - h\nu_{R(St)} = h\nu_v \qquad \nu_0 - \nu_{R(St)} = \nu_v$$
$$h\nu_{R(aSt)} - h\nu_o = h\nu_v \qquad \nu_{R(aSt)} - \nu_0 = \nu_v$$

Hence, the difference in frequency between the exciting radiation and the scattered radiation is characteristic of the molecule under study and is independent of

the frequency of the exciting radiation. Boltzmanns law states that the population of the first excited state is much smaller than that of the ground state at room temperature. Hence, the intensity of the anti-Stokes Raman bands is much lower than the Stokes bands. For this reason, it is the measurement of Stokes bands which are of most importance in Raman spectroscopy. When a molecule is placed in an electric field, there may be an induced dipole moment (μ_{ind}) where the centre of negative charge in the molecule is shifted with respect to the central positive nuclear charge. The degree of this shift is proportional to the intensity of the applied electric field, E:

$$\mu_{ind} = \alpha E$$

α is a proportionality constant, called the polarisability, which is characteristic of the molecule. The degree of polarisability of a molecule depends on the mobility of its electrons and is always a non-zero quantity. It is a function of the shape and size of the molecule and is usually anisotropic, i.e. varies with the direction in space. Because the Raman phenomenon is a result of the interaction of photons with the electrons of the molecule in question, the resulting change in the polarisation of each bond will have an effect on the Raman intensity and frequency of the bands observed.

When Raman spectroscopy is combined with infrared spectroscopy, a picture of the vibrational spectrum of a molecule in the ground state can be built up. If the vibration results in a change in the dipole moment of the molecule, it is IR active. To be Raman active, the vibration must result in a change in polarisability in the molecule. There is a rule of mutual exclusion, originating from group theory, which states that if there is a centre of symmetry in the molecule, a vibration which is active in the infrared spectrum is inactive in the Raman and vice versa.[3] If there is no centre of symmetry in a molecule, a number of vibrations may exist in both spectra. Totally symmetric vibrations are better, or sometimes only, seen in the Raman spectrum. Raman spectra were measured with a Renishaw 1000 micro-Raman system. The excitation wavelength was 514.5 nm from an Ar^+ ion laser (Laser Physics Reliant 150 Select Multi-Line) with a typical laser power of 3 mW in order to avoid excessive heating. The 100 × magnifying objective of the Leica microscope was capable of focusing the beam into a spot of approximately 1 μm diameter.

2.1.3. X-Ray Diffraction (XRD)

X-ray diffraction (XRD) involves the interaction of electromagnetic radiation with a wavelength (λ) of approximately 0.1 nm, with the atoms in the solid.[4] Because the distances between the atoms in a crystal structure are comparable with the wavelength of the incoming radiation, crystals can diffract X-rays. The variation in the resulting intensities is caused by regions of constructive and destructive interference called a diffraction pattern. Depending on the interference conditions, each atom plane produces a series of *n* reflections. From the patterns obtained, the interlayer spaces (d_{hkl}) can be calculated using the Bragg equation.

The Bragg equation

$$\sin\theta = \frac{n\lambda}{2d}$$

$$n\lambda = 2d\sin\theta$$

describes the diffraction of x-rays by a crystal as reflection from the net planes. θ is the glancing plane (2θ is the diffraction angle) and d is the net plane spacing.

The x-ray diffraction pattern obtained is a plot of diffracted x-ray intensity against diffraction angle. The diffraction intensity is a function of the unit cell contents while the diffraction angle is function of the unit cell dimensions. The outcome of this is that identical unit cells with the same contents give the same diffraction pattern, i.e. each compound has its own set of characteristic d values and intensities which can be used for identification. Therefore, the diffraction pattern is like a fingerprint of the specimen. This fingerprint may exhibit slight changes between samples, however. The half widths of the reflections are inversely proportional to the crystallite sizes and directly proportional to the concentration and magnitude of structural defects. The cell constants, crystal system and space group of the specimen may be determined from the powder diffraction pattern. For a cubic crystal system,

$$\frac{1}{d} = \frac{h^2 + k^2 + l^2}{a^2}$$ where a is a cell constant

From squaring the Bragg equation,

$$\sin^2\theta = \frac{\lambda^2}{4d^2}$$

it may be taken that

$$\sin^2\theta = \frac{\lambda^2}{4a^2}(h^2 + k^2 + l^2)$$

If cell constants have been worked out, all reflections can then be indexed. For X-rays, the crystallite size does not begin to affect the diffraction pattern until the crystallites (or, more precisely, the coherent scattering domains) become smaller than 0.5 μm. Scherrer, in 1918, derived an equation to describe the broadening of a reflection in terms of the crystallite size:

$$D = \frac{K\lambda}{B\cos\theta}$$

where D is the crystallite size, K is a constant (taken as 0.9), λ is the wavelength of the radiation employed (for all measurements in this thesis, λ = 1.5406 Å) and B is the line broadening. This broadening is measured from the increased peak width at half peak height, obtained from the Warren formula:

$$B = \sqrt{B_m^2 + B_s^2}$$

where B_m is the measured peak width at half height and B_s is the standard peak width at half height obtained from a commercial sample. It should be noted that the error of determination is 20-30%. For this reason, sizes determined from XRD will differ slightly from electron microscopy size analyses.

In order to produce an XRD pattern a monochromatic beam of X-rays is required. This is produced by hitting an anode of a pure sample of a particular metal with high energy electrons in a sealed vacuum tube. Once a pure metal is used, the wavelength of the X-ray beam produced may be known. Copper is the most commonly used metal for this purpose and the strongest wavelength produced is 1.5406 Å. The main aim of XRD analysis is to identify the crystalline phases present in the sample. The phases can be identified by comparison of the sample data (peaks and relative intensities) with a set of standard references provided by the Joint Committee on Powder Diffraction Standards (JCPDS) database.

X-Rays cause relatively little damage to an objects surface, unlike electrons which have a scattering power several orders of magnitude greater, which leads to more radiation damage. X-ray analysis generally deals with crystalline matter, either single crystals or crystalline powders.

A lattice is a repeating structure of points in space and the lattice constant refers to the distance between unit cells in a crystal lattice. Three dimensional lattices

generally have three lattice constants, referred to as *a*, *b* and *c*. In the case of cubic crystal structures, all of the constants are equal and are only referred to as *a*. Figure 2.2 depicts the lattice points, rows and planes. The origin has been denoted 000 and the a, b and c axes intersect at this origin.

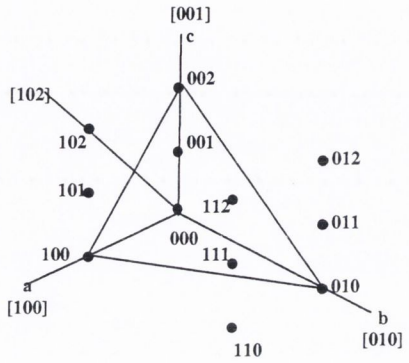

Figure 2.2 Notation of lattice points, rows and planes

Figure 2.2 depicts lattice points, which are given as a set of three numbers without any brackets – 100, 101, 110, 102, etc. 100 is a point which is one unit along the *a* axis, 101 is at a point one unit from *a* and *c*, etc. The Lattice planes are defined in terms of Miller indices, which are reciprocals of the intercepts of the planes on the coordinate axes. In Figure 2.2, the plane intercepts the *a* axis at 100, the *b* axis at 010 and the *c* axis at 002 (see the triangle). The Miller index is thus given as (221), i.e. the reciprocal of the points at *a*, *b* and *c* given as whole numbers. So, a Miller index refers to a family of parallel lattice planes at a distance of *d* apart perpendicular to that plane.

Magnetite, maghemite and cobalt ferrite have the same cubic structure and their lattice constants differ by only a small amount, where *a* is 0.839, 0.834, and 0.838 nm respectively.[5] X-Ray powder diffraction was performed using a Siemens-500 X-Ray diffractometer. Powder samples were deposited on silica glass using silica gel to adhere the sample to the glass surface. Overnight spectra were run for all samples. Diffractograms were then compared to the JCPDS database.

2.1.4. Mössbauer spectroscopy

Rudolf Mössbauer discovered the nuclear Mössbauer effect in 1958, for which he received the Nobel Prize in 1961. Mössbauer established the experimental

conditions as well as theoretical description of the occurance of the nuclear resonant absorption (or fluorescence) of γ-rays. A nucleus in the excited state (energy E = E_e) has a certain lifetime, τ. In order to return to the ground state (E_g), energy is released by the emission of a γ-quantum of energy:

$$E_0 = E_e - E_g$$

A nearby nucleus in the ground state may absorb this γ-quantum of energy and be promoted to the excited state. This is a phenomenon known as nuclear resonant absorption of γ-rays. The mean lifetime of excited states of the Mössbauer isotopes are in the range of $10^{-6} - 10^{-9}$ s. Once a spectrum is obtained, a standard reference is required against which other signals can be referred.

The resonance spectrum is very sensitive to energy variations of the γ-radiation. The surrounding electrons interact with the positively charged nucleus, which are termed hyperfine interactions. This perturbation shifts or splits degenerate nuclear levels. The interactions observable by Mössbauer measurements are the isomer shift (δ), magnetic splitting and quadrupole splitting interactions.

Pileni *et. al.* have reported the Mössbauer spectra of 3 nm $CoFe_2O_4$ nanocrystals. They have found that as the temperature increases, there is a broadening of the lines and the appearance of a doublet, whose intensity grows at the expense of the sextet. This observation is characteristic of superparamagnetic material. Mössbauer spectra were carried out using a ^{57}Fe source in a Rhodium matrix. The model drives were MR250 and MR260, with Princeton amplifiers.

2.1.5. Magnetisation measurements

Magnetisation measurements were carried out on a SQUID (Superconducting Quantum Interference Device) magnetometer, which are currently the most sensitive magnetometer devices available. In order to make measurements, it is necessary to cool the device with liquid helium (4 K). Advantages a SQUID has over other vibrating sample magnetometers are that, along with an increased sensitivity for the detection of magnetic fields, measurements can be made over a wide temperature scale (4 to 300 K).

2.1.6. Electron Microscopy

Transmission electron microscopy (TEM) images were taken on a Hitachi H-7000. The TEM was operated at a beam voltage of 100 kV. Samples for TEM were prepared by deposition and drying of a drop of the powder dispersed in ethanol or distilled water onto a formvar coated 400 mesh copper grid. Scanning electron microscopy (SEM) images of the samples were obtained using a Hitachi S-4300 scanning electron microscope, which was operated at 5.0 kV. Samples were stuck to an aluminium stub and then gold-coated before imaging.

2.1.6.1.Transmission Electron Microscopy (TEM)

The first transmission electron microscope was developed by Max Knoll and Ernst Ruska in 1931. It is similar in design to a traditional light microscope, with the main difference being that an electron beam, instead of a light source, is used to visualise the sample. The electron microscopy technique uses a beam of high energy electrons to provide information on a specimen, including the topography (surface features), morphology (size, shape and distribution of the particles), composition (elements making up the sample may be determined) and crystallographic information (the atomic arrangement and lattice spacings may be studied).

An electron source (traditionally a thermionic gun) provides a stream of electrons, which are then accelarated towards the sample using a positive electrical potential. Two condenser lenses focus the electrons into a steady, narrow beam. Apertures and lenses focus this monochromatic beam onto the sample. The first lens determines the spot size and the second lens allows the spot to be pinpointed onto the sample. High angle electrons (those which are not moving directly down the optical path) may be blocked out by using a condenser aperture. When the electron beam is transmitted through the sample, only the electrons which are not blocked by the sample are allowed through. This produces an image which is passed down through the column through a series of lenses. When the electrons reach the bottom, a phosphor image screen generates light which allows the user to view the image.

A series of interactions occur between the sample and the electron beam and these may be utilised to determine the physical and chemical properties of the sample (Figure 2.3). When electrons from the beam encounter a nucleus in the sample, the resulting Coulombic attractions result in the deflection of the electrons path. Some of

these interactions and the resulting information which may be obtained from them are outlined below.

- Unscattered electrons. These electrons are transmitted through the sample without any interactions with the specimen. Their occurance depends on the thickness of the sample. The brightest areas of the image are those which have the greatest concentration of unscattered electrons. The darker areas are those which have interacted with the incoming electron beam and have scattered the electrons.

- Elastically scattered electrons. These electrons have deviated from their original path because of interactions with the sample. However, their interaction has caused no loss of energy to the sample. Because the electrons are scattered according to Bragg's Law, they will be scattered by the same angle when they come into contact with the same atomic spacings. These elastically scattered electrons can be collected to form a diffraction pattern of the sample.

- Inelastically scattered electrons. These interactions are similar to those above, except in this case there is a loss of energy to the surroundings. The magnitude of the energy loss will depend on the element the electrons have interacted with. The energy lost can excite vibrations at the surface of the sample and the resulting energy loss peaks can be observed. This technique is called Electron Energy Loss Spectroscopy (EELS).

One drawback to TEM is that the amount of clustering in the sample could be overestimated due to possible aggregation during the sample preparation. Also, to report statistically significant results a large number of crystal sizes are required.

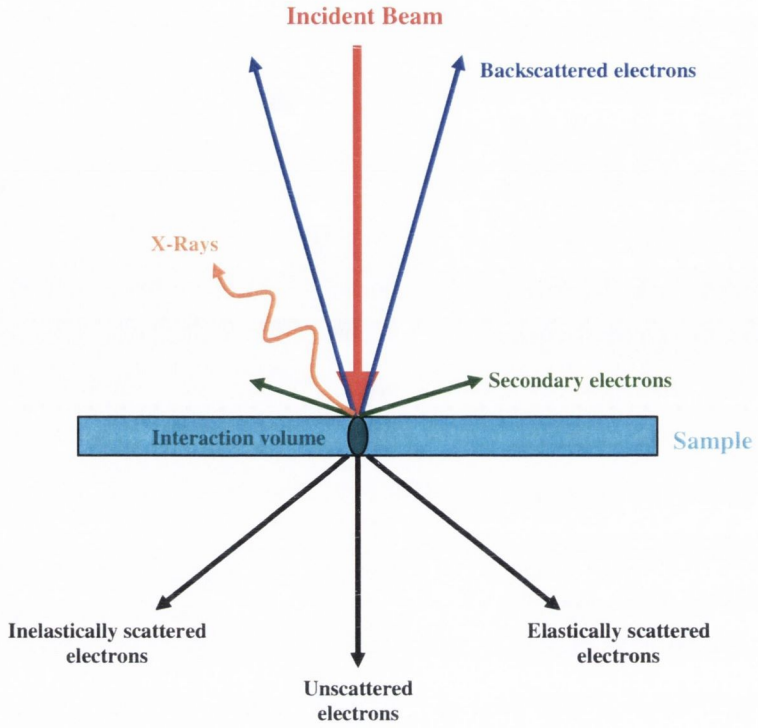

Figure 2.3 Electron interactions which occur in electron microscopy

2.1.6.2.Scanning Electron Microscopy (SEM)

Scanning electron microscopy (SEM) scans a beam of focused high energy electrons across the surface of the sample to be characterised. Again, there are interactions of the beam with the sample. The most important interactions in SEM are detailed below.

- Backscattered electrons. When electrons interact with the sample, they may encounter the nuclei of atoms within that sample. The negatively charged electron will be attracted to this positive charge and gravitate towards it. If they interact at an angle close to that of the incident beam, they may be backscattered. The fast moving electrons can circle the nucleus and come back out of the sample. The production and number of backscattered electrons produced depends on the atomic number of the specimen being imaged. The higher the atomic number, the more likely it is to have an interaction of the electrons with the nucleus. These backscattered electrons may be used to produce an image which will give details of the specimen in terms of the

elements which make it up - a brighter image will be found for higher atomic numbered elements.

- Secondary electrons. These are formed when the electrons interact with the electrons of the sample, instead of the nucleus. When this happens, the incoming electrons will loose some energy to the sample electrons. This results in a slight deflection in the path of the incoming electron and the ionisation of the sample electron. The ionised electrons exit the sample at a slower pace than backscattered electrons and are termed secondary electrons. Secondary electrons are then collected by a detector with a positive potential applied to it. Because of their low energy, only secondary electrons produced near the surface of the sample may be collected. These give an impression of the topography of the surface and are most important in the SEM technique.
- X-Rays. Once a secondary electron is produced, there is a resulting vacancy in the shell (usually the K-shell) of the ionised atom. A higher energy electron in an outer energy level can "fall" down to the lower level and fill this vacancy. As the electron falls, it emits its excess energy in the form of X-rays. The X-rays produced are characteristic of the element in the sample and can be detected and separated into an energy spectrum, to give an elemental composition of the sample, in a technique called Energy Dispersive X-ray Analysis (EDX).

2.1.7. Thermal Gravimetric Analysis (TGA)

Thermal analysis measures the changes in physical properties of a substance as a function of temperature.[6] In order to determine mass changes in the sample, a thermobalance is used. This combines a microbalance with a furnace and temperature programmer. The sensitivity of the thermobalance used is 1 μg. There may be considerable differences found when solid samples of similar chemical composition are heated. This may be due to defects, porosity or surface properties of the sample. In general, ground powders behave very differently to their bulk counterparts. Small samples are preferred for TGA, as large masses can lead to non-homogeneous heating throughout the sample. The signal output, or TGA trace, may be electronically differentiated to give a derivative thermogravimetric (DTG) curve.

The TGA was carried out on a Pyris 1 TGA from Perkin Elmer and the samples were burned in air at a constant heating rate of 10 °C/min from 30 to 900 °C.

2.1.8. Ultraviolet (UV), fluorescence spectroscopy and Confocal Microscopy

UV-Visible absorption spectra (200-700nm) were recorded using a Cary 300 scan UV-Vis spectrophotometer. A pair of double side frosted quartz cells with a light path of 1 cm and a volume capacity of ≥3 mL were used in all UV experiments. Fluorescence spectra were performed on a LS-50B Perkin Elmer luminescence spectrometer, with a 150W Xenon lamp. A quartz cell with four polished windows and a 3.5 mL volume capacity was employed in all fluorescence spectroscopy measurements. For confocal microscopy, the human THP-1 monocyte cell line was obtained from the European Collection of Animal Cell Cultures (ECACC, Salisbury, UK). Cells were grown in RPMI 1640 medium supplemented with 10% heat-inactivated fetal bovine serum, 2 mM l-glutamine/L, 100 μg penicillin/ml and 100 mg streptomycin/ml, and incubated at 37 °C in 5% CO_2. To induce monocyte to macrophage differentiation, THP-1 cells were cultured in the presence of 100 ng/ml PMA for 72 hours. Cells were then washed three times with HBSS before use. THP-1 cells were incubated with a 1 in 100 dilution with the nanocomposite material. Live cell imaging was performed in Lab-Tek chambered coverglass slides (Nunc). Images were acquired by fluorescence microscopy (Nikon Eclipse TE 300) and on the UtraView Live Cell Imager confocal microscopy workstation (Perkin-Elmer Life Sciences, Warrington, UK) (Nikon Eclipse TE 2000-U). Processing was performed using Ultra View LCI.

2.1.9. Nuclear Magnetic Resonance Dispersion (NMRD) techniques

The Nuclear Magnetic Resonance Dispersion (NMRD) technique allows tracking of the proton relaxivity profile over a wide range of magnetic fields (Figure 2.4). By checking the field dependence on the proton longitudinal relaxation rate a profile of the colloidal aqueous suspension may be built up. The spin lattice relaxivity, r_1, is related to the observed spin lattice relaxation time, T_1 as follows:

$$R_{1(obs)} = \frac{1}{T_{1(obs)}} = \frac{1}{T_{1(diam)}} + \frac{1}{T_{1(para)}}$$
$$= \frac{1}{T_{1(diam)}} + r_1[Fe] \quad (1)$$

where $T_{1(diam)}$ is the native relaxation time of the supporting fluid (water) and r_1 is the relaxivity of the agent.

It is the coupling of proton spins with larger magnetic moments which enhances the relaxation of water and allows the use of these magnetic materials as contrast agents for MRI. The relaxation process occurs because of interactions between water protons and the magnetic entity. There are two theories which help to explain this interaction.[7] Inner and outer sphere theories describe the relaxation mechanisms for paramagnetic ions. Inner sphere theory deals with the exchange which may occur between coordinated water molecules and the bulk water surrounding the sample. Outer sphere theory applies to the relaxation induced by the diffusion of water molecules in the local magnetic gradients of the paramagnetic hydrated species. The inner sphere component of the relaxation provides the larger contribution, since the distance between a paramagnetic ion and a coordinated water molecule is shorter than between a hydrated ion and a diffusing water molecule.

In order to determine the iron concentration required to calculate the relaxivity of the magnetic fluid, atomic absorption spectroscopy was employed. This determination must be carried out with the utmost care, as an incorrect iron determination could greatly distort the relaxivity values in the NMRD profile. The atomic absorption method has the advantage that it is highly sensitive and accurate for the determination of iron. A solution of iron is atomised by mixing with acetylene and igniting it in a flame. Once atomised, the free element can absorb its characteristic wavelength. For iron, this wavelength is 248.3 nm. A Fe-cathode lamp is shone through the flame containing the sample. The monochromator detects the spectrum line emitted by the sample and a photomultiplier detects the amount of light absorbed by the sample and this can be directly related to the amount of element in the sample.

To determine the amount of iron present in a given sample, a known volume was taken (typically between 0.3 and 0.5 mL) immediately following an NMRD experiment. The iron oxide nanoparticles were dissolved *via* the addition of several

drops of concentrated HCl. A yellow solution formed which was then boiled on a hotplate. Once the volume of the solution was reduced to a few drops, 25 mL Millipore water was added and the solution was returned to the hotplate. After boiling for several minutes, the solution was cooled to room temperature, transferred to a volumetric flask and made up to the mark with Millipore water. The resulting atomic absorption of this solution was measured against a set of standard solutions containing 0.5, 1.0, 1.5, 2.0, and 2.5 mM iron. The absorbance values, when plotted, gave a straight line which could be used to determine the unknown solution concentration. An example of one of the calibration curves is shown in Figure 2.5.

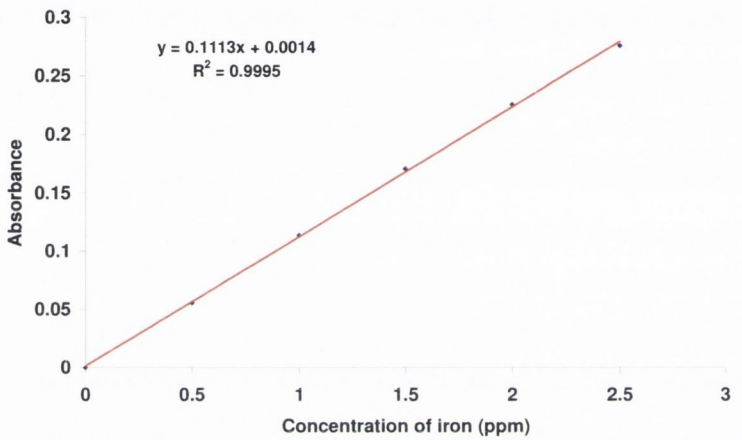

Figure 2.4 Standard calibration curve for iron concentration determinations in the range 0.5 – 2.5 mM iron by atomic absorption spectroscopy

^{1}H NMR and ^{13}C NMR spectra were recorded using a Bruker Avance DPX400 NMR instrument. ^{28}Si NMR spectra were recorded using a Bruker MSL 300 high-field multi-nuclear NMR instrument. All NMR spectra were obtained using d-DMSO, $CDCl_3$ or C_6D_6 dried over sodium metal. ^{1}H T_1 measurements (NMRD) were made in the frequency range 10 kHz-20 MHz using a Spinmaster Fast Field Cycling Relaxometer operating at a measurement frequency of 9.25 MHz.

2.1.10. Photo-Correlation Spectroscopy (PCS)

Photon correlation spectroscopy (PCS) or dynamic light scattering (DLS) may be employed as a sizing technique for measuring particles in the sub-micron range.[8-10] It is a non-destructive technique, which gives information not only on the average particle size, but also measures the width of the particle distribution called the

polydispersity index (PDI). While electron microscopy measures the primary particle size of a dry sample, photon-correlation spectroscopy probes the diffusion process allowing the determination of the hydrodynamic radius of the sample, which is generally some percent higher.[11]

Small particles suspended in fluid may undergo random movements, called Brownian motion. Photo-correlation spectroscopy uses the Brownian motion of the particles to alter the intensity of light diffused by the suspension when irradiated by a laser beam. Mathematical analysis of this alteration allows determination of the mean hydrodynamic volume and hence diameter of the particles in the suspension.

PCS gives intensity-weighted means and polydispersities of the hydrodynamic radius. The hydrodynamic size of coated nanoparticles is greater than the core sizes, usually measured by TEM. This is because, with the addition of a shell around the primary particles, the hydrodynamic radius is increased. Also, intensity- and volume-weighted (hydrodynamic) sizes are larger than volume- and number-weighted sizes.[10] Photon correlation spectroscopy measurements were carried out using a Malvern High Performance Particle sizer at 25 °C. Aqueous samples were placed in disposable cuvettes and loaded into the sample chamber. A low power (60 mW) He-Ne laser, with a wavelength of 632.8 nm, was used as the light source and the measurements were made at a detection angle of 7 ° (backscatter).

2.2. Starting materials

Ferric chloride hexahydrate ($FeCl_3 \cdot 6H_2O$) and ammonium hydroxide (NH_4OH, 0.88M) were obtained from BDH Chemicals. Ferrous chloride tetrahydrate ($FeCl_2 \cdot 4H_2O$), sodium tert-butoxide ($NaOBu^t$), iron (II) bromide ($FeBr_2$), 4,4',4'',4'''-(21H, 23H-porphine-15, 10, 15, 20-tetrayl) tetrakis (benzoic acid), Protoporphyrin IX, sodium silicate, tetramethylammonium hydroxide (TMAH), potassium bromide (IR grade) and acridine orange base were obtained as powders from Aldrich. Herring and Salmon sperm DNA were obtained in dry form from Sigma and were stored at 4 °C. Poly(allylamine hydrochloride) and Poly(sodium 4-styrenesulfonate), both in powder form and of an average molecular weight of 70,000 g, were obtained from Aldrich. Tetraethylorthosilicate ($Si(OEt)_4$) and 3-aminopropyltriethoxysilane were obtained in sure-seal bottles under argon from Aldrich to prevent polymerisation with water from the air.

2.3. Solutions and solvents

2.3.1. Dry solvents

Tetrahydrofuran was purified by standing over potassium hydroxide overnight to remove any peroxides. The solvent was then distilled over calcium hydride. Finally, to ensure the solvent was water free, it was distilled over a sodium-potassium alloy and benzophenone under argon and then condensed into a reaction flask. Benzophenone forms a blue ketyl once the solvent is dry. Methanol was dried over magnesium turnings prior to use and distilled. Millipore water was deoxygenated by boiling for 30 minutes and drying under argon.

2.3.2. Buffer solutions

3 mM phosphate buffer, pH 7.3, was made up of potassium dihydrogen phosphate (0.023 g; 1.66×10^{-4} mol), potassium hydrogen phosphate (0.023 g; 1.33×10^{-4} mol) and sodium chloride (0.876 g; 1.49×10^{-2} mol) dissolved in 100 mL Millipore water. The pH of the buffer was tested and found to be 7.2. Spectroscopic grade solvents were used for UV and fluorescence spectroscopy, except where THF was used, which was distilled prior to use.

2.4. Experimental procedures

2.4.1. Experimental details for Chapter 3

All manipulations were carried out under vacuum or argon by Schlenk techniques using a vacuum line with a fitted liquid nitrogen trap.

2.4.1.1. Preparation of heterometallic precursor $[(THF)NaFe(BuO^t)_3]_2$ (1)

$NaOBu^t$ (5.49 g, 0.057 mol) was added to $FeBr_2$ (4.03 g, 0.018 mol) in THF (50 ml). The mixture was stirred for 24 h at the ambient temperature. A grey precipitate and black filtrate was formed. After settling overnight, this was filtered under argon. The filtrate was dried under vacuum to give green crystals of **1** (Yield: 4.08 g, 61 %), which were analysed by IR and NMR spectroscopy.

IR (Nujol, cm^{-1}): 3401 (br), 1020 (s), 1019 (s), 979 (w), 799 (s), 554 (s).

^1H NMR (δ, ppm): 12.3 (br, 36H, μ_2-OBu^t), 10.4 (v. br., 8H, THF), 5.2 (br, 8H, THF), -3.5 (v. br., 18H, μ_3-OBu^t).

2.4.1.2. Preparation of magnetite nanocrystals from heterometallic precursor, $[(THF)NaFe(BuO^t)_3]_2$

$NaOBu^t$ (5.49 g, 0.057 mol) was added to $FeBr_2$ (4.03 g, 0.018 mol) in THF (50 ml). The mixture was stirred for 24 h at the ambient temperature. The mixture was carefully hydrolysed by Millipore water (40 cm^3) under argon. The resultant mixture was stirred for one hour, after which 10ml Millipore water was added. The reaction vessel was then ultrasonically (30 kHz, 130 W) irradiated at the ambient temperature for 2 hours at the required temperature. The water layer was removed and further 40ml-distilled water was added. The reaction vessel was returned to the ultrasonic bath for 1 hour. After each hour, the water layer was removed and replaced with 40mL-distilled water to achieve a neutral pH. When each experiment was completed, a black precipitate remained which was washed with 20mL ethanol, followed by 10mL acetone. The product was then dried in vacuum at room temperature to give a black powder of Fe_3O_4 (yield: 0.46 g, 93.3 %). The black powder was characterised by IR, Raman and Mössbauer spectroscopy, TEM and SEM, Magnetisation measurements and XRD patterns. This experiment was repeated 9 times at different temperatures and ultrasonic treatment times in order to establish the optimum reaction conditions for magnetite nanocrystal formation. The details are given in Table 1.

Table 2.1 Experimental design for 2.5.2.2.

Factorial 1			Factorial 2		
Sample	Time (hours)	Temperature (°C)	Sample	Time (hours)	Temperature (°C)
S1	4	20	S6	8	30
S2	8	20	S7	10	30
S3	4	70	S8	8	80
S4	8	70	S9	10	80
S5	6	50			

IR (KBr, cm^{-1}): 3391 (br), 1627 (s), 586 (br), 448 (br).

2.4.2. Experimental details for Chapter 4

All manipulations were carried out under vacuum or argon by Schlenk techniques using a vacuum line with a fitted liquid nitrogen trap.

2.4.2.1. Preparation of metallorganic precursor, $[Fe(OBu^t)_2(THF)]_2$ (2)

$NaOBu^t$ (0.42g, 4.32mmol) was added to $FeBr_2$ (0.46g, 2.13mmol) in THF (approx. 100ml). The mixture was stirred for 24 hours at the ambient temperature. A grey precipitate and dark filtrate was formed. After settling overnight, this was filtered under argon and the filtrate dried under vacuum. This yielded a green powder of **2** (Yield: 0.746 g, 64 %) which was characterised by IR and NMR spectroscopy.

IR (Nujol, cm^{-1}): 3411 (br), 1022 (w), 957 (w)

^1H NMR (δ, ppm): 3.6 (br, 8H, THF), 1.4 (br, 8H,), 1.1 (br, 18H, μ_2-OBu^t), 0.3 (br, 18H, terminal-OBu^t).

2.4.2.2. Preparation of iron oxide-silica nanocomposites from a metallorganic precursor

$NaOBu^t$ (0.42g, 4.32mmol) was added to $FeBr_2$ (0.46g, 2.13mmol) in THF (approx. 100ml). The mixture was stirred for 24 hours at the ambient temperature. Tetraethyl orthosilicate (Aldrich, 98%) was added according to the required silicon amounts of 0.5at%, 1at%, 2at%, 5at%, 10at%, 20at%, and 30at%, labelled FS1, FS2, FS3, FS4, FS5, FS6, and FS7 respectively. The mixture was carefully hydrolysed by Millipore water (20ml) and was ultrasonically (30 kHz, 130 W) irradiated at the ambient temperature for two hours. The water layer was removed and further 20 ml distilled water added. The reaction vessel was placed again to ultrasound for one hour. This process was repeated once more. The black precipitate was filtered, washed with ethanol and dried under vacuum (Yield 88 %).

IR (KBr, cm^{-1}): 3400 (br), 1620 (br), 1260 (w), 1030 (s), 580 (s).

2.4.3. Experimental details for Chapter 5

2.4.3.1. Preparation of octaaminopropylsilsesquioxane hydrochloride ($T_8NH_3^+Cl^-$)

Concentrated HCl (20mL) was added to a stirring solution of 3-aminopropyltriethoxysilane (15mL; 0.063mol) in dry methanol (200mL). This

mixture was stirred at room temperature for 1 hour, then left to stand in a stoppered round bottomed flask for five weeks. The product began to crystallise out of solution after three weeks. The filtrate was reduced to approximately ¾ of its original volume. The product was obtained in 29.7% yield (2.73g) by filtering the reaction mixture, washing with cold, dry methanol and dried under vacuum.

IR (KBr, cm^{-1}): 3024 (br), 1601 (s), 1495 (s), 1126(br), 818 (br).

^1H NMR (400 MHz, DMSO-d_6, 25°C): δ 8.25 (s, NH_3, 24 H), 2.83 (t, CH_2N, 16 H), 1.78 (m, $SiCH_2CH_2$, 16 H), 0.78 (t, $SiCH_2$, 16 H). ^{13}C NMR (100 MHz, DMSO-d_6, 25°C): δ 41.01 (s, CH_2N), 20.62 (s, $SiCH_2CH_2$), 8.40 (s, $SiCH_2$). ^{29}Si NMR (300 MHz, MeOH, 25°C): δ -66.4 (s). Mass spectrum (Electrospray mass spectrometer): calc. For $C_{24}H_{72}Cl_8N_8O_{12}Si_8$, $[M + H - 8\ HCl]^+$ *m/z* 881.29, found 881.29.

2.4.3.2. Preparation of magnetite - $T_8NH_3^+Cl^-$ nanocomposites

$FeCl_3.6H_2O$ (1.1g, 4mmol) and $FeCl_2.4H_2O$ (0.4g, 2mmol) were dissolved in 100mL-deoxygenated water and 100mL of 1.0M NaCl aqueous solutions. Sodium chloride was used to adjust the ionic strength of the iron solutions. Ammonia solution was added until the pH reached 9. The dark, magnetic precipitate was washed with deoxygenated water (5×20mL). The particles were dried under vacuum and the yield was recorded (0.454g, 98% yield). A suspension of the particles (0.11g) in millipore water (20mL) was prepared by placing the suspension in ultrasound for 30 minutes. Octaaminopropylsilsesquioxane hydrochloride (0.2 g, 0.17 mmol) was dissolved in millipore water (10mL) and added to the magnetic suspension. The mixture was shaken overnight to give a stable suspension. A sample was dried for IR analysis and XRD. NMRD and TEM analysis was carried out on the stable suspension.

IR (KBr, cm^{-1}): 3367 (br), 1619 (br), 1261 (w), 986 (br), 810 (b), 584 (br).

2.4.3.3. Preparation of magnetite - $T_8NH_3^+Cl^-$ - porphyrin nanoocomposites

Magnetic fluid (10mL; as synthesised in 8.2.3.2) was placed in a sample tube. 4, 4', 4'', 4''', -(21H, 23H-Porphine-5, 10, 15, 20–tetrayl) tetrakis–(benzoic acid) (0.005g, 0.0063mmol) with 1 mL dry ethanol was added. The mixture was shaken overnight to result in a stable magnetic fluid. A sample was dried for IR analysis and XRD. NMRD analysis, TEM, UV-vis and fluorescence spectroscopy was carried out on the stable suspension.

IR (KBr, cm^{-1}): 3367 (br), 1603 (br), 1527 (br), 1388 (br), 1089 (br), 1021 (br), 803 (s), 582 (br).

2.4.3.4.Synthesis of covalently bound porphyrin-magnetite nanoparticles

2.4.3.4.1. Preparation of silica coated nanoparticles

Stock solutions of 25 mL of each of 1 M $FeCl_3.6H_2O$ (6.56 g, 0.024 mol), 0.5 M $FeCl_2.4H_2O$ (2.48 g, 0.012 mol), and 0.4 M HCl were made up with Millipore water. NaOH solution (0.5 M, 250 mL) was heated to 80°C and the iron solution was added dropwise. After one hour of stirring with heat, the black magnetic nanoparticles were washed with Millipore water (5 × 20 mL) until neutral. A sample of the nanoparticles (1 g) was dispersed in tetramethylammonium hydroxide (30 mL) and made up to 570 mL with Millipore water. 0.58% activated sodium silicate (430 mL) was added to the nanoparticle suspension. The sodium silicate was activated by passing through a regenerated cation exchange resin. After two hours stirring, the magnetic fluid was transferred into dialysis tubing and dialysed against Millipore water brought to pH 10 by the addition of tetramethylammonium hydroxide. The dialysis tubing was prepared by boiling tubing of the required length in 2% (w/v) sodium bicarbonate (100 mL) and 1mM EDTA (100 mL) at pH 8.0 for ten minutes. The tubing was rinsed with Millipore water then boiled for ten minutes in 1mM EDTA followed by Millipore water rinsing. After 24 hour dialysis, the solution was brought to pH 8.0 by the addition of dilute HCl. The particles were washed and finally dried under vacuum. Yield = 98 %.

IR (KBr, cm^{-1}):3286 (br), 1625 (s), 1087 (br), 947 (s), 579 (br).

2.4.3.4.2. Reaction of silica coated nanoparticles with protoporphyrin

Protoporphyrin IX (0.1 g; 0.177 mmol) was dissolved in dry THF (20 mL). *N*-(3-Dimethylaminopropyl)-*N'*-ethylcarbodiimide (0.17 g; 0.887 mmol) was added to the stirring deep red solution and the reaction mixture was stirred for 3 hours at 0 °C. The reaction was carried out in the dark to prevent any possible photobleaching of the porphryin. 3-Aminopropyltriethoxysilane (83 μL; 0.355 mmol) in 2 mL dry THF was added to the porphyrin solution at 0 °C. The reaction mixture was brought to room temperature and allowed to react overnight. Silica coated magnetite nanoparticles

(0.1 g) were added to the reaction vessel with triethylamine (300 μL) and allowed to react for 24 hours. The mixture was centrifuged and the particles were washed with bench THF (5 × 40 mL) to remove any unreacted porphyrin or unwanted side-products. The particles were finally washed with water.

IR (KBr, cm^{-1}): 3286 (br), 2945 (br), 2500 (s), 1621 (s), 1473 (s), 1080 (br), 901 (br), 579 (br).

2.4.4. Experimental details for Chapter 6

2.4.4.1. DNA solutions

Herring or Salmon DNA was dissolved in 100mL autoclaved water to prevent contamination. The concentration of stock DNA solutions was determined spectrophotometrically using an extinction coefficient of 6600 M^{-1} cm^{-1} at 260 nm. Single stranded DNA was prepared by boiling the solution for 10 minutes to denature the duplex strands, followed by rapid cooling in ice. DNA solutions were used immediately after their preparation.

2.4.4.2. Preparation of double stranded DNA-magnetite nanocomposites

$FeCl_3$ (1.1g; 4mmol) and $FeCl_2$ (0.4g; 2 mmol) were dissolved in 100mL deoxygenated water and 100mL sodium chloride solution. Aliquots of 10mL of this solution were added to 10mL Herring or Salmon DNA of a predetermined concentration. Ammonia solution (0.88 M) was added until the pH reached 9. The resulting black precipitate was washed with deoxygenated water until washings were neutral and was then dried under vacuum. All final neutral washings were kept for analysis by NMRD.

IR (KBr, cm^{-1}): 3433 (br), 1647 (s), 1220 (br), 1081 (w), 580 (s).

2.4.4.3. Preparation of single stranded DNA-magnetite nanocomposites

Aliquots of 10mL of the iron solution (prepared as described in 2.5.5.2) were immediately added to 10mL of single stranded DNA solutions of a predetermined concentration under argon. Ammonia solution (0.88 M) was added until the pH reached 9. The resulting black precipitate was washed with deoxygenated water until

washings were neutral, dried in vacuum. All solutions with final neutral washings were kept for analysis by NMRD.

IR (KBr, cm^{-1}): 3400 (br), 1632 (s), 1401 (s), 1228 (br), 1080 (w), 572 (s).

2.4.5. Experimental details for Chapter 7

2.4.5.1. Preparation of polyelectrolyte solutions

The polyelectrolytes employed in these experiments were poly(sodium-4-styrene)sulfonate and poly(allylamine) hydrochloride. A predetermined mass of polyelectrolyte was dissolved in 10 mL Millipore water.

2.4.5.2. Preparation of polyelectrolyte-magnetite nanocomposites

$FeCl_3.6H_2O$ (1.1g; 4mmol) and $FeCl_2.4H_2O$ (0.4g; 2 mmol) were dissolved in 100mL deoxygenated water. Aliquots of this solution were added to polyelectrolyte solutions of known concentrations. The experiments carried out are listed in Table 3. The solution was allowed to stir at room temperature for 15 minutes. Magnetic nanoparticles were precipitated *via* the addition of ammonia solution until the pH reached 9. The resulting black precipitate was washed with Millipore water (5 × 20 mL) and the final washes kept for NMRD analysis. The precipitate was dried under vacuum and analysed.

IR (KBr, cm^{-1}):3419 (br), 1624 (br), 1401 (w), 1180 (br), 1035 (w), 1006 (w), 579 (br).

Table 2.2 Polyelectrolyte stabilised nanoparticle experiments

Sample	Vol iron soln taken (mL)	PSS conc (M)	Sample	Vol iron soln taken (mL)	PSS conc (M)
A	25	4.08×10^{-4}	N	25	4.08×10^{-5}
B	10	3.57×10^{-4}	O	10	3.57×10^{-5}
C	5	2.38×10^{-4}	P	25	2.04×10^{-5}
D	25	2.04×10^{-4}	Q	25	8.16×10^{-6}
E	10	1.78×10^{-4}	R	5	1.9×10^{-5}
F	50	1.19×10^{-4}	S	10	1.43×10^{-5}
G	25	1.02×10^{-4}	T	7.5	1.22×10^{-5}
H	50	2.38×10^{-5}	U	10	7.14×10^{-6}
I	75	4.2×10^{-5}	V	1	1.29×10^{-5}
J	5	9.52×10^{-5}	W	1	1.29×10^{-6}

K	10	7.14×10^{-5}	X	2.5	5.71×10^{-6}
L	1	6.49×10^{-5}	Y	5	9.52×10^{-6}
M	5	4.76×10^{-5}	Z	5	9.52×10^{-7}

2.4.5.3. Preparation of polyelectrolyte-cobalt ferrite nanocomposites

$FeCl_2$ (0.79 g; 4mmol) and $Co(NO_3)_2.6H_2O$ (0.58 g; 2 mmol) were dissolved in 100mL deoxygenated water. Aliquots of this solution were added to polyelectrolyte solutions of known concentrations. The same experiment design as used as in Table 2.2. The solution was allowed to stir at room temperature for 15 minutes. Ammonia solution was added until the pH reached 9. The solution was heated to 85 °C for 2 hours. The resulting black precipitate was washed with Millipore water (5 × 20 mL) and the final washes kept for NMRD analysis. The precipitate was dried under vacuum and analysed.

IR (KBr, cm^{-1}): 3478 (br), 2954 (w), 1629 (w), 1407 (w), 1263 (w), 1070 (br), 586 (s).

References

[1] U. Schwertmann, R. M. Cornell, *Iron Oxides in the Laboratory*, WILEY-VCH Verlag GmbH, Weinheim, **2000**.

[2] H. Gunzler, H. U. Gremlich, *IR Spectroscopy*, WILEY-VCH Verlag GmbH Weinheim, **2002**.

[3] H. Baranska, A. Lubudinska, J. Terpinski, *Laser Raman Spectroscopy: analytical applications*, Horwood, **1987**.

[4] R. M. Cornell, U. Schwertmann, *The Iron Oxides*, Wiley VCH Verlag GmbH and Co., Weinheim, **1996**.

[5] J. Park, K. J. An, Y. S. Hwang, J. G. Park, H. J. Noh, J. Y. Kim, J. H. Park, N. M. Hwang, T. Hyeon, *Nature Materials* **2004**, *3*, 891.

[6] M. E. Brown, *Introduction to Thermal Analysis: Techniques and Applications*, Chapman and Hall, University Press, Cambridge, Cambridge, **1988**.

[7] Y. Gossuin, A. Roch, R. N. Muller, P. Gillis, *Journal of Magnetic Resonance* **2002**, *158*, 36.

[8] R. Veyret, T. Delair, C. Pichot, A. Elaissari, *Journal of Magnetism and Magnetic Materials* **2005**, *295*, 155.

[9] M. Willert, R. Rothe, K. Landfester, M. Antonietti, *Chemistry of Materials* **2001**, *13*, 4681.

[10] T. Rheinlander, T. Priester, M. Thommes, *Journal of Magnetism and Magnetic Materials* **2003**, *256*, 252.

[11] B. DeMeulenaer, P. Vandermeeren, J. Vanderdeelen, L. Baert, *Particle & Particle Systems Characterization* **1996**, *13*, 130.

Chapter 3: Magnetite nanocrystals from metallorganic precursors

3.1. Introduction

Ordered systems of magnetite nanocrystals are frequently found in nature, including meteorites, microorganisms, and the brains of homing pigeons.[1] For example, magnetite nanocrystals may be formed intracellularly *via* a biologically controlled mineralisation process in terrestrial magnetotactic bacteria, such as the MV-1 strain (Figure 3.1).[2] The magnetosomes (grains of magnetic minerals) arrange themselves in a chain-like structure, which are then attached within the bacterium *via* an unknown anchor-like element. These chains within the bacterium act as a magnetic system for orientation. This biomineralisation process has also been found to occur in the human brain, which might be related to the interaction of environmental magnetic fields with the human central nervous system.[3]

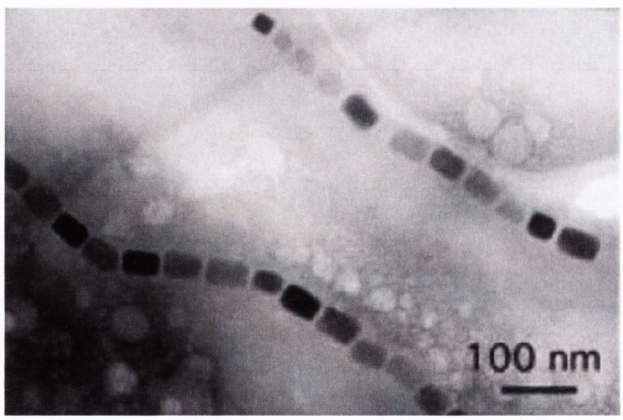

Figure 3.1 Magnetite nanocrystal chains found in the terrestrial bacterial strain MV-1[2]

During the past few years, there were several reports on the structure of nanosized magnetite crystals found in the Martian meteorite ALH84001.[4, 5] These Martian magnetite nanocrystals have similar physical and chemical properties to terrestrial magnetotactic bacteria, in particular the MV-1 strain.[6] The shape of these nanocrystals has been characterised as truncated hexaoctahedra (Figure 3.2). There has been much debate as to whether these truncated hexa-octahedral magnetite nanocrystals provide evidence of former life on Mars. The argument lies in the exact determination of their morphology and shape. As reported by Thomas-Keprta *et. al.*,

"there are no known reports of inorganic processes to explain the observation of truncated hexa-octahedral magnetites in a terrestrial sample".[5] There have been many attempts to reproduce this crystal form in an inorganic laboratory process. Golden *et. al.*[7] reported the preparation of magnetite nanocrystals with a morphology corresponding to that of the MV-1 strain using a method which involved the thermal decomposition of iron-rich carbonates by heating up to 470°C.

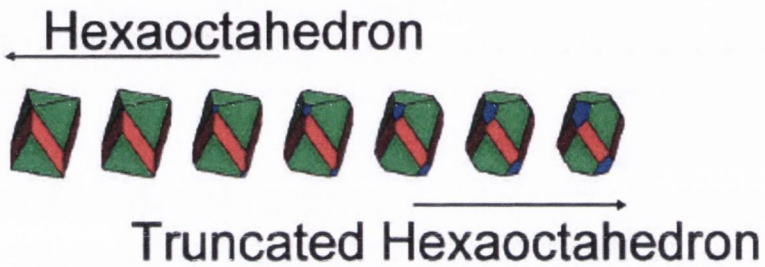

Figure 3.2 The transition from hexa-octahedral to truncated hexa-octahedral crystal behaviour is created by elongating the [111] axis. The degree of truncation varies in MV-1 and ALH84001 magnetite samples.[5]

Recently, synthetic research has concentrated on the preparation of monodisperse magnetic nanoparticles as, especially in biomedicine, uniformity in shape and size is an important prerequisite for use as diagnostic and treatment tools. In the case of magnetic nanoparticles, properties such as superparamagnetism[8] (a single magnetic domain where the particle is in a state of uniform magnetisation at any field) are highly dependant on particle size and distribution. Also when considering these particles for use as biomedical agents, their size must be comparable to that of the tissue in question. This can range from 10-100 μm, for a cell, down to several nanometers, in the case of a gene.[9] The coprecipitation method is arguably the preferred preparative technique for the preparation of magnetite[10, 11], whereby Fe(II) and Fe(III) are reacted in the presence of NH_4OH. Recently, Hyeon *et. al.*[12] reported the use of a reverse micelle technique for the production of uniform, monodisperse magnetite nanoparticles. Other techniques include microemulsions[13, 14] and high temperature decomposition of organic precursors.[15, 16] However, the majority of these methods require high temperatures and may not always lead to the formation of nanocrystalline magnetite with controlled particle size.

The main aim of this work is to avoid these harsh conditions and develop a quick and easy one-step sol-gel low temperature synthesis of magnetite nanocrystals using a single source metallorganic precursor. The preparation of the first iron (II) heterometallic alkoxide $[(THF)NaFe(O^tBu)_3]_2$ has been published and is now employed in the preparation of magnetite nanocrystals.[17] One advantage of this method is that it is a very quick, one step procedure for the preparation of magnetic nanocrystals by the hydrolysis and ultrasonic treatment of an Fe (II) *tert*-butoxide precursor without using any additional stabilising agent. As part of this work, magnetite nanoparticles have been prepared by a sol-gel and ultrasonic processing route using a single source metallorganic precursor.[17] This new process for magnetite production afforded nanocrystalline particles which had, up to then, not been reported for a room temperature synthesis. One interesting point to note about these nanocrystals was their resemblance to the magnetite nanocrystals commonly found in terrestrial magnetotactic bacteria, such as the MV-1 strain.[2]

3.2. Preparation and characterisation of magnetite nanocrystals

3.2.1. Preparation and characterisation of metallorganic Fe(II) precursor

The preparation of $[(THF)NaFe(OBu^t)_3]_2$ (**1**) was performed according to a published procedure.[17] The reaction of iron (II) bromide with three equivalents of sodium *tert*-butoxide in dry THF at ambient temperature goes with the precipitation of sodium bromide affording the heterometallic iron (II) alkoxide $[(THF)NaFe(OBu^t)_3]_2$ (**1**) (Scheme 3.1). The reaction mixture was filtered under argon to remove the sodium bromide precipitate and the dark liquid was dried to yield grey crystals of (**1**). The compound is extremely moisture and air sensitive. The colour immediately changes in air to orange due to oxidation of Fe(II) to Fe(III).

$$3\ Na(OBu^t) + FeBr_2 \xrightarrow[-NaBr]{THF} [(THF)NaFe(OBu^t)_3]_2$$

Scheme 3.1 Preparation of the Fe(II) alkoxide, (1)

Compound **1** has been characterised by ^1H NMR and IR spectroscopy. In the ^1H NMR (d-C_6D_6) (Appendix 1), two broad peaks for the OBu^t protons are observed, one

at 12.3 ppm (for the μ_2-OBu^t bridging groups) and the other further upfield at -3.5 ppm (for the μ_3-OBu^t bridging groups). Since chemical shifts are sensitive to intermolecular effects, the interaction of the protons from the bridging butoxides with the unpaired Fe^{2+} electrons causes a considerable shift as above. The signal for the μ_3-OBu^t bridging groups occurs so far upfield because they are attached to the iron atoms. The negative spin of the magnetic iron causes a shift upfield while a positive spin causes a downfield shift for the μ_2-OBu^t bridging protons. The THF peaks occur at 10.4 ppm and 5.2 ppm. The presence of the paramagnetic iron (II) species is clearly observed by the broadness of the peaks.

An IR spectrum of compound (1) (see Appendix 2) shows a broad OH stretch present at 3401 cm^{-1}. The Nujol bands at 2954, 2854, 1460 and 376 $cm^{-1}$are easily distinguishable. The symmetric stretch due to the C-O-C group in THF is seen at 1020 cm^{-1} and the asymmetric stretch is seen at 979 cm^{-1}. The carbon-oxygen band of the butoxide group is found at 1019 cm^{-1}. The stretch at 799 cm^{-1} may be due to the metal-oxygen bridge between the butoxide and the iron atom. The stretch at 554 cm^{-1} was assigned to Fe-O. All IR and ^{1}H NMR spectra corresponded to those reported previously.[17]

According to X-ray crystallography of **1**, which has been previously reported,[17] each of the iron atoms are coordinated by two μ_2- and two μ_3-OBu^t bridging groups. Each sodium atom is coordinated by the oxygen atoms of two μ_2- and one μ_3-OBu^t groups and one THF molecule in a distorted tetrahedron arrangement.

3.2.2. Preparation of magnetite nanocrystals by sol gel processing

The heterometallic precursor, $[(THF)NaFe(^tBuO)_3]_2$, was employed in the preparation of magnetite nanocrystals. A solution of the $[(THF)NaFe(^tBuO)_3]_2$ precursor in THF was first hydrolysed with doubly distilled water (Scheme 3.2). The following ultrasonic and thermal treatment for four hours afforded a black precipitate. The residual aqueous solution was found to have a basic pH of 10. The precipitate was washed five times with double distilled water, then with ethanol and finally dried in vacuum at the room temperature. The product (sample S1) has been characterised by X-ray powder diffraction (XRD), transmission (TEM) and scanning electron microscopy (SEM), Infrared (IR), Raman and Mössbauer spectroscopy, and magnetization measurements.

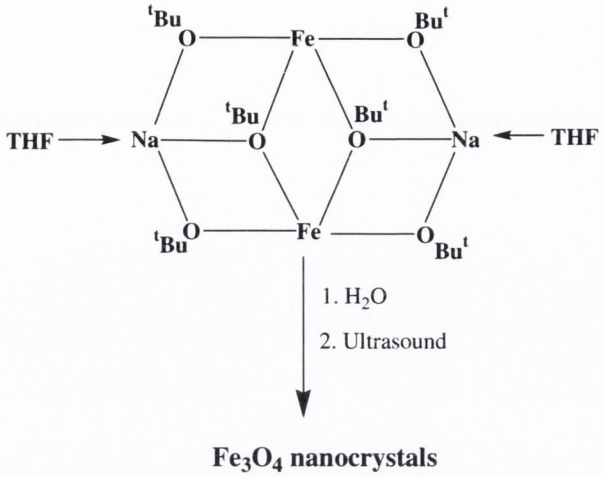

Scheme 3.2 Preparation of magnetite nanocrystals. Reagents and conditions: (i) double distilled water, 1 h; (ii) ultrasound, 40-50°C, 4 h

3.2.3. Characterisation of magnetite nanocrystals

3.2.3.1. Infrared Spectroscopy

An infrared spectrum of S1 was carried out in KBr from 4000 to 400 cm^{-1} (Figure 3.3). Two absorption bands are expected below 1000 cm^{-1}, which are found to occur in the spectra of most metallic oxides.[18] The sample shows two stretches for Fe-O, as expected for magnetite, at 586 and 448 cm^{-1}. There is a stretching vibration found at 3391 cm^{-1} incorporating contributions from both symmetrical (ν_1) and asymmetrical (ν_3) modes of the O-H bonds which are attached to the surface iron atoms.[19] The presence of these hydroxyl groups on the surface of the nanoparticles is expected. Because the surface iron atoms have unoccupied d-orbitals, they act as Lewis acids and can react with water molecules which will share their lone pairs of electrons with iron. After absorption, the water molecules will dissociate to leave the nanoparticle surface coated with hydroxyl groups coordinated to the underlying iron atoms. This hydroxylation process for iron oxides is a fast occuring one, taking place in a matter of minutes.[20] Once the surface hydroxyl groups are present, there is a possibility of water adsorption *via* hydrogen bonding. The presence of an adsorbed water layer is confirmed by a stretch for the vibrational mode of water molecules found at 1627 cm^{-1}.[21]

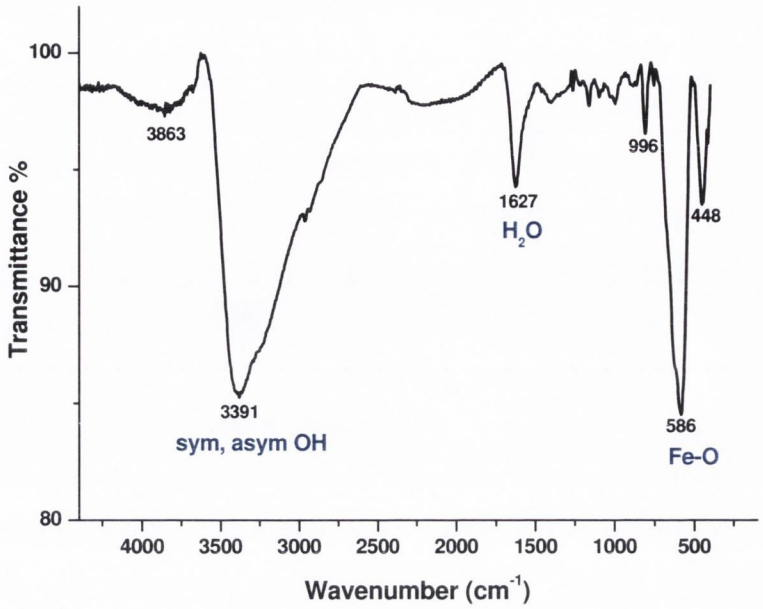

Figure 3.3 IR spectrum from a KBr disk of magnetite nanocrystals prepared from heterometallic precursor (1)

3.2.3.2. Raman Spectroscopy

Micro-Raman spectroscopy was carried out on the nanocrystalline sample S1. By focusing the laser beam, the local spot temperature can be increased by several hundred degrees. This can cause an oxidation of the samples and as a result the shift in wavenumber of the Raman modes. This problem must be taken into account in Raman measurements of the iron oxides as those containing Fe^{2+} ions (e.g. magnetite) may be readily oxidised at high temperatures in the open air. Oxidation of magnetite due to this laser effect has been previously reported[22] and it has been found that, with increasing laser power, the characteristic peaks for magnetite shift and the spectrum is similar to the cation-deficient maghemite (γ-Fe_2O_3). Eventually the magnetite bands disappear altogether, leaving the extremely stable haematite (α-Fe_2O_3), which contains only the *tri*valent iron species. Heating at the laser focussing spot is confirmed in Figure 3.4. The Raman laser is focussed in the centre of the pictures. Figure 3.4(a) shows the magnetite sample prior to Raman treatment. The laser power was set to 10 mW and run for 30 seconds with 10 spectra accumulations (total experimental time was 5 minutes). Even though the laser is not set to the maximum

power and the experimental time is relatively short, oxidation of the magnetite is apparent from a colour change (see Figure 3.4(b)) from black magnetite to the characteristic red colour of haematite.

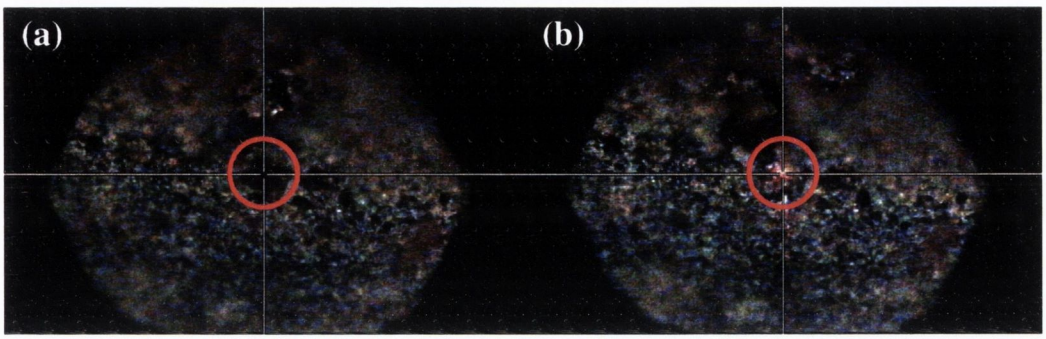

Figure 3.4 Images taken of magnetite nanocrystal samples (a) before and (b) after high power laser Raman treatment. The central spot is the position of the Raman laser. The red colour of 4(b) is indicative of an oxidation of magnetite to haematite

The effect of the laser power is also seen in the Raman spectrum (Figure 3.5). The red spectrum is that for sample S1 after the high laser power experiment. The strong bands at 218, 288, 400 and 593 cm^{-1} are assigned as haematite peaks.[23] The peak at 656 cm^{-1} may be attributed to maghemite.[24]

In order to avoid these oxidation effects, a lower powered laser Raman study (3 mW) was carried out on the sample. This led to the disappearance of the bands for oxidised material and the emergence of the characteristic broad peak for magnetite at 680 cm^{-1}. The peaks for magnetite are also noted to be broad, while the haematite peaks are sharper, which is to be expected.[25] The peaks are attributed as A_{1g} (680 cm^{-1}), $T_{2g}(2)$ (496 cm^{-1}), E_g (400 cm^{-1}) and $T_{2g}(1)$ (297 cm^{-1}). These are in good agreement with the reported values in the literature.[22-25]

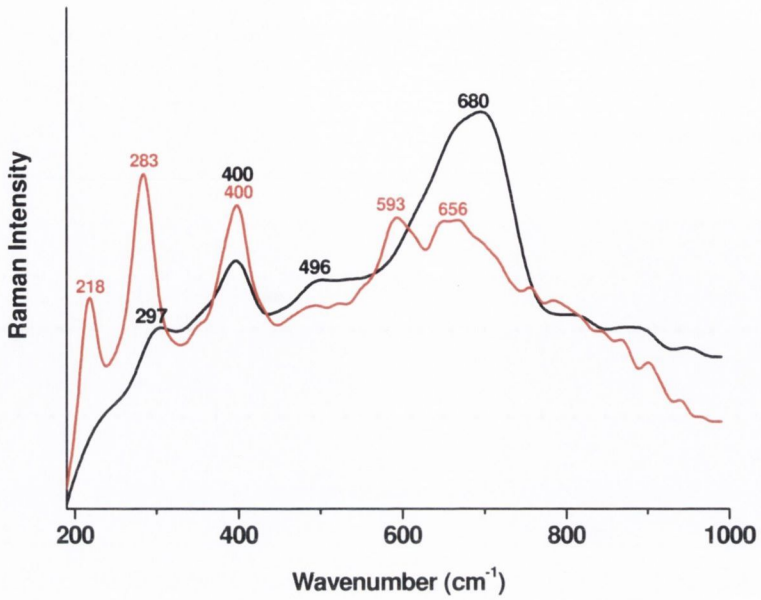

Figure 3.5 High powered (red) and low powered (black) laser Raman spectra of magnetite nanocrystals prepared from heterometallic precursor (1)

3.2.3.3. Magnetisation measurements

Room temperature magnetisation measurements were carried out by Dr. Robert Gunning at the School of Physics, Trinity College (Table 3.1). The magnetisation curve was characteristic for ferromagnetic material, showing a very small coercive field H_C = 16 mT (Figure 3.6). The magnetisation in a field of 5 T at room temperature has a value of σ = 30 J T^{-1} kg^{-1} and is not completely saturated at this field. To try to completely saturate the field, the spectrum was repeated at 5 K.

Table 3.1 Magnetisation measurements for sample S1

Applied field (T)	Temperature (K)	Magnetisation ($JT^{-1}kg^{-1}$)	Coercivity (mT)	Remanence (T)
5	300	30	22	5
5	5	39	22	6.5

The magnetisation (σ) at 5T was found to be 39 J T^{-1} kg^{-1} and is unsaturated even at this field. There is also a noted decrease in the maximum magnetisation values in comparison to bulk magnetite (where σ = 90 J T^{-1} kg^{-1}).[20] These results indicate there are two different contributions to the magnetisation; the first, which is

saturated by the magnetic field, corresponds to a bulk ferrimagnetic phase, and the second, which is not saturated, corresponds to superparamagnetic nanoparticles.

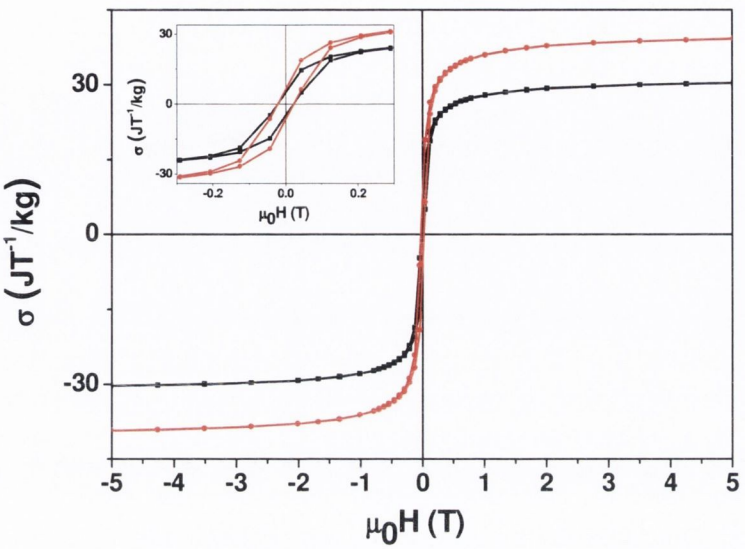

Figure 3.6 Magnetisation curve of the magnetite nanocrystals collected at 300 K (black curve) and 5 K (red curve). The inset shows close-up of the hysteresis curve near 0 T.

3.2.3.4. Mössbauer Spectroscopy

Mössbauer spectroscopy is a very important technique, which is used to distinguish between magnetite and maghemite. Since Fe^{2+} only occurs in Fe_3O_4, the isomer shift in the spectrum is evidence of magnetite. All Mössbauer spectra were carried out by Dr. Alexious Douvalis at the University of Ioannina, Greece.

The Mössbauer spectra recorded at 300K (room temperature, RT), 150 K and 19 K are compared in Figure 3.7. A set of five components was used to fit the RT spectrum, and the fitted Mössbauer parameters suggest the presence of magnetite nanoparticles in a distribution of different sizes (Table 3.2).

Isomer shift (IS - relative to α-Fe at RT) and hyperfine magnetic field (B_{hf}) values of the pair of two well defined magnetically split sextets with relatively narrow lines and almost zero quadrupole shifts (2ε) are 0.30 mms^{-1}, 48.3 T and 0.64 mms^{-1}, 45.3 T respectively. These components correspond to the Fe^{3+} (A-) and $Fe^{2.5+}$ (B-) sites of relatively large (> 130 nm) bulk magnetite crystals. The absorption area ratio of these components is around 1:1 suggesting a non-stoichiometric $Fe_{3-x}O_4$ phase.

There is a broad magnetically split sextet with IS of 0.40 mms^{-1} and B_{hf} of 41.5 T. The intermediate IS (between 0.30 mms^{-1} and 0.64 mms^{-1}) and the low B_{hf} values can be attributed to magnetite particles with sizes quite close, but above the superparamagnetic limit (6-10 nm) at RT.[26, 27]

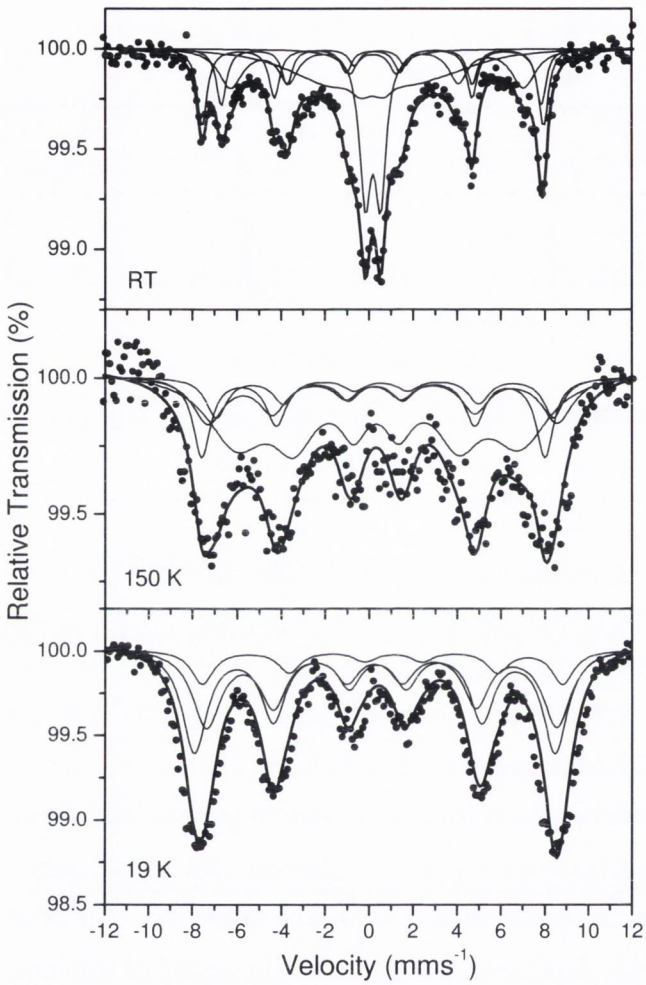

Figure 3.7 Mössbauer spectra of magnetite nanocrystals collected at RT, 150 K, and 19 K.

Merging of the A- and B- site components is a striking characteristic for magnetite nanoparticles of this size.[26] In addition, there are two more components – a narrow superparamagnetic component, and a magnetically collapsing broad component with IS values of 0.29 mms^{-1} and 0.38 mms^{-1} respectively. These correspond to $Fe_{3-x}O_4$ nanoparticles with sizes between 6 and 10 nm and below the superparamagnetic size limit (< 6 nm). The lower IS value of the component corresponding to the superparamagnetic particles suggests that the composition is

close to maghemite (γ-Fe_2O_3). The absorption areas are 31%, 21%, 29% and 19% for the bulk particles, the intermediate size ones, the particles with sizes in the range of the superparamagnetic-size limit and the superparamagnetic particles respectively. The characteristics of the Mössbauer spectra for each group of nanoparticles are in good agreement with earlier reports on magnetite nanoparticles of different size distribution.[26]

Table 3.2 Room temperature Mössbauer parameters for magnetite nanocrystal sample

Isomer shift (Fe) mm/s	ΔE_q electric quadrupole interaction mm/s	Magnetic hyperfine field (B_{hf}) T	Assigned contributions
0.31	-0.01	49.2	Fe^{3+} (A)
0.65	0.03	45.9	$Fe^{2.5+}$ (B)
0.40	0.07	41.0	$Fe_{3-x}O_4$ (0<x<0.3) Nano large
0.25	-0.30	15.4	$Fe_{3-x}O_4$ (0<x<0.3) Nano intermediate
0.26	0.68	0.0	$Fe_{3-x}O_4$ (0<x<0.3) Nano very small

As can be seen in Figure 3.7, by contrast to the room temperature spectrum, in the spectrum at 150 K the lines start to broaden and the central paramagnetic contribution disappears. This suggests a change in the superparamagnetic relaxation, which causes the appearance of a non-zero hyperfine magnetic splitting for smaller particles. A set of four components with broad lines was used to fit the spectrum. The first three components are the same as those found for the RT spectrum. The fourth component contains the merged contributions of the smaller particles. All absorption areas (30%-bulk, 19% intermediate, 51%- small nanoparticles) are in agreement with the corresponding RT values.

At 19 K, the spectrum remains broad, with no indication of a superparamagnetic component. Three components were used to fit the spectra. Two of them correspond to Fe^{3+} and Fe^{2+} ions of the large $Fe_{3-x}O_4$. The third component, with average IS and lower B_{hf} values, represents smaller. The absorption areas are 60% and

40% respectively, which is in good agreement with the results obtained for the RT and 150 K spectra.

3.2.3.5. Electron Microscopy

Transmission electron microscopy (TEM) images (see Figure 3.8 (a)-(c)) have shown truncated hexa-octahedral magnetite nanocrystals. The average particle size was found to be 33 ± 16 nm. To determine the average particle size, the diameter of 100 particles was taken and the average calculated. Scanning electron microscopy (SEM) images (Figure 3.8d) confirm the uniform nanocrystalline morphology of the entire sample.

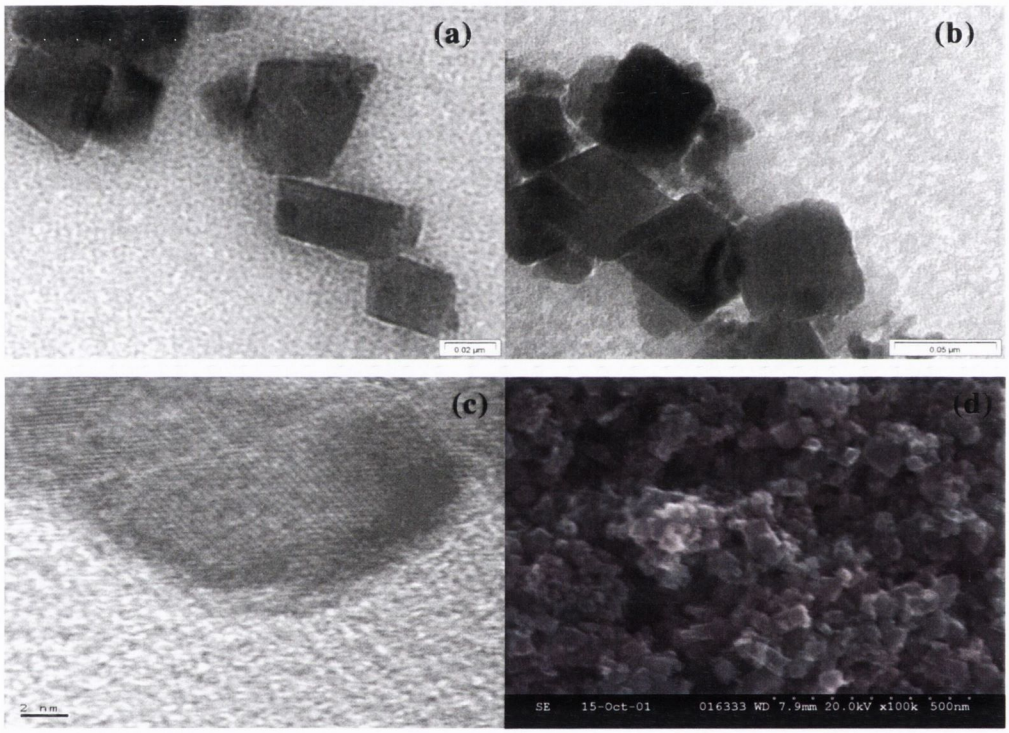

Figure 3.8 (a)(b) TEM images of magnetite nanocrystals, **(c)** HRTEM of magnetite nanocrystals and (d) SEM image of magnetite nanocrystals

3.3. Optimisation of the synthesis of magnetic nanoparticles and investigation of their size and morphology using statistical analysis

3.3.1. Statistical design

A statistical analysis of the magnetite nanocrystals was carried out, in order to optimise the conditions for the preparation of magnetite nanoparticles of a uniform size distribution. The sizes of the nanoparticles were studied by transmission electron microscopy (TEM). The samples were also characterised *via* IR and Raman spectroscopy, XRD and magnetisation measurements. The main factors involved in the preparation of these particles are temperature and time of the ultrasonic treatment. The ultrasonic process breaks the particles down to a nanometre scale.

Varying each of these conditions one at a time would be very inefficient and costly. Also, by changing one at a time, nothing can be deduced about the interactions between these factors. It is better to design an experiment where the factors can be changed simultaneously in a systematic way. This allows an estimation of the effects of the variables and their interactions. Therefore a factorial design approach has been chosen for this study. Here, the factorial design experiment is employed in the form of a response surface model, where the results can be represented graphically to represent the area of the optimum result. This allows us to check when we are approaching the maximum conditions, when we reach the maximum and when we have gone beyond it.

The design employed was a 2^2 factorial with one centre point. The best conditions known were taken as the starting point, varying the temperature from 20 °C to 70 °C and the time in ultrasound from 4 to 8 hours according to the following design (Table 3.3). This initial design was carried out in a random order (S1, S5, S2, S4, S3). In order to generate a surface size response plot, it was decided to extend the study to include temperatures of 30°C and 80°C and two ultrasound times of 8 and 10 hours (S6, S7, S8 and S9).

Table 3.3 Factorial design for the preparation of magnetic nanocrystals

Factorial 1			Factorial 2		
Sample	Time (hours)	Temperature (°C)	Sample	Time (hours)	Temperature (°C)
S1	4	20	S6	8	30
S2	8	20	S7	10	30
S3	4	70	S8	8	80
S4	8	70	S9	10	80
S5	6	50			

3.3.2. Characterisation of samples

3.3.2.1. Infrared spectroscopy

Infrared spectra of S1-S9 were carried out in KBr from 4000 cm^{-1} to 400 cm^{-1} (Figure 3.9). The two absorption bands expected for magnetite are found at 580 and 460 cm^{-1}. A stretching vibration at 3400 cm^{-1}, corresponding to the combined symmetrical (ν_1) and asymmetrical (ν_3) modes of the O-H bonds attached to the surface iron atoms, was found for all samples. The IR spectra obtained for all samples were similar, showing the same bands.

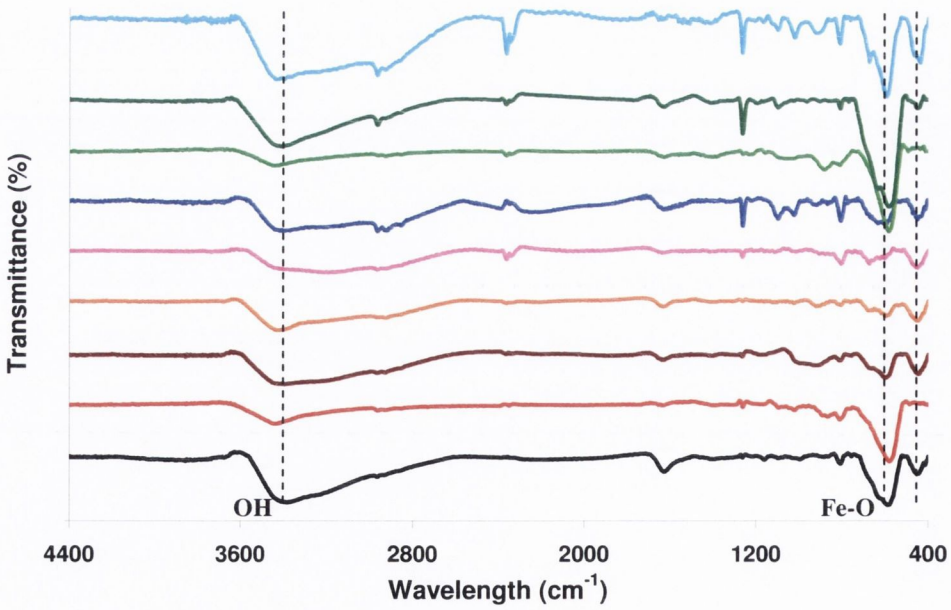

Figure 3.9 Infrared spectra of, from bottom to top, S1, S2, S3, S4, S5, S6, S7, S8 and S9. Pressed KBr disks show Fe-O stretch at ca. 570cm^{-1}

3.3.2.2. Raman spectroscopy

Figure 3.10 shows typical Raman spectra recorded for various samples of magnetic nanoparticles. There are 5 active Raman bands for magnetite, 4 of which may be seen at ambient conditions (Table 3.4).

Table 3.4 Raman bands for samples S1-S9, where * denotes magnetite, # maghemite and ^ hematite (sh denotes shoulder).

Sample	Raman intensities (cm^{-1}) and mode symmetry			
	A_{1g}	T_{2g}	E_g	E_g
S1	680 (*)		400(#)	297(*)
S2	698(*)			
S3	662(*)	607(#)	402(^)	290(^)
S4	600(^)	494(^)	398(#)	286(^)
S5	674(*)			
S6	658(*)	604(#)	400(^)	293(^)
S7	694(*)			284(*)
S8	711 (sh 672)(#)		403(#)	
S9	667(*)			

There are several bands found at around 300 and 410-420 cm^{-1} for samples S3, S4 and S6. It has been reported that these bands belong to the characteristic spectrum of haematite representing the $E_g(3)$ and $E_g(4)$ modes, respectively.[25] Samples S1 and S8 reveal the presence of some amount of maghemite, while samples S2, S7 and S9 give a characteristic spectrum of magnetite. A spectrum collected of S5 indicates that the sample is primarily magnetite, but there may be some trace amount of oxidised product also present.

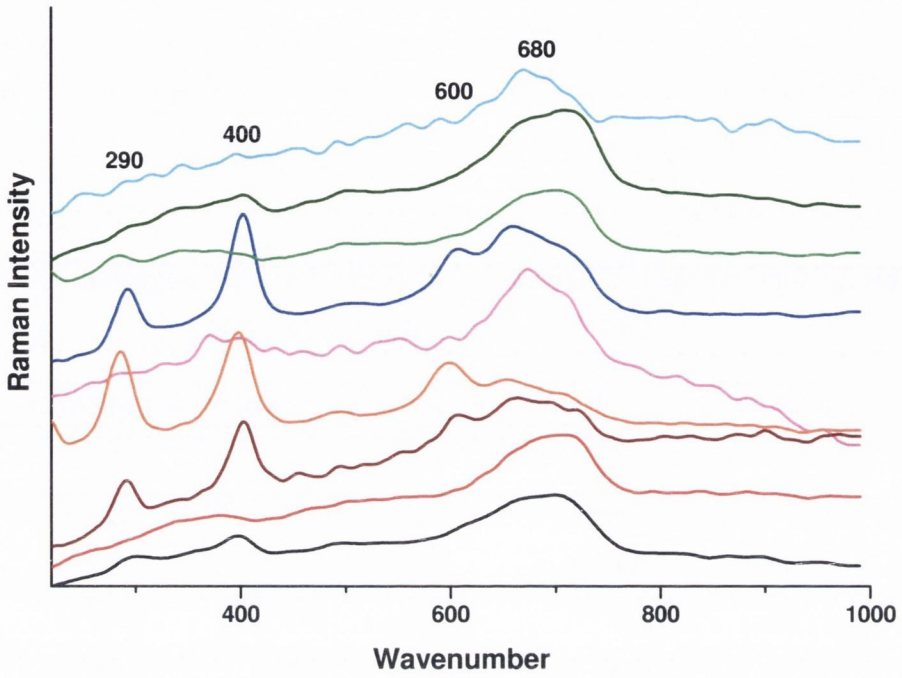

Figure 3.10 Raman spectra of, from bottom to top, S1 (black), S2 (red), S3 (maroon), S4 (orange), S5 (pink), S6 (blue), S7 (light green), S8 (green) and S9 (turquoise).

3.3.2.3. X-ray diffraction

XRD analysis (see Figure 3.11) reveals the presence of several iron oxide phases in several samples prepared. Crystalline phases found in the samples were identified using data contained in the JCPDS database. The most common phase found in these samples is that of magnetite (*). However, in preparations where the temperature setting is highest, there is an emergence of both the maghemite (#) and hematite (^) phases. This oxidation from Fe(II)/Fe(III) magnetite phase to the Fe(III) maghemite (γ-Fe_2O_3) and hematite (α-Fe_2O_3) phases is expected for samples prepared at higher temperature.[20] Oxidation may also be brought about by long ultrasonic treatment time, as ultrasound produces high temperatures and pressures *via* cavitation processes. The diffractogram data for magnetite and maghemite are very similar, however, the peak found at 41 degrees 2θ and the shoulders at peaks 54, 63 and 87 degrees 2θ may be attributed to contributions from an α-Fe_2O_3 phase. Sample S1 is predominantly magnetite, with a peak at 40.5 degrees 2θ which may be attributed to maghemite. Some organic material may also be present in some of these samples, most notably S2

and S7, (broad peak between 10 and 30 degrees 2θ) in the XRD pattern. This indicates that organic product formed during the reaction (e.g. *tert*-butanol) is not completely removed during the washing process. Sample S2 is found to coincide with the data for magnetite, while the hematite phase is found to emerge in samples S3, S4, and S5.

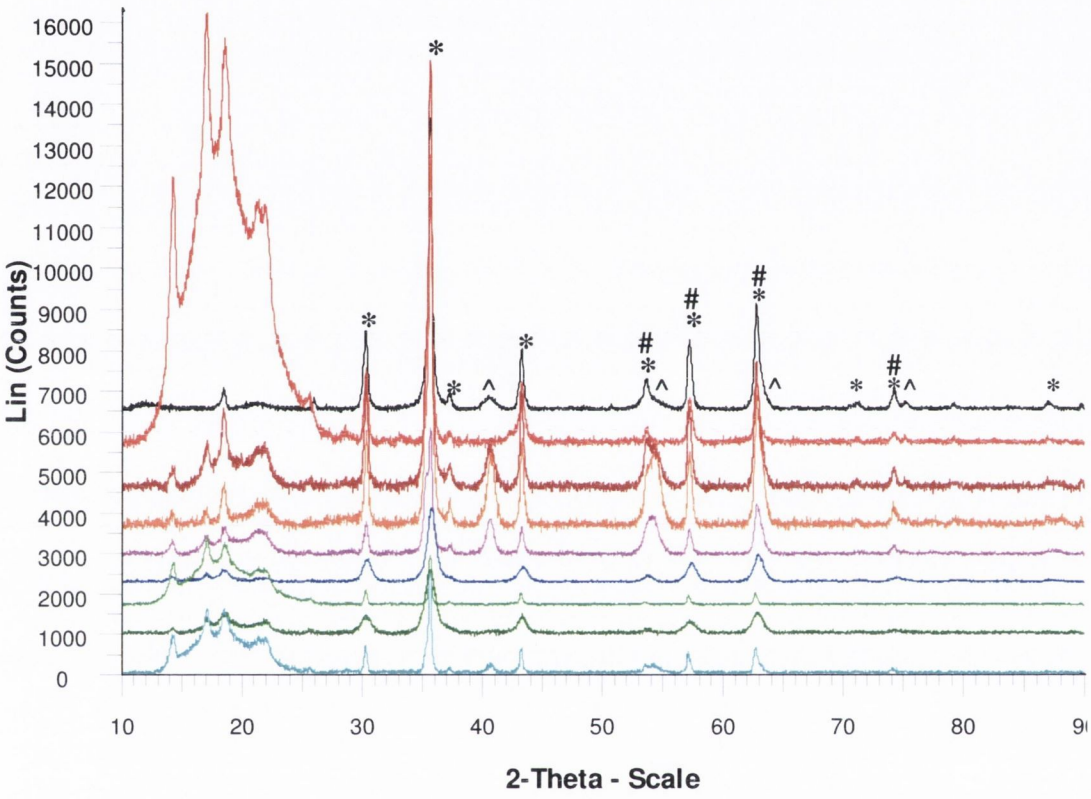

Figure 3.11 XRD analysis of magnetite nanocrystal samples, where * denotes magnetite, # maghemite and ^ hematite: S1 (black), S2 (red), S3 (maroon), S4 (orange), S5 (pink), S6 (blue), S7 (light green), S8 (green), and S9 (turquoise).

From these results, it is clear that an increase in temperature accompanied with an increase in time spent in ultrasound results in the enrichment of the samples with the maghemite hexagonal and hematite phases

XRD analysis (Figure 3.11) shows the predominant phase of S7 and S9 to be that of magnetite. There is a slight shift in the peaks for samples S8, which may indicate the presence of maghemite. The broadness of the peaks for sample S6 makes it difficult to distinguish between magnetite and maghemite.

The sample size was also calculated using the Debye-Scherrer equation and are presented in Table 3.6:

$$D = \frac{0.9\lambda}{B\cos\theta}$$

where D = Particle size

λ = wavelength (1.5406 Å)

$$B = \sqrt{(\text{PWHM}_{\text{observed sample}})^2 - (\text{PWHM}_{\text{reference sample}})^2}$$

Equation 3.1: Scherrer equation for particle size determination from X-ray diffraction studied (PWHM is the peak width at half maximum)

The peak width at half maximum for a reference sample was determined from a standard commercial magnetite sample. For the observed sample, the peak width at half maximum of the largest peak (35.5 degrees 2θ) was taken. This gave a value of 17.75 degrees 2θ for θ.

3.3.2.4. Magnetisation measurements

The samples were measured in a vibrating sample magnetometer (VSM), in fields of up to 1.1 T (see Figure 3.12).

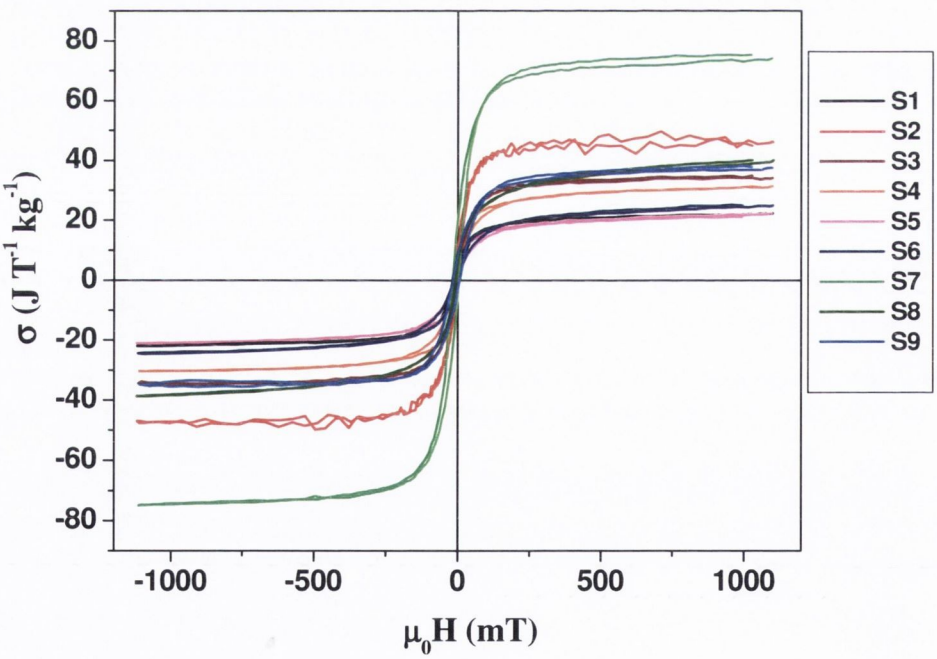

Figure 3.12 Magnetisation curves for samples S1(black), S2 (red), S3 (maroon), S4 (orange), S5 (pink), S6 (blue), S7 (light green), S8 (green) and S9 (turquoise).

While the samples which underwent a longer reaction time were saturated in this field, samples with a shorter reaction time were not. This may be due to a paramagnetic or superparamagnetic fraction – either a different phase (paramagnetic) or a fraction with smaller crystallite size (superparamagnetic). The magnetization at 1.1 T increased with the total reaction time of the sample.

Table 3.5 Magnetisation, coercivity and remanence values for samples S1 – S9, taken at 1.1 T and 300 K

Sample	Magnetisation ($JT^{-1}kg^{-1}$)	Coercivity (mT)	Remanence (T)
S1	22.4	14.8	5.3
S2	46.5	10.5	9.8
S3	35.1	7.5	4.5
S4	31.6	18.3	9.5
S5	22.3	17.7	6.3
S6	25.1	14.1	4.9
S7	73.4	17.1	19.7
S8	40.2	8	6.2
S9	37.7	17.3	8.3

In order to better observe the changes of magnetisation values with temperature and time spent in ultrasound, the values have been plotted in Figure 3.13 below.

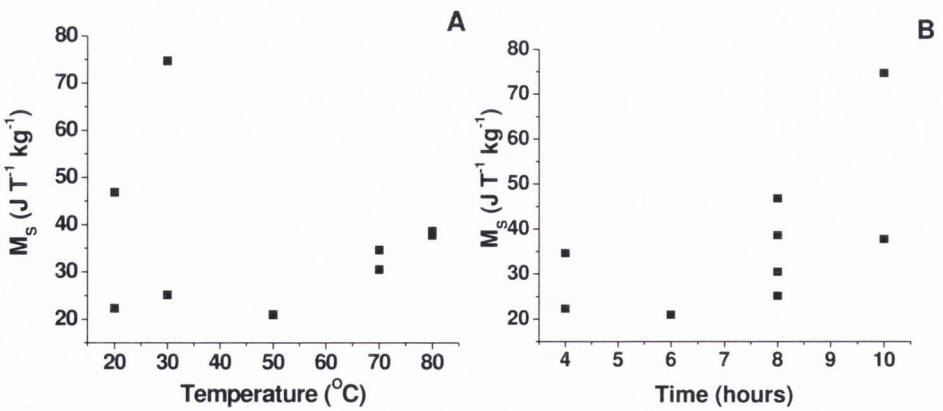

Figure 3.13 Magnetisation values versus time, showing increase in magnetisation at 1.1 T as time in ultrasound is increased

Graph A (Figure 3.13) shows an initial increase in the values of magnetisation as the temperature increases from 20 to 30 °C. Once a temperature of 50 °C is reached, the magnetisation once again drops to 22.3 J T^{-1} kg^{-1}. An increase is again noted as the temperature is raised to 80 °C. The trend seen from graph A indicates that to keep the magnetisation low, lower temperatures are required. The exception to this is at 30 °C, but this is at the longest time in ultrasound (10 hours). Graph B (Figure 3.13) shows a general increase in magnetisation values with longer times in ultrasound. The magnetization reached a peak for samples reacted at temperature of 30 °C. For this temperature, a value of 73.4 J T^{-1} kg^{-1} was obtained.

Taking both these variables into account, it is clear that the best conditions for obtaining a high magnetization is in the region of 10 hours reaction time at a temperature of around 30 °C (Figure 3.14).

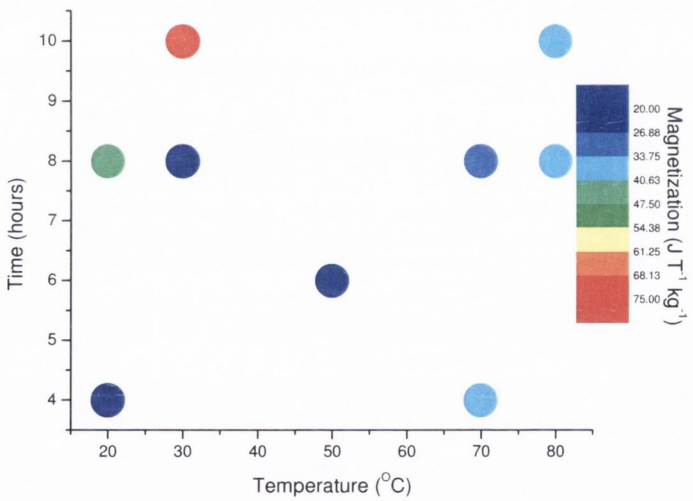

Figure 3.14 Representation of the magnetisation values and their variation with temperature and time spent in ultrasound

The value of the saturation magnetisation for these samples never matched that of the reported value for bulk magnetite (92 J T^{-1} kg^{-1}).[28] Particle size and crystallinity has been reported to influence the saturation magnetisation values. Liao *et. al.*[29] have prepared polyacrylic acid (PAA) bound magnetite nanoparticles with a saturation magnetisation of 63.2 J T^{-1} kg^{-1} for bare magnetite nanoparticles and 61.7 J T^{-1} kg^{-1} for PAA coated particles. They attributed the reduction in magnetisation to a

decrease in the particle size and the accompanied increase in surface area. The energy of a magnetic particle in the presence of an external magnetic field is proportional to its size, or conversely the number of molecules within a single magnetic domain. When this energy becomes comparable with thermal energy, the magnetic moment can be reduced by thermal fluctuations. For an inverse spinel structure, such as magnetite, the structure may become disordered at the surface of the particles.[30] This effect of disorder is more pronounced for smaller particles, hence a lower saturation magnetisation value. Small quantities of impurities may also act to suppress the magnetic moment by dispersing the exchange constant.

Wang and coworkers[31] have reported the synthesis of magnetite nanocrystals from a hydrothermal process. Nanocrystals hydrothermally formed at 140 °C have a saturation magnetisation of 86 J T^{-1} kg^{-1}, while the sample formed at 100 °C has M_s = 12.3 J T^{-1} kg^{-1}. The authors comment on the tendency of saturation magnetisation values to increase with improved crystallinity. A decrease in M_s may be due to the disordered surface layer which could act as a non-magnetic layer and decrease the magnetisation values. The contribution to the saturation magnetisation from the surface, where the magnetic moments have different orientations, to the magnetite nanoparticle are smaller than that from the inside of the particle, which is ferromagnetically ordered.[32] The larger the particle, the more the magnetism is contributed to from the bulk ordered inner part of the particle and the higher the saturation magnetisation. Well-crystallised samples would be expected to have a thinner surface layer, narrower cation distribution and less superparamagnetic relaxation, all of which would contribute to an increase in the saturation magnetisation.[31] Coarser particles exhibit higher saturation magnetisation values compared to superparamagnetic nanoparticles (<10 nm).[13] Typical superparamagnetic particles show almost immeasurable coercivity and remenence.[32]

Higher magnetisation values indicate that the particle population of sample S7 is more likely made up of bulk-like material, i.e. larger particles. An increase in the saturation magnetisation value of sample S7 may also be due to the crystallinity of the particles. Superparamagnetic nanoparticles (i.e. particles with a size of 10 nm or less) tend to show lower magnetisation values with no hysteresis and no saturation at high field. In order to confirm the particle size and whether the particles are crystalline, electron microscopy images were recorded of all samples.

3.3.2.5. Electron microscopy

TEM analysis (Figure 3.15) reveals the presence of hexaoctahedrally shaped magnetite nanocrystals in the most of the samples.

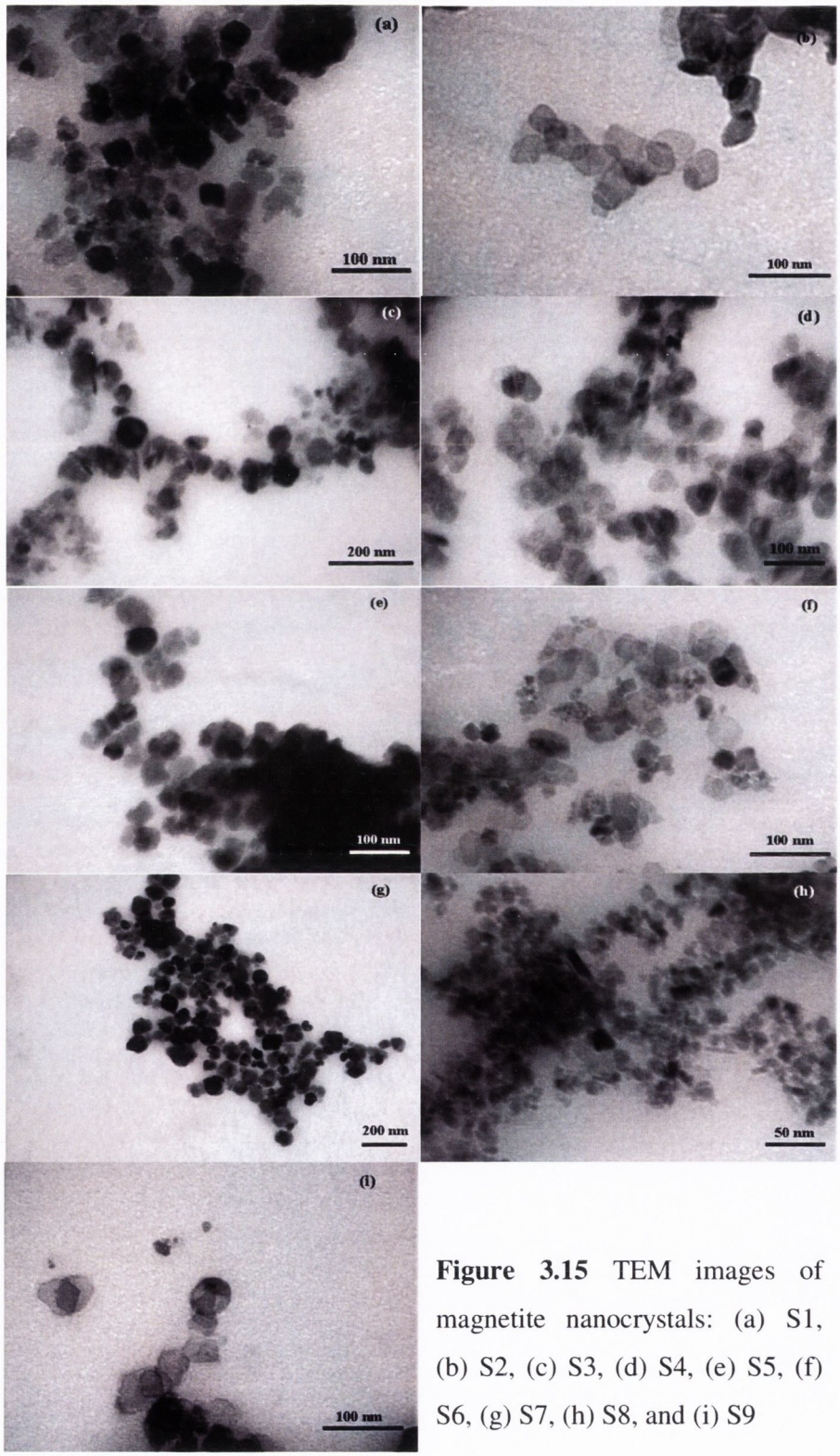

Figure 3.15 TEM images of magnetite nanocrystals: (a) S1, (b) S2, (c) S3, (d) S4, (e) S5, (f) S6, (g) S7, (h) S8, and (i) S9

There is a large size distribution found for several samples, in particular for samples S3, S7, and S9. This indicates that longer times spent in ultrasound accompanied by high temperatures leads to the formation of particles of different sizes. For example, sample S9 is found to be made up of two main sizes (Figure 3.16(i)). The crystallinity of the samples is evident from TEM.

To schematically represent the results, the size distributions from an average size of 100 particles of each sample have been plotted. The particle histograms for each sample are plotted in Figure 3.16. The average particle size was then taken to plot a 3-D surface graph.

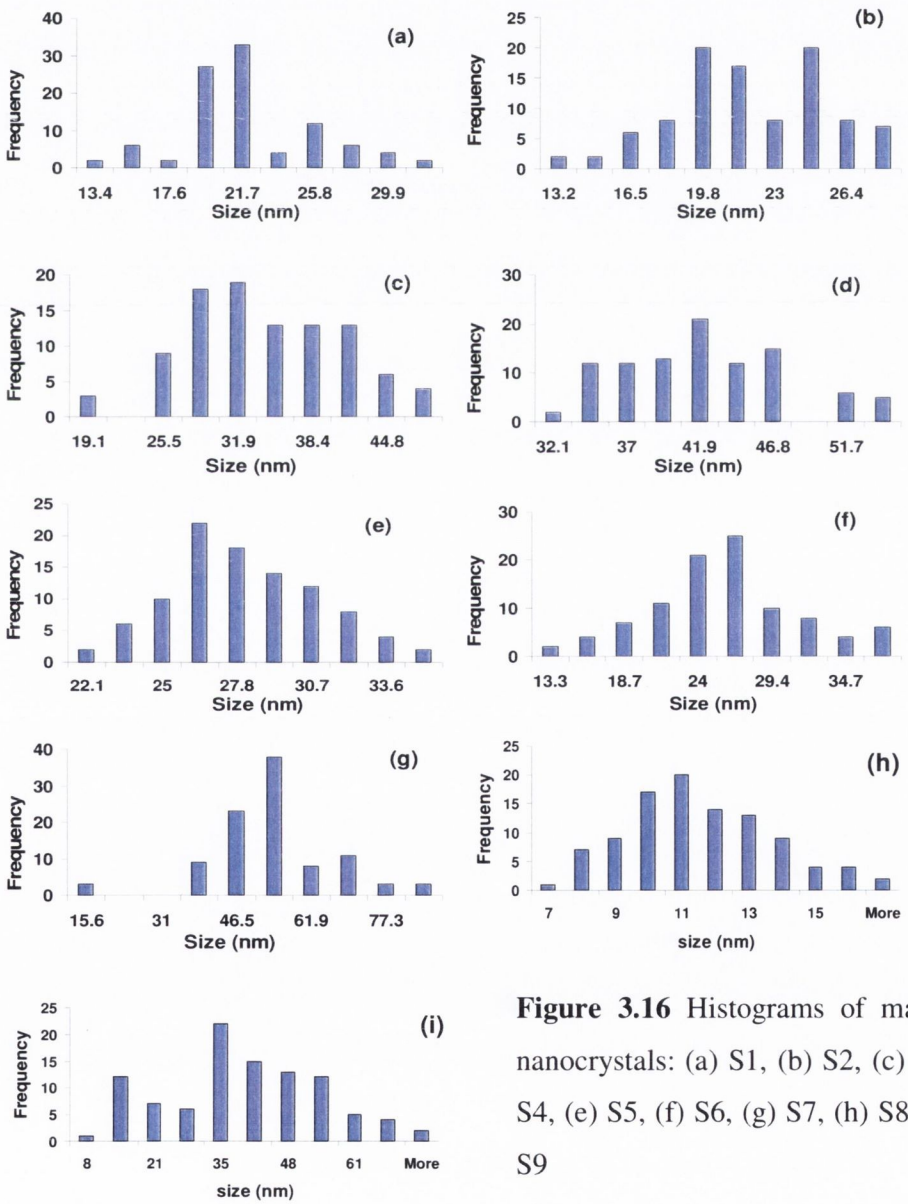

Figure 3.16 Histograms of magnetite nanocrystals: (a) S1, (b) S2, (c) S3, (d) S4, (e) S5, (f) S6, (g) S7, (h) S8 and (i) S9

3.4. Findings of statistical design

The average particle sizes calculated from TEM measurements and estimated from XRD using the Debye-Scherrer equation are detailed in Table 3.6 below. The X-ray measurements gave smaller sizes than those obtained from TEM studies. This behaviour has been previously reported and attributed to the presence of a non-crystalline material on the particle surface.[33] These results were used to obtain a graphical representation of the data as shown in Figure 3.17.

Table 3.6 Factorial design for magnetite nanocrystals with varying levels of ultrasonic time and temperature treatment. Response measured as particle size and standard deviation of 100 particles taken from TEM images. Size also monitored *via* Scherrer equation and X-ray diffraction information.

Sample	Time (hours)	Temperature (°C)	Size (nm) (TEM)	Standard Deviation	Size (nm) (XRD)
S1	4	20	21	2	17
S2	8	20	21	3	13
S3	4	70	34	7	8
S4	8	70	41	5	12
S5	6	50	26	2	10
S6	8	30	25	5	4
S7	10	30	50	12	27
S8	8	80	11	2	7
S9	10	80	36	15	23

The plot was obtained by employing Origin 7.5 program. By inputting the X (Time in ultrasound) and Y (temperature) values into a matrix with the response (average particle size) as the Z-values, we were able to obtain a surface map. From this graphical representation (Figure 3.17), it is easier to see where the region of smallest particle size is obtained and at what levels our factors must be in order to achieve this. From the plotted surface response, it can be seen that the particle size may be kept to a minimum at the lowest levels of temperature and at longer ultrasound times. From the characterisation analysis, even though the surface

response plot indicates the best particle size at highest temperature and on of the longest ultrasound times, there is an oxidation to maghemite at these conditions.

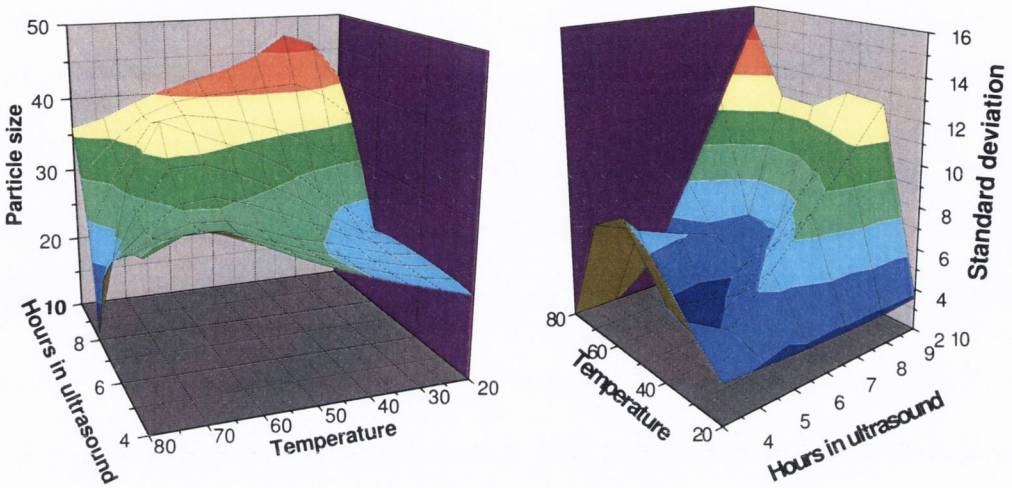

Figure 3.17: (a) Surface response curve for magnetite nanocrystals with varying temperature and time in ultrasound and the corresponding response measured as the particle size in nanometres; **(b)** Surface response curve for magnetite nanocrystals with varying temperature and time in ultrasound and the corresponding response measured as the standard deviation of particle size in nanometres.

3.5. Discussion on the mechanism for the formation of magnetite nanocrystals

Because of their crosslinking ability under hydrolysis conditions, metallorganic compounds can be used to make oligomers and polymers. The technique applied for the preparation of $[(THF)NaFe(O^tBu)_3]_2$ is a ligand exchange or metathesis reaction between a metal halide (iron (II) bromide) and an alkali metal alkoxide (sodium *tert*-butoxide). This is a common technique which generally gives very good yields. There is an exchange of bromide with butoxide ligands on the iron centres. The general mechanism for a metathesis exchange reaction is outlined below (Scheme 3.3) In this case, the metathesis takes place with the production of sodium bromide, which is noted as a precipitate during the reaction. A β-hydrogen elimination is avoided here as the tertiary butoxide has a beta carbon without any hydrogen atoms.

$$L_nM\text{-}X + M'\text{-}Y \longrightarrow L_nM\text{-}Y + M'\text{-}X$$

Scheme 3.3 General mechanism for metathesis exchange reaction

One of the techniques employed in the preparation of metal oxides is the sol gel method. This involves the preparation of a solution of metal alkoxide followed by controlled hydrolysis to yield a gel containing a hydrated form of the metal oxide. The sol-gel technique is employed in this work as it provides a one-step procedure for the preparation of iron oxide nanoparticles. The mechanism for the growth of the magnetite nanocrystals involves first hydrolysis of the $[(THF)NaFe(O^tBu)_3]_2$ which results in the formation of iron (II) and sodium hydroxides and tert-butanol. The pH was measured over the course of a reaction and upon hydrolysis of the metallorganic precursor was found to be 10. This is due to the formation of sodium hydroxide. It has been previously reported that magnetic nanocrystal formation depends on the presence of a strong base such as NaOH in the reaction mixture.[34, 35] The basic pH was necessary for the formation of magnetite nanocrystals. Previously,[36] it has been shown that hydrolysis of an iron (II) alkoxide precursor at neutral (5-6) pH gave only spherical amorphous magnetite nanoparticles. In this work, the heterometallic iron alkoxide $[(THF)NaFe(O^tBu)_3]_2$ was a very convenient single source precursor, providing not only iron oxide but also sodium hydroxide for pH control. The ultrasonic treatment is also important in this preparation. Pure ultrasound produces its effect through cavitation bubbles, which are thought to be the cause of erosion of particles in the vicinity of these bubbles. This is due to the explosion or implosion of the bubbles during the ultrasonic process, which may in turn produce microcavities with temperatures of many thousands of degrees and pressures of several hundreds of atmospheres.[37] As water and THF are the solvent in these experiments, the maximum bubble core temperature that can be reached is 4000 K, which causes the formation of H, OH, OOH and THF derivative radicals.[37] These radicals have been reported to form hydrogen peroxide, which may contribute to the oxidation of iron (II) oxides to Fe (III).[38]

3.6. Conclusions

Various magnetic iron oxide nanoparticles have been prepared using metallorganic iron (II) precursor $[(THF)NaFe(O^tBu)_3]_2$. The size, shape and

morphology of magnetic nanoparticles strongly depend on conditions of the process including temperature and time of the ultrasonic treatment.

It has been noted that the smallest sized particles (11±2 nm) were obtained at ultrasound levels of 8 hours and a temperature level of 80 °C. However, XRD analysis confirms the presence of maghemite in this sample. Therefore, we reject this as our optimum result. The best results both for particle size and yield of magnetite are obtained for sample S2 at lowest temperature (20 °C) with 8 hours in ultrasound (21±3 nm). The result obtained for particles prepared at 30 °C and 8 hours ultrasound (Sample S6, 25±5 nm) is close to this optimum result, thereby displaying the robustness of the experimental design. When time in ultrasound is increased, this causes an oxidation of the magnetite nanocrystals to the maghemite phase. During the ultrasound process, tiny bubbles are formed which may collapse or explode to create localised areas of high temperature (up to 4000 K) and pressure. These are thought to break down the particles to a nanometre scale. However, longer times spent in ultrasound may then lead to an increase in oxidation of the nanocrystals. This is in agreement with our findings. It has also been found that an increase in temperature leads to the transformation of the magnetite nanocrystals to maghemite nanoparticles. High temperatures accompanied with longer times in ultrasound yielded particles with the broadest size distribution. These results are confirmed by TEM, XRD and Raman spectroscopy.

The factorial design experiment was employed in the form of a response surface model, where the results can be represented graphically to represent the area of the optimum result. This allowed us to check when we are approaching the optimum conditions for particle size, when we reach the optimum and when we have gone beyond it. The design also allows particles of a certain size and distribution to be prepared by checking the conditions on the graph.

At ultrasound times of 8 hours, the particle size and spread are found to decrease. This is due to the break down of the particles by the ultrasonic effects. However, an increase in ultrasound times brings with it an increase in localised heating effects, which results in greater particle size, as determined by TEM and magnetisation measurements. The largest particle size has been found for sample S7 (30 °C and 10 hours ultrasound) and correspondingly, the saturation magnetisation value for this sample was also found to be the highest value obtained in the study

(73.4 J T^{-1} kg^{-1}). These results are in agreement with reported observations, where the magnetisation values decrease with decreasing particle size.[39]

The use of a statistical study provided an approach for the optimisation of nanocrystal preparation by varying temperature and ultrasonic treatment. From the results obtained, the best conditions for magnetite nanocrystals formation with a narrow size distribution have been identified. This approach could be used for optimisation of synthesis for the preparation of various nanoparticles and is not only confined to the preparation of iron oxides.

References

[1] M. Hanzlik, C. Heunemann, E. Holtkamp-Rotzler, M. Winklhofer, N. Petersen, G. Fleissner, *Biometals* **2000**, *13*, 325.

[2] B. Devouard, M. Posfai, X. Hua, D. A. Bazylinski, R. B. Frankel, P. R. Buseck, *American Mineralogist* **1998**, *83*, 1387.

[3] J. L. Kirschvink, M. M. Walker, C. E. Diebel, *Current Opinion in Neurobiology* **2001**, *11*, 462.

[4] P. R. Buseck, R. E. Dunin-Borkowski, B. Devouard, R. B. Frankel, M. R. McCartney, P. A. Midgley, M. Posfai, M. Weyland, *Proceedings of the National Academy of Sciences of the United States of America* **2001**, *98*, 13490.

[5] K. L. Thomas-Keprta, S. J. Clemett, D. A. Bazylinski, J. L. Kirschvink, D. S. McKay, S. J. Wentworth, H. Vali, E. K. Gibson, M. F. McKay, C. S. Romanek, *Proceedings of the National Academy of Sciences of the United States of America* **2001**, *98*, 2164.

[6] S. J. Clemett, K. L. Thomas-Keprta, J. Shimmin, M. Morphew, J. R. McIntosh, D. A. Bazylinski, J. L. Kirschvink, S. J. Wentworth, D. S. McKay, H. Vali, E. K. Gibson, C. S. Romanek, *American Mineralogist* **2002**, *87*, 1727.

[7] D. C. Golden, D. W. Ming, C. S. Schwandt, H. V. Lauer, R. A. Socki, R. V. Morris, G. E. Lofgren, G. A. McKay, *American Mineralogist* **2001**, *86*, 370.

[8] P. Tartaj, M. D. Morales, S. Veintemillas-Verdaguer, T. Gonzalez-Carreno, C. J. Serna, *Journal of Physics D-Applied Physics* **2003**, *36*, R182.

[9] Q. A. Pankhurst, J. Connolly, S. K. Jones, J. Dobson, *Journal of Physics D-Applied Physics* **2003**, *36*, R167.

[10] R. Massart, *IEEE Transactions on Magnetics* **1981**, *17*, 1247.

[11] Y. S. Kang, S. Risbud, J. F. Rabolt, P. Stroeve, *Chemistry of Materials* **1996**, *8*, 2209.

[12] Y. Lee, J. Lee, C. J. Bae, J. G. Park, H. J. Noh, J. H. Park, T. Hyeon, *Advanced Functional Materials* **2005**, *15*, 503.

[13] Z. H. Zhou, J. Wang, X. Liu, H. S. O. Chan, *Journal of Materials Chemistry* **2001**, *11*, 1704.

[14] J. A. L. Perez, M. A. L. Quintela, J. Mira, J. Rivas, S. W. Charles, *Journal of Physical Chemistry B* **1997**, *101*, 8045.

[15] J. M. Vargas, R. D. Zysler, *Nanotechnology* **2005**, *16*, 1474.

[16] Z. Li, L. Wei, M. Y. Gao, H. Lei, *Advanced Materials* **2005**, *17*, 1001.

[17] Y. K. Gun'ko, U. Cristmann, V. G. Kessler, *European Journal of Inorganic Chemistry* **2002**, 1029.

[18] R. D. Waldron, *Physical Review* **1955**, *99*, 1727.

[19] S. Y. Venyaminov, F. G. Prendergast, *Analytical Biochemistry* **1997**, *248*, 234.

[20] R. M. Cornell, U. Schwertmann, *The Iron Oxides*, Wiley VCH Verlag GmbH and Co., Weinheim, **1996**.

[21] X. L. Duan, D. R. Yuan, Z. H. Sun, H. Q. Sun, D. Xu, M. K. Lv, *Journal of Crystal Growth* **2003**, *252*, 4.

[22] O. N. Shebanova, P. Lazor, *Journal of Raman Spectroscopy* **2003**, *34*, 845.

[23] I. R. Beattie, T. R. Gilson, *Journal of the Chemical Society A -Inorganic Physical Theoretical* **1970**, 980.

[24] A. Wang, L. A. Haskin, B. L. Jolliff, in *Lunar and Planetary Institute Conference Abstracts*, p. 1819.

[25] O. N. Shebanova, P. Lazor, *Journal of Solid State Chemistry* **2003**, *174*, 424.

[26] G. F. Goya, T. S. Berquo, F. C. Fonseca, M. P. Morales, *Journal of Applied Physics* **2003**, *94*, 3520.

[27] S. Morup, H. Topsoe, J. Lipka, *Journal de Physique* **1976**, *37*, 287.

[28] K. Woo, J. Hong, S. Choi, H. W. Lee, J. P. Ahn, C. S. Kim, S. W. Lee, *Chemistry of Materials* **2004**, *16*, 2814.

[29] M. H. Liao, D. H. Chen, *Journal of Materials Chemistry* **2002**, *12*, 3654.

[30] C. R. Lin, Y. M. Chu, S. C. Wang, *Materials Letters* **2006**, *60*, 447.

[31] J. Wang, J. J. Sun, Q. Sun, Q. W. Chen, *Materials Research Bulletin* **2003**, *38*, 1113.

[32] Z. L. Liu, Y. J. Liu, K. L. Yao, Z. H. Ding, J. Tao, X. Wang, *Journal of Materials Synthesis and Processing* **2002**, *10*, 83.

[33] M. Blanco-Mantecon, K. O'Grady, *Journal of Magnetism and Magnetic Materials* **2006**, *296*, 124.

[34] D. Y. Godovsky, A. V. Varfolomeev, G. D. Efremova, V. M. Cherepanov, G. A. Kapustin, A. V. Volkov, M. A. Moskvina, *Advanced Materials for Optics and Electronics* **1999**, *9*, 87.

[35] S. Santra, R. Tapec, N. Theodoropoulou, J. Dobson, A. Hebard, W. H. Tan, *Langmuir* **2001**, *17*, 2900.

[36] G. B. Biddlecombe, Y. K. Gun'ko, J. M. Kelly, S. C. Pillai, J. M. D. Coey, M. Venkatesan, A. P. Douvalis, *Journal of Materials Chemistry* **2001**, *11*, 2937.

[37] T. J. Mason, *Chemical Society Reviews* **1997**, *26*, 443.

[38] R. V. Kumar, Y. Koltypin, Y. S. Cohen, Y. Cohen, D. Aurbach, O. Palchik, I. Felner, A. Gedanken, *Journal of Materials Chemistry* **2000**, *10*, 1125.

[39] X. Cao, Y. Koltypin, G. Katabi, R. Prozorov, *Journal of Materials Chemistry* **1997**, *7*, 1007.

Chapter 4: New iron oxide-silica nanocomposites

4.1. Introduction

Research on nano-scale magnetic materials treated with silica has received considerable attention owing to the potential of these materials in many technological applications, including catalysis[1-3] and information storage[4, 5]. Because the properties of magnetic materials are size dependant, this has led to an even greater increase of interest in this area. In particular, maghemite (γ-Fe_2O_3) particles in silica have been intensively studied. This is because of the ease of synthesis of γ-Fe_2O_3, which possesses only one oxidation state, compared to the requirement of two oxidation states in stoichiometric amounts for Fe_3O_4 (magnetite). Also, nanosized γ-Fe_2O_3 transforms to α-Fe_2O_3 (haematite) at 350 °C, but this transformation can be avoided if the particles are protected with a shell or outer layer.[6]

Magnetic silica-iron oxide nanocomposites have attracted particular interest in the past few years. For many applications, a silica coating on the magnetic nanoparticles would be advantageous. Silica-coated magnetic nanoparticles are hydrophilic and stable against biodegradation that improves their biocompatibility and facilitates their biomedical utilization. Furthermore, the ease of silica surface modification[5] allows further modifications to perform biolabeling, drug targeting, and drug delivery. In addition, nanosized γ-Fe_2O_3 transforms to α-Fe_2O_3 (haematite) at 350 °C, but this transformation can be avoided if the particles are protected with a shell or outer layer.[6] Finally, it has been shown that the magnetic properties of γ-Fe_2O_3 nanoparticles can be enhanced by silica and octadecyltrihydrosilane coating.[7]

One of the most widely used approaches for synthesising iron oxide-silica nanocomposite materials (Figure 4.1) is *via* a sol-gel process.[8-11] This involves the use of silicon alkoxides (usually tetraethyl orthosilicate) as a silica source.[12] The magnetic components may be added in the form of preformed magnetic particles[13] or an iron source may be added to the silica and the particles formed *in situ*.[14] One of the advantages to using an *in situ* method is that the particles may be embedded within a matrix or coating of silica and hence are protected from oxidation.

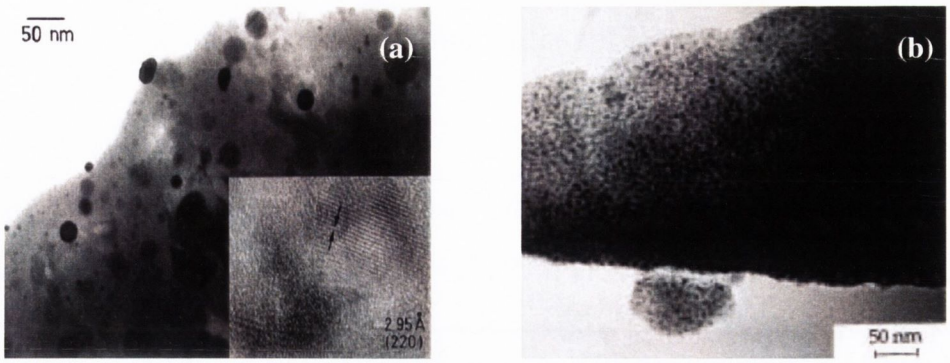

Figure 4.1 TEM images of previously reported iron oxide-silica nanocomposites[8, 14]

The particle size too may be controlled by using a stabiliser.[15] For example, Cannas *et. al.*[16] have studied the effect of silica on the resulting particle size and have found that depending on the gelation time, the nanoparticle size could be controlled between 10 and 4 nm. In order to bypass the use of high temperatures during the sol-gel process, Xue *et. al.*[17] have developed a mechanical milling procedure which they employ after preparation of the sol-gel. This method requires the use of a ball mill at 900 rpm for 30 hours to yield γ-Fe_2O_3 nanoparticles embedded within a silica matrix.

The sol-gel technique has been widely employed to generate new nanostructured materials. For example, Zhang *et. al.*[18] have reported the preparation of titanium dioxide (TiO_2) nanotubes *via* the use of tetraethyl orthosilicate (TEOS) in a sol-gel experiment. By varying the concentration of silica in a series of experiments, the authors showed that the best concentration for the optimum number of TiO_2 nanotubes was 5 at% TEOS. One drawback with this method is the use of high temperatures (up to 600 °C) which could lead to oxidation of samples if used for magnetic nanoparticles. However, the use of heat could be avoided if ultrasound is employed. In this way, high temperatures and pressures could be instantaneously generated and then dissipated in the local environment of the particles but would not lead to the oxidation of the sample.[19] Ultrasonic processes have been used previously in particle coating procedures. For example, an ultrasonic probe has been used to coat γ-Fe_2O_3 nanoparticles with octadecyltrihydrosilane by Shafi *et. al.* who have used thermogravimetric analysis to probe the particle surface coating by the silane.[7]

4.2. Aims of this chapter

The main aim of this part of the work is to prepare and characterize new iron oxide-silica nanocomposite materials. To produce these nanocomposites, a sol-gel method combined with ultrasonic treatment will be employed, using a different iron precursor from that used in Chapter 3. A metallorganic iron (II) tert-butoxide will be used as the iron precursor and tetraethyl orthosilicate as the silica precursor. In this work, the nanocomposite formation is to be carried out *in situ* making this a convenient single step method for the preparation of iron oxide-silica nanocomposite materials. The composites are to be investigated by FTIR and Raman spectroscopy, XRD patterns, TGA, Mössbauer spectroscopy, magnetisation measurements, and SEM and TEM analysis. This work is expected to contribute to the further development of magnetic nanocomposite materials.

4.3. Synthesis and characterisation of metallorganic Fe(II) precursor

Metallorganic precursor $[Fe(OBu^t)_2(THF)]_2$ has been synthesised by reaction between two equivalents of sodium *tert*-butoxide and one equivalent of iron (II) bromide in dry THF. The reaction results in the formation of dark solution and a precipitate of sodium bromide. The product $[Fe(OBu^t)_2(THF)]_2$ is, like the heterometallic precursor from Chapter 3 ($[(THF)NaFe(OBu^t)_3]_2$), extremely air and moisture sensitive and demonstrates a colour change from dark green to orange upon exposure to the air.

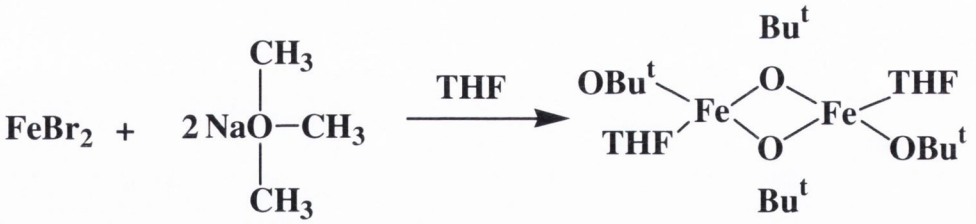

(2)

Scheme 4.1 Preparation of metallorganic precursor $[Fe(OBu^t)_2(THF)]_2$ (2)

The product has been characterised by ^1H NMR and FTIR spectroscopy. The ^1H NMR spectrum (Appendix 4) carried out in dry degassed C_6D_6 of $[Fe(OBu^t)_2(THF)]_2$ reveals very two broad peaks for the butoxide protons, one found at 0.3 ppm corresponding to the μ_2-OBu^t bridging group and the other at 1.1 ppm representing the terminal OBu^t groups. Two broad peaks corresponding THF are

found at 3.6 and 1.4 ppm, with the later appearing as a shoulder on the terminal butoxide peak. There is some shift and a significant broadening of the peaks due to the presence of the paramagnetic iron ion.

An IR spectrum (Appendix 5) was carried out in Nujol using a nitrogen bag to prevent oxidation. The symmetric and asymmetric C-O-C stretches for THF were found at 1022 and 957 cm^{-1} respectively. Any Fe-O bands are masked by Nujol peaks.

4.3.1 Preparation and characterisation of magnetic nanoparticles from metallorganic precursor

4.3.1.1 Preparation of magnetic nanoparticles

The metallorganic precursor, $[Fe(OBu^t)_2(THF)]_2$, was used as an iron source for the preparation of magnetic nanoparticles. A solution of the precursor as prepared in THF in the presence of sodium bromide was hydrolysed with doubly distilled water and treated with ultrasound for several hours (Scheme 4.2). This yielded a black precipitate which was then dried under vacuum. The product was characterised by electron microscopy, TGA and Mössbauer spectroscopy.

4.3.2 Characterisation of magnetite nanoparticles

4.3.2.1 Electron Microscopy

The iron oxide samples were dispersed in ethanol using ultrasound for ten minutes and a drop placed on a copper formvar grid. The images (Figure 4.2) revealed particles with a quite broad size distribution. There is evidence from TEM of the formation of crystalline particles, but these are not as uniform as those obtained for the heterometallic precursor $[(THF)NaFe(OBu^t)_3]_2$.

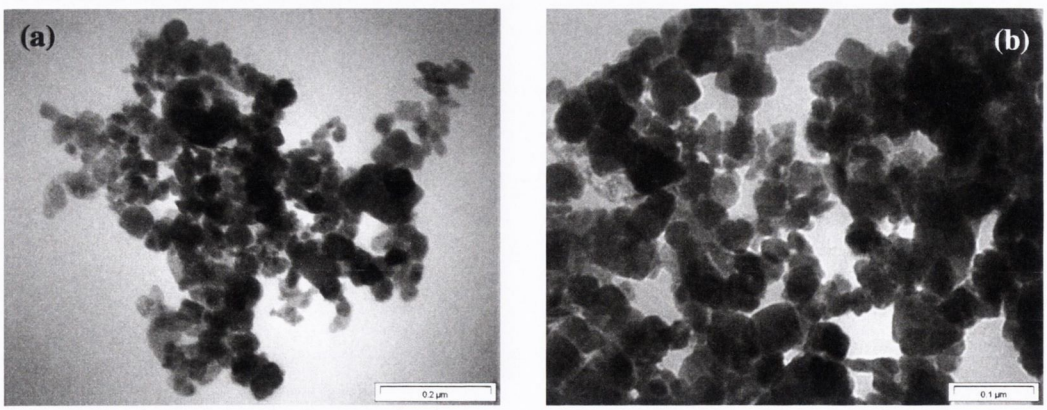

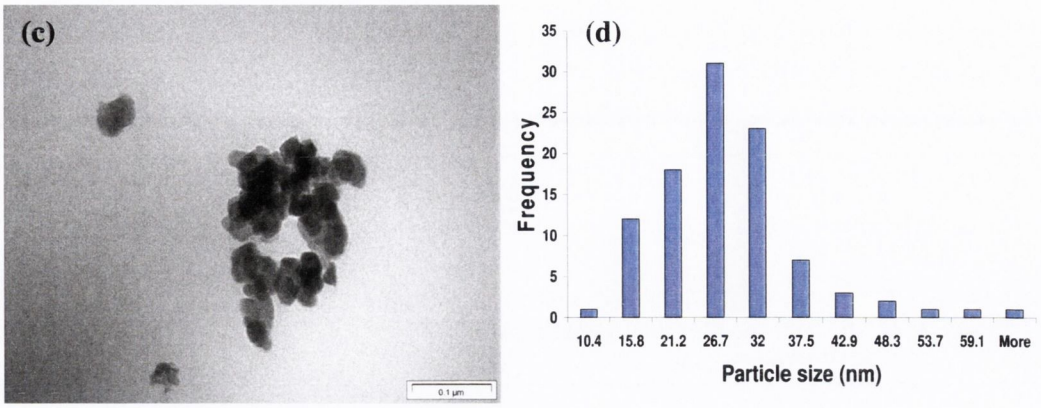

Figure 4.2 (a)-(c) TEM images and **(d)** particle size histogram of nanoparticles prepared from metallorganic precursor, $[Fe(OBu^t)_2(THF)]_2$

The particle size distribution was calculated by measuring the average size from 100 particles (Figure 4.2d). The average particle size was found to be 25.4 nm and the standard deviation is 9.5 nm.

4.3.2.2 Thermogravimetric analysis (TGA)

TGA analysis was carried out on the iron oxide sample to determine any mass loss as a result of surface groups which are removed during the heating process (see Figure 4.3). Thermal stability studies such as these can reveal information about the surface structure of the particles, in particular the presence of solvents and surface-associated water molecules.

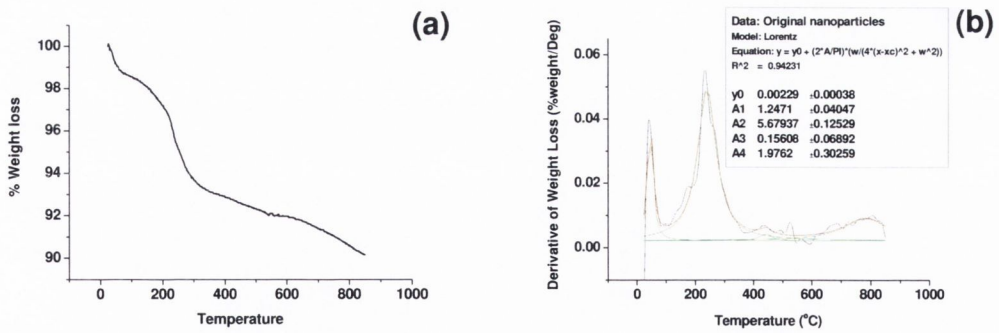

Figure 4.3 (a) TGA curve and **(b)** derivative for nanoparticles prepared from metallorganic precursor, $[Fe(OBu^t)_2(THF)]_2$

It can be often more informative to study the derivative of TGA traces, as it is easier to note the temperatures at which mass loss occurs and also the percentage loss

(see Figure 4b). The derivatives of the TGA curves were determined using the Origin program and a Lorenzian fit established for each peak.

Mass losses between room temperature and 180 °C may correspond to weakly bonded or physisorbed species onto the surface of the particles. For example, the sample reveals a loss at approximately 47 °C. This is attributed to the loss of tetrahydrofuran, which must be still present in the sample. The loss of other volatile species, such as ethanol, should occur at approximately 120 °C.[17] Strongly adsorbed water and dehydration of surface hydroxy ligands are lost above 250 °C. Reported DTA traces have revealed that exothermic signals occur at 600 °C and are due to the transition of the material from amorphous to crystalline phases.[15]

4.3.2.3 Mössbauer Spectroscopy

In the Mössbauer spectrum, a least square fit is applied to the experimental data in order to determine the particle size and to check the stoichiometry of the sample in question. The spectrum obtained for this sample is characteristic of non-stoichiometric magnetite, which a line splitting due to the presence of the two iron ions present (Figure 4.4). There is a distribution of hyperfine magnetic fields, caused by the different iron ion environments in the structure, leading to a small line broadening.

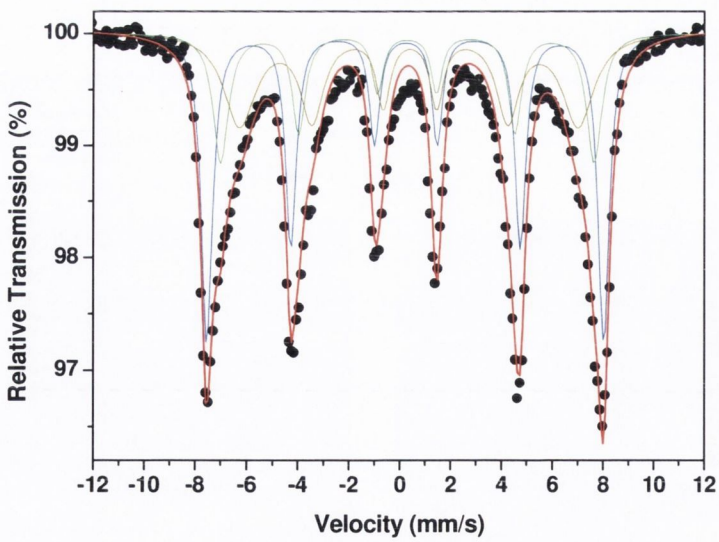

Figure 4.4 Mössbauer spectrum of magnetite nanoparticles prepared from metallorganic precursor, $[Fe(OBu^t)_2(THF)]_2$

4.4 Silica-iron oxide nanocomposites

4.4.1 Preparation of iron oxide-silica nanocomposites

A solution of the precursor $[Fe(OBu^t)_2(THF)]_2$ as prepared in Section 4.3 was stirred for 24 hours at the ambient temperature. Tetraethyl orthosilicate (TEOS, Aldrich, 98%) was added according to the required silicon amounts of 0.5at%, 1at%, 2at%, 5at%, 7.5at%, 10at%, 15at%, 20at% and 30at%, labelled FS1, FS2, FS3, FS4, FS5, FS6, FS7, FS8 and FS9 respectively. The mixture was carefully hydrolysed by doubly distilled water (20 ml) and was ultrasonically (30 kHz, 130 W) irradiated at the ambient temperature for two hours. The water layer was removed and further 20 ml distilled water added. The reaction vessel was placed again to ultrasound for one hour. This process was repeated once more. The black precipitate was filtered and dried under vacuum.

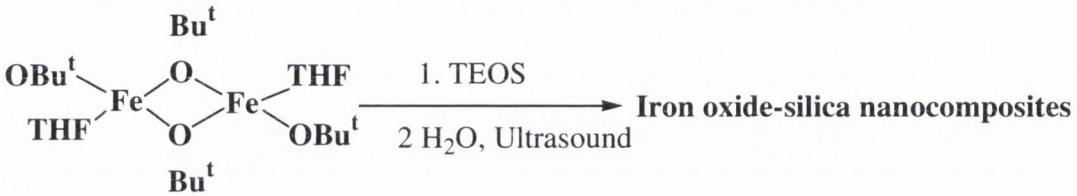

Scheme 4.2 Preparation of iron oxide-silica nanocomposites from metallorganic precursor. *Reagents and conditions*: (i) Addition of required amount TEOS; (ii) distilled water and ultrasound, RT, 2 h.

The products obtained have been studied by FTIR and Raman spectroscopy, XRD patterns, TGA, Mössbauer spectroscopy, magnetization measurements and TEM analysis.

4.4.2 Characterisation of iron oxide-silica nanocomposites

4.4.2.1 FTIR spectroscopy

Infrared spectra of all samples were carried out in KBr from 4000 to 400 cm^{-1} (Figure 4.5). For maghemite, a number of stretches have been reported in the Fe-O range with broad IR bands at 700, 640-660, 620, 580, 560, 460, 430, 390, and 305 cm^{-1}.[20] In the case of FS1, Fe-O stretches consistent with maghemite are found at 455 and 675 cm^{-1} respectively.

For most samples, the presence of two bands representing the Fe-O stretches is typical, with the exception of samples FS5 and FS7 where a stretch at approximately

580 cm^{-1} is found. For most spectra, a band at approximately 800 cm^{-1} is also noted. This band has been previously assigned to $(Fe^{3+})_2OH$ deformation.[21] Stretches at approximately 1030 and 1260 cm^{-1} are assigned as asymmetric Si-O-Si stretches.[10] As the concentration of silica present in the samples increases, the asymmetric Si-O-Si stretches increase in intensity.

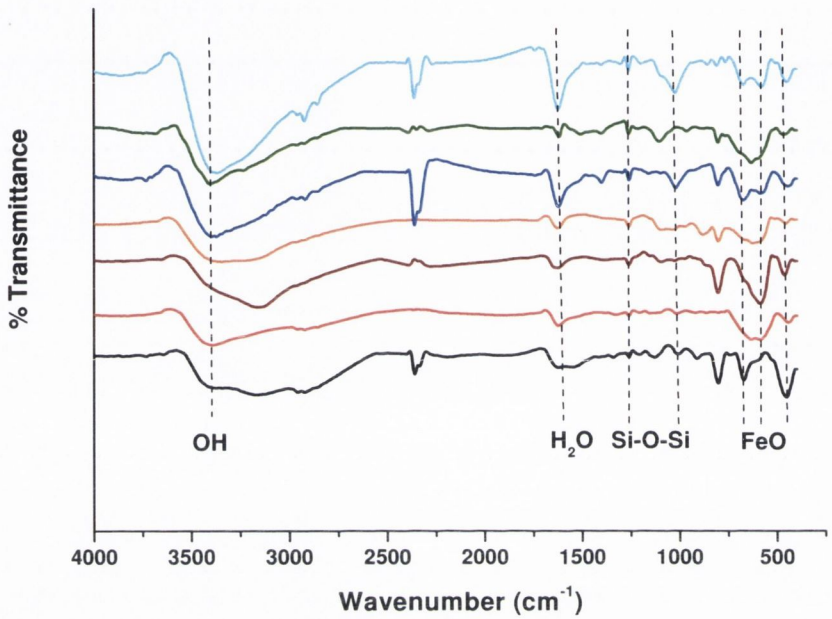

Figure 4.5 IR spectra from a KBr disk of iron oxide-silica nanocomposites from metallorganic precursor (2), from bottom to top: FS1 (black), FS2 (red), FS3 (maroon), FS4 (orange), FS6 (blue), FS8 (green) and FS9 (turquoise)

Table 4.1 IR stretches for iron oxide-silica nanocomposites

Sample	Wavenumbers for selected IR stretches					
FS1	455, 675	805	918	-	1638	3396
FS2	449, 632	-	1007	1263	1627	3391
FS3	462, 593	809	1102	1268	1631	3162
FS4	458, 624	801	1044	1267	1622	3359
FS6	448, 548, 674	803	1022	1264	1626	3388
FS8	469, 636	803	1109	1268	1619	3409
FS9	456, 583, 678	804	1026	1269	1631	3370

The vibrational stretching mode for water is found in all samples at 1620 cm^{-1} while the stretching vibrational contributions from the symmetrical (ν_1) and

asymmetrical (ν_3) modes of the O-H bonds, attached to the surface iron atoms,[22] is found at ca. 3400 cm^{-1}.

4.4.2.2 Raman spectroscopy

Raman spectra were recorded for all samples (Figure 4.6). As was the case with nanocrystals described in Chapter 3 prepared from a metallorganic precursor, these samples were studied using a low laser power to prevent phase transition into Fe(III) oxides by heat effects of the laser.

Spectra were run from 2000 to 200 cm^{-1} (see Appendix 6 for a table of all peaks). Compared to the spectrum for magnetite, there are a greater number of Raman and infrared-active modes for maghemite.[23] The structure of maghemite is close to that of the inverse spinel of magnetite, but differs in that there are vacancies distributed on the cation sublattice.[24] Cation vacancies exist in the structure to compensate for the oxidation of the larger Fe^{2+} ions. The structure adopted by maghemite has been found to form an ordered superlattice, which results from an ordering of the cations and these vacancies. Each unit cell of γ-Fe_2O_3 contains 32 oxygen ions, 21⅓ Fe^{3+} ions and 2⅓ vacancies giving the molecular formula $(Fe)(Fe_{5/3}\square_{1/3})O_3$.[25] The extent of the vacancy ordering depends on the sample preparation method and this, in turn, has an effect on the resulting Raman spectrum.

The reported observed wavenumbers for maghemite are 350 (T_1), 500 (E), and 700 cm^{-1} (A_1).[23] These are in good agreement for the observed peaks found for these samples, where the peaks are found at approximately 690 and 495 cm^{-1} with the final peak shifted, possible due to oxidative laser effects, to 300 cm^{-1}.

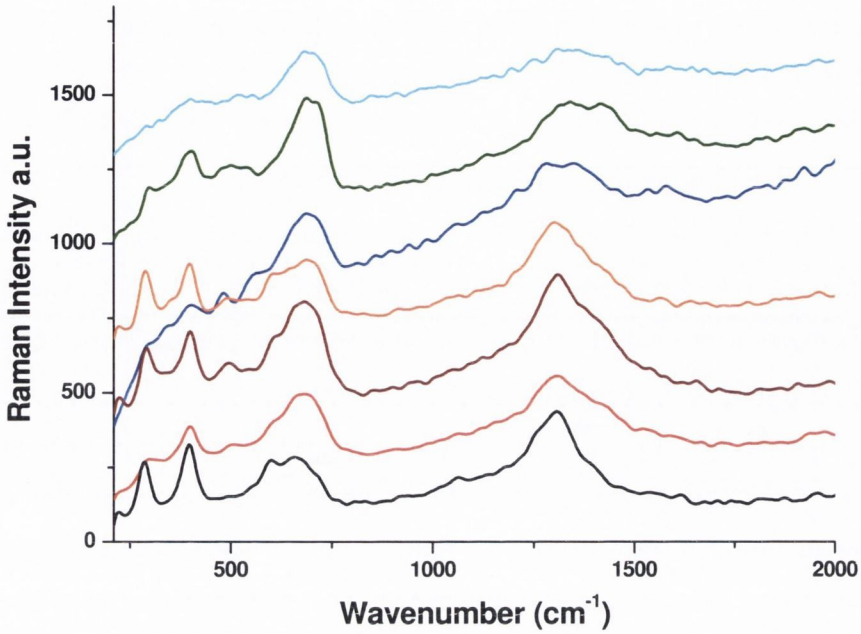

Figure 4.6 Raman spectra of, from bottom to top, FS1 (black), FS2 (red), FS3 (maroon), FS4 (orange), S6 (blue), FS8 (green) and FS9 (turquoise)

4.4.2.3 X-ray diffraction

X-Ray diffraction patterns were collected of all samples (FS1 – FS9). The diffraction patterns are shown in Figure 4.7, along with the peak positions corresponding to the standard maghemite phase (taken from the JCPDS database). The diffraction patterns reveal the presence of a cubic iron oxide spinel phase. However, because the powder diffraction patterns for the two iron oxide phases magnetite and maghemite are very similar and the diffraction lines are broad due to the presence of smaller crystallites, a distinction between the two is not straightforward.[26] The lattice parameters, when compared to the database values, for all samples appear to be closer to maghemite. The broad reflection at 35.7° is attributed to the formation of nanosized crystallites of maghemite.[27] The broadening of the diffraction patterns for nanoparticulate material is well documented in the literature.[28] Line broadening may be taken as an indication that the observed particles are a few nanometers in diameter[29] or that the material formed is amorphous in nature.[6]

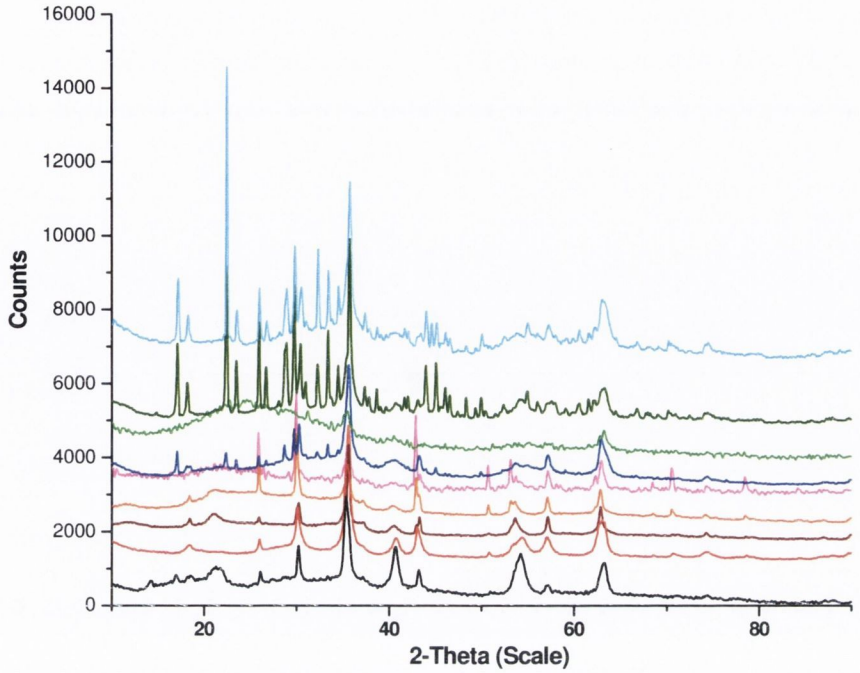

Figure 4.7 XRD patterns for iron oxide-silica nanocomposites, from bottom to top: FS1 (black), FS2 (red), FS3 (maroon), FS4 (orange), FS5 (pink), FS6 (blue), FS7 (light green), FS8 (green) and FS9 (turquoise)

For many of the reported procedures for the preparation of iron oxide-silica nanocomposites, the diffraction peaks observed for the materials at short reaction times or before heat treatment are weak.[27, 30, 31] The purpose of heat treatment in these cases was to stabilise the maghemite phase.[30] It has been reported that the iron oxide phase becomes crystalline at temperatures greater than 700 °C to give diffraction patterns corresponding to maghemite, while above 900 °C the haematite phase is formed.[14] In the case of extended reaction times, a report on the use of mechanical milling for the preparation of nanocomposites has revealed that by extending the reaction time from 10 to 20 hours more peaks attributed to the spinel phase were found.[17] An increase to 30 hours was found to cause a phase change to haematite. In the case of samples FS1 – FS9, there was no additional reaction time or heat treatment required to sharpen the iron oxide phase peaks.

The interlayer spacings (d_{hkl}) were calculated from the Bragg equation (Table 4.2). Once the lattice spacings are known, it is possible to calculate the lattice parameter *a* from the interplanar spacing of the most intense peak. For maghemite, this peak corresponds to the (311) hkl line.

Table 4.2 Lattice parameters and interplanar spacings for samples FS1 – FS10. Theoretical values for maghemite (γ-Fe_2O_3) and magnetite (Fe_3O_4) taken from references[20, 32]

Sample		(hkl)					
		1	2	3	4	5	6
	$a_{(311)}$	(220)	(311)	(400)	(422)	(511)	(440)
FS1	0.8426	0.2928	0.2540	0.2092	0.1697	0.1601	0.1474
FS2	0.8403	0.2976	0.2534	0.2102	0.1682	0.1614	0.1474
FS3	0.8368	0.2928	0.2523	0.2077	0.1711	0.1614	0.1485
FS4	0.8514	0.2976	0.2567	0.2102	0.1711	0.1614	0.1478
FS5	0.8379	0.2996	0.2527	0.2116	0.1725	0.1616	0.1481
FS6	0.8354	0.2976	0.2514	0.2102	0.1720	0.1614	0.1474
FS7	0.8403	0.2966	0.2534	0.2091	0.1689	0.1614	0.1473
FS8	0.8335	0.2976	0.2513	0.2102	0.1742	0.1614	0.1474
FS9	0.8321	0.2976	0.2509	0.2056	0.1674	0.1614	0.1470
γ-Fe_2O_3	***0.834***	***0.295***	***0.2514***	***0.2086***	***0.1701***	***0.1604***	***0.1474***
Fe_3O_4	***0.839***	***0.2967***	***0.2532***	***0.2099***	***0.1715***	***0.1616***	***0.1484***

The (hkl) crystalline planes have been identified as (220), (311), (400), (422), (511) and (440)[33] which correspond to angles of 30, 35.5, 43, 54, 57 and 63 degrees 2θ respectively. From the interplanar spacings and lattice parameters calculated for all samples, it appears that there is a trend for the particles with lower silica concentration to adopt the magnetite structure. With increasing silica concentration it is noted that the lattice parameters for the samples are closer to the maghemite values. This observation is similar to that reported by Zhang *et. al.*[18] who found that, upon increasing the silicon content in their titania samples, a phase transformation occurred.

The Scherrer formula was used in conjunction with TEM results to determine the particle sizes. The mean crystallite diameter has been estimated from the (311) reflection. The calculated values are given in Table 4.3.

Table 4.3 Nanorod sizes as calculated from the Scherrer equation and TEM data

Sample	XRD (Scherrer formula, nm)	TEM Mean (nm) ± S.D.
FS1	11	33.1 ± 13
FS2	16	28.6 ± 9
FS3	19	34.4 ± 13
FS4	17	34.8 ± 12
FS5	7	26.5 ± 8
FS6	11	19 ± 5
FS7	6	18.6 ± 6
FS8	20	29 ± 6
FS9	9	22 ± 5

A broad peak around 20° is attributed to amorphous silica.[34] Additional peaks occur for samples with higher silica concentration, in particular the peaks at 17.2, 18.2 and 22.5 degrees 2θ are found to increase with increasing silica content. These peaks cannot be attributed to any iron oxide phase. It is most likely that these peaks are caused by the presence of several silica polymorphs. The JCPDS database shows that the triclinic and hexagonal phases of silicon dioxide coincide with the majority of extra peaks observed.

4.4.2.4 Thermogravimetric analysis (TGA)

Thermogravimetric analysis was carried out on all samples to investigate the structural evolution with increasing temperature over time in the final products (see Figure 4.8). The derivatives of the TGA curves for each sample were determined using the Origin program and a Lorenzian fit established for each peak (Appendix 7). All temperatures at which a mass loss is recorded are shown in Table 4.4.

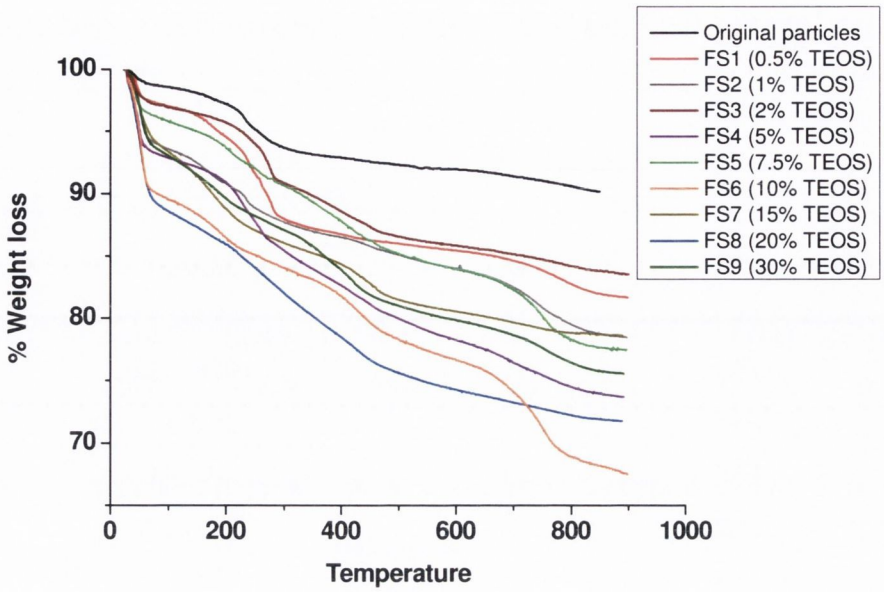

Figure 4.8 TGA curves for samples FS1 – FS9, including data for the original samples

Table 4.4 Temperatures at which mass loss occurs for sample S1 – S9 from TGA traces

Sample	Temperatures				
Original	41	-	232	-	804
FS1	46	176	-	460	707
FS2	49	171	233	447	741
FS3	43	-	274	400	772
FS4	46	-	243	422	728
FS5	41	-	230	403	757
FS6	52	-	193	429	752
FS7	46	177	-	446	712
FS8	49	-	243	-	797
FS9	51	189	-	407	757

Silica gels are said to be dry once the physically adsorbed water is completely removed and occurs between 100 and 180 °C. However, a dried gel often contains a large concentration of hydroxyl groups on the surface[35] which may be desorbed between 500 and 800 °C. All spectra show losses for THF below 100 °C and weakly

adsorbed water up to 275 °C. Derivatives for all TGA curves given in Figure 4.8 may be found in Appendix 7.

4.4.2.5 Electron microscopy

TEM analysis was carried out on all samples (Figures 4.9 and 4.10). Analysis of iron oxide-silica samples reveals that, with increasing silica concentration, there is an increase in the number of rod-like shaped nanoparticles. According to TEM images the sample FS1 (0.5% TEOS) consists mainly of nanocrystalline material, with an average particle size of 37 nm (Figure 4.9a). The majority of particles are plate-like in appearance. However, even with such a low concentration of silica present during the preparation, there are some rod-shaped nanoparticles also present (with an average size of 32 nm). An increase in the silica concentration causes the formation of more rod-shaped particles, but the predominant shape is still plate-like for sample FS2 (Figure 4.9b).

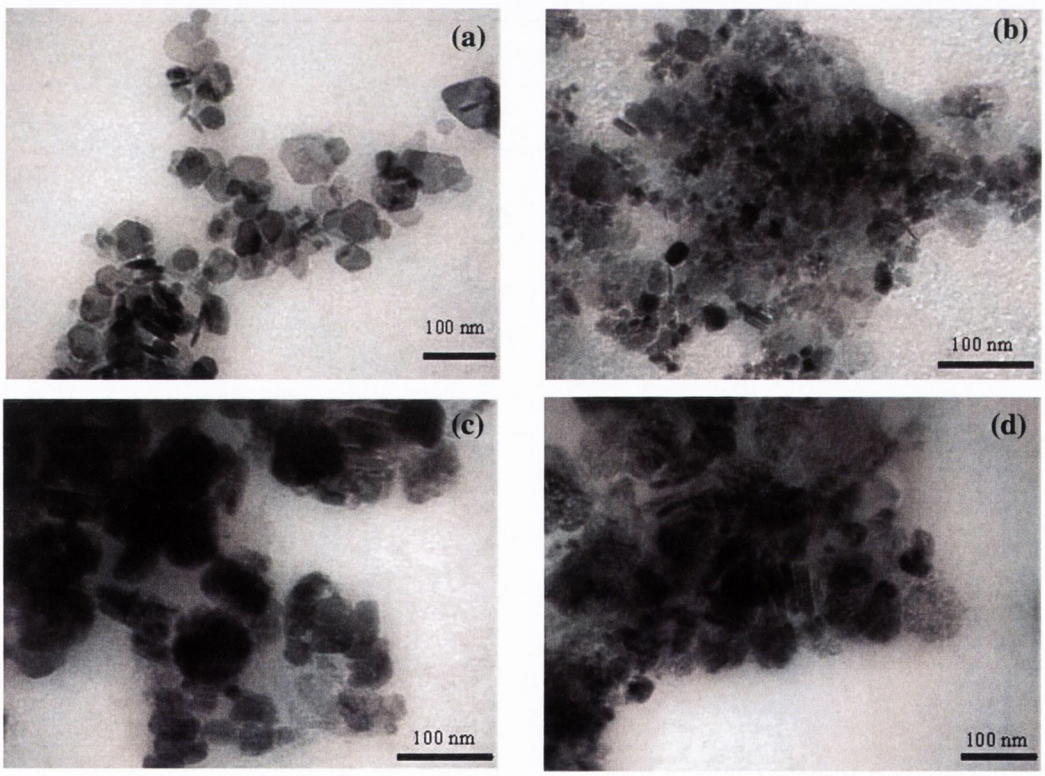

Figure 4.9 TEM images of **(a)** FS1 (0.5 % TEOS), **(b)** FS2 (1 % TEOS), **(c)** FS3 (2 % TEOS), **(d)** FS4 (5 % TEOS)

Samples FS3 and FS4 reveal large particles which have a grainy appearance (Figure 4.9 c, d). The rod-like particles appear to be stacking in groups of 2 – 3. These samples may give an indication of how the nanorods form. The grainy appearance of the large nanoparticles may infer that they are being broken down into smaller entities which could be forming the nanorod particles.

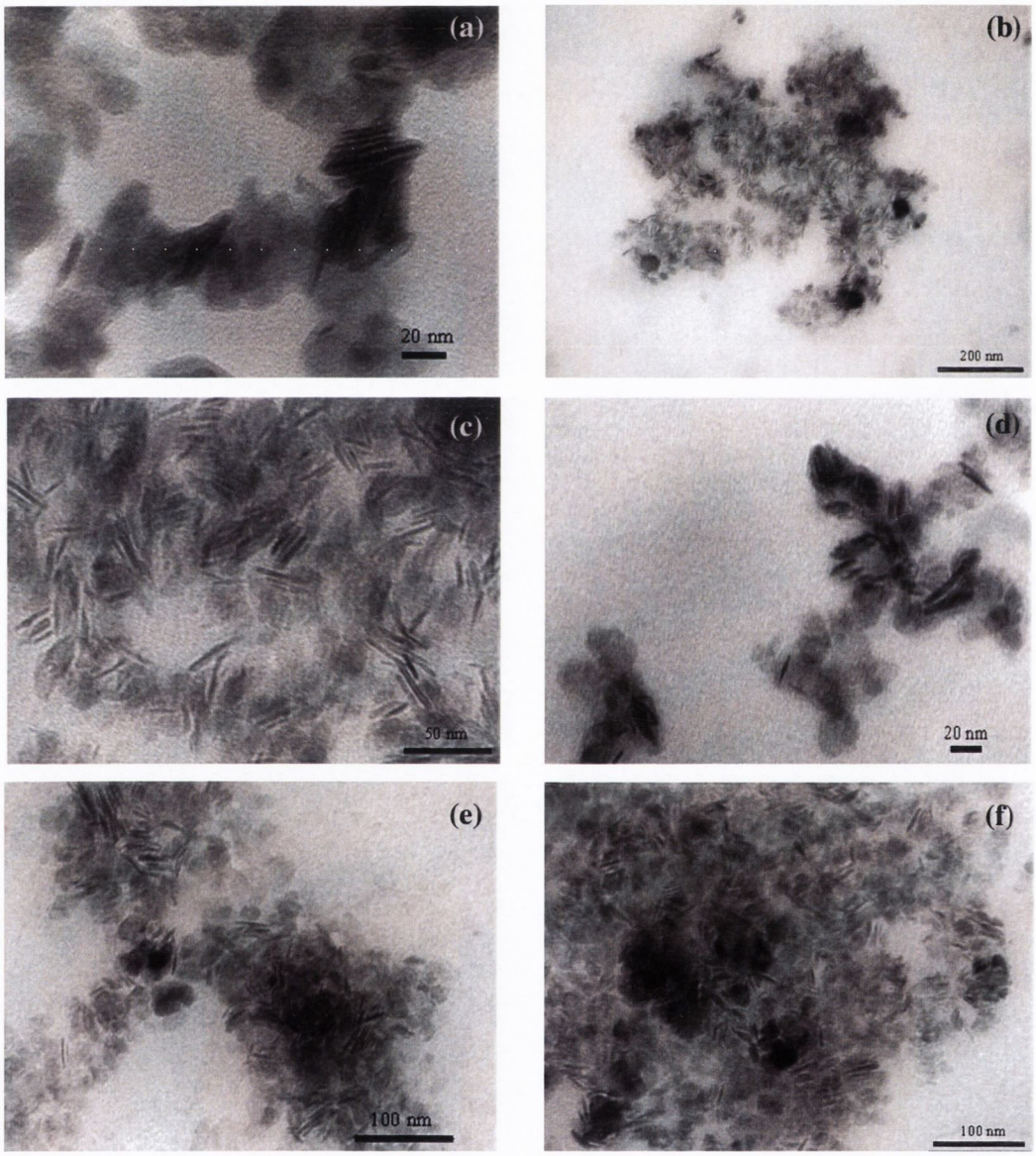

Figure 4.10 TEM images of **(a)** FS5 (7.5 % TEOS), **(b), (c)** FS6 (10 % TEOS), **(d)** FS7 (15 % TEOS), **(e)** FS8 (20 % TEOS) and **(f)** FS9 (30 % TEOS)

Sample FS6 reveals the starkest change in the morphology of the composite (Figure 4.10). Here, the sample is made predominantly of uniform nanorods with an

average particle size of 20 nm. Again, the stacking of the rods is evident. Increasing the silica concentration from 15 to 20 % (samples FS7 and FS8 respectively) causes aggregation to occur. This is also true for the highest silica concentration of 30 % (sample FS9). This aggregation may be explained by the excess silica "gluing" the nanorods and particles together. It is clear from the TEM images that samples FS6 (10 %) and FS9 (30 %) contain mostly nanorods. However, there is also an increased presence of amorphous shapeless material (presumably silica) at higher (20 and 30 %) content of silica.

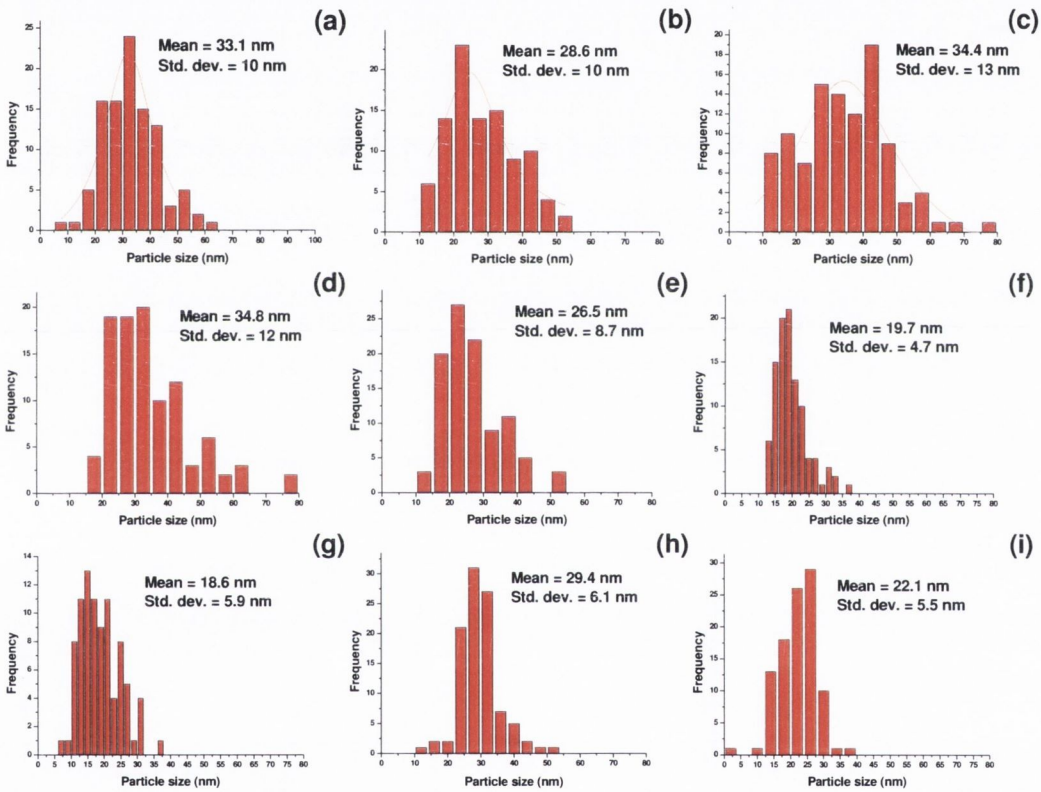

Figure 4.11 Histograms showing average particle size (N = 100) for samples (a) FS1, (b) FS2, (c) FS3, (d) FS4, (e) FS5, (f) FS6, (g) FS7, (h) FS8 and (i) FS9. Note as silica concentration is increased, the overall trend is a decrease in particle size.

In order to further study the morphology of these nanorods, high resolution TEM (HRTEM) images were taken of sample FS5 in Queens University Belfast (see Figure 4.12). These images reveal that the nanorods are made up of a crystalline material. Atomic resolution was possible and reveals a lattice spacing of 2.48 Å. This lattice spacing distance corresponds to the [311] lattice plane of maghemite.[20]

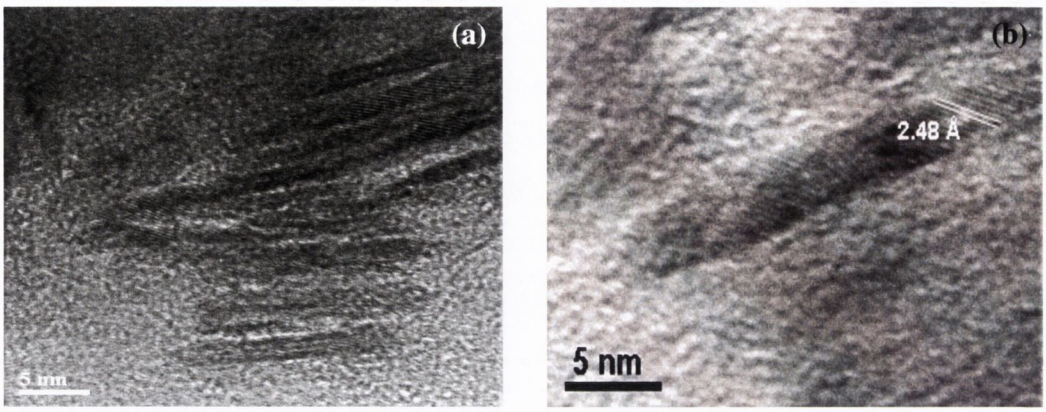

Figure 4.12 HRTEM images of FS5 (10%). Figure (b) shows a close-up of one of the nanorods, with lattice spacing 2.48 Å

Bright and dark field images of sample FS5 were also taken using a scanning tunneling electron microscope (STEM) in Japan. Dark field images are created by using back scattered electrons, thereby giving an impression of the elemental composition of the samples – the heavier the backscattered electrons, the brighter the contrast. As can be seen in Figure 4.13 below, the more concentrated areas of nanorods give the brightest contrast indicating the presence of a heavier element, in this case, iron.

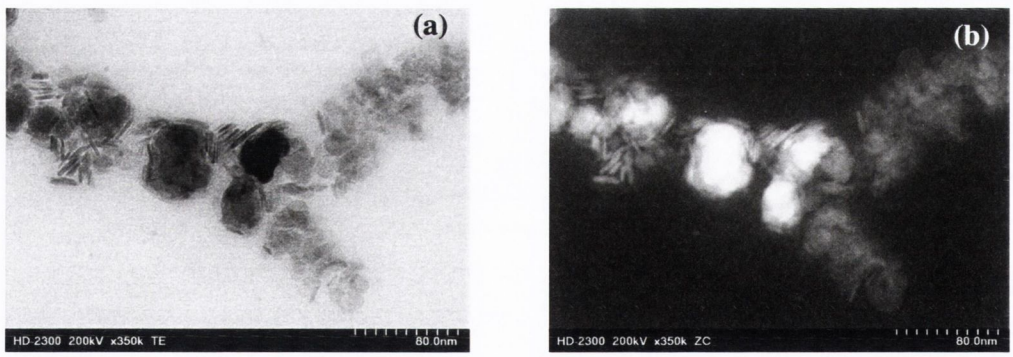

Figure 4.13 (a) Bright field and **(b)** dark field images of sample FS5 (10% TEOS)

The STEM technique distinguishes between elements in TEM imaging. This technique is based on selective detection of the elements from their backscattered electrons. For sample FS6, this was carried out to selectively monitor the backscattered electrons for iron, oxygen and silicon (Figure 4.14). For iron, it is found that it is observed only in the regions containing nanorods or particles. Silicon

is observed throughout the sample as is oxygen, but they are both concentrated wherever there are particles.

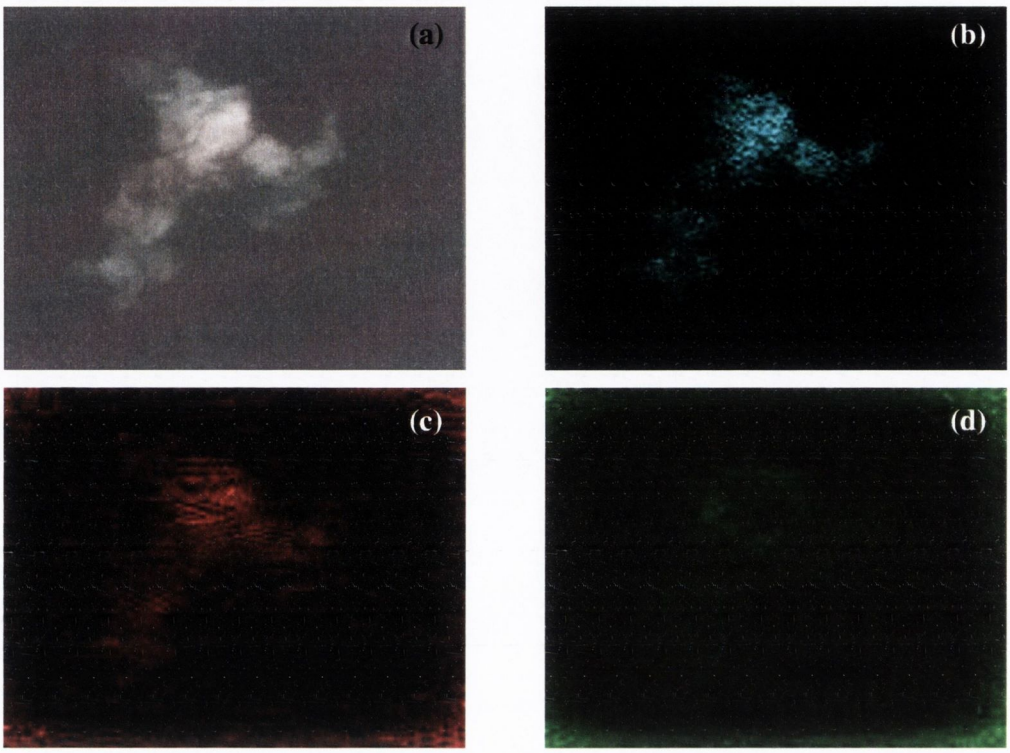

Figure 4.14 STEM image of sample FS6 revealing (a) dark field image; regions of (b) iron, (c) oxygen and (d) silicon.

High resolution imaging and analysis was also performed on sample FS9 using an STEM. Figure 4.15 shows an annular dark-field (ADF) image of a region of sample FS9. Annular dark-field imaging collects relatively high angle (> 70 mrad) elastic scattering as the electrons are transmitted through the sample. It therefore has a strong sensitivity to atomic number, and is sometime referred to as Z-contrast imaging. The iron containing regions are therefore clearly observed as being brighter in the images.

By recording electron energy-loss spectra (EELS) for various positions of the illuminating beam, compositional maps may also be produced. Figure 4.15 shows Fe and Si compositional maps. As expected, both the rods and other nanoparticulate material contain Fe. The Si can be seen to surround the Fe containing material up to some distance from the nanoparticles. From this, it may be observed that the nanorods are coated with silica.

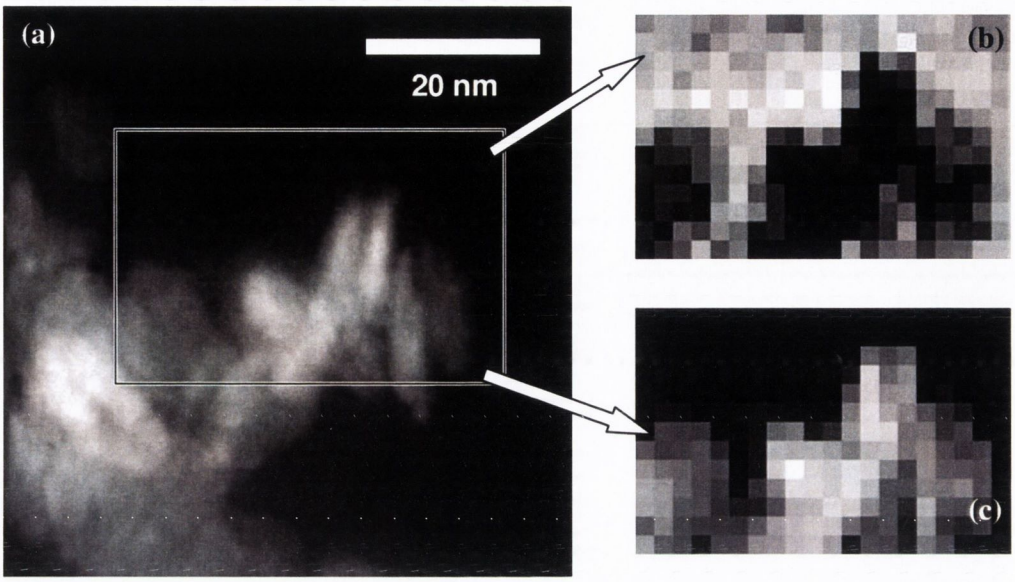

Figure 4.15 STEM image of a region of sample 66 (30% Si). The square annotation shows the region used for the composition mapping in figures (b) and (c). EELS spectra of a map of the intensity of (b) the Si L-edge recorded using an energy window width 10 eV centred on 108 eV energy-loss and (c) Fe $M_{2,3}$ edge recorded using an energy window width 10 eV centred on 58 eV energy loss.

At higher magnifications, many of the plate-like nanoparticles showed the 0.48 nm lattice spacing expected for the (111) plane spacing of maghemite (Figure 4.16). In contrast, none of the rods showed this spacing, but Figure 4.16 does show a 0.34 nm (211) spacing of maghemite.

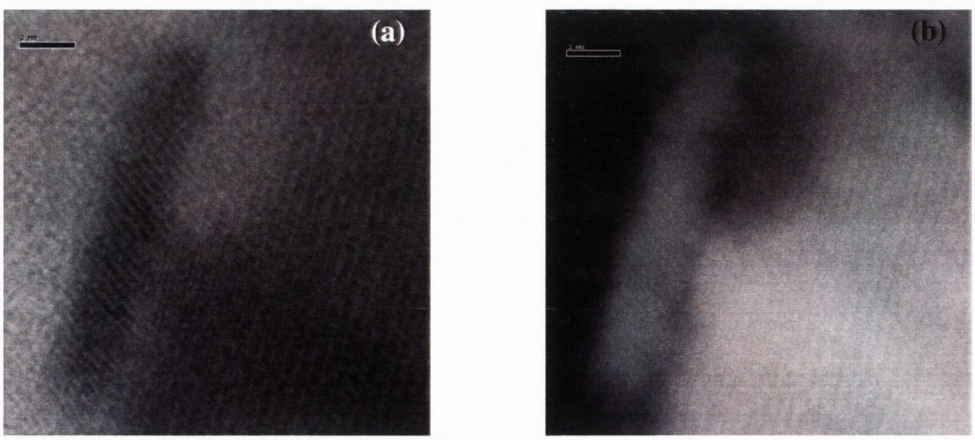

Figure 4.16 High-resolution (a) BF and (b) ADF STEM image of a region of an isolated nanorod attached to a large nanoparticle.

Care was needed when imaging this sample. Electron irradiation in the STEM was observed to cause a change in the nanorod structure resulting in observed lattice spacings more consistent with haematite. The hematite {110} planes have a spacing of 0.25 nm and have been observed for samples which have been irradiated for a period of time (Figure 4.17).

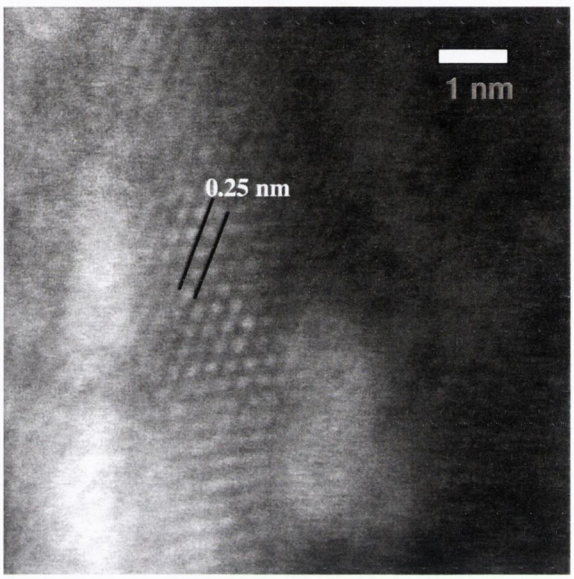

Figure 4.17 High-resolution ADF STEM image of a region of one of the nanowires shown in Figure 4.16. A degree of sample drift during the scan has distorted the lattice very slightly.

4.4.2.6 EDX analysis

Energy dispersive X-ray analysis (EDX) was carried out on all samples (Figure 4.18). It is possible to determine the elements present in the sample using this technique. In order to obtain EDX scans, the samples were pressed into disks, much like an IR KBr disk and mounted on an aluminium stub. It is noted that an increase of silicon is the general trend followed through the samples.

For all samples, the presence of iron, silicon, oxygen, sodium and bromine is noted. Sodium bromide is a by-product of the reaction. It is possible that not all of the sodium bromide is removed after washing the particles.

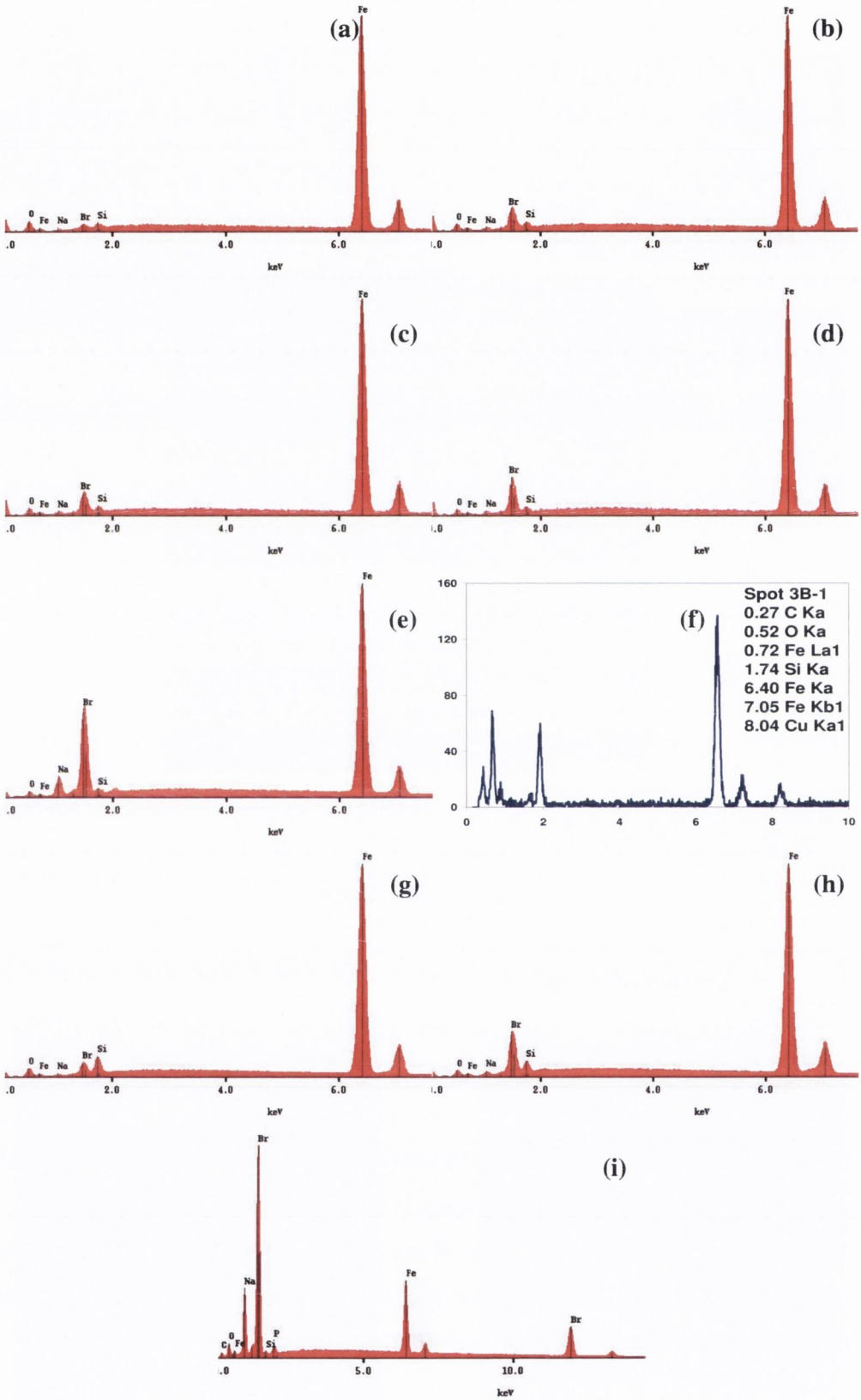

Figure 4.18 EDX analysis of samples (a) FS1, (b) FS2, (c) FS3, (d) FS4, (e) FS5, (f) FS6, (g) FS7, (h) FS8 and (i) FS9

EDX analysis was carried out on several regions of sample FS6 in order to ascertain what the larger nanoparticles and nanorods were composed of (Figure 4.19). Three spots were chosen from an STEM image of sample FS5: 3B-1 (a bundle of nanorods), 3B-2 (a single nanorod) and 3B-3 (the surrounding area of the nanorods). The EDX pattern for spots 3B-1 and 3B-2 are similar with peaks found at the same positions. Peaks for iron, oxygen and silicon have been observed for both particle types. For the nanorod on, a larger peak is seen for silicon than for the cluster of material (3B-1). This may be due to a shell of silica surround the nanorod, which may not be the case for the larger material. Spot 3B-3 of the surrounding area reveals only a peak for silicon, which suggests that the silica is coating the particles up to some distance away. This observation is consistent with the EELS data (Figure 4.15)

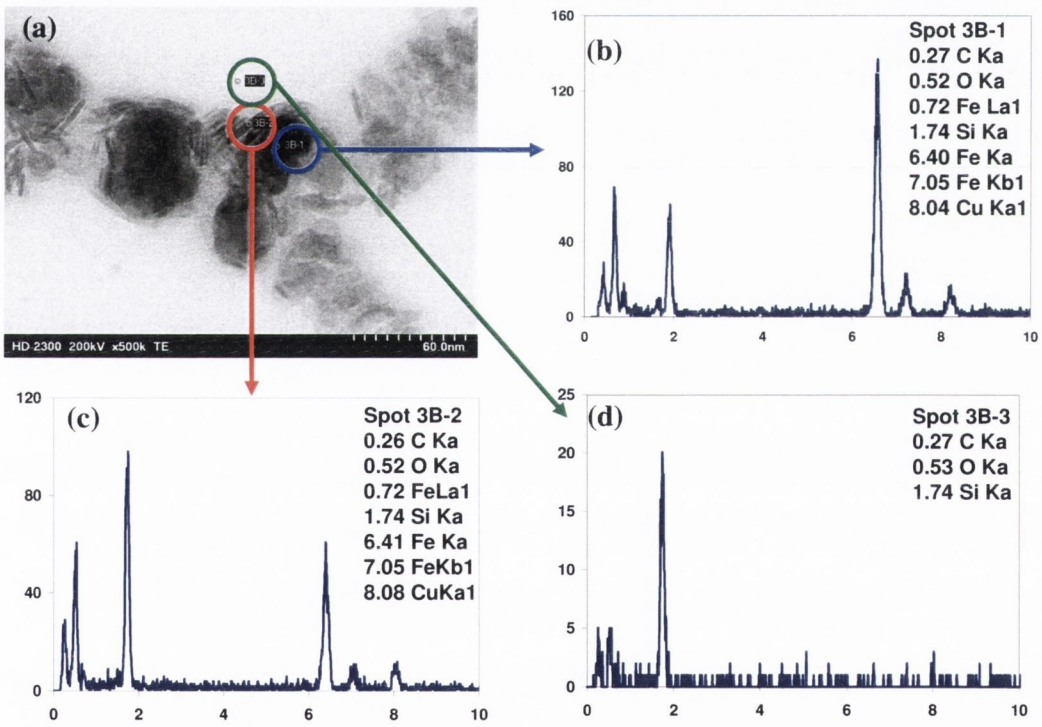

Figure 4.19 (a) Bright field image of sample FS5 showing EDX spots 3B-1 (blue circle), 3B-2 (red circle) and 3B-3 (green circle); EDX patterns of **(b)** spot 3B-1, **(c)** spot 3B-2 and **(d)** spot 3B-3.

4.4.2.7 Mössbauer spectroscopy

Mössbauer spectra of all samples were recorded at 298 K and 77 K and are shown in Figure 4.20. At 298 K, both paramagnetic and magnetically split contributions appear in all spectra. A combination of magnetically split and paramagnetic components was used to fit the spectra. The IS values at RT for most components lie in the range between 0.29 $mm \cdot s^{-1}$ and 0.39 $mm \cdot s^{-1}$ for all samples, although a few exceptions with higher values between 0.45 $mm \cdot s^{-1}$ and 0.54 $mm \cdot s^{-1}$ also appear. The former range of values is characteristic for the Fe^{3+} ions on the tetrahedral and octahedral sites of the spinel oxide γ-Fe_2O_3 structure. However the components showing increased IS values correspond to iron ions with valence state close to the intermediate between Fe^{2+} and Fe^{3+} (otherwise denoted as $Fe^{2.5+}$). So in the cases where these components appear in the spectrum (samples FS2, FS5, FS7.5 and FS10), it is more accurate to refer to the structure of the iron oxide particles as $Fe_{3-x}O_4$ rather than maghemite. All magnetically split components for all samples show rather broad resonant lines. The line broadening results from various sources: a) the distribution of sizes of individual particles; b) the distribution of different near neighbour iron environments, due to different levels of oxidation in these particles (different x values for the $Fe_{3-x}O_4$ stoichiometry) especially occurring on the surface layers[36]; and c) the differences in the surface magnetic anisotropy of the particles and spin canting effects, which become more important as the particles become smaller in size.[36-38]

The paramagnetic components of the samples prepared with low TEOS concentration (FS0.5-FS2) also show broad lines, but this broadening is reduced for the samples prepared with higher TEOS concentration. This increased line-width of the paramagnetic part for samples FS0.5, FS1 and FS2 is a consequence of the distribution of particle sizes and the $Fe_{3-x}O_4$ stoichiometry. The line-width reduction for samples with higher TEOS concentrations (samples FS5-FS15) indicates a narrowing of the distribution of the particle sizes. The particles with increased sizes (above 10 nm) are responsible for the appearance of the magnetically split components at RT. However the large asymmetric broadening of the magnetic resonant lines in samples FS0.5 and FS1 implies that the sizes for the majority of these particles in these samples are not very far above this limit – the asymmetric line broadening of the magnetic Mössbauer resonant lines increases as the particle size

approaches the superparamagnetic-size limit,[36, 38-40] and is a striking characteristic for these type of compounds with particle size distribution centred closed to that limit.

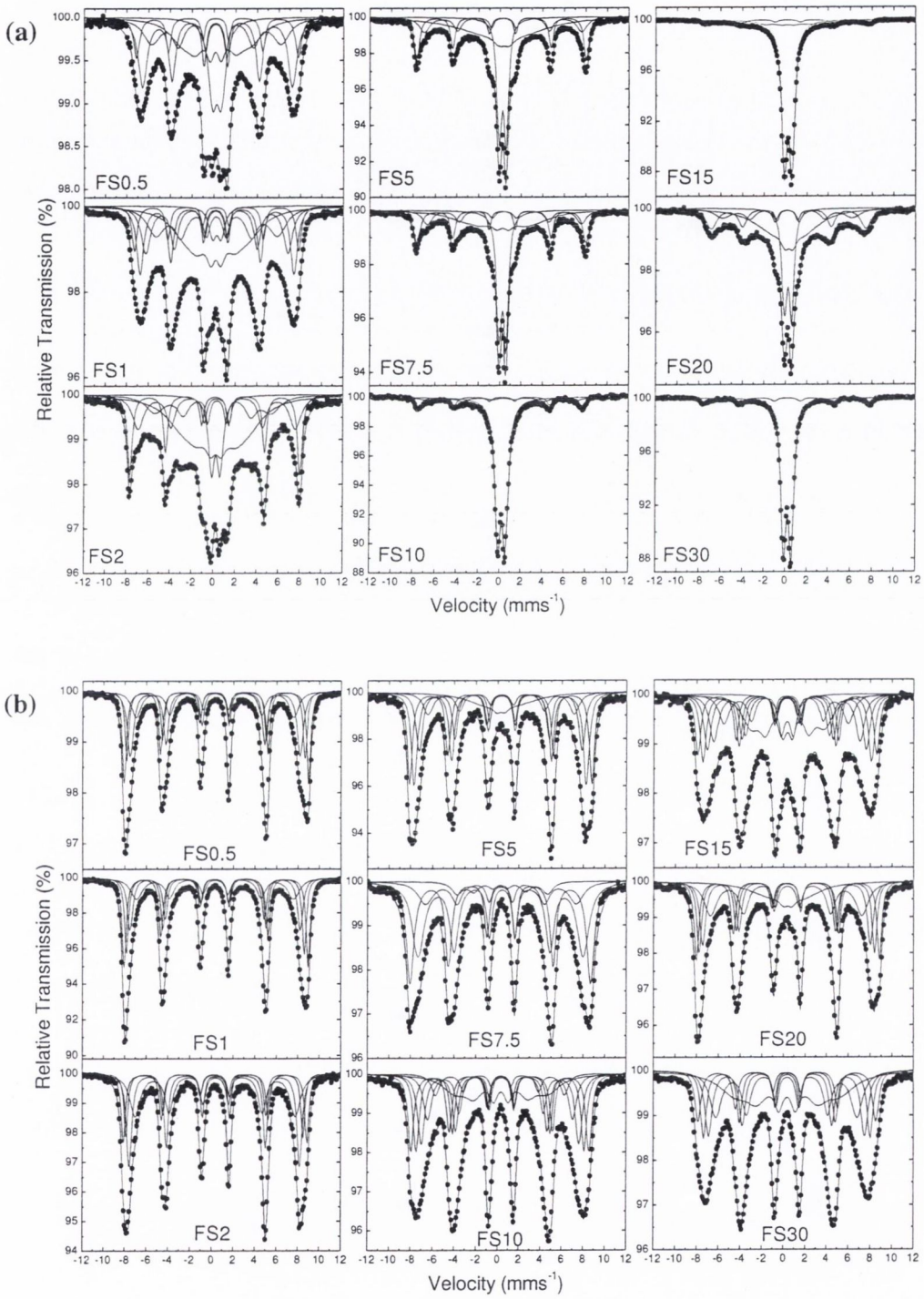

Figure 4.20 Mössbauer spectra of all samples (a) at room temperature and (b) at 77K

From the spectra recorded at 298 K, it is evident that samples with the lowest TEOS concentrations (FS0.5 and FS1) have the widest size distributions, while for higher TEOS concentrations, the size distribution narrows. For intermediate TEOS concentrations (FS2, FS5, FS7.5 and FS10), there are two particle size populations; one group corresponding to relatively large particles with a $Fe_{3-x}O_4$ stoichiometry and bulk-like behaviour, and another having very small sizes, clear superparamagnetic behaviour, and pure γ-Fe_2O_3 stoichiometry. Intermediate-sized particles are also present in the samples, but their number reduces as the TEOS concentration increases and so does the number of the large sized particles, in favour of the number of the fine superparamagnetic particles. For the spectra recorded at 77 K, the influence of superparamagnetic phenomena to the MS reduces when the temperature drops from RT to 77 K, but is still present for some subgroups of very low-sized particles, for which the complete cease of thermal fluctuation of their magnetization is yet to take place.

4.4.2.8 Magnetisation measurements

Magnetisation curves of all samples recorded at 298 K and 77 K are shown in Figure 4.21. At 298 K, there is a characteristic non-saturation tendency for all samples, even at fields up to $\mu_0 H = 2$ T. The σ values at this field (σ_{2T}) vary according to the different TEOS concentrations, but in all cases are much lower than the expected value for bulk γ-Fe_2O_3 (75 Am^2kg^{-1}) or Fe_3O_4 (92 Am^2kg^{-1}).[41, 42] The coercivities ($\mu_0 H_C$) at 298 K are around 10 mT for all samples except FS0.5 which is higher at around 25 mT, and at 77 K they range from 14 mT to 24 mT, except again for sample FS0.5 which reaches 70 mT. The value of coercivity depends on various factors including shape-dependency of the magnetic substances.[42] The coercivity of bulk-like γ-Fe_2O_3 at 298 K is 38 mT.[41] For all samples, there is a large reduction in the H_C values relative to the bulk value, which can be attributed to reduced particle size effect, a behavior quite characteristic for small particles systems about or below the critical single-domain size.[38, 42]

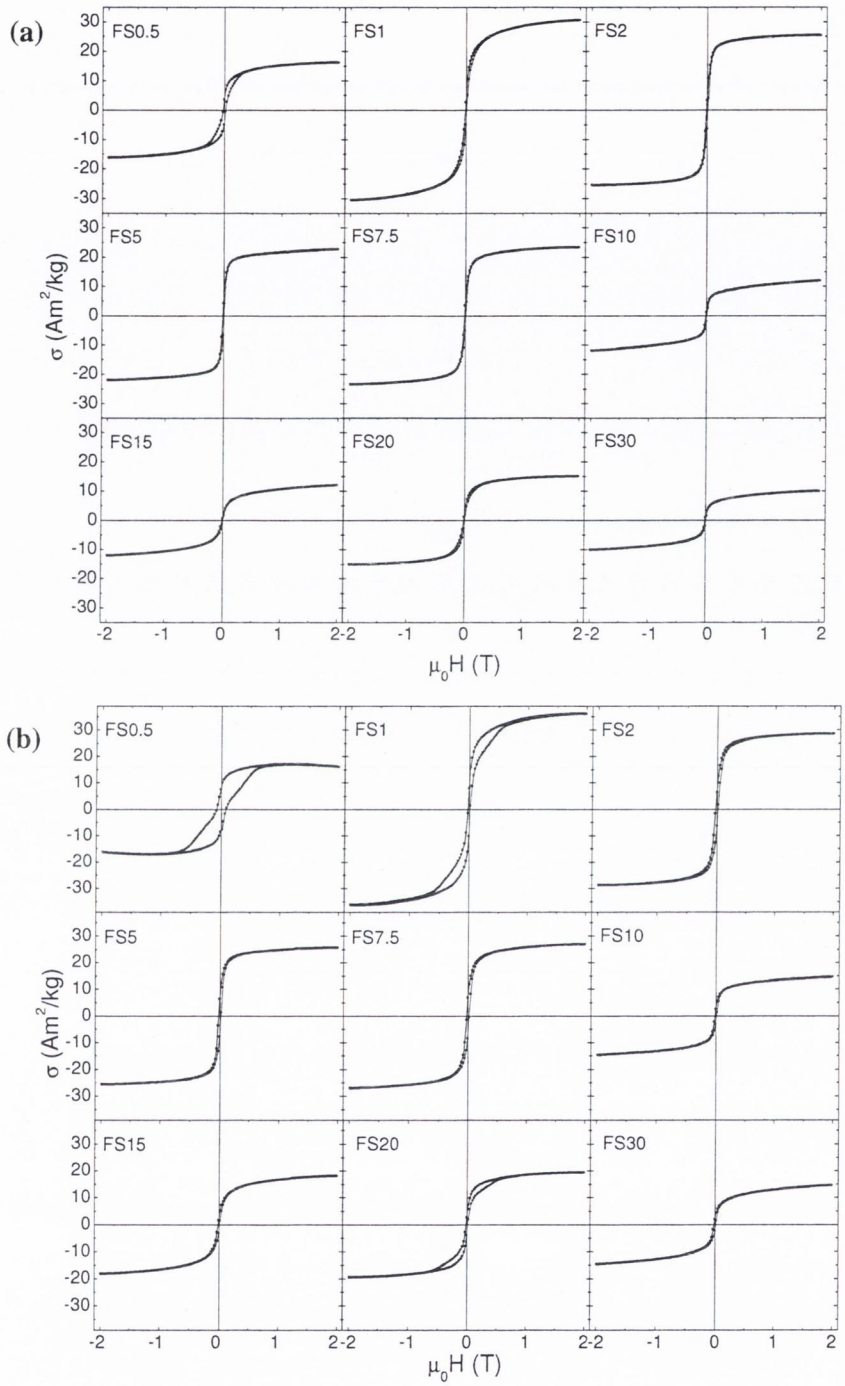

Figure 4.21 Magnetisation curves for all samples at (a) 298 K and (b) 77 K

The reduction of the σ_{2T} values is observed at 298 K as a general trend as the TEOS concentration increases and is shown in Figure 4.22. At 77 K the behaviour is similar. The reduction of the σ_{2T} values with increased TEOS concentration in the samples reflects the increase of the number of superparamagnetic smaller-sized

particles with respect to the total number of particles in the particle size distribution of the corresponding samples. All the above results are characteristics of a ferrimagnetic system of fine $Fe_{3-x}O_4$ particles, which shows partially or full superparamagnetic behavior at room temperature. The samples have different magnetic properties as a result of their particle size, shape and chemical composition distribution.

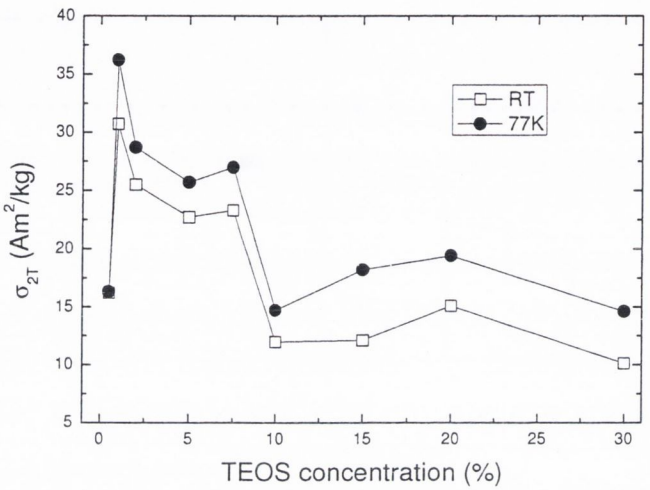

Figure 4.22 Saturation magnetisation values versus TEOS concentration. A decrease in the values is noted as the TEOS concentration increases, due to the presence of more superparamagnetic particles.

4.5 Proposed mechanism

The formation of rod-like maghemite-silica composites at higher concentrations of TEOS can be explained by the effect of mesoporous silica. We believe that initially formed magnetite seeds are trapped in the mesoporous silica channels which form at higher concentrations of TEOS. This initiates preferential growth of the nanoparticles in one direction within the silica channel giving silica coated nanorods. Similar phenomena have been reported for various metal oxide mesostructured silica nanocomposites.[43] In this report, composites have been prepared using various inorganic metal salts and high ratios of TEOS (the metal:silicon ratio is 1:3 or 1:5). Initially, a silica gel is formed and this is calcined at 550 °C. In our case the use of metallorganic iron(II) precursor, low ratios of TEOS (10-30%) and ultrasound have allowed the preparation of silica coated γ-Fe_2O_3 nanorods and whiskers.

From IR studies, the presence of OH groups most likely located on the iron oxide surface has been noted. The presence of the silica surrounding the particles has been confirmed by EEL spectroscopy and EDX analysis. We have observed a degree of self-assembly in our iron oxide-silica samples. We have found that our nanocomposites assemble into groups of between 2 and 10 rods together forming whisker -like structures.

4.6 Conclusions

New iron oxide-silica nanocomposite materials have been successfully prepared in a simple one-step procedure. This involved the use of an alkoxysilane in the presence of a metallorganic precursor which was previously shown to form magnetite nanoparticles under ultrasonic and hydrolytic conditions. We have found that the concentration of TEOS in the reaction mixture is an important factor in determining the final nanocomposite morphology. Rod-like particles are found to form with increasing silica concentration. Maghemite has been found to form large needle-like structures before, but these were in the micron size range and were not of a uniform size.[44] It has been found that under certain conditions, namely the addition of 10 % TEOS solution followed by hydrolysis and ultrasonic treatment, almost uniform nanorods of maghemite may be formed. These nanorods display superparamagnetic behaviour at room temperature and, from microscopic studies, are surrounded by a layer of silica.

The presence of a silica shell around the nanorods improves their stability, magnetic characteristics, biocompatability and provides a site for further functionalisation. Therefore, these materials might have a range of potential applications in biotechnology, medicine (e.g. magnetic fluids), catalysis and information technology.

References

[1] C. R. F. Lund, J. A. Dumesic, *Journal of Physical Chemistry* **1982**, *86*, 130.

[2] F. Hong, B. L. Yang, L. H. Schwartz, H. H. Kung, *Journal of Physical Chemistry* **1984**, *88*, 2525.

[3] S. Martinez, M. Meseguer, L. Casas, E. Rodriguez, E. Molins, M. Moreno-Manas, A. Roig, R. M. Sebastian, A. Vallribera, *Tetrahedron* **2003**, *59*, 1553.

[4] E. Katz, I. Willner, *Chemical Communications* **2005**, 5641.

[5] H. Kodama, S. Momose, T. Sugimoto, T. Uzumaki, A. Tanaka, *IEEE Transactions on Magnetics* **2005**, *41*, 665.

[6] S. Solinas, G. Piccaluga, M. P. Morales, C. J. Serna, *Acta Materialia* **2001**, *49*, 2805.

[7] K. V. P. M. Shafi, A. Ulman, A. Dyal, X. Z. Yan, N. L. Yang, C. Estournes, L. Fournes, A. Wattiaux, H. White, M. Rafailovich, *Chemistry of Materials* **2002**, *14*, 1778.

[8] F. del Monte, M. P. Morales, D. Levy, A. Fernandez, M. Ocana, A. Roig, E. Molins, K. Ogrady, C. J. Serna, *Langmuir* **1997**, *13*, 3627.

[9] M. F. Casula, A. Corrias, G. Paschina, *Journal of Non-Crystalline Solids* **2001**, *293*, 25.

[10] C. Savii, M. Popovici, C. Enache, J. Subrt, D. Niznansky, S. Bakardzieva, C. Caizer, I. Hrianca, *Solid State Ionics* **2002**, *151*, 219.

[11] I. K. Battisha, H. H. Afify, I. M. Hamada, *Journal of Magnetism and Magnetic Materials* **2005**, *292*, 440.

[12] S. A. P. Sanchez, S. Ponce-Castaneda, J. R. Martinez, F. Ruiz, Y. Chumakov, O. Dominguez, *Journal of Non-Crystalline Solids* **2003**, *325*, 251.

[13] C. Chaneac, E. Tronc, J. P. Jolivet, *Journal of Materials Chemistry* **1996**, *6*, 1905.

[14] C. Cannas, D. Gatteschi, A. Musinu, G. Piccaluga, C. Sangregorio, *Journal of Physical Chemistry B* **1998**, *102*, 7721.

[15] G. Ennas, A. Musinu, G. Piccaluga, D. Zedda, D. Gatteschi, C. Sangregorio, J. L. Stanger, G. Concas, G. Spano, *Chemistry of Materials* **1998**, *10*, 495.

[16] C. Cannas, A. Musinu, G. Navarra, G. Piccaluga, *Physical Chemistry Chemical Physics* **2004**, *6*, 3530.

[17] J. M. Xue, Z. H. Zhou, J. Wang, *Journal of the American Ceramic Society* **2002**, *85*, 807.

[18] Y. H. Zhang, A. Reller, *Chemical Communications* **2002**, 606.

[19] S. A. Corr, Y. K. Gun'ko, A. P. Douvalis, M. Venkatesan, R. D. Gunning, *Journal of Materials Chemistry* **2004**, *14*, 944.

[20] R. M. Cornell, U. Schwertmann, *The Iron Oxides*, Wiley VCH Verlag GmbH and Co., Weinheim, **1996**.

[21] C. I. Fialips, D. F. Huo, L. B. Yan, J. Wu, J. W. Stucki, *American Mineralogist* **2002**, *87*, 630.

[22] S. Y. Venyaminov, F. G. Prendergast, *Analytical Biochemistry* **1997**, *248*, 234.

[23] I. Chamritski, G. Burns, *Journal of Physical Chemistry B* **2005**, *109*, 4965.

[24] A. N. Shmakov, G. N. Kryukova, S. V. Tsybulya, A. L. Chuvilin, L. P. Solovyeva, *Journal of Applied Crystallography* **1995**, *28*, 141.

[25] K. Haneda, A. H. Morrish, *Solid State Communications* **1977**, *22*, 779.

[26] M. Popovici, M. Gich, A. Roig, L. Casas, E. Molins, C. Savii, D. Becherescu, J. Sort, S. Surinach, J. S. Munoz, M. D. Baro, J. Nogues, *Langmuir* **2004**, *20*, 1425.

[27] A. Bourlinos, A. Simopoulos, D. Petridis, H. Okumura, G. Hadjipanayis, *Advanced Materials* **2001**, *13*, 289.

[28] S. Santra, R. Tapec, N. Theodoropoulou, J. Dobson, A. Hebard, W. H. Tan, *Langmuir* **2001**, *17*, 2900.

[29] C. Cannas, M. F. Casula, G. Concas, A. Corrias, D. Gatteschi, A. Falqui, A. Musinu, C. Sangregorio, G. Spano, *Journal of Materials Chemistry* **2001**, *11*, 3180.

[30] C. Caizer, C. Savii, M. Popovici, *Materials Science and Engineering B-Solid State Materials for Advanced Technology* **2003**, *97*, 129.

[31] L. Casas, A. Roig, E. Rodriguez, E. Molins, J. Tejada, J. Sort, *Journal of Non-Crystalline Solids* **2001**, *285*, 37.

[32] Y. K. Sun, L. Duan, Z. R. Guo, D. M. Yun, M. Ma, L. Xu, Y. Zhang, N. Gu, *Journal of Magnetism and Magnetic Materials* **2005**, *285*, 65.

[33] M. Ma, Y. Zhang, W. Yu, H. Y. Shen, H. Q. Zhang, N. Gu, *Colloids and Surfaces A-Physicochemical and Engineering Aspects* **2003**, *212*, 219.

[34] Y. P. He, S. Q. Wang, C. R. Li, Y. M. Miao, Z. Y. Wu, B. S. Zou, *Journal of Physics D-Applied Physics* **2005**, *38*, 1342.

[35] L. L. Hench, J. K. West, *Chemical Reviews* **1990**, *90*, 33.

[36] R. E. Vandenberghe, E. De Grave, *Mössbauer Effect Studies of Oxidic Spinels-Mössbauer Spectroscopy Applied to Inorganic Chemistry, Vol. 3*, Plenum Press, New York, **1989**.

[37] J. M. D. Coey, *Physical Review Letters* **1971**, *27*, 1140.

[38] G. F. Goya, T. S. Berquo, F. C. Fonseca, M. P. Morales, *Journal of Applied Physics* **2003**, *94*, 3520.

[39] S. Mørup, H. Topsøe, J. Lipka, *Journal de Physique Collogue C6* **1976**, *37*, 287.

[40] P. Roggwiller, W. Kundig, *Solid State Communications* **1973**, *12*, 901.

[41] D. Craik, *Magnetism: Principles and Applications*, John Wiley & Sons, Chichester, **1995**.

[42] B. D. Cullity, *Introduction to Magnetic Materials*, Addison-Wesley, Reading-Massachusetts, **1972**.

[43] H. F. Yang, Q. Y. Lu, F. Gao, Q. H. Shi, Y. Yan, F. Q. Zhang, S. H. Xie, B. Tu, D. Y. Zhao, *Advanced Functional Materials* **2005**, *15*, 1377.

[44] Y. S. Kang, S. Risbud, J. F. Rabolt, P. Stroeve, *Chemistry of Materials* **1996**, *8*, 2209.

Chapter 5: Two-in-one magnetic fluorescent nanocomposites

5.1. Introduction

Magnetic nanomaterials are of immense importance in the emerging field of nanomedicine.[1, 2] In particular, the use of magnetic nanoparticles as diagnostic tools in MRI contrast agents,[3, 4] as mediators for hyperthermic cancer treatment,[5, 6] and as drug delivery vehicles,[7] are rapidly expanding fields. It has been suggested that, as their small size increases their blood circulation time, magnetic nanoparticles could be functionalised *via* conjugation to various monoclonal antibodies, peptides, or proteins to achieve their targeted localisation.[8] Some recent research has also focused on the preparation and biological applications of dye-containing fluorescent magnetic nanoparticles.[9-13]

Currently, fluorescent semiconducting nanoparticles (refered to as quantum dots) [10] have been shown as promising materials for bio-labelling,[11] biological imaging,[12] and highly specific detectors in biological assays.[13] The combination of magnetic nanoparticles with fluorescent properties is therefore an attractive prospect, enabling the engineering of a targeted-nanoscale photonic device which can be manipulated within the body via an external magnetic field.

Porphyrins are biocompatible fluorescent compounds which have been used as efficient photosensitisers for photodynamic therapy, a technique whereby tumour tissue is destroyed by the uptake of the dye and subsequent irradiation with visible light.[14, 15] Magnetic nanoparticles stabilised by fluorescent molecules, such as porphyrins, would offer great diagnostic and therapeutic possibilities and would have the potential to be positioned by an applied external magnetic field. However, the fabrication of useful composites presents several challenges, primarily because the magnetic cores normally quench the porphyrin fluorescence. This problem can be partially resolved by covalent bonding of porphyrin to magnetite nanoparticles incorporating an appropriate spacer.[12]

There have been few reports of magnetic fluorescent nanocomposites in recent years. Gu *et. al.*[12] have reported the preparation of magnetite nanoparticles treated with a dopamine functionalised diamino porphyrin moiety. These authors have demonstrated the possible use of these nanocomposites as hyperthemic agents by measuring the uptake of the particles by the cancer cell line HeLa (Figure 5.1).

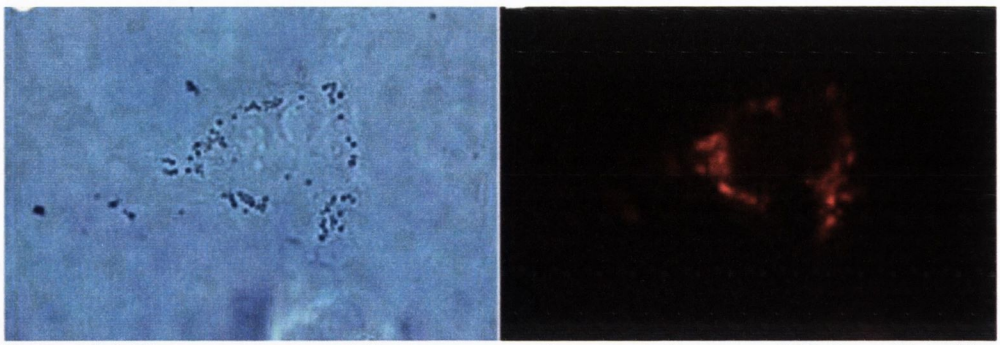

Figure 5.1 Phase contrast and fluorescence microscopy images of HeLa cells taking up porphyrin functionalised magnetite nanoparticles[12]

There have also been reports of coumarin and rhodamine coated magnetite nanoparticles.[16] These authors have coated a commercially available ferrofluid (EMG 304 from Ferrofluids) with amorphous silica. The organic dyes are incorporated during the coating process – in effect, the dye is trapped in the silica shell.

This chapter describes the preparation of magnetic nanoparticles and their subsequent functionalisation with a fluorescent moiety to produce nanomaterials encompassing both magnetic and fluorescent properties. The combination of these properties present several challenges, as magnetic nanoparticles may act to quench the fluorescence of our fluorophore. In order to prepare these nanocomposites, two methods were used. One involved the preparation of ionically linked nanocomposites, using a polyhedral oligosilsesquioxane (POSS)[19] as a stabilising agent. The other method was to prepare silica coated magnetite nanoparticles to react with an ethoxy silane modified porphyrin to produce a covalently linked composite.

5.2. Preparation of magnetite-POSS fluorescent nanocomposites

This part of the work is focused on the synthesis and characterisation of fluorescent magnetite nanocomposites based on magnetite nanoparticles, a polyhedral octaaminopropylsilsesquioxane and fluorescent derivatives (porphyrin, salicylic acid and acridine). The potential of some of the nanocomposites as MRI contrast agents is demonstrated and their behaviour in macrophage and bone osteoblast live cells is also investigated.

5.2.1. Preparation of magnetite nanoparticles

The particles used in this chapter have been prepared differently from those prepared in Chapters 3 and 4. Here, instead of using metallorganic precursors, magnetite nanoparticles have been produced by the coprecipitation reaction according to published procedures.[17] The chemical reaction for the precipitation of Fe_3O_4 nanoparticles is presented by equation:

$$Fe^{2+} + 2Fe^{3+} + 8OH^- \longrightarrow Fe_3O_4 + 4H_2O$$

A complete precipitation of magnetite is expected at a pH of approximately 10 while keeping the Fe^{3+}/Fe^{2+} ratio at 2:1 in a non-oxidising environment.[18] The scheme for formation may be given as:[19]

$$Fe^{2+} + 2OH^- \longrightarrow Fe(OH)_2$$

$$2Fe^{3+} + 6OH^- \longrightarrow 2Fe(OH)_3$$

$$Fe(OH)_2 + 2Fe(OH)_3 \longrightarrow Fe_3O_4 + 4H_2O$$

Scheme 5.1 Preparation of magnetite nanoparticles *via* coprecipitation

Once the base is added to the solution, $Fe(OH)_2$ and $Fe(OH)_3$ react to form Fe_3O_4 as noted by the formation of a black precipitate. In order to ensure the purity of magnetite, the ratio of Fe^{3+}/Fe^{2+} must be kept at 2:1. If this is not the case and the ratio is above two, maghemite may appear as an impurity in the product. Below a ratio of 2, the product formed is unstable and readily oxidised in air.[20] The particles have been characterised by IR, Raman spectroscopy, Magnetisation measurements and TEM analysis.

5.2.1.1. Characterisation of magnetic nanoparticles

5.2.1.1.1. FTIR and Raman spectroscopy

The FTIR spectrum for the magnetite nanoparticles alone (Figure 5.2) shows a stretching vibration at 3375 cm^{-1} which incorporates the contributions from both symmetrical (ν_1) and asymmetrical (ν_3) modes of the O-H bonds which are attached to the surface iron atoms. The presence of an adsorbed water layer is confirmed by a stretch for the vibrational mode of water found at 1629 cm^{-1}. The absorption band at 581 cm^{-1} is attributed to the Fe-O bonds.

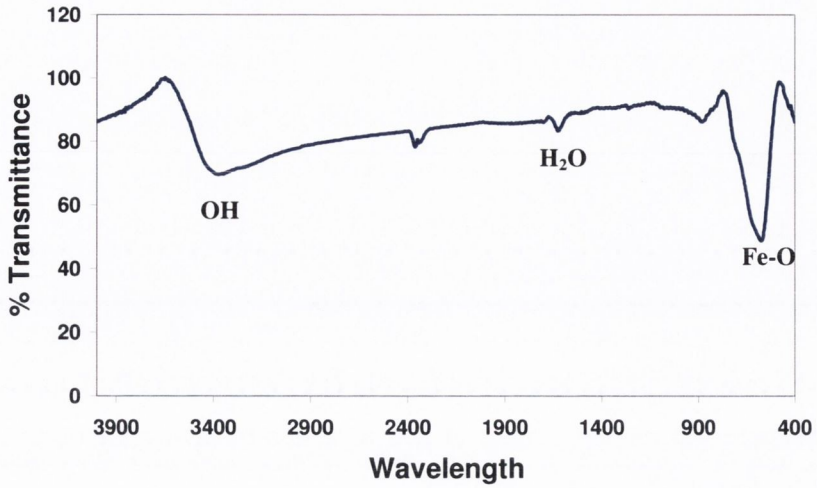

Figure 5.2 IR spectrum of magnetite nanoparticles prepared *via* coprecipitation method

A Raman spectrum carried out on the coprecipitated magnetite sample shows a broad peak at 680 cm^{-1} (Figure 5.3), which is expected for magnetite.[21] There are no peaks for haematite observed.

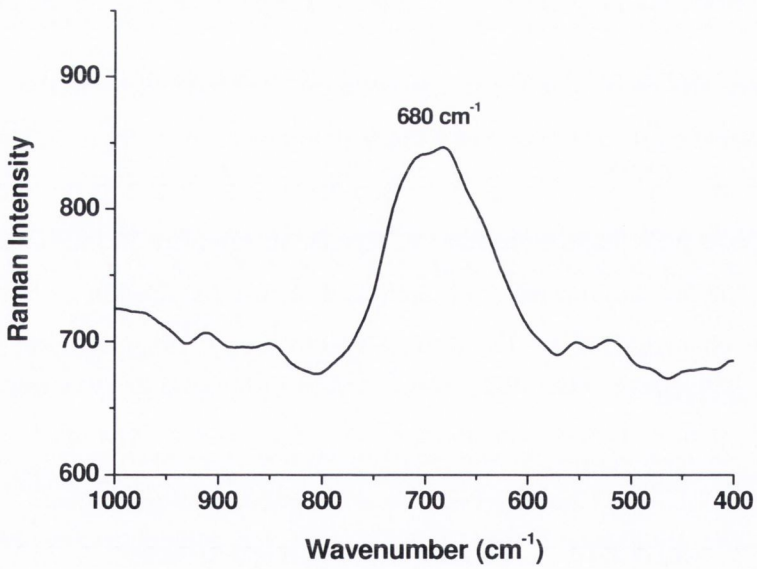

Figure 5.3 Raman spectrum of magnetite nanoparticles showing the characteristic peak for magnetite at 680 cm^{-1}

5.2.1.1.2. X-Ray diffraction

A dry powder sample was used to analyse the XRD pattern of the nanoparticles. The observed diffraction pattern coincides with the JCPDS database for magnetite, which is shown in Figure 5.4 as a series of red lines. The two additional peaks observed at 34 and 38.5 degrees 2θ are due to the tungsten lamp in the XRD machine and not the sample. The average particle size has been calculated from the peak width at half height maximum, which occurs at 35.5 degrees 2θ for magnetite, using the Debye-Scherrer equation.[22] The average particle size was found to be 6 nm.

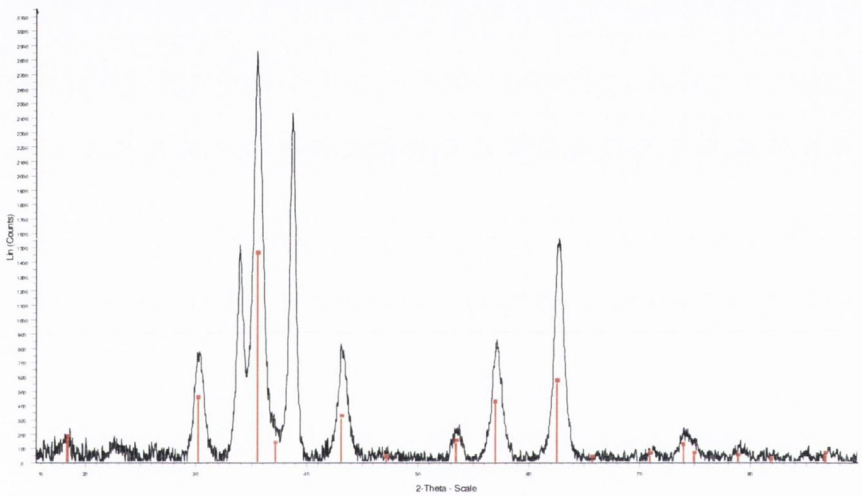

Figure 5.4 XRD pattern for magnetite nanoparticles synthesised *via* coprecipitation method

The interlayer spacings (d_{hkl}), calculated using the Bragg equation, agree well with the data for standard magnetite (Table 1). The *a* lattice parameter was calculated as 0.840 nm from the (311) reflection, which coincides closely with the value for magnetite (0.839 nm).

Table 5.1 Lattice parameters and interlayer spacings for magnetite nanoparticles

Sample	(hkl)					
	1	2	3	4	5	6
Prepared Fe_3O_4	0.294	0.254	0.210	0.171	0.164	0.148
Standard Fe_3O_4	0.296	0.253	0.209	0.171	0.161	0.148

5.2.1.1.3. Electron Microscopy

Samples for TEM were prepared *via* dispersion of the nanoparticles in ethanol for 15 minutes in ultrasound and a drop was placed on a copper formvar grid (Figure 5.5).

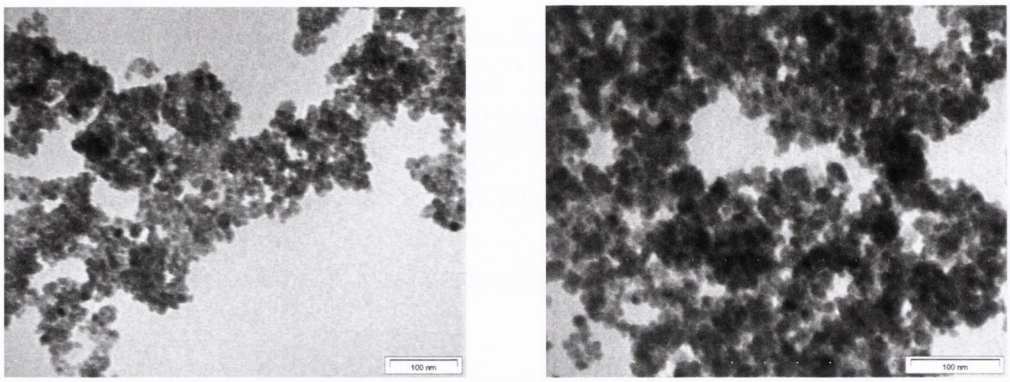

Figure 5.5 TEM images of magnetite nanoparticles prepared from coprecipitation method

The particles appear spherical in shape and the average particle size was calculated as 9.6 ± 1.8 nm (Figure 5.6). This value is close to the one found using the Scherrer equation.

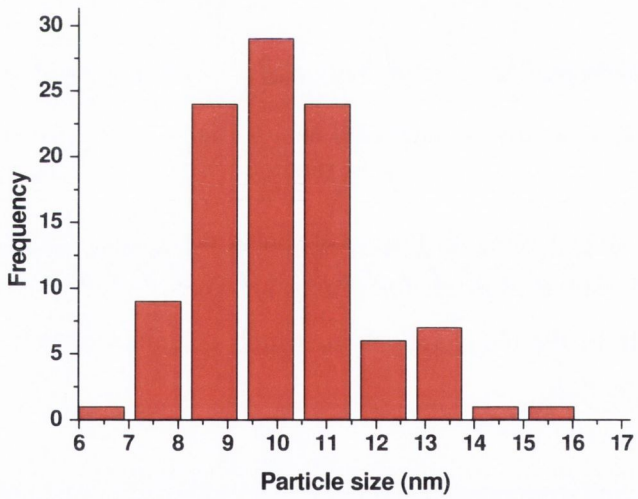

Figure 5.6 Histogram of magnetite nanoparticles prepared from coprecipitation method

5.2.1.1.4. Magnetisation measurements

Figure 5.7 shows the magnetisation curve of the magnetite nanoparticles. Magnetisation measurements are very sensitive to the particle size and spread. If the sample consists of small particles, the total magnetisation decreases with decreasing

particle size because these particles may be superparamagnetic, a state where each particle acts a spin. Figure 5.7 demonstrates that the characteristics of typical superparamagnetic material is observed, with the curve showing almost immeasurable coercivity (H_c = 18.9 Oe) and remanence (B_r = 1.29 Am^2/kg). The saturation magnetisation at room temperature is found to be M_s = 59.8 Am^2/kg, which is considerably less than that reported for bulk magnetite (92 Am^2/kg). The value obtained for these particles is in good agreement with values reported for particles prepared in this manner (M_s = 50.27 emu/kg[23], M_s = 49.1 emu/kg[24] and 54 emu/kg.[25]

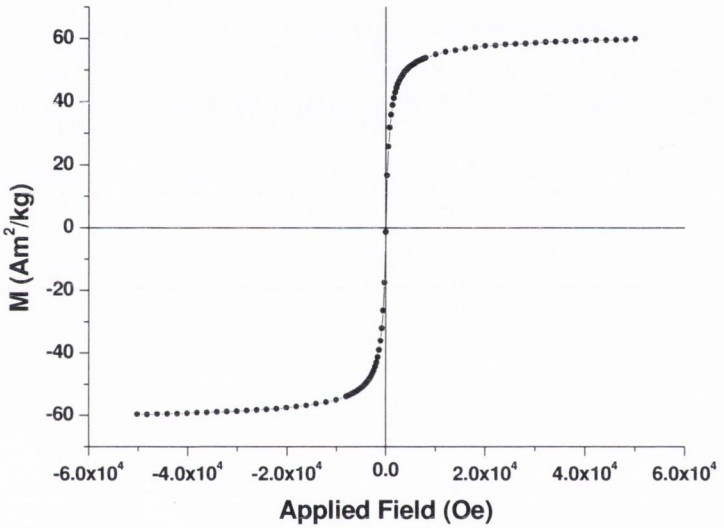

Figure 5.7 Magnetisation measurements of magnetite nanoparticles prepared from coprecipitation technique

5.2.1.2. Synthesis and characterisation of polyhedral oligosilsesquioxane (POSS) stabiliser

Polyhedral oligosilsesquioxanes are a class of three-dimensional siloxane molecules, which may be synthesised by the hydrolytic condensation of trifunctional organosilicon monomers (i.e. $RSiX_3$, where X is a halogen or alkoxy group). Silsesquioxanes are of the general formula $(RSiO_{1.5})_n$, where n is an even number and R is typically an organic group attached to Si via Si-C bonds.[26] These compounds are often described as being either "fully-condensed"[27] or "incompletely-condensed"[28] frameworks. Completely condensed silsesquioxanes have the general formula as above, while incompletely-condensed silsesquioxanes also possess terminal reactive Si-OH groups.

Hydrolytic condensation reactions provide a successful route to the synthesis of multigram quantities of fully condensed POSS networks containing 6, 8, 10, or 12 Si atoms.[29] Fully condensed frameworks may be synthesised in either polar or nonpolar solvents under acidic[30] or basic[29] conditions. The major product yielded in kinetically controlled acidic reactions is a relatively insoluble octameric silsesquioxane which crystallises out of solution. In the case of basic reactions, it can be more difficult to obtain a discrete cluster as bases or other nucleophiles can react with the Si-O-Si framework to produce a resin, consisting of incompletely condensed species.[31]

The POSS molecule octaaminosilsesquioxane (Figure 5.8) has been used in this work to act as a stabiliser for magnetic nanoparticles. It was envisaged that the OH rich surface of the nanoparticles (as determined by IR spectroscopy) would interact ionically with the NH_3^+ terminated POSS. The chosen silsesquioxane, which is highly water soluble, was expected to stabilise the magnetic particles in water. The previously reported synthesis[32] was followed, which required a 5 week acid catalysed condensation of 3-aminopropyltriethoxysilane in a methanol solution. This gave a white crystalline powder in a 30% yield.

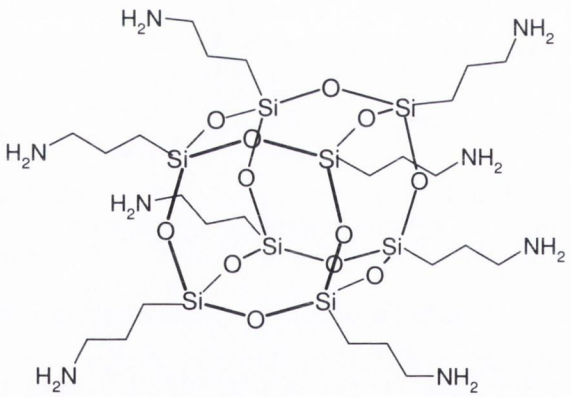

Figure 5.8 Structure of the POSS framework, octaaminosilsesquioxane

5.2.1.3. Characterisation of POSS stabiliser

5.2.1.3.1. NMR and Mass spectroscopy results for $T_8NH_3^+Cl^-$

^1H and ^{13}C NMR spectra were carried out in DMSO-d_6. In the proton spectrum (Figure 5.9), the singlet at 8.25 ppm is attributed to the NH_3 proton contribution. The propyl chain from each corner Si atom to the amine functionality gives three distinct peak systems in the spectrum. The CH_2N protons are found to give a triplet at 2.83 ppm, while the $SiCH_2CH_2$ protons come in as a multiplet further

upfield at 1.78 ppm. The final proton set, $SiCH_2$, are found to form a triplet system at 0.78 ppm.

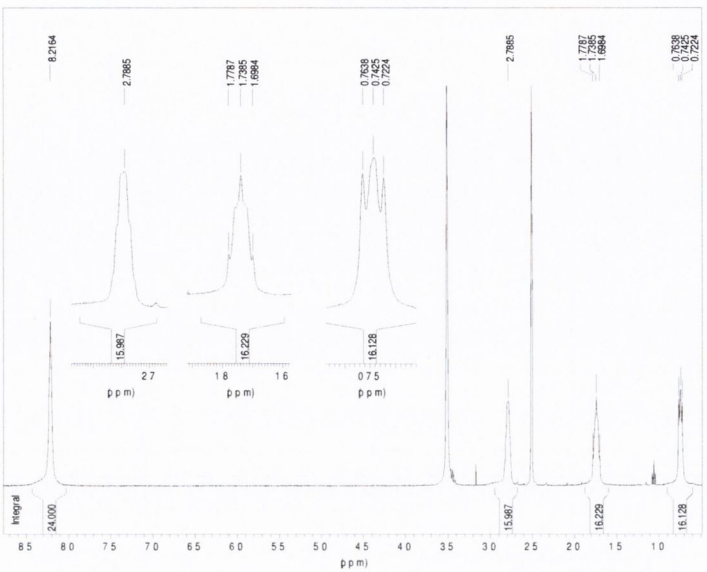

Figure 5.9 ^{1}H NMR of octaaminosilsesquioxane carried out in DMSO-d_6

The ^{13}C NMR data (Figure 5.10a) reveals the presence of a singlet for each carbon atom in the propyl chain. These are found at 41.01 (CH_2N), 20.62 ($SiCH_2CH_2$) and 8.40 ($SiCH_2$). A ^{29}Si NMR was carried out using methanol as the solvent (Figure 5.10b). This revealed a single peak at -66.4 ppm. This is indicative of a fully condensed oligosilsesquioxane. A multiplet of peaks centred in this area would indicate that the silsesquioxane has not fully condensed and therefore may undergo a polymerisation process. The formation of a fully condensed POSS molecule was also confirmed by mass spectrometry.

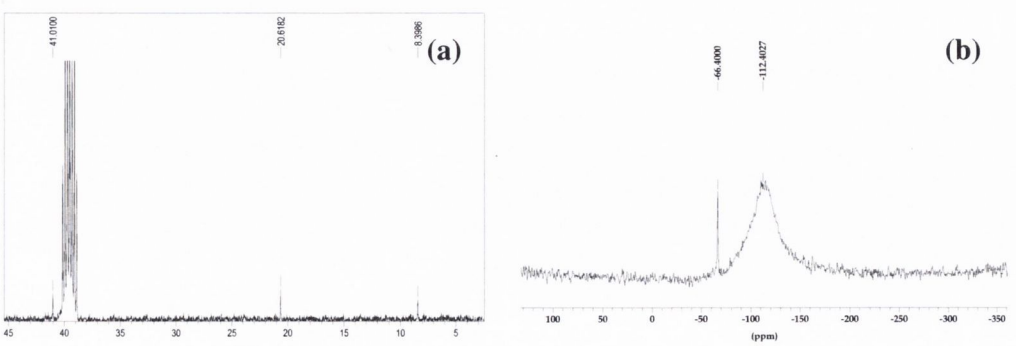

Figure 5.10 (a) ^{13}C of octaaminosilsesquioxance carried out in DMSO-d_6 and **(b)** ^{29}Si NMR carried out in methanol

5.2.1.3.2. IR spectroscopy of $T_8NH_3^+Cl^-$

An IR spectrum was carried out in KBr (Figure 5.11). Stretches at 3024 cm^{-1} and 1601 cm^{-1} may be attributed to some water still present in the sample. N-H stretching and wagging vibrations are seen at 1495 and 818 cm^{-1} respectively. The broad stretch at 1126 cm^{-1} is for Si-O-Si stretching vibrations.

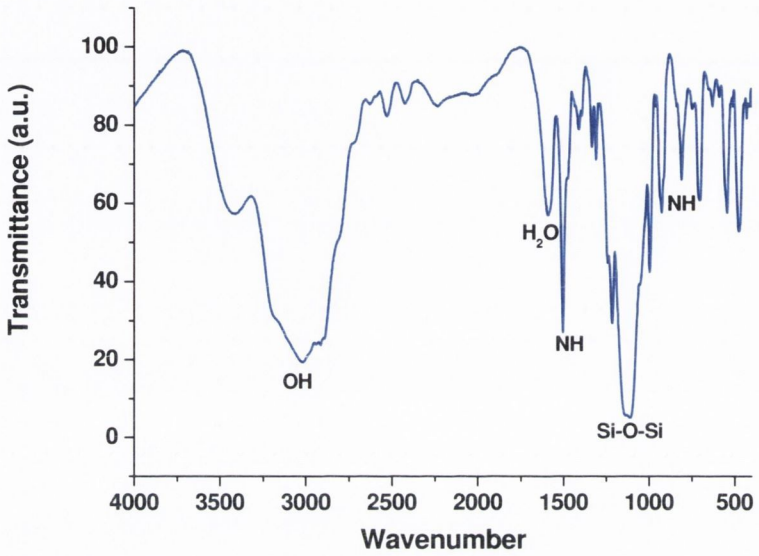

Figure 5.11 IR spectrum of octaaminosilsesquioxane carried out in KBr

5.2.1.4. Preparation of magnetite- porphyrin composites

A porphyrin derivative with carboxylic acid groups [4, 4', 4'', 4'''-(21H, 23H) Porphine-5, 10, 15, 20- tetrayl) tetrakis-(benzoic acid)] was chosen, as these groups were expected to bind to $-NH_3^+$ groups of the POSS molecules via ionic and hydrogen bonding. The interaction between polyamines and coproporphyrin tetranions has been previously reported.[33]

This porphyrin derivative was available from Aldrich. The process was performed according to Scheme 5.3. Briefly, magnetite nanoparticles were reacted with $T_8NH_3^+Cl^-$ by stirring overnight. After centrifugation to remove any large aggregates, the porphyrin complex was added with 1 mL methanol and shaken overnight to produce a stable magnetic fluid.

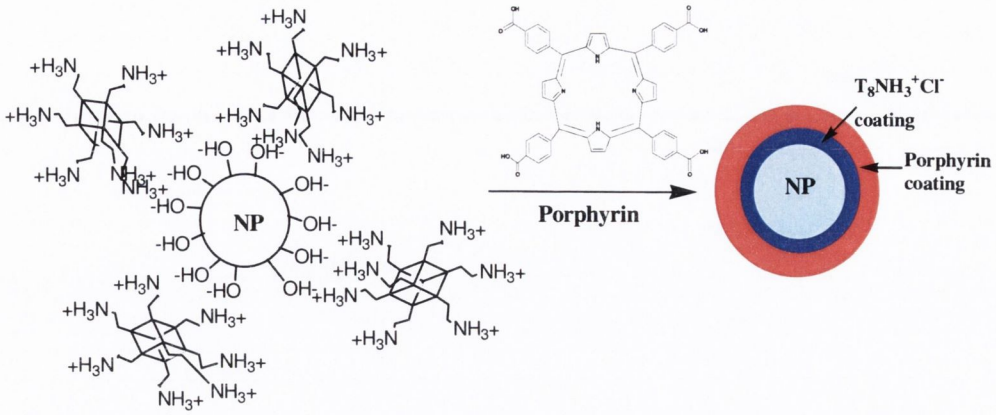

Scheme 5.2 Schematic presentation of the preparation of magnetic-fluorescent nanocomposites

The nature of the interaction between the octaaminosilsesquioxane and the porphyrin compound has been studied *via* UV-vis and fluorescence spectroscopy (Figure 5.12). The pyrrole nitrogens of the porphyrin ring have been reportedly protonated at pH 5 and the pK_a of the carboxylic acid functions are also around 5.[34] Therefore, below pH 5 the porphyrin complex is a doubly charged diacid. At pH 5, the carboxylic acid groups are ionised and the Soret band maximum is found at 414 nm. It has been previously reported that with the addition of diamines to solutions of carboxylate functionalised porphyrins causes a decrease in the fluorescence intensity.[33]

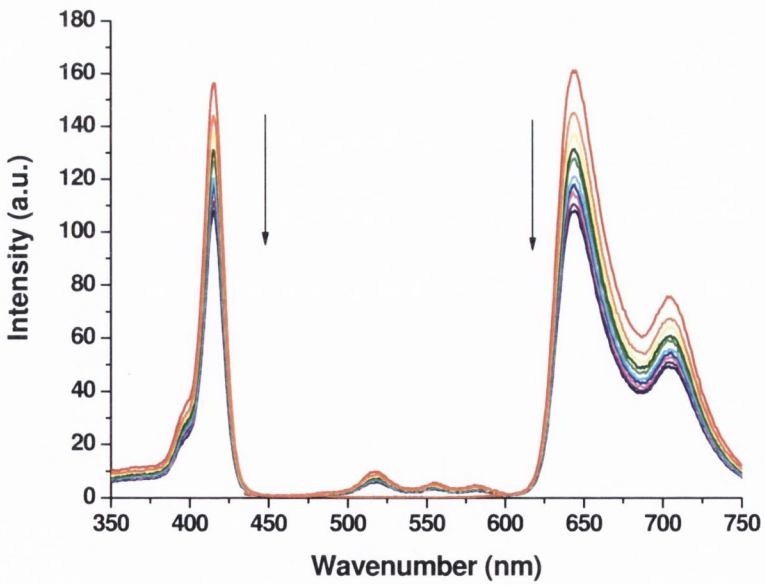

Figure 5.12 Fluorescence spectra (emission and excitation) of porphyrin complex with increasing concentration of $T_8NH_3^+Cl^-$. Fluorescence intensity decreases with increasing $T_8NH_3^+Cl^-$ concentration.

5.2.1.5. Characterisation of the magnetic composite material

5.2.1.5.1. FTIR spectroscopy

FTIR spectra were carried out in KBr of the magnetite nanoparticles, the magnetite-$T_8NH_3^+Cl^-$ composite and the magnetite-$T_8NH_3^+Cl^-$ - porphyrin nanocomposite (Figure 5.13). Spectra were also taken of the $T_8NH_3^+Cl^-$ spacer and porphyrin molecule to compare with the nanocomposites.

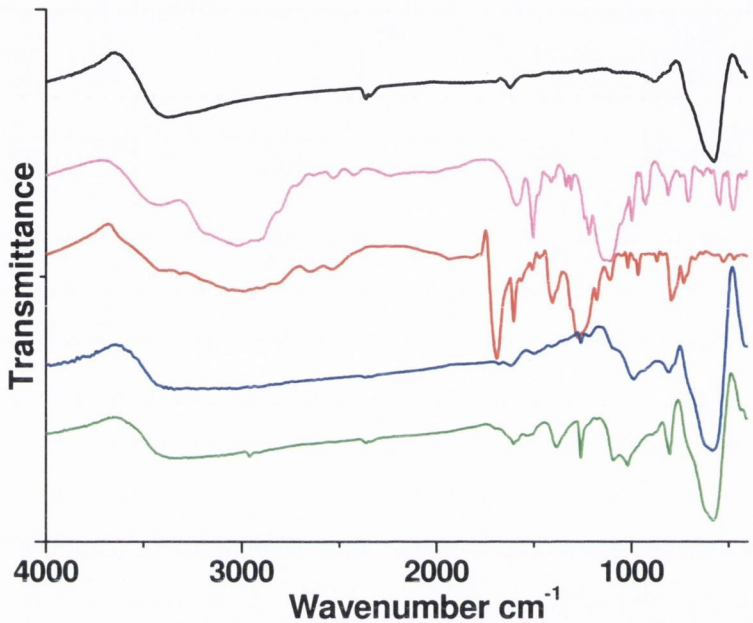

Figure 5.13 IR spectra of, from top to bottom, Fe_3O_4 (black curve), $T_8NH_3^+Cl^-$ spacer (pink curve), porphyrin complex (red curve), magnetite-$T_8NH_3^+Cl^-$ composite (blue curve) and magnetite-$T_8NH_3^+Cl^-$ -porphyrin composite (green curve).

The porphyrin complex reveals a stretch at 3424 cm^{-1}, which is for OH groups, most likely some water present in the sample. The peak at 3025 cm^{-1} is that of the OH groups of carboxylic acid attached to the benzoic acid. The stretches at 1596 and 1504 cm^{-1} are carbonyl and NH stretches, respectively. The broad stretch at 1129 cm^{-1} may be attributed to contributions from C-H and C-C bonds. The magnetite-$T_8NH_3^+Cl^-$ nanocomposite reveals a stretch at 3367 cm^{-1} for surface OH groups and a stretch at 1619 cm^{-1}, which is a contribution for surface associated water molecules. Asymmetric Si-O-Si stretches are found at 1261 and 986 cm^{-1}, while stretches are seen at 810 cm^{-1} for NH wagging and 584 cm^{-1} for Fe-O bonds. For the porphyrin treated magnetite-$T_8NH_3^+Cl^-$ nanocomposite, the stretches at 3367 cm^{-1} and 1603 cm^{-1} remain for the OH groups bound to and water molecules associated with the nanoparticle surface respectively. When compared to the spectrum for porphyrin

only, it is noted that the stretch at 3016 cm^{-1} for OH groups of the carboxylic acid attached to the benzoic acid does not appear for the composite material. This indicates that the carboxylic acid group of the porphyrin derivative is deprotonated in the nanocomposite material. A carbonyl stretch for the benzoic acid is found at 1527 cm^{-1}. Combined contributions for C-H and C-C stretches occur between 1388 and 1089 cm^{-1}. Asymmetric Si-O-Si stretches from the $T_8NH_3^+Cl^-$ stabiliser occur at 1021 cm^{-1}. The N-H wagging and Fe-O stretches occur at 803 and 582 cm^{-1} respectively.

5.2.1.5.2. X-ray diffraction

Powder X-ray diffraction (XRD) patterns coincide with the JCPDS database for magnetite (Figure 5.14).

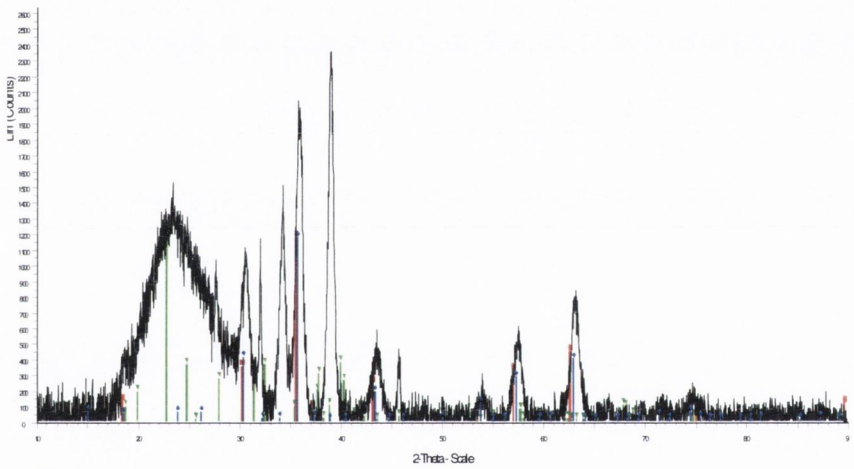

Figure 5.14 XRD pattern of porphyrin-$T_8NH_3^+Cl^-$ - magnetite nanocomposite, which overlaps with the JCPDS data for magnetite (blue lines). The peaks at 30.5 and 34.5 degrees 2θ appear due to the tungsten lamp present in the XRD machine. The green lines in the pattern represent the database spectrum for silicon dioxide, which overlaps with the broad peak at 24 degrees 2θ

Table 5.2 Lattice parameters and interplanar spacings for nanocomposite

Sample	(hkl)					
	1	2	3	4	5	6
Nanocomposite	0.293	0.252	0.208	0.170	0.160	0.147
Fe_3O_4	0.296	0.253	0.209	0.171	0.161	0.148

The interlayer spacings (d_{hkl}) were calculated from the Bragg equation (Table 5.2). The lattice parameter *a* has been calculated from the interplanar spacing of the most intense peak, which for magnetite is the (311) hkl line. The *a* lattice parameter for the nanocomposite is 0.836 nm, which coincides well with the value for magnetite (0.839 nm).

5.2.1.5.3. Electron microscopy

The presence of this additional stabiliser contributes to an enhancement of the water stability of the nanoparticles, with no visible precipitation of the particles on exposure to 0.5 T magnetic field. TEM images (Figure 5.15) of the $T_8NH_3^+Cl^-$ composites have shown the aggregation of magnetite nanoparticles by the POSS stabiliser, with further aggregation noted on addition of the porphyrin. The presence of a core-shell structure is also noted.

The particle size is found to be 12 ± 2nm (for N=100 particles). By analyzing the HRTEM images (Figure 5.15d) of a single functionalized magnetite nanoparticle, the lattice spacing between two planes is 4.82 Å, corresponding to the distance of two (111) planes in Fe_3O_4.

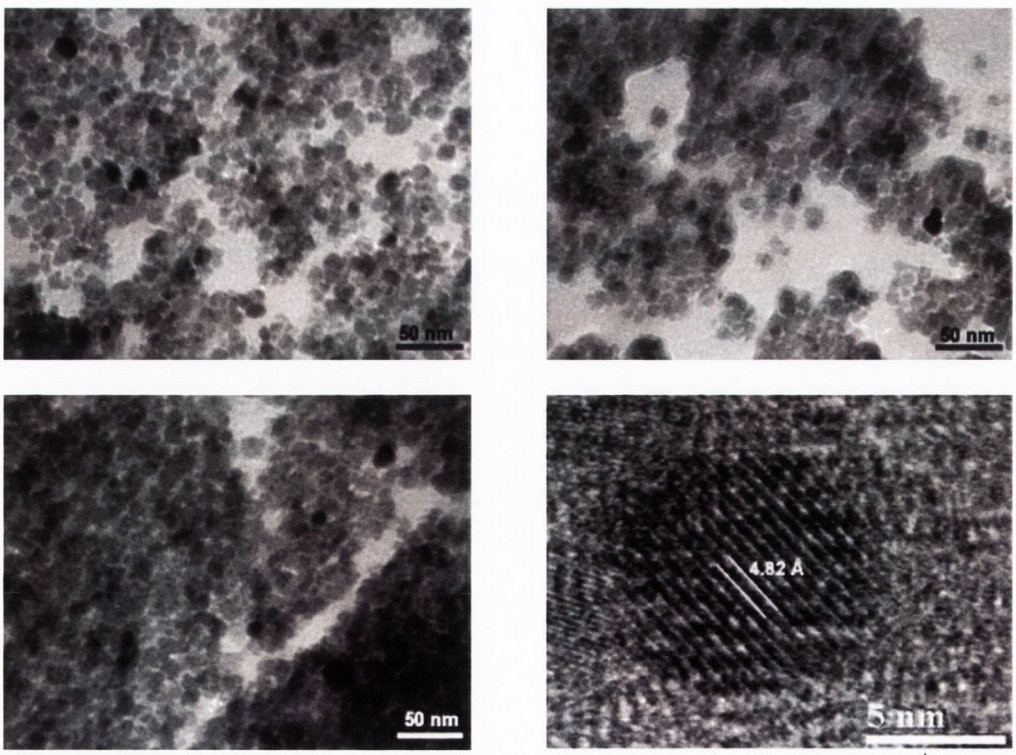

Figure 5.15 **(a)** Magnetite nanoparticles; functionalised with **(b)** $T_8NH_3^+Cl^-$; **(c)** with $T_8NH_3^+Cl^-$ and porphyrin, **(d)** HRTEM of $T_8NH_3^+Cl^-$porphyrin composite

5.2.1.5.4. UV-vis and Fluorescence spectroscopy

An absorption spectrum of the porphyrin nanocomposite reveals a peak at 413 nm (Figure 5.16). The spectrum is follows an incline, which is a consequence of scattering by the magnetic nanoparticles. Fluorescence studies were performed in order to ensure porphyrin attachment and to check if the presence of the $T_8NH_3^+Cl^-$ prevented quenching (Figure 5.17). Because of the paramagnetic nature of magnetite, the luminescence of porphyrin attached to the nanoparticle may be quenched. Fluorescence spectra of $T_8NH_3^+Cl$-porphyrin-magnetite composite in phosphate buffer (3mM, pH 7.2) have shown emission peaks at 646 and 709 nm, with absorption peaks at 413, 518, 556 and 585 nm (Figure 5.17). The fluorescence of the composites proves that $T_8NH_3^+$ ions surrounding magnetite nanoparticles prevent the quenching of the luminescence of the bound porphyrin moieties.

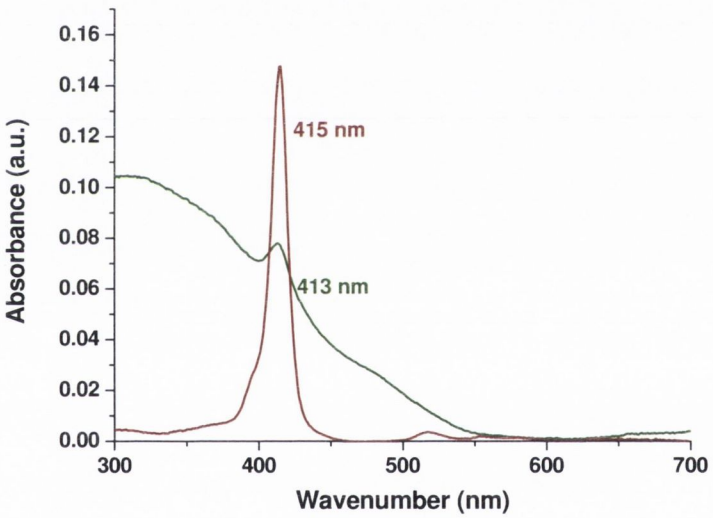

Figure 5.16 UV spectrum of (maroon) original porphyrin solution and (green) porphyrin-$T_8NH_3^+Cl^-$ -magnetite nanocomposite

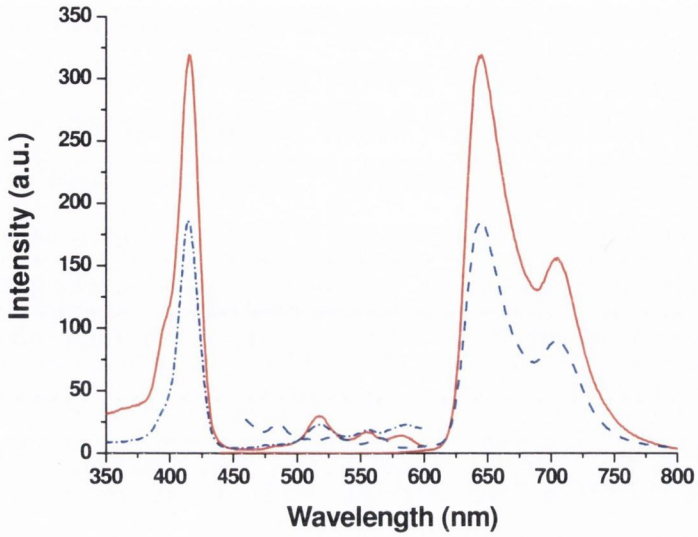

Figure 5.17 Emission and excitation spectra of original porphyrin (red line) [1.4 × 10^{-9}M in phosphate buffer] and porphyrin functionalised $T_8NH_3^+Cl^-$-magnetite nanocomposites (blue dashed line) [360 μL of particle suspension, made up to 3mL with phosphate buffer] (dashed line). λ_{em} = 413 nm, λ_{ex} = 650 nm.

5.2.1.5.5. Dynamic NMR measurements

The effect of these nanoparticle composites on the water proton spin-lattice relaxation time T_1 has been measured by NMR dispersion (NMRD), allowing the determination of the frequency dependence of the relaxivity r_1 via equation 1 (where T_1(water) is the native relaxation time of the supporting fluid (water) and r_1 is independent of the concentration of the magnetic fluid).

$$R_{1(obs)} = \frac{1}{T_{1(obs)}} = \frac{1}{T_{1(water)}} + \frac{1}{T_{1(para)}} = \frac{1}{T_{1(diam)}} + r_1[Fe] \qquad (1)$$

The presence of the strongly magnetic particle affects the NMR response of the ^1H nuclei of the solvent (water). NMRD is a sensitive indicator of the nature of the magnetic moment and the water exchange with the particle or cluster.

The magnetic nature of the nanoparticle composites and their MRI contrast efficiency was assessed by nuclear magnetic resonance dispersion (NMRD), where the frequency dependence of the spin-lattice relaxation is measured. The water relaxation rate enhancement due to the superparamagnetic particles is expressed as concentration independent relaxivity, r_1 units $s^{-1}mM^{-1}$ (of Fe). The NMRD profiles obtained for both the $T_8NH_3Cl^-$ -magnetite and $T_8NH_3^+Cl^-$ -porphyrin-magnetite are shown in Figure 5.18.

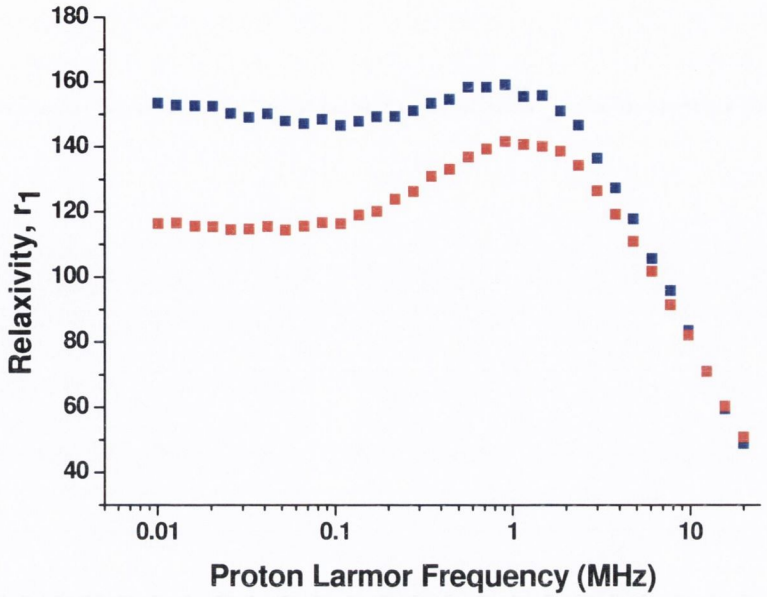

Figure 5.18 NMRD response recorded at 25±1°C, of $T_8NH_3^+Cl^-$ -magnetite (■) and porphyrin functionalised $T_8NH_3^+Cl^-$ -magnetite (•) nanocomposites.

The relaxivity values obtained for these samples are higher than those for commercial nanoparticulate MRI contrast agents at 20 MHz, which makes them promising for use as MRI contrast agents. While TEM demonstrates that the particles are in the superparamagnetic size range, the observed r_1 maxima clearly indicate[35] that a significant proportion, ca. 60 mol%, of the magnetisation is superparamagnetic. However, the high low field relaxivity shows that the remaining magnetisation is magnetically blocked. This is most likely due to strong anisotropic interparticle interactions in the magnetic nanoclusters. PCS measurements obtained agree with this observation, giving a Z-average of 82 nm with a PDI of 0.415.

5.2.2. Biological applications of magnetic-fluorescent nanocomposites

Initially we have investigated the uptake and cellular localisation of porphyrin-$T_8NH_3^+Cl^-$ -magnetite nanocomposites in live THP-1 cells. Intracellular accumulation of the nanoparticles was analysed by confocal microscopy (Figure 5.19).

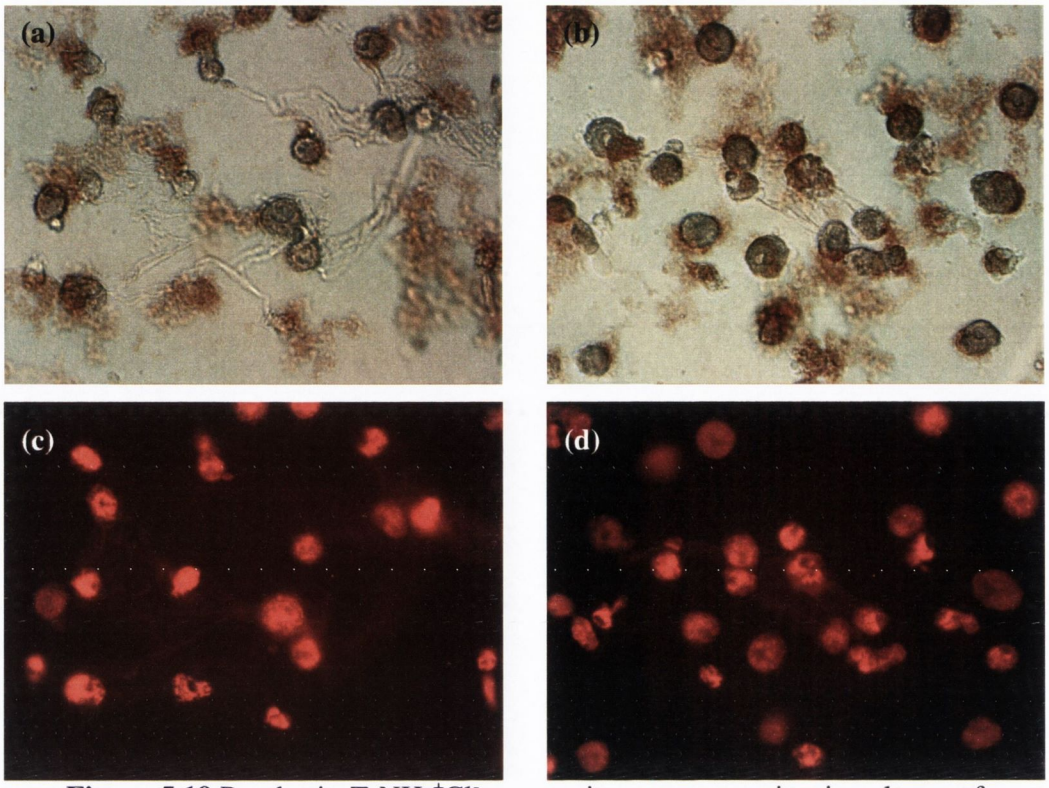

Figure 5.19 Porphyrin-$T_8NH_3^+Cl^-$ -magnetite nanocomposites in cultures of macrophages. (a), (b) Light images and (c), (d) corresponding fluorescent images

THP-1 cells were differentiated to macrophages (as described in the experimental chapter) and the nanocomposites were added at a 1 in 100 dilution followed by incubation for the indicated times at 37 °C. Vigorous washing with PBS followed the incubation period to detach the loosely bound nanoparticles. Confocal imaging found that the porphyrin-$T_8NH_3^+Cl^-$ -magnetite nanocomposites are taken up by the macrophages and sequestered to the cytoplasm within 10 minutes, significantly increasing the fluorescent signal due to intracellular particle accumulation, compared to the non-ingested nanocomposites (Figure 5.19).

Incubation studies with live osteoblast (MC3T3-E1) cells (ATCC, USA) were also carried out with the porphyrin-$T_8NH_3^+Cl^-$-magnetite nanocomposites. They were found to be actively taken up by the cells. Cells were imaged under confocal and phase contrast microscopy. Nanoparticles with an initial density of 10^{11} particles/mL were stabilised for 2 hours in the cell culture medium (α-MEM, ATCC, USA), and added to adherent MC3T3-E1 cells at a final concentration of 10^6 particles/mL and incubated at 37°C, 5% CO_2 and 95% RH for 30 minutes on glass coverslip.

The images shown in Figure 5.20 are taken from different batches of MC3T3-E1 cells and are representative of the extent of magnetic particles uptake by groups of cells (Figure 5.20a,b) and of localisation of the particles in specific organelles within a cell (Figure 5.20c,d).

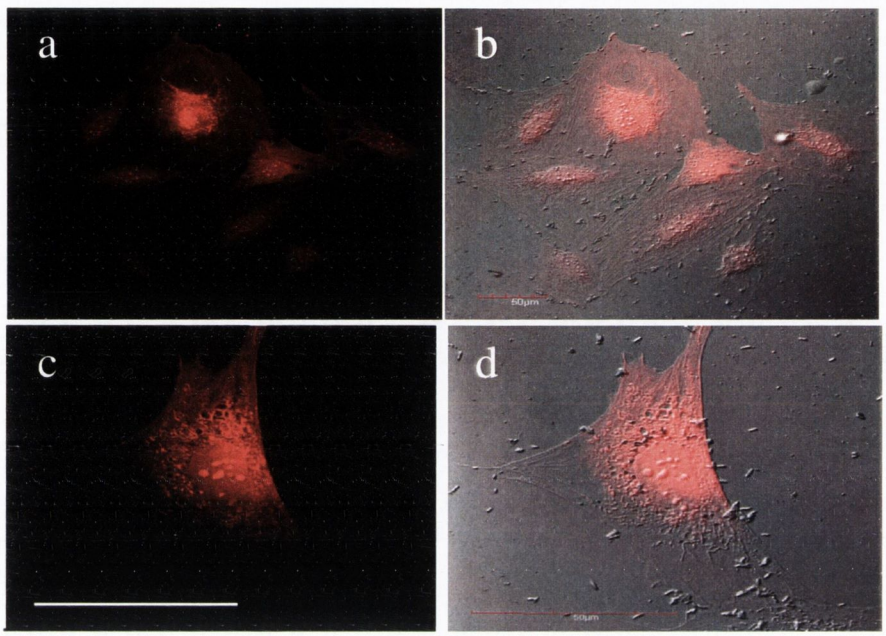

Figure 5.20 Uptake of particles by osteoblast cells. Population imaging a) confocal image (λ_{em}= 504 nm, λ_{ex}= 604 nm) and b) overlay with phase contrast (mag. × 40, Scale bar = 50 μm). Single cell imaging. c) confocal image (λ_{em}= 504 nm, λ_{ex}= 604 nm) and d) with combined phase contrast (mag. × 60, Scale bar= 50 μm)

As observed in confocal microscopy, diffuse cytoplasmic staining was observed with noted accumulation of the dye-bound particles in regions surrounding the nucleus. These regions may correspond to the endoplasmic reticulum and the mitochondria. The reticulum and the mitochondria support vital cell functions and it is likely that these particles may be attracted to the iron containing proteins contained within these organelles.

The aggregated magnetic porphyrin nanocomposites are most likely taken up by the cells *via* endocytosis. The nanocomposites also exhibit a distinctive subcellular distribution corresponding to the location of the mitochondria, endoplasmic reticulum and nuclei. This phenomenon, as well as an unusually strong increase of the fluorescence inside the cells after particle uptake, might be related to dissociation of the components in the magnetic–fluorescent nanocomposites. We

believe that porphyrin species released from the composites in this case are no longer exposed to the partial quenching effects by paramagnetic oxide cores.

In order to ensure that the fluorescence was due to the porphyrin-magnetite nanocomposite, a control experiment was also carried out where the cells were incubated with a solution of the porphyrin dye only (in the same concentration range). In all cases, there was no uptake of the porphyrin dye alone (Figure 5.21). The circled areas in Figure 5.21 represent cells and the lack of intense red fluorescence indicates that the cells do not take up the free porphyrin. In addition all free porphyrin dye samples were not bright, due to fast photobleaching of porphyrin species located outside cells.

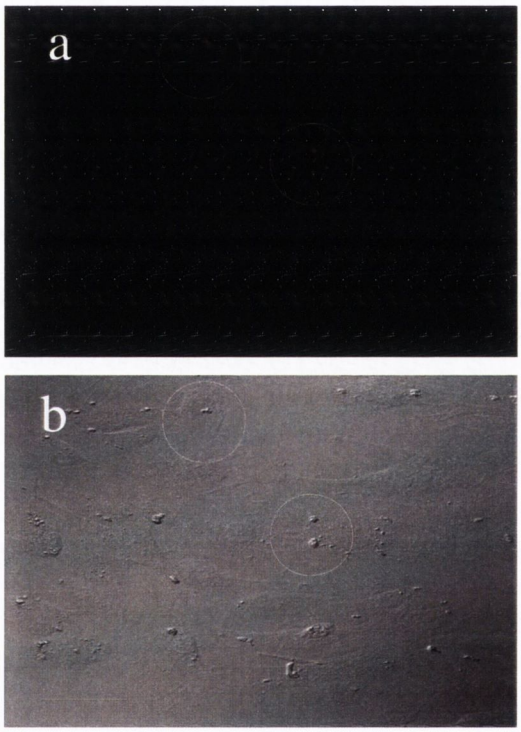

Figure 5.21 MC3T3-E1 cells cultured for two days in cell medium mixed with porphyrin. (a) Confocal image showing no uptake by cells of porphyrin dye. (λ_{em}= 504 nm, λ_{exc}= 604 nm). (b) Matching phase contrast image. (mag. x 40, scale bar = 50 μm).

5.2.3. Attempted studies on other fluorescent magnetite-POSS nanocomposites

5.2.3.1. Magnetite - $T_8NH_3^+Cl^-$ -salicylic acid nanocomposites

In this experiment salicylic acid (*o*-hydroxybenzoic acid) was chosen as a stabiliser for the magnetite-$T_8NH_3^+Cl^-$ nanocomposite because of its medicinal uses. It may be converted to aspirin by the esterification of the ortho hydroxyl group.

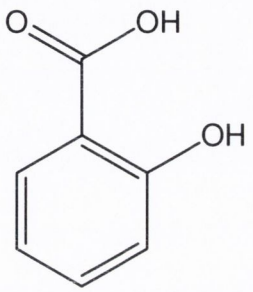

Figure 5.22 *o*-hydroxybenzoic acid (salicylic acid)

According to absorbance spectra, there are three peaks in the spectrum for salicylic acid: 202, 232, and 302 nm. Upon reaction with the magnetite-$T_8NH_3^+Cl^-$ nanocomposite, absorption and fluorescence spectra were obtained (Figure 5.23). It is difficult to detect exactly where the peak occurs in the absorbance spectrum due to a scattering of the light by the nanoparticles. The fluorescence spectrum of the composite shows a shift of the luminescence peak from 408 to 422 nm.

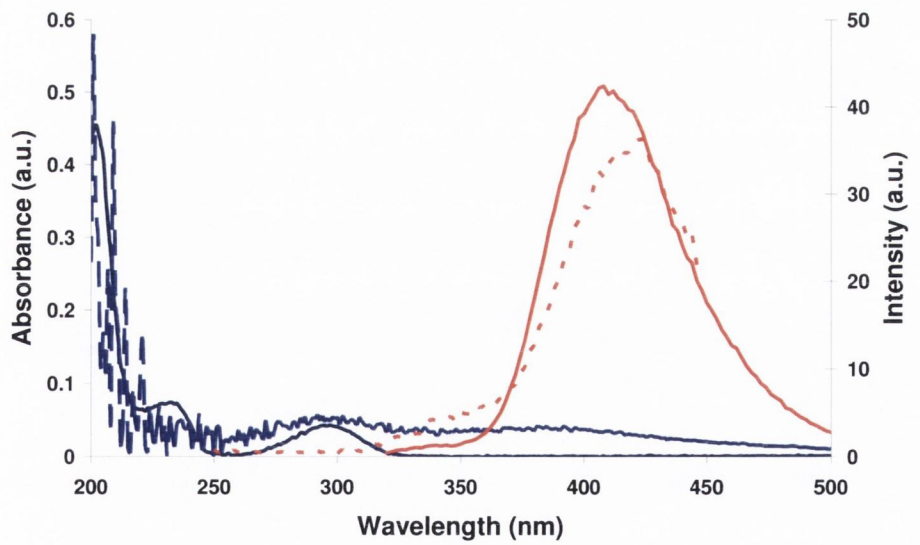

Figure 5.23 Absorbance (blue) and fluorescence (red) spectra of original salicylic acid solution (solid line) and the nanocomposite (dashed line). λ_{ex} = 232 nm.

To investigate the biocompatibility of these nanocomposites, the macrophage cell line THP-1 was incubated with a sample of the particles.

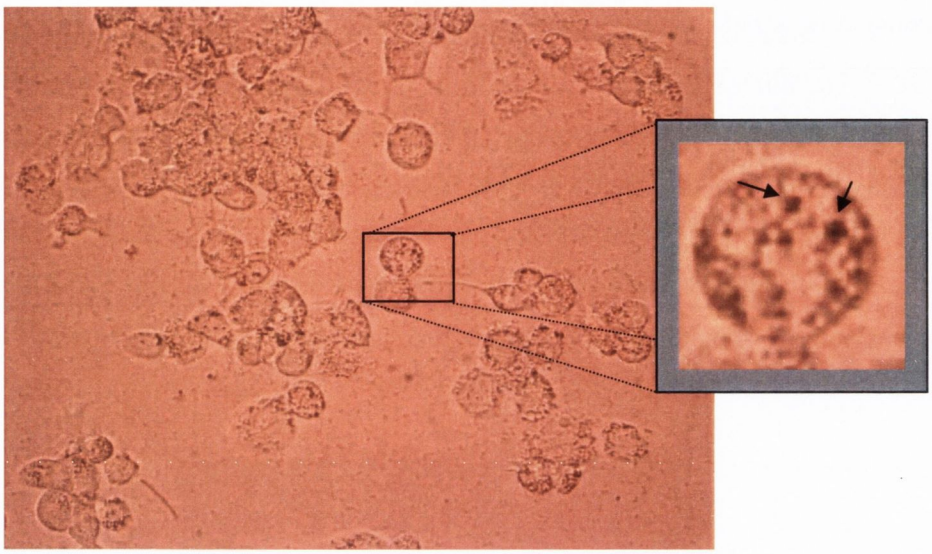

Figure 5.24 Light microscopy image of macrophage THP-1 cells; close up reveals particles located in the cell cytoplasm (see arrows).

Light microscopy images revealed an accumulation of the particles in the cell cytoplasm (Figure 5.24). Unfortunately, due to very poor fluorescence of the particles, it was not possible to obtain confocal images of the localised particles.

5.2.3.2. Magnetite nanoparticles functionalised with $T_8NH_3^+Cl^-$ and subsequent treatment with 9-Acridinecarboxylic acid

9-Acridinecarboxylic acid was also chosen for the biological activity of its derivatives. Its parent molecule, acridine is the starting material for the production for many dyes and DNA intercalating agents.

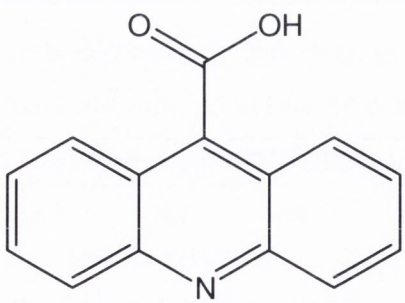

Figure 5.25 9-Acridinecarboxylic acid

Absorbance spectra were recorded for a stock solution of 9-acridinecarboxylic acid in methanol (Figure 5.26). There are two peaks observed: 251 and 355 nm. An emission peak at 424 nm was observed when excited at either wavelength.

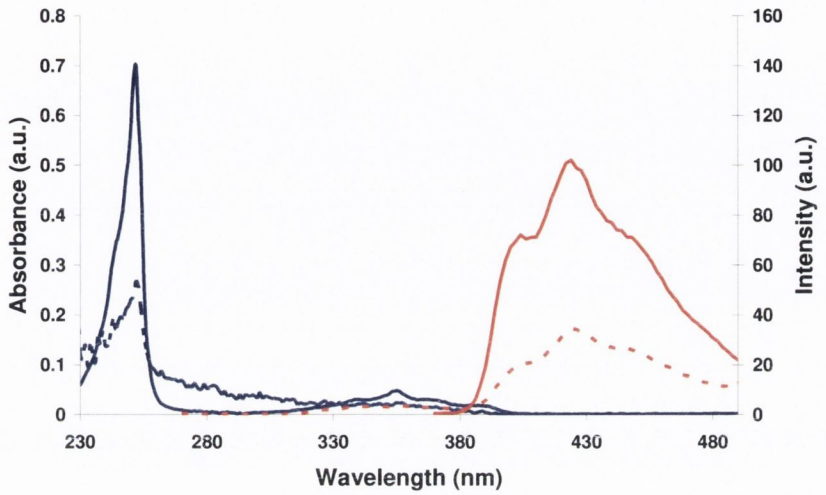

Figure 5.26 Absorbance (blue) and fluorescence (red) spectra of original acridinecarboxylic acid solution (solid line) and nanocomposite (dashed line). λ_{ex} = 424 nm.

Absorbance and fluorescence spectra obtained for the nanocomposite functionalised with 9-acridinecarboxylic acid reveal the presence of the fluorophore (Figure 5.26). As was the case with the salicylic acid composite, a scattering effect was observed in the absorption spectrum. There was no observable shift in the fluorescence spectrum.

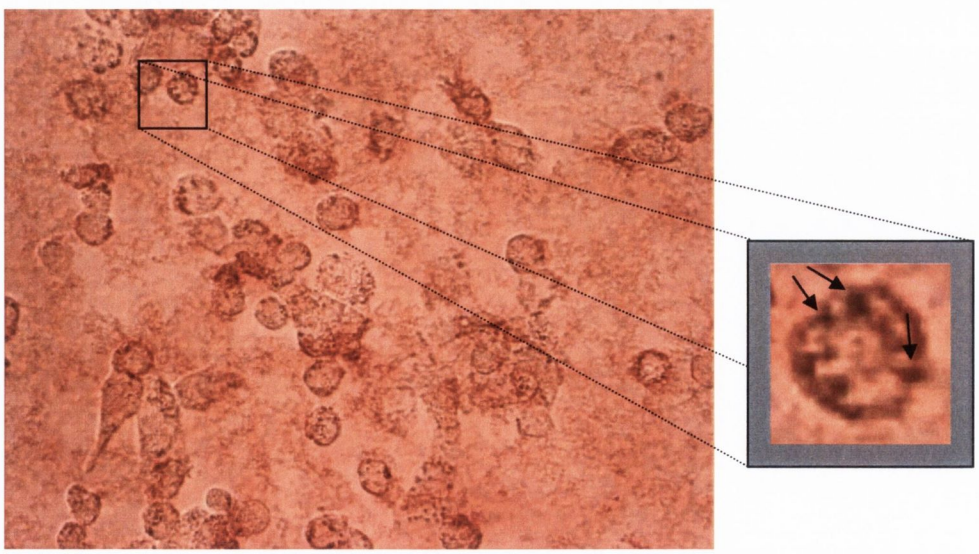

Figure 5.27 Light image of macrophage THP-1 cells with close up showing uptake of particles into cytoplasm.

Cell uptake studies were also carried out using live macrophage THP-1 cells (Figure 27). Light microscopy again revealed these composites enter the cell and are located in the cell cytoplasm. No fluorescent confocal microscopy images were obtained for these nanocomposites.

5.3. Preparation of magnetic nanocomposites covalently functionalised with fluorescent molecules

5.3.1. Preparation of silica coated magnetic nanoparticles

Magnetite nanoparticles were prepared *via* the coprecipitation technique as described in section 5.2.1. Prior to binding the fluorescent molecules to the magnetic nanoparticles, a thin shell of silica was introduced to the nanoparticle surface. There are several reasons for choosing silica as a coating for the particles. Not only are further surface modifications possible, but the silica coating may also reduce any cytotoxic effects of the bare nanoparticles.[36] The silica coating also provides a barrier to quenching of any fluorophores by the magnetic cores.[37] Because the isoelectric point of magnetite is at pH 7, it is necessary to further coat the particles in order to make them stable in the pH region 6-10. Application of a thin layer of silica lowers this isoelectric point to approximately pH 3, which increases the stability near neutral pH.[38] One advantage silica coating has over double-surfactant layers and organic surface layers such as lauric acid and oleic acid is that, once bound, there is no risk of desorbtion as they are covalently linked as opposed to ionically associated to the particle surface. Not only is the silica shell chemically inert and optically transparent, it will help to prevent particle aggregation.[39] For the preparation of silica coated magnetite nanoparticles, a method reported by Philipse *et. al.*[38] is partly employed. This involves dispersing the bare nanoparticles using tetramethylammonium hydroxide to form a stable magnetic fluid followed by coating with a monolayer of sodium silicate. A 3-aminopropyltriethoxysilane-modified protoporphyrin can then be directly attached to the particle surface via a base-catalysed condensation between the ethoxysilane derivative and silanol groups of the silica coating of magnetic nanoparticles.

5.3.2. Reaction with fluorescent molecules

The fluorescent component was prepared *via* reaction of the porphyrin Protoporphyrin IX with 3-aminopropyltriethoxysilane. Amide bond formation was

achieved between the molecules by employing the coupling reagent *N*-(3-Dimethylaminopropyl)-*N'*-ethylcarbodiimide (EDCI) (Scheme 5.3). EDC is a water soluble compound which promotes the formation of an amide bond between carboxylic acids and amines by activating the carboxyl to form a urea intermediate which can readily react with the amino group.

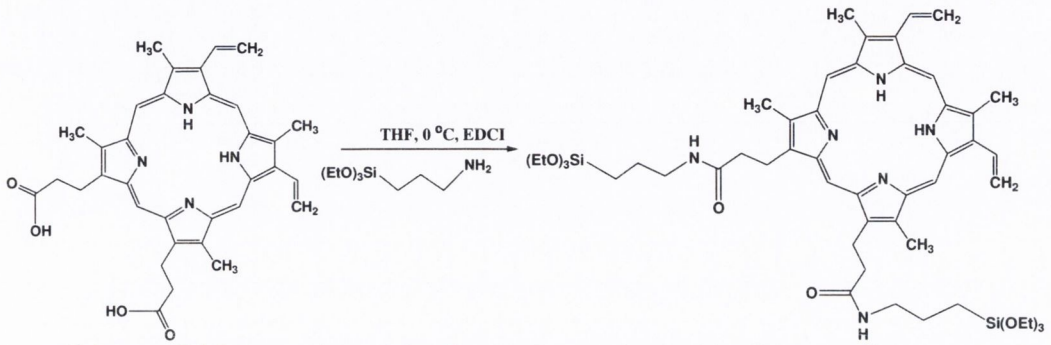

Scheme 5.3 Preparation of the fluorescent moiety with silane spacing group

Once the amide bond has been formed, it is important to keep the compound free of water and air, since the three siloxane groups may be hydrolysed to silanols. To avoid any unwanted reactions, the compound was used immediately after preparation. The approach here is to react the siloxane groups with the silanol moieties present on the surface of the nanoparticles.

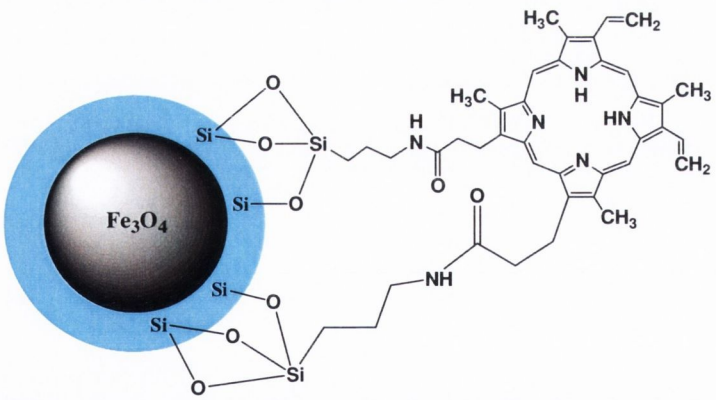

Scheme 5.4 Covalently linked Protoporphyrin IX with silane coated magnetite. Turquoise shell around nanoparticle represents silica coating.

5.3.3. Characterisation of covalently linked magnetic fluorescent nanocomposites

5.3.3.1. FTIR spectroscopy

FTIR spectra of the silica coated magnetite nanoparticles before and after reaction with the protoporphyrin were recorded in KBr (Figure 5.28). The silica

coated particles have stretches at 579, 1087, 1625 and 3286 cm^{-1} corresponding to the Fe-O, Si-O-Si, and water stretches respectively. The stretch found at 947 cm^{-1} is due to the presence of Fe-O-Si bonds in the sample.

For the nanocomposite material, again Fe-O and water stretches are found at 579, 1621 and 3286 cm^{-1} respectively. The Fe-O-Si stretch is this time masked by the NH wagging from the porphyrin centred at at 901 cm^{-1}. NH stretches are found at 1473 cm^{-1}. Aromatic and aliphatic stretches associated with the porphyrin are found at 2500 and 2945 cm^{-1} respectively.

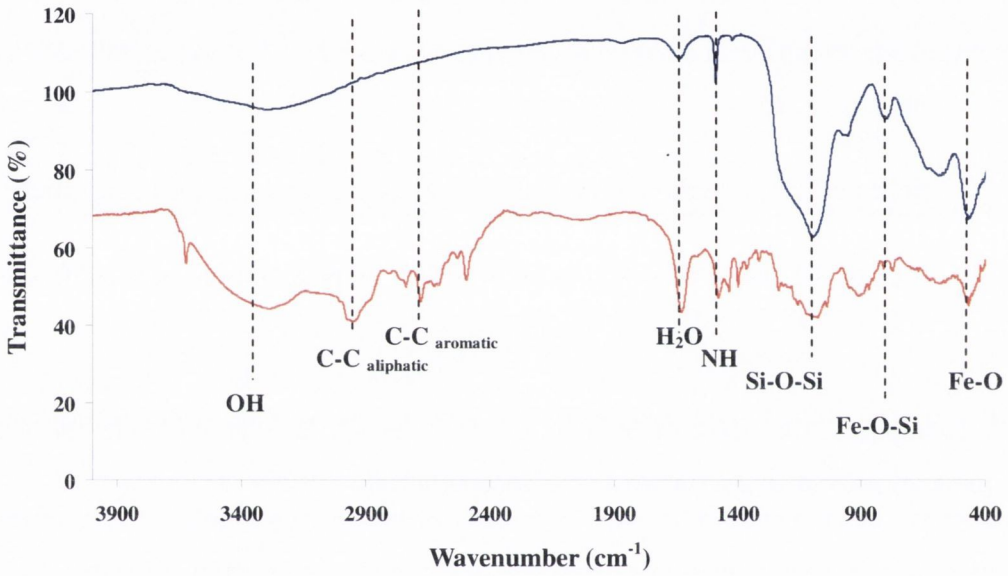

Figure 5.28 IR spectra for silica coated magnetite nanoparticles (blue) and porphyrin-nanocomposite (red) carried out in KBr

5.3.3.2. Electron microscopy

TEM images taken of the silane coated nanoparticles reveal the presence of a core-shell structure (Figure 5.29). The silane coating on the particles has a average thickness of 3 nm and the particles are found to aggregate in group of approximately ten particles. Upon reaction with the 3-aminopropyltriethoxysilane modified protoporphyrin, the coating thickness is found to slightly increase to 4 nm.

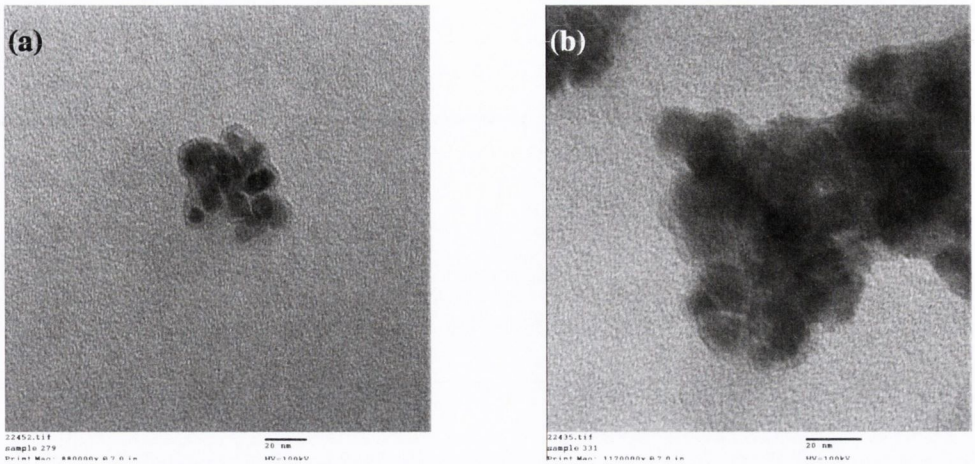

Figure 5.29 TEM images of (a) silane coated nanoparticles and (b) after treatment with protoporphyrin

5.3.3.3. UV-vis absorption and Fluorescence spectroscopy

Absorbance spectra of the original protoporphyrin and the porphyrin-nanocomposite were carried out in THF (Figure 5.30). Peaks at 406, 505, 538, 577 and 632 nm were observed for a solution of protoporphyrin. The main band is found to be shifted by 11 nm in the nanocomposite sample to 395 nm. The spectrum for the nanocomposite also appears broader when compared to the original porphyrin. This is due to a scattering of the incoming light by the nanoparticle suspension.

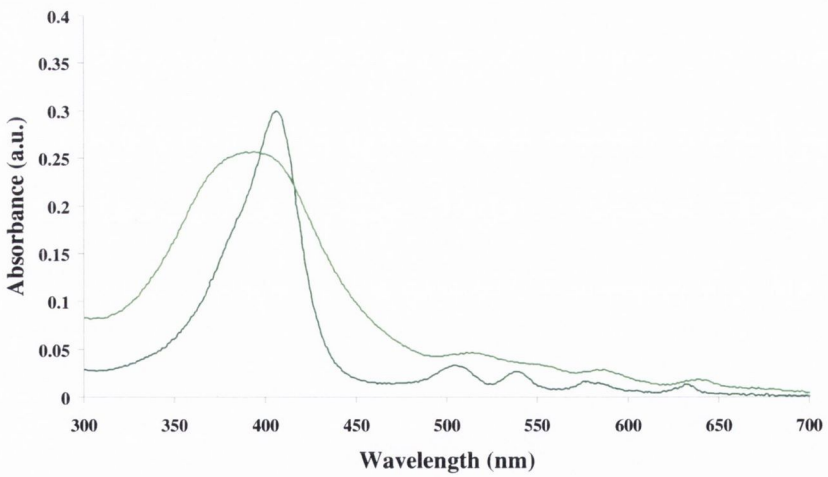

Figure 5.30 Absorbance spectra of original protoporphyrin (dark green line) [1.57 × 10^{-6} M] and porphyrin-nanocomposite [100µL particle suspension in 3mL THF]. λ_{em} = 633 nm, λ_{ex} = 406 nm.

To confirm that the nanocomposites were indeed fluorescent, emission and excitation spectra were recorded (Figure 5.31). The emission spectra were obtained using an excitation wavelength (λ_{ex}) of 406 nm, while for excitation, λ_{em} was 633 nm. Emission peaks and corresponding excitation peaks were observed for the nanocomposite. There was a slight shift in the positioning of one of the bands in the emission spectra: the peak at 702 nm in the original porphyrin spectrum was shifted to 678 nm in the composite. This blue shift may be due to the potential of the porphyrin molecules to π-π stack.

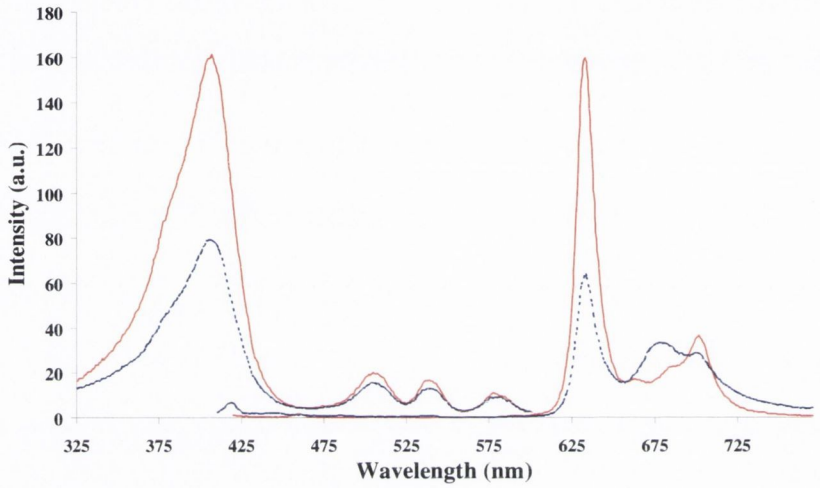

Figure 5.31 Emission and excitation spectra of original porphyrin (red line) [5.23 × 10^{-7} M in phosphate buffer] and porphyrin functionalised $T_8NH_3^+Cl^-$-magnetite nanocomposites (blue line) [100 μL of particle suspension, made up to 3mL with THF]

5.3.3.4. Confocal imaging

Localisation of these nanocomposites in live THP-1 human macrophage cells was studied. Confocal images were recorded of the nanocomposite incubated in THP-1 cells after 72 hours. The particles were found to be localised into the cell cytoplasm (Figure 5.32).

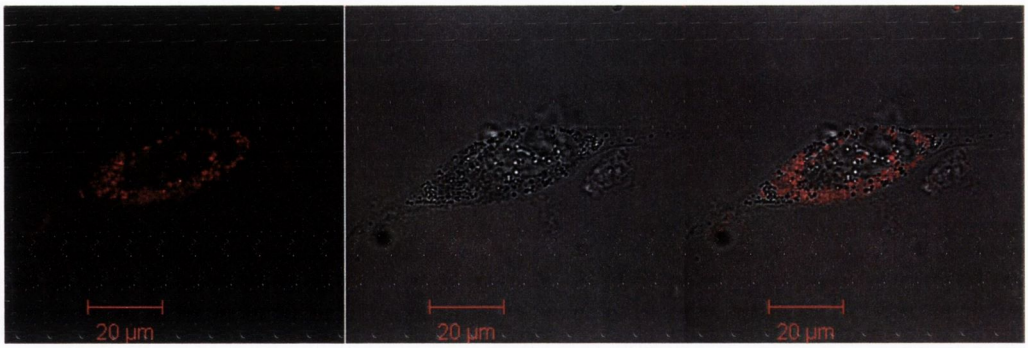

Figure 5.32: **(a)** Confocal image of THP-1 macrophage cell, **(b)** bright field image and **(c)** overlay image of THP-1 macrophage cell with localised magnetic nanocomposite. $\lambda_{ex} = 561$ nm

Initial toxicity studies have found that after 3 days internalisation, the nanocomposite does not have any harmful effects on the THP-1 cells. Video footage of the confocal imaging showing the fluorescence intensity going through the cell (from the bottom to the top of the cell) shows that the fluorescence is most intense in the centre of the cell, indicating that the particles are indeed localised internally and not sitting on the cells outer membrane.

5.4. Conclusions

A range of nanocomposites have been prepared, which have both magnetic and fluorescent properties. Also, a new non-covalent approach for the preparation of fluorescent magnetic nanocomposites using ionic POSS molecules has been developed. In these composites, fluorescent dye molecules are bound to POSS-magnetite aggregates *via* non-covalent ionic or hydrogen bonding. NMRD studies have shown that these nanocomposites aggregate into larger magnetic clusters with strong anisotropic interparticle interactions that increase the low-field relaxivity in the ionically linked case. While this covalent approach did not always produce composites which were fluorescent in cell culture medium under confocal microscope, these results are nevertheless important for potential targeted drug delivery applications. Confocal microscopy images of magnetite-POSS-porphyrin composites have clearly demonstrated that the magnetic particles and dyes are indeed localised in the THP-1 cells most likely by endocytosis. The nanocomposites also exhibited a distinctive subcellular distribution entering into the locations corresponding to the mitochondria, endoplasmic reticulum and nuclei. We believe that the ionically linked

porphyrin nanocomposites dissociate into the components inside cells. As a result, the porphyrin species is released from the composites demonstrating specific cellular localisation and enhanced fluorescence inside the cells after particle uptake. This opens up several intriguing possibilities. Firstly, the reduction of the overall size of the composites might enable better penetration of porphyrin molecules into size restricted intracellular compartments. Secondly, such intracellular fragmentation of the nanocomposites could potentially serve as a basis both for new subcellular imaging contrast agents and for targeted drug release systems. Magnetic fluids based on these composites might also potentially serve as contrast agents for MRI imaging and agents for two in one hyperthermia and photodynamic cancer therapy.

Covalently bound porphyrin functionalised magnetite nanocomposites have also been successfully prepared. The uptake of these nanocomposites have into phagocytic cells has been studied, with the particles located in the cytoplasm around the nucleus. Initial toxicity results were encouraging, with no deleterious effects noted in the cells after 3 days exposure to the nanocomposite.

Thus magnetic suspensions of new fluorescent-magnetite nanocomposites have shown a potential as organelle specific diagnostic markers which could be detected by MRI or fluorescent confocal imaging. The results of this study also indicate that these nanocomposites could potentially serve as drug delivery systems. These systems may have important applications in diagnostics and the treatment of degenerative and chronic diseases associated with overactive phagocytic responses, such as autoimmune disorders and osteoporosis. Future work will involve more detailed studies of the nature of the fluorescent-magnetic nanocomposites and the intracellular mechanisms of their interaction with live cells.

References

[1] Q. A. Pankhurst, J. Connolly, S. K. Jones, J. Dobson, *Journal of Physics D-Applied Physics* **2003**, *36*, R167.

[2] C. Bergemann, D. Muller-Schulte, J. Oster, L. Brassard, A. S. Lubbe, *Journal of Magnetism and Magnetic Materials* **1999**, *194*, 45.

[3] R. M. Muller, A. Roch, J. M. Colet, A. Ouakssim, P. Gillis, A. E. Merbach, E. Toth, in *The Chemistry of Contrast Agents in Medical Magnetic Resonance Imaging*, John Wiley & Sons, New York, **2001**, pp. 417.

[4] D. K. Kim, Y. Zhang, J. Kehr, T. Klason, B. Bjelke, M. Muhammed, *Journal of Magnetism and Magnetic Materials* **2001**, *225*, 256.

[5] A. Jordan, R. Scholz, P. Wust, H. Fahling, R. Felix, *Journal of Magnetism and Magnetic Materials* **1999**, *201*, 413.

[6] A. Jordan, R. Scholz, K. Maier-Hauff, M. Johannsen, P. Wust, J. Nadobny, H. Schirra, H. Schmidt, S. Deger, S. Loening, W. Lanksch, R. Felix, *Journal of Magnetism and Magnetic Materials* **2001**, *225*, 118.

[7] C. C. Berry, A. S. G. Curtis, *Journal of Physics D-Applied Physics* **2003**, *36*, R198.

[8] L. G. Remsen, C. I. McCormick, S. RomanGoldstein, G. Nilaver, R. Weissleder, A. Bogdanov, K. E. Hellstrom, I. Hellstrom, R. A. Kroll, E. A. Neuwelt, *American Journal of Neuroradiology* **1996**, *17*, 411.

[9] M. Mikhaylova, D. K. Kim, C. C. Berry, A. Zagorodni, M. Toprak, A. S. G. Curtis, M. Muhammed, *Chemistry of Materials* **2004**, *16*, 2344.

[10] L. Levy, Y. Sahoo, K. S. Kim, E. J. Bergey, P. N. Prasad, *Chemistry of Materials* **2002**, *14*, 3715.

[11] H. C. Lu, G. S. Yi, S. Y. Zhao, D. P. Chen, L. H. Guo, J. Cheng, *Journal of Materials Chemistry* **2004**, *14*, 1336.

[12] H. W. Gu, K. M. Xu, Z. M. Yang, C. K. Chang, B. Xu, *Chemical Communications* **2005**, 4270.

[13] F. Bertorelle, C. Wilhelm, J. Roger, F. Gazeau, C. Menager, V. Cabuil, *Langmuir* **2006**, *22*, 5385.

[14] R. Bonnett, *Chemical Society Reviews* **1995**, *24*, 19.

[15] I. Cecic, M. Korbelik, *Cancer Letters* **2002**, *183*, 43.

[16] Y. Lu, Y. D. Yin, B. T. Mayers, Y. N. Xia, *Nano Letters* **2002**, *2*, 183.

[17] R. Massart, *IEEE Transactions on Magnetics* **1981**, *17*, 1247.

[18] D. K. Kim, M. Mikhaylova, Y. Zhang, M. Muhammed, *Chemistry of Materials* **2003**, *15*, 1617.

[19] B. P. Jia, L. Gao, *Journal of the American Ceramic Society* **2006**, *89*, 1739.

[20] S. Y. Lian, E. Wang, Z. H. Kang, Y. P. Bai, L. Gao, M. Jiang, C. W. Hu, L. Xu, *Solid State Communications* **2004**, *129*, 485.

[21] O. N. Shebanova, P. Lazor, *Journal of Solid State Chemistry* **2003**, *174*, 424.

[22] R. M. Cornell, U. Schwertmann, *The Iron Oxides*, Wiley VCH Verlag GmbH and Co., Weinheim, **1996**.

[23] Z. L. Liu, Y. J. Liu, K. L. Yao, Z. H. Ding, J. Tao, X. Wang, *Journal of Materials Synthesis and Processing* **2002**, *10*, 83.

[24] C. R. Lin, Y. M. Chu, S. C. Wang, *Materials Letters* **2006**, *60*, 447.

[25] J. Lee, T. Isobe, M. Senna, *Journal of Colloid and Interface Science* **1996**, *177*, 490.

[26] P. G. Harrison, *Journal of Organometallic Chemistry* **1997**, *542*, 141.

[27] D. Neumann, M. Fisher, L. Tran, J. G. Matisons, *Journal of the American Chemical Society* **2002**, *124*, 13998.

[28] F. J. Feher, T. A. Budzichowski, R. L. Blanski, K. J. Weller, J. W. Ziller, *Organometallics* **1991**, *10*, 2526.

[29] E. Rikowski, H. C. Marsmann, *Polyhedron* **1997**, *16*, 3357.

[30] P. A. Agaskar, *Inorganic Chemistry* **1991**, *30*, 2707.

[31] F. J. Feher, T. A. Budzichowski, *Journal of Organometallic Chemistry* **1989**, *379*, 33.

[32] F. J. Feher, K. D. Wyndham, D. Soulivong, F. Nguyen, *Journal of the Chemical Society-Dalton Transactions* **1999**, 1491.

[33] A. Flores-Villalobos, H. Morales-Rojas, S. Escalante-Tovar, A. K. Yatsimirsky, *Journal of Physical Organic Chemistry* **2002**, *15*, 83.

[34] M. Y. Choi, J. A. Pollard, M. A. Webb, J. L. McHale, *Journal of the American Chemical Society* **2003**, *125*, 810.

[35] S. J. Byrne, S. A. Corr, Y. K. Gun'ko, J. M. Kelly, D. F. Brougham, S. Ghosh, *Chemical Communications* **2004**, 2560.

[36] P. Tartaj, M. D. Morales, S. Veintemillas-Verdaguer, T. Gonzalez-Carreno, C. J. Serna, *Journal of Physics D-Applied Physics* **2003**, *36*, R182.

[37] T. Ung, L. M. Liz-Marzan, P. Mulvaney, *Langmuir* **1998**, *14*, 3740.

[38] A. P. Philipse, M. P. B. Vanbruggen, C. Pathmamanoharan, *Langmuir* **1994**, *10*, 92.

[39] L. M. LizMarzan, M. Giersig, P. Mulvaney, *Langmuir* **1996**, *12*, 4329.

Chapter 6: DNA-magnetite nanocomposites and their interactions with fluorescent dyes

6.1. Introduction

DNA represents an exciting prospect as a template for nanoassemblies due to its small size (approximately 2 nm in diameter), its repeating structure (a helical pitch of 3.4 – 3.6 nm) and its functional groups.[1, 2] The use of DNA for this purpose has been exploited by many groups. In 1996, Mirkin[3] and Alivisatos[4] independently reported the use of thiolated oligonucleotides to functionalise gold nanoparticles, which could be then be hybridised with their complementary DNA partners to form regular nanoparticle assemblies. Alivisatos *et. al.*[4] showed *via* TEM studies that their assemblies could be made up of nanoparticles with a regular spacing between them (Figure 6.1), while Mirkin *et. al.*[3] demonstrated the reversibility of their process by denaturation.

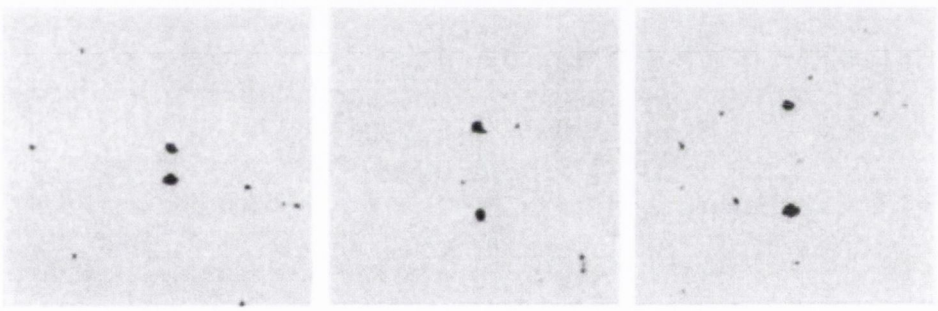

Figure 6.1 Nucleic acid functionalised gold nanoparticles showing the nearest, average and furthest dimers from the same sample.[4]

Since these reports, there has been a wealth of publications in the area of DNA-nanoparticle assemblies. Warner *et. al.* described a method for the assembly of cationically functionalised gold nanoparticles onto the negatively charged backbone of DNA and the observation of linear chains, ribbon-like assemblies and branched structures of the nanoparticles embedded in the DNA.[5] Similar structures have also been reported by Yan and LaBean *et. al.*,[6] but they have employed the recognition ability of biotinylated DNA with streptavidin coated gold nanoparticles. Mirkin *et. al.* have reported the preparation of bio-barcodes composed of protein specific probes which have been functionalised with oligonucleotide-modified 13 nm gold nanoparticles.[7] These devices can detect multiple proteins present in a solution by

virtue of the fact that the DNA sequences employed are different for each protein, therefore their melting temperatures will vary. Also, any protein-DNA interaction results in particle aggregation, which causes shifts in the absorption spectra of the gold nanoparticles. By using this technique, these workers have shown that multiple proteins may be separated and identified. This is not a trivial problem, as expensive and time-consuming assays are usually required to detect proteins.

It is intriguing to consider whether DNA-conjugated magnetite nanoparticles could serve as target-directed MRI contrast agents for cancer diagnosis. Previously Mornet *et al.* have reported the association of magnetite nanoparticles with double stranded DNA.[8] Weissleder and coworkers have studied the effect of oligonucleotide hybridisation on the spin-spin relaxation time of the surrounding water protons and have found that upon hybridisation of complementary oligonucleotide-functionalised magnetic particles, the resulting aggregation of particles causes a significant change in the T_2 relaxation time. They found these changes to be reversible with heating and demonstrated that the oligonucleotides may be recovered from the particle sensors.[9, 10]

The growth of copper,[11] palladium[12] and silver[13] in the presence of DNA has been reported, with wire-like, branched and clustered assemblies found to form. The use of DNA as a template for the formation of nanowires of magnetite had not been reported.

Aminoacridines such as acridine orange (Figure 6.2) are known to possess anti-viral and anti-bacterial properties.[14] These effects are thought to occur due to interactions of the acridine molecules with the bacterial and viral DNA. Because the development of some bacteria is RNA controlled, the presence of an acridine intercalator can act to retard their growth.[15]

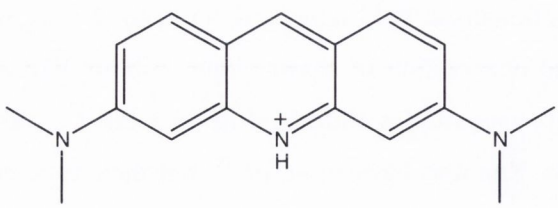

Figure 6.2 Structure of the acridine orange, or 3,6-bisdimethylaminoacridinium, cation

At high phosphate-to-drug ratios acridine drugs are found to intercalate between hydrogen bonded DNA base pairs.[16] Lerman has proposed that the acridines intercalate between neighbouring base pairs in a plane perpendicular to the helix axis. This space is created by a local untwisting of the helical backbone, which allows the base pairs to separate without breaking their hydrogen bonds. The acridine molecule may then insert itself into the space provided (Figure 6.3).

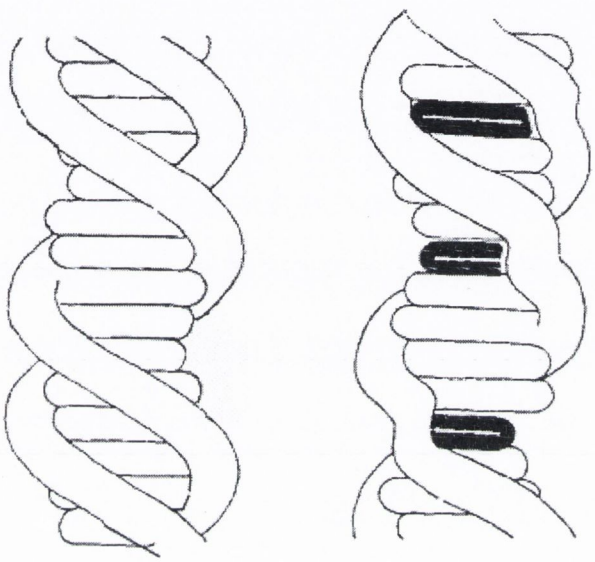

Figure 6.3 Structure of **(a)** normal DNA and **(b)** upon intercalation of acridine orange, as proposed by Lerman[17]

The absorption spectrum of the acridines have been extensively studied and the cationic acridine orange has been found to undergo dimerisation and aggregation in aqueous solution has been reported by Löber for concentrations as low as 2×10^{-5} M.[18] When aromatic ring-containing dyes interact with a macromolecule, such as DNA, there is a displacement of their absorption spectra. For aminoacridines, such as acridine orange, these wavelengths are shifted to longer wavelengths when bound as single cations, while the reversal of this trend is seen when the acridine is bound as dimers or aggregates.[14]

The mode of interaction of dye molecules with DNA is thought to occur *via* two processes.[19] Firstly, a strong binding mode, or an intercalation of the dye between two successive base pairs in the double helix, which involves 20-25% of the DNA phosphate groups. Secondly a weaker, electrostatic interaction is thought to occur involving the remaining phosphate groups. At low phosphorus/dye (P/D) ratios, the

monomer spectrum is observed. Fredericq *et. al.*[20] have reported that at P/D > 4, the monomeric spectrum of acridine orange with DNA is seen with the main band shifted from 492 m to 502 nm for the intercalated species. At lower P/D ratios (i.e. higher dye concentrations), the band at 500 nm decreases and there is the emergence of a new band in the range 455-485 nm which is attributed to the dimer species. The dimer species are formed because every intercalated dye molecule may act as a further binding site for free acridine orange molecules present in the solution. Once the free molecule binds to an intercalated molecule, it forms a spectroscopically distinct dimer species and hence a new band is seen in the absorbance spectrum (Figure 6.4). Denatured DNA studies have also been previously carried out[20] and the band for the intercalated monomer was found to occur at 502 nm. Intercalation may occur in the denatured samples due to the presence of a small number of base pairs which may form during the partial renaturation of DNA which can occur during cooling.

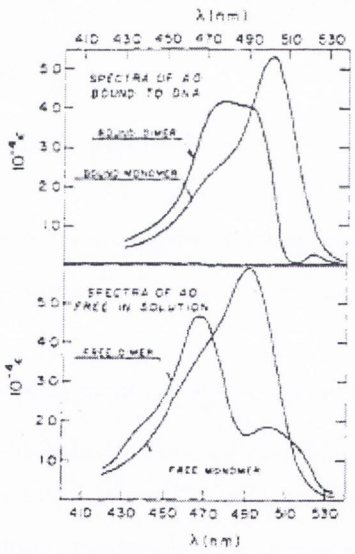

Figure 6.4 Spectra for the acridine orange monomer and dimer bound to DNA, compared to free monomer and dimer aqueous solutions[20]

6.1.1. Aims of this work

The main aim of this part of the project is to prepare new magnetic nanoparticle – DNA nanocomposites using DNA as a stabiliser and investigates properties of these materials. It is expected that the regular structure of DNA will serve as a template to produce quasi one-dimensional nanoassemblies. It is hoped that the DNA will also lend a degree of water stability to the magnetic nanoparticles in order to generate a

family of magnetic fluids, which may have potential applications as MRI contrast agents. The NMRD properties of such fluids will be examined, as will the possibility of nanowire formation. It is envisaged that, if the particles are grown in the presence of DNA, they can be aligned into wires upon application of an external magnetic field. DNA studies will be carried out using the double stranded and denatured forms of both Herring and Salmon sperm DNA. Once the magnetite-DNA nanocomposites are made, intercalation studies with acridine based dyes will be carried out in order to generate magnetic-fluorescent nanocomposites. In order to avoid any dimerisation of acridine orange in our samples, the concentration was kept at 10^{-6} M.

6.2. Herring and Salmon DNA

Two types of DNA were used in the synthesis of the nanocomposites. Herring and Salmon sperm were chosen as they are readily available (both were ordered from Aldrich) and are relatively cheap. The coprecipitation technique was used to conjugate the DNA macromolecules *in situ* to the nanoparticles during their formation. In order to better understand the interactions of the DNA with the nanoparticles, experiments were carried out with the single and double stranded versions of both sets of DNA. DNA samples were denatured by boiling for 10 minutes and then cooling in ice. The extent of denaturation was monitored by measuring the UV-vis absorbance spectrum of the DNA at 260 nm, where the bases absorb strongly. The spectrum of DNA measured at pH 7 always shows two peaks, at 204 and 258 nm. The native DNA may be denatured by boiling at 100 °C for ten minutes and then cooling rapidly (Figure 6.5). An increase in the optical density of 41 % and a red shift of 3 nm of the peak at 258 nm has been previously reported.

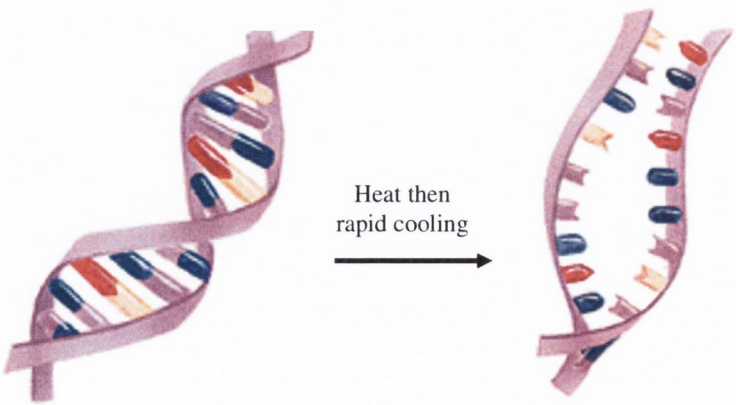

Figure 6.5 Representation of the denaturation of duplex DNA by heat followed by rapid cooling in ice. Reproduced from[21]

The results obtained for single stranded Herring samples are in good agreement with these observations. The absorbance of the peak at 258 nm increases from 0.92 to 1.54, representing an increase of 67 % (Figure 6.6). Proteins are found to absorb UV light at 280 nm, while a peak at 260 nm is for DNA. The A_{260} : A_{280} ratios of a DNA solution are used as indicators of protein or RNA concentrations. The ratio should be in the range of 1.8. Higher ratios are often due to RNA concentration; lower ratios indicate the presence of protein. For the Herring DNA above, the A_{260} : A_{280} ratio is found to be 1.75.

The concentration of the DNA solutions could be worked out from the absorption spectra, by taking the extinction coefficient to be 6600 $M^{-1}cm^{-1}$ and using the Lambert-Beer law.

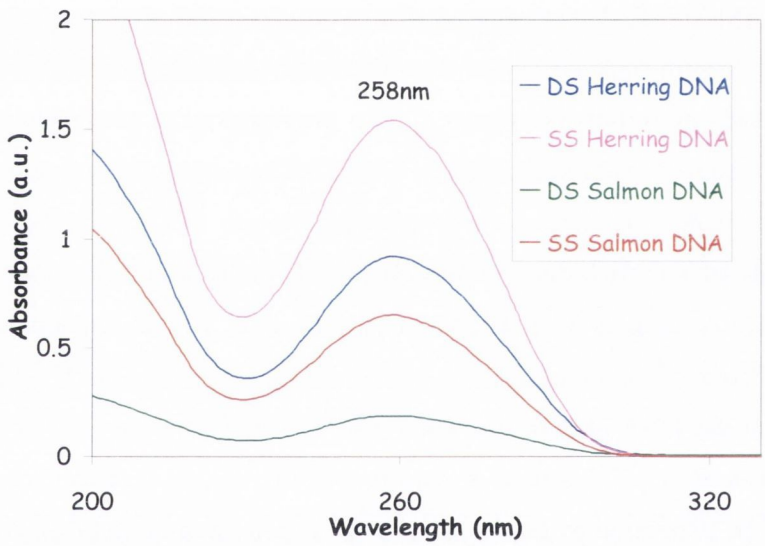

Figure 6.6 Absorption spectra of duplex and denatured DNA solutions, where DS and SS refer to double and single stranded DNA respectively

6.3. DNA –magnetite nanocomposites

6.3.1. Preparation of Herring and Salmon DNA nanocomposites

Samples of magnetite were prepared by reacting a mixture of ferrous and ferric chloride (2:1 molar ratio) with ammonia in a degassed water solution containing herring-sperm or salmon-sperm DNA, either duplex (double-stranded) or after denaturation (substantially single-stranded) at 100 °C. It was hoped that the DNA would act to stabilise the particles as they formed, leading to the formation of a stable aqueous suspension. The duplex and denatured Herring and Salmon samples

were labelled DH1, SH1, DS1 and SS1 respectively. Upon addition of ammonia solution, a black precipitate formed immediately. The suspension was left to stir for one hour before removing the any liquid by decantation. The particles were washed with Millipore water (5 × 20 mL), at which point the washings were neutral. The final three washes were found to be stable magnetic nanoparticle suspensions. The final wash was kept for NMRD and PCS studies. The black precipitate was dried under vacuum and analysed *via* IR, XRD and Magnetisation measurements.

6.3.2. Characterisation of DNA-magnetite nanocomposites

6.3.2.1. FTIR spectroscopy

FTIR spectra were recorded of the DNA-magnetite nanocomposites (Figure 6.7). All samples reveal stretches at 3433, 1647, 1220, 1081 and 592 cm^{-1}. These represent OH groups on the particle surface, associated water molecules with the surface, asymmetric and symmetric phosphate stretches and a Fe-O stretch respectively.

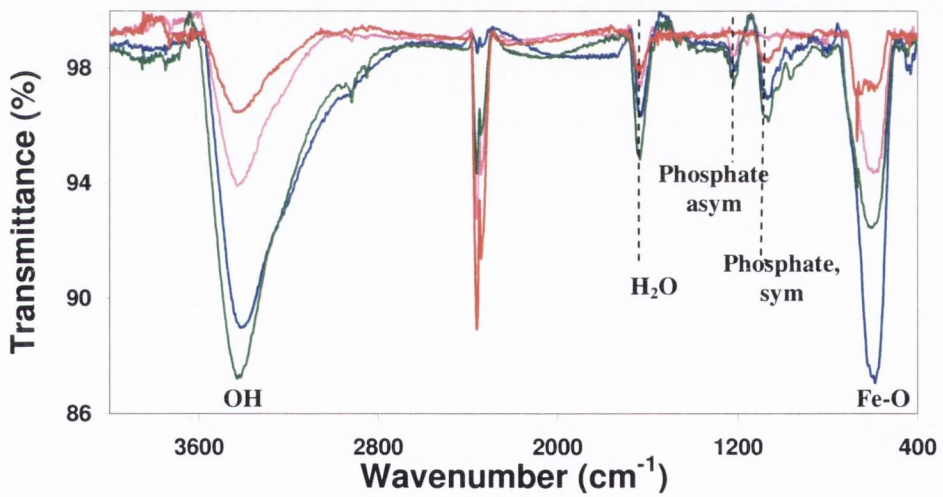

Figure 6.7 IR spectra of DH1 (blue) and SH1 (pink) Herring and DS1 (red) and SS1 (green) Salmon DNA-magnetite nanocomposites

6.3.2.2. Raman spectroscopy

Raman spectra were recorded for all samples (Figure 6.8) in order to confirm the formation of magnetite. The peak at 670 cm^{-1} characteristic for magnetite was observed for all samples.

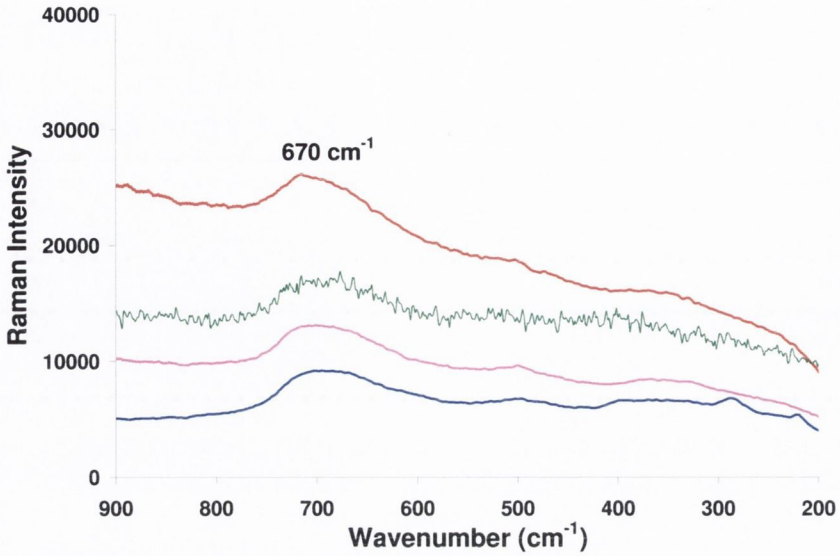

Figure 6.8 Raman spectra of Herring samples DH1 (blue) and SH1 (pink) and Salmon samples DS1 (red) and SS1 (green) DNA-magnetite nanocomposites

6.3.2.3. UV-vis spectroscopy

In order to establish that there is DNA present on the particle surface, absorbance spectra were recorded (Figure 6.9). For the salmon DNA samples, it is easier to see the DNA peak which occurs at 280 nm. For the Herring DNA samples, the peaks appear flatter, as the particles in suspension act to scatter the UV light. The denatured samples appear at a higher absorbance value than their duplex counterparts, which is to be expected (Figure 6.6).

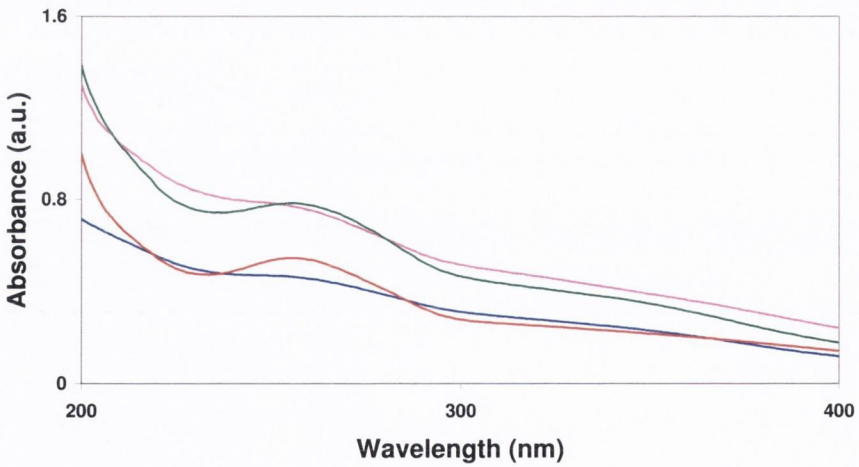

Figure 6.9 Absorption spectra of duplex (blue) and denatured (pink) Herring and duplex (red) and denatured (green) Salmon DNA-magnetite nanocomposites

6.3.2.4. Electron microscopy results

TEM microscopy was performed on the samples from the final washings of the DNA-magnetite nanocomposites. 10 μL of the suspension was placed on a copper formvar grid and dried either alone or in the presence of a 0.5 T magnetic field (Figure 6.10). The purpose of the magnetic field application was to check for any particular assemblies which the DNA might encourage. For the particles dried without the application of a magnetic field, there were no uniform assemblies formed for nanoparticles grown in the presence of duplex Herring DNA. For the most part, the particles are arranged in large clusters. Some randomly distributed chains with large aggregates present were seen for the particle grown with denatured Herring DNA. The samples dried in the 0.5 T magnetic field, however, were found to have large ribbon-like assemblies in the case of the duplex DNA and more chain- or wire-like assemblies for the denatured samples.

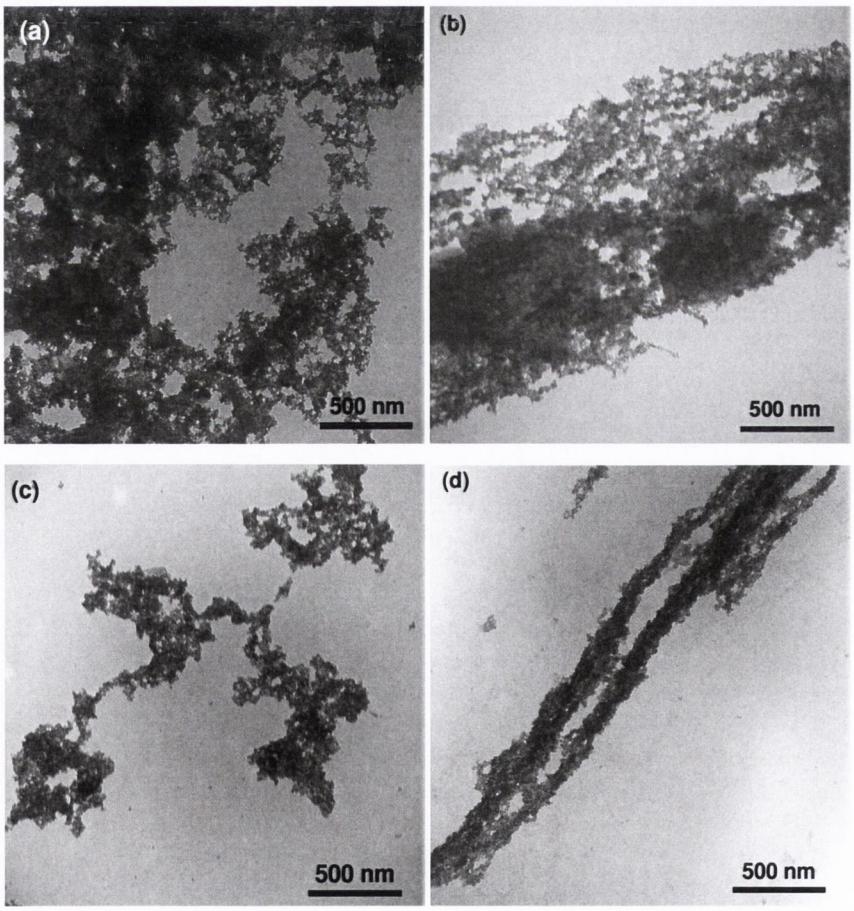

Figure 6.10 TEM images of DH1 (**a**) alone and (**b**) dried in 0.5 T magnetic field; SH1 (**c**) alone and (**d**) dried in 0.5 T magnetic field. The scale bar for all images is 500 nm.

Size distributions were calculated for all samples in order to determine if the particles are superparamagnetic (below 10 nm) (Figure 6.11).

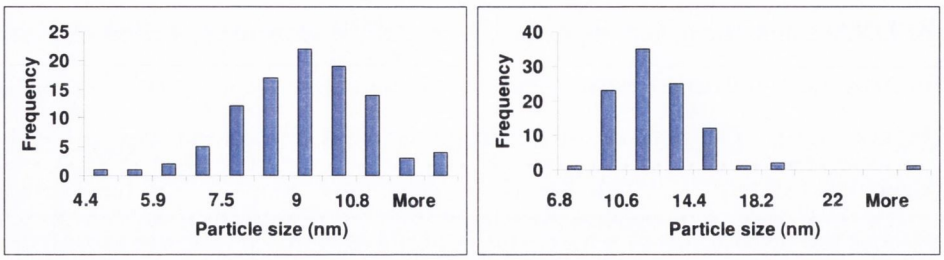

Figure 6.11 Histograms of the particle sizes for (a) SH1 (b) DH1 DNA-magnetite samples

It has been found that for the single stranded samples, the particle sizes were found to be 8.8 ± 1.6 nm while in the double stranded case the particle size was just at the superparamagnetic limit (10.5 ± 2.6 nm). The change in the particle size is a result of the DNA type used. For denatured DNA, the DNA strands have unwound to form single strands. This denaturing process makes the phosphate backbone more easily accessible for growing particles. The iron metal ions interacting with phosphate groups act as nucleation sites for the growth of the iron oxide nanoparticles and once the particles have formed, the DNA can then act as a stabiliser for the particles, wrapping the particles and inhibiting further growth. In contrast, the phosphate backbone in duplex DNA is wound in a helical fashion, making it harder in this case for the particles to bind to the phosphate groups.

The same experiments were carried out using Salmon DNA. Again these nanocomposites were found to arrange in a chain-like fashion (Figure 6.12).

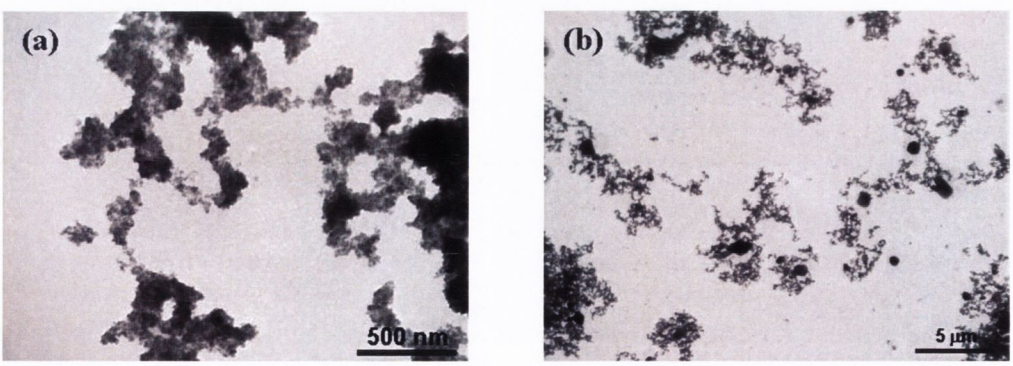

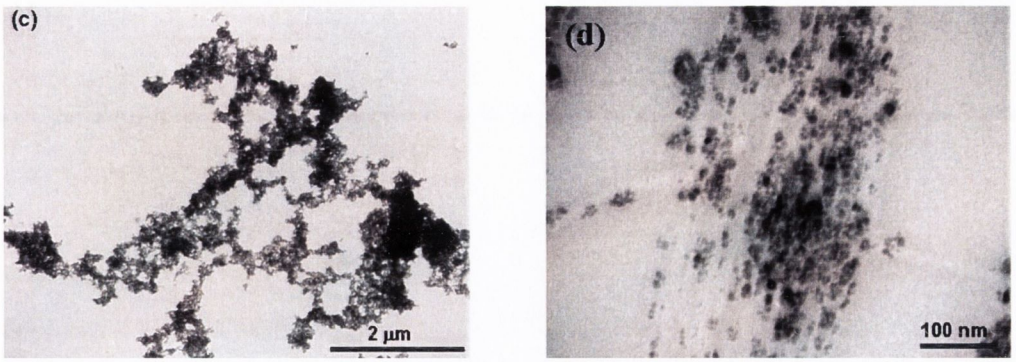

Figure 6.12 TEM images of (a), (b) DS1; (c) SS1 alone and (d) SS1 dried in 0.5 T magnetic field

In contrast to the single chains found for Herring DNA nanocomposites, this material tends to form clusters of strings, arranged in a rope-like structure. This is most likely to affect the nanoparticle water stability. In fact, the duplex Salmon DNA-magnetite samples did not produce a stable suspension in water. The average particle sizes for the duplex (DS1) and denatured (SS1) DNA samples are 13.4 ± 2 nm and 10.1 ± 1.6 nm respectively (Figure 6.13). Again, the denatured DNA-magnetite samples were found to form the larger particles.

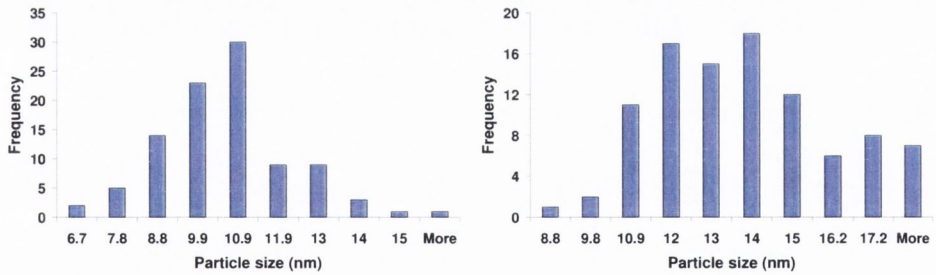

Figure 6.13 Histograms of the particle sizes for (a) SS1 (b) DS1 Salmon DNA-magnetite samples

The similar preparation of magnetite nanocomposites using single stranded Herring DNA gave uniform nanowires when aligned in the presence of an external magnetic field. To further investigate this, a series of experiments were carried out, increasing the amount of DNA stabiliser used each time. TEM analysis was performed to check for the presence of nanowires after application of a magnetic field. The images are shown in Figure 6.13, while the experimental setup is given in Table 6.1.

Table 6.1 Experimental setup for the investigation of nanowire formation with increasing denatured Herring DNA concentration

Sample	Iron volume	DNA mass	Nanowire length (μm)	Nanowire width (nm)
SHN1	10 mL	0.003 g	2.3 ± 1.3	188 ± 53
SHN2	10 mL	0.006 g	4.4 ± 3	160 ± 20
SHN3	10 mL	0.012 g	11.2 ± 6	142 ± 40
SHN4	10 mL	0.024 g	37 ± 16	513 ± 35

The samples were prepared by placing a 10 μL onto a copper formvar grid. One set of grids was allowed to dry naturally, while the others were placed in a perpendicular 0.5 T magnetic field and dried overnight. TEM images of all samples were recorded. (Figure 6.14).

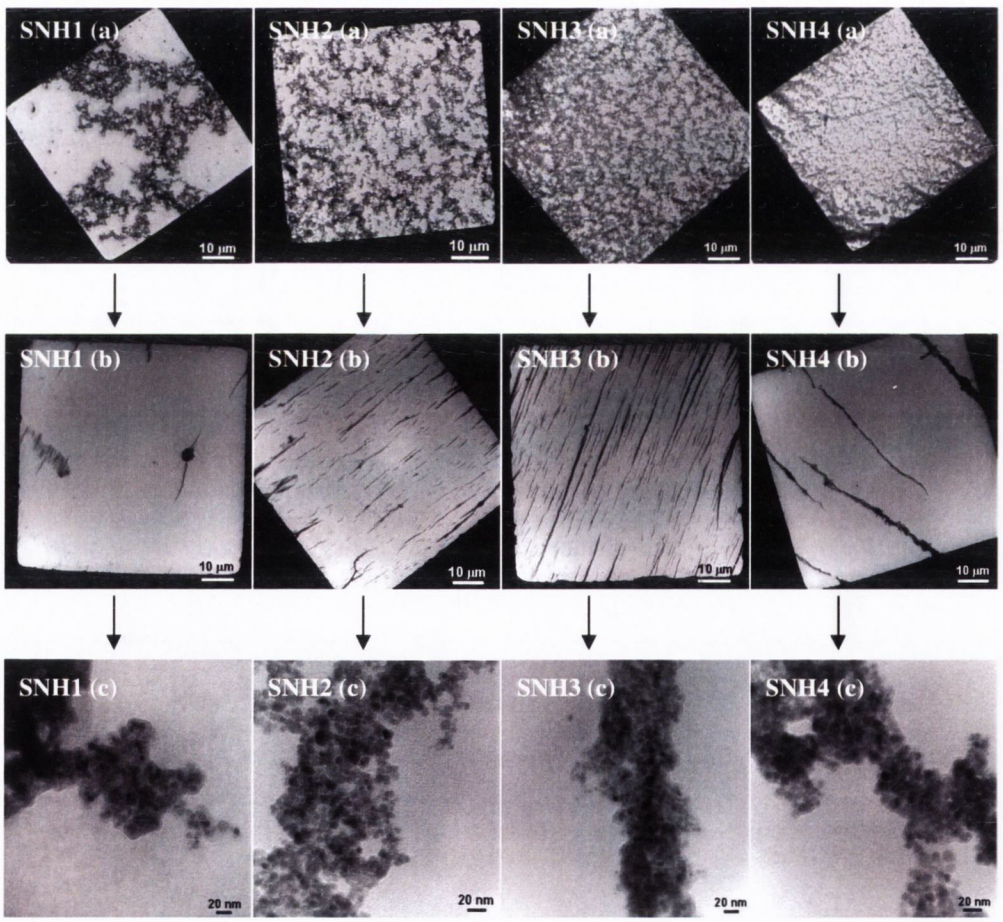

Figure 6.14 TEM images of (a) samples without a magnetic field; (b), (c) dried in the presence of a perpendicular magnetic field

In the absence of a magnetic field, the particles are found to form aggregates. Upon application of a magnetic field (0.5 T), there is the formation of nanowires. For the sample with the least amount of DNA (SHN1), there are relatively few wires formed and those which are tend to aggregate together. They are also quite short in comparison to other samples (2.3 ± 1.3 μm). As the DNA concentration increases, the wires formed get longer. Moving from sample SHN2 to SHN3, the nanowire length increases from 4.4 to 11.2 μm. Finally, for the most concentrated DNA sample (SHN4), the longest (37 μm) and thickest (513 nm) nanowires are formed. This may be explained as a crosslinking of DNA between individual nanowires.

It is important to mention that the first chain-like magnetic assemblies have been reported recently by Butter *et. al.*, who have employed the technique of cryo-TEM to observe chains of metallic iron particles.[22] By increasing the particle size, they have noted the transformation from separate particles to linear structures and branched chains.

6.3.2.5. Dynamic NMR measurements

To see how this magnetic field induced orientation might affect the spin-lattice relaxivity, we have employed the technique of NMRD on our prepared solutions (Figure 15). The spin lattice relaxivity, r_1, is related to the observed spin lattice relaxation time, T_1 as follows:

$$R_{1(obs)} = \frac{1}{T_{1(obs)}} = \frac{1}{T_{1(diam)}} + \frac{1}{T_{1(para)}} = \frac{1}{T_{1(diam)}} + r_1[Fe] \qquad (1)$$

where $T_{1(diam)}$ is the native relaxation time of the supporting fluid (water) and the concentration, which by convention is given in mM. Thus r_1 has units of $s^{-1}mM^{-1}$ and is independent of the concentration of the magnetic fluid.

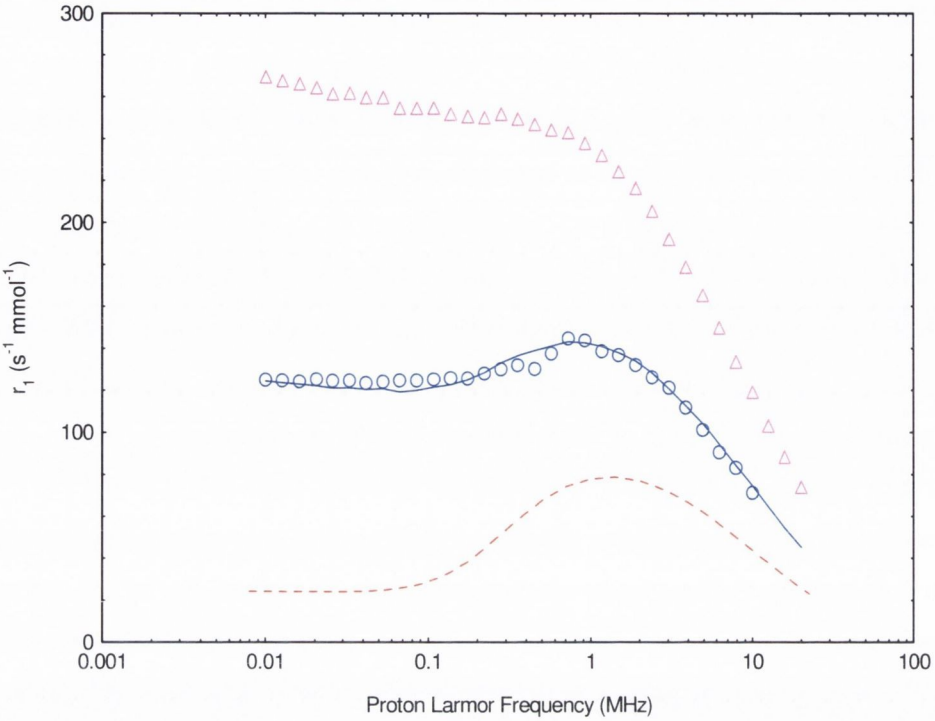

Figure 6.15: (△) NMRD relaxation curve recorded at a measuring frequency of 9.25 MHz for single-stranded herring DNA-magnetite nanocomposites; (○) double-stranded herring DNA-magnetite nanocomposites; (—) simulated curve for a two component system (see text below); (- -) simulated curve for a distribution of superparamagnetic particles of magnetite. All measurements were carried out at 23.5°C ± 1 °C

All reported NMRD curves were stable and repeatable. When single-stranded DNA was used in preparing the nanocomposite the NMRD curve (△) is characterised by an unusual dual power law dependence of T_1 on frequency. The NMRD response for these aggregates shows the relaxivity at low field is extraordinarily high. One possible explanation for this is that the surrounding water molecules are ordered on the surface of aggregates.

For complex particulate systems it has been established that the contributions to the overall relaxivity from magnetic material in different components of the suspension is often additive. In such cases the paramagnetic contribution to the relaxivity is given by equation 2:

$$r_1 = \sum_i x_i r_{1i} \qquad (2)$$

where x_i is the mole fraction of Fe in component i, with relaxivity r_{1i}. The solid curve in the figure is based on equation 2, assuming a two-phase system. The first phase is a superparamagnetic fraction with x_{spm}=0.59 and r_{1spm} taken from the simulated NMRD response of a fully dispersed polydisperse nanoparticle suspension with particle distribution consistent with the TEM results for this sample (dashed curve). The second phase is aggregated magnetite where x_{agg}=1-x_{spm}=0.41, and r_{1agg} is taken from the single-stranded nanocomposite (Δ). Thus there is only one free parameter in the fit; the SPM mole fraction. The good quality of this fit to the data, demonstrates that in the double-stranded nanocomposite (O) more than half the material is nanoparticulate while the residue is agglomerated, and that the relaxation due to the two populations is additive. These NMRD observations are consistent with the magnetic ordering results; the single stranded preparations show greater tendency to agglomerate in this case in the NMRD field, which is varied from 0 to 0.5T.

NMRD analysis was carried out on the single stranded Salmon DNA-magnetite samples to investigate if similar behaviour was observed as in the case of Herring DNA composites (Figure 6.16). However, a lower relaxivity was noted, with a decrease in suspension stability when compared to the Herring DNA samples.

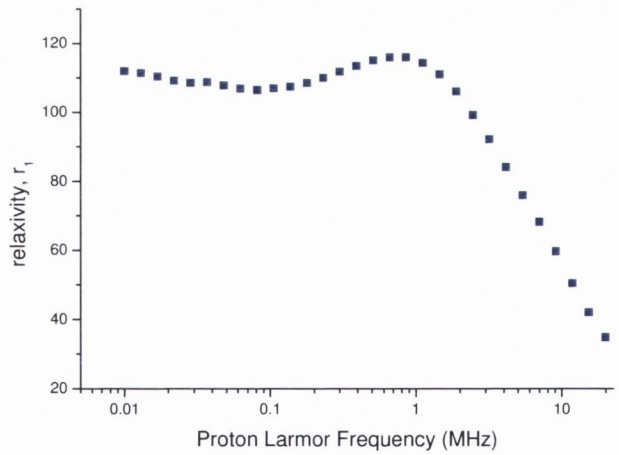

Figure 6.16 NMRD profile of denatured Salmon DNA-magnetite nanocomposite

This observed decrease in relaxivity may be caused by a clustering in the material, which is confirmed by TEM analysis. The clumping of particles also contributes to the reduction of suspension stability.

6.4. Investigation of intercalation of Herring and Salmon DNA-magnetite nanocomposites with Acridine orange

We expected that in magnetite-DNA nanocomposites described above, the base pairs of DNA molecules should be available for intercalation. In order to investigate this, the DNA-magnetite nanocomposites were reacted with aliquots of the known DNA intercalator acridine orange. Spectra of acridine orange in phosphate buffer were recorded. The absorbance spectrum reveals peaks at 493 nm, with a corresponding peak at 529 nm in the emission spectrum (Appendix 8). Preliminary intercalation studies were also carried out with both Salmon and Herring DNA. Firstly, the intercalation of double and single stranded Herring and Salmon DNA was investigated *via* titration analysis of DNA against the intercalator acridine orange. The absorption and emission data for duplex Herring and Salmon DNA are shown in Figures 6.17 and 6.18. All other titrations are given in Appendix 9.

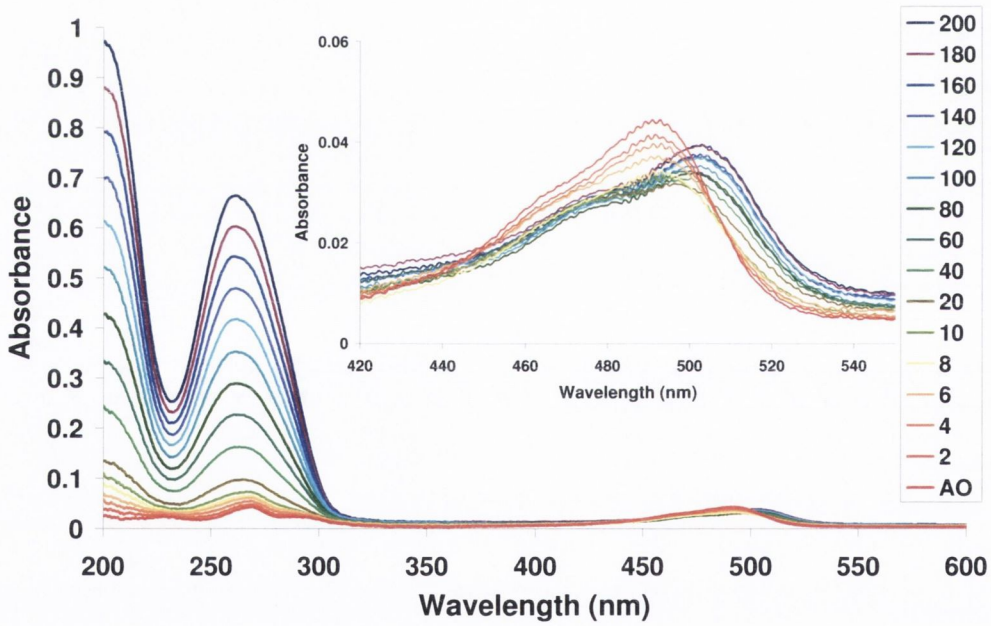

Figure 6.17: Absorption spectra showing the change observed when acridine dye only (9.2×10^{-7} M) is bound to double stranded Herring DNA (9.2×10^{-5} M). Inset shows changes in 493 nm band. The red curve is the original acridine orange solution and the legend shows the curves as 200 μL DNA solution is added.

Upon interaction with the double stranded Herring DNA, the absorbance peak for acridine orange is found to increase and shift from 493 to 503 nm. The intrinsic

binding constant has been determined by monitoring the absorbance at 493 nm after each addition of DNA and was found to be 2.9×10^5 M^{-1},[23] which is close to the values previously reported of 1.8×10^5 M^{-1}.[24] The absorption intercalation data, along with binding constants, for duplex Salmon and denatured Herring and Salmon are included in Appendix 9. Similar behaviour was observed in these samples when acridine orange is added.

The same experiment was analysed by fluorescence spectroscopy and the emission and corresponding excitation spectra for duplex Salmon DNA intercalating with acridine orange are shown in Figure 6.18. As DNA is added to the acridine orange solution, the fluorescence intensity is found to initially decrease (29 % decrease upon addition of 8 μL DNA). Upon further addition of DNA, the intensity value increases by 47 % (25 % compared to the original acridine orange spectrum). Similar behaviour is noted for denatured Herring (43 % decrease, followed by 62 % increase), denatured Salmon (33 % decrease, followed by 20 % increase) and duplex Herring (59 % decrease, followed by 67 % increase) DNA (Appendix 10).

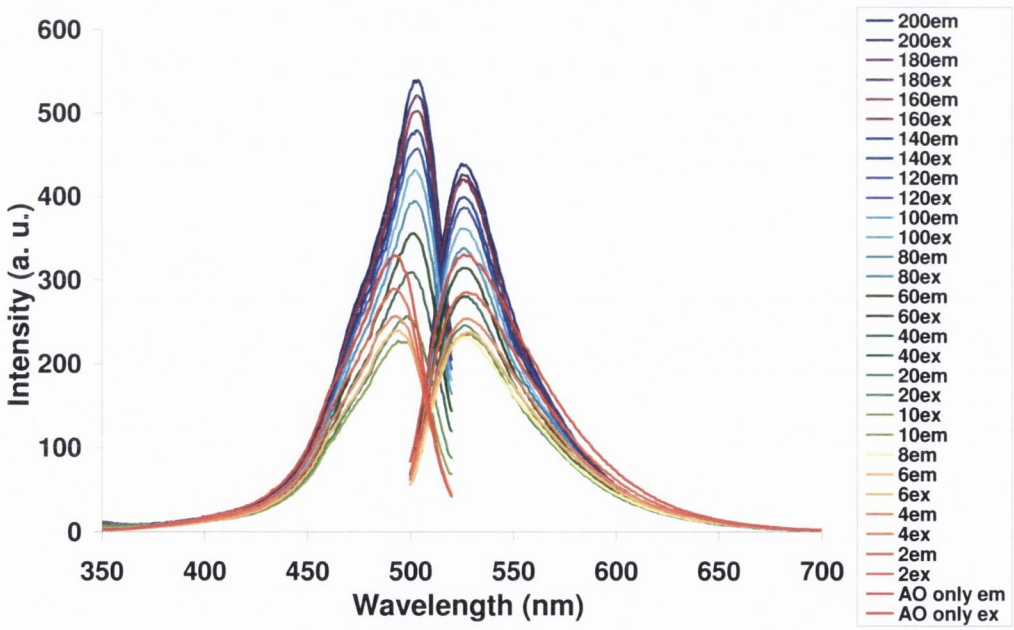

Figure 6.18 Fluorescence spectra of duplex Salmon DNA intercalated with acridine orange (λ_{em} = 493 nm, λ_{ex} = 527 nm). The intensity decreases initially upon addition of DNA and then is found to increase. The red curve is the original acridine orange spectrum (9.2×10^{-7} M) and the legend shows the curves as aliquots of DNA solution (9.2×10^{-5} M) are added (up to 200 μL).

When the acridine orange is allowed to react with the DNA-magnetite nanocomposites, the absorption and fluorescence spectra are monitored. The spectra for the Herring DNA samples are shown in Figure 6.19. For the DH1 sample, the emission intensity is found to increase by 19 %. An increase in fluorescence intensity is consistent with the intercalation of the acridine orange to the DNA. In contrast, the SH1 sample shows a decrease in the fluorescence intensity. This behaviour may be similar to the initial decrease noted for acridine orange intercalating with DNA, or could be due to quenching of the fluorescence by the magnetic nanoparticles. Because there is no double helix for the single stranded DNA, there is only an electrostatic interaction of the acridine orange with the DNA. Once magnetic nanoparticles are aligned along the single DNA strands, any acridine orange ionically associated to the same DNA strand may experience the quenching effects of the particles. This may be the reason for the observed decrease in the fluorescence intensity of the acridine orange denatured DNA-magnetite nanocomposites. For the duplex DNA samples, the helical conformation of the DNA makes it more difficult for the particles to form in the first instance. Once they have formed, they are only associated with the phosphate backbone, away from the base pairs. In this case, there is not so much of a risk of quenching by the particles.

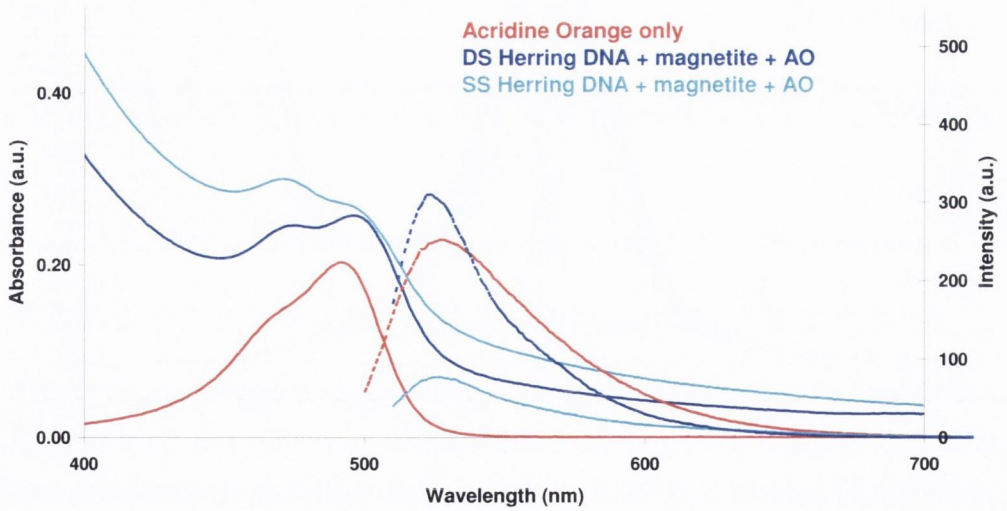

Figure 6.19 Absorption (solid lines) and emission (dotted lines) spectra of acridine orange (red), double stranded DH1 (blue) and SH1 (light blue), where λ_{em} = 493 nm and λ_{ex} = 527 nm

Similar results were obtained for the DS1 and SS1 samples, with an increase in fluorescence intensity noted for the double stranded samples and a decrease observed in the single stranded samples (Figure 6.20).

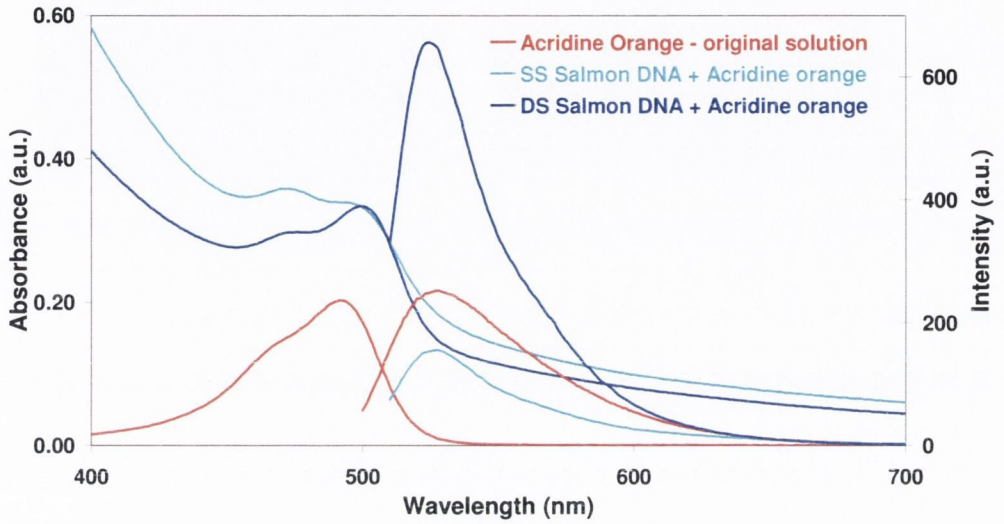

Figure 6.20 Absorption (solid lines) and emission (dotted lines) spectra of acridine orange (red), DS1 (blue) and SS1 (light blue), where λ_{em} = 493 nm and λ_{ex} = 527 nm

Confocal microscopy images were taken of the duplex Herring (DH1) and Salmon (DS1) DNA nanocomposites (Figure 6.21). The presence of clustered fluorescent material was observed in both samples. The lifetimes found for the acridine orange DH1 and SS1 intercalated nanocomposites were 4.7 ns and 4.9 ns respectively. Compared to acridine orange alone, which has a lifetime of 9.7 ns, these are relatively shorter. This reduction in lifetime is most likely caused by the interaction with the magnetic nanoparticles acridine orange resulting in partial quenching the luminescence.

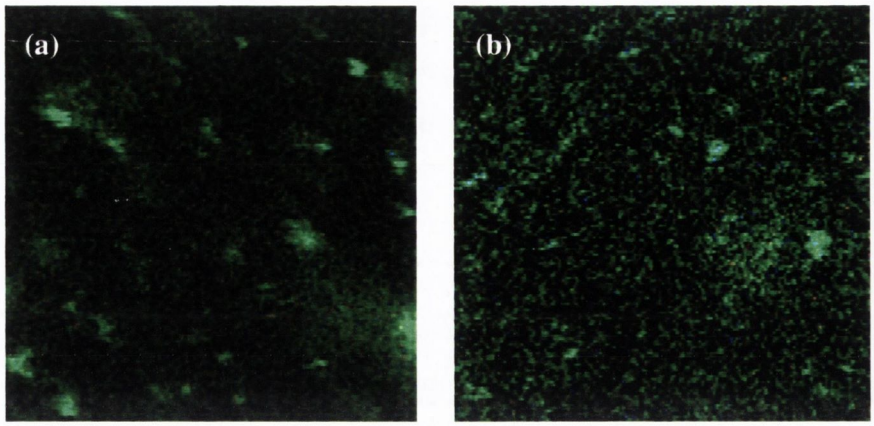

Figure 6.21 Confocal images of (a) DS Herring and (b) SS Salmon magnetic nanocomposites treated with acridine orange

6.5. Conclusions

Thus long-range ordered chains of predominantly single stranded herring DNA-magnetite nanocomposites have been prepared. TEM analysis is consistent with magnetite nanoparticles bound to the DNA phosphate groups, acting as a cross linker between strands, thereby increasing the chain length to micron size. In aqueous suspension these materials undergo aggregation, the suspensions exhibit an unprecedented dual power law dependence of the water T_1 on frequency with very high relaxivity at low field. This suggests that such materials might be potentially useful for low field MRI. [21] Studies of the interaction between DNA-magnetite nanocomposites and acridine orange dye have shown intercalation of acridine and enhancement of the luminescence in the case of double stranded DNA samples. In contrast, denatured (single stranded) DNA magnetite nanocomposites have shown only quenching of acridine luminescence and no intercalation.

Future work will include a study of these particles bound to synthetic DNA of define sequence and varying length and also an investigation into the stability of this composite in cells, so us to access the role of enzymatic degradation and cellular uptake.

References

[1] H. Yan, N. C. Seeman, *Journal of Supramolecular Chemistry* **2001**, *1*, 229.

[2] N. C. Seeman, *Nature* **2003**, *421*, 427.

[3] C. A. Mirkin, R. L. Letsinger, R. C. Mucic, J. J. Storhoff, *Nature* **1996**, *382*, 607.

[4] A. P. Alivisatos, K. P. Johnsson, X. G. Peng, T. E. Wilson, C. J. Loweth, M. P. Bruchez, P. G. Schultz, *Nature* **1996**, *382*, 609.

[5] M. G. Warner, J. E. Hutchison, *Nature Materials* **2003**, *2*, 272.

[6] H. Y. Li, S. H. Park, J. H. Reif, T. H. Labean, H. Yan, *Journal of the American Chemical Society* **2004**, *126*, 418.

[7] J. M. Nam, S. J. Park, C. A. Mirkin, *Journal of the American Chemical Society* **2002**, *124*, 3820.

[8] S. Mornet, A. Vekris, J. Bonnet, E. Duguet, F. Grasset, J. H. Choy, J. Portier, *Materials Letters* **2000**, *42*, 183.

[9] L. Josephson, J. M. Perez, R. Weissleder, *Angewandte Chemie-International Edition* **2001**, *40*, 3204.

[10] J. M. Perez, T. O'Loughin, F. J. Simeone, R. Weissleder, L. Josephson, *Journal of the American Chemical Society* **2002**, *124*, 2856.

[11] C. F. Monson, A. T. Woolley, *Nano Letters* **2003**, *3*, 359.

[12] J. Richter, R. Seidel, R. Kirsch, M. Mertig, W. Pompe, J. Plaschke, H. K. Schackert, *Advanced Materials* **2000**, *12*, 507.

[13] H. A. Becerril, R. M. Stoltenberg, D. R. Wheeler, R. C. Davis, J. N. Harb, A. T. Woolley, *Journal of the American Chemical Society* **2005**, *127*, 2828.

[14] R. M. Acheson, A. Weissberger, E. C. Taylor, *Acridines. The Chemistry of Heterocyclic Compounds*, Interscience Publishers Inc, New York, **1956**.

[15] A. R. Peacocke, J. N. H. Skerrett, *Transactions of the Faraday Society* **1956**, *52*, 261.

[16] S. Georghiou, *Photochemistry and Photobiology* **1977**, *26*, 59.

[17] L. S. Lerman, *Journal of Cellular and Comparative Physiology* **1964**, *64*, 1.

[18] G. Lober, *Photochemistry and Photobiology* **1968**, *8*, 23.

[19] R. W. Armstrong, U. P. Strauss, T. Kurucsev, *Journal of the American Chemical Society* **1970**, *92*, 3174.

[20] Frederic.E, C. Houssier, *Biopolymers* **1972**, *11*, 2281.

[21] J. H. Cho, J. F. Quinn, F. Caruso, *Journal of the American Chemical Society* **2004**, *126*, 2270.

[22] K. Butter, P. H. H. Bomans, P. M. Frederik, G. J. Vroege, A. P. Philipse, *Nature Materials* **2003**, *2*, 88.

[23] C. V. Kumar, E. H. A. Punzalan, W. B. Tan, *Tetrahedron* **2000**, *56*, 7027.

[24] G. Lober, G. Achtert, *Biopolymers* **1969**, *8*, 595.

Chapter 7: Polyelectrolyte stabilised magnetite and cobalt ferrite nanoparticles

7.1. Introduction

Biological polyelectrolytes molecules such as DNA have been a popular choice of template for the preparation of self assembled nanostructured materials in recent years. It has been demonstrated above that denatured (mostly single stranded) DNA can serve as an excellent stabiliser for magnetite nanoparticles (Chapter 6). The next logical step forward was to employ commercially available polyelectrolytes in place of DNA using the same approach. It was envisaged that these charged macromolecules would again provide sites for particle growth and act as templates for nanowire formation. Reasons for this include the fact that polyelectrolytes provide a 1-D structure with a high length to width aspect ratio along which nanoparticles may be aligned. It is important that the stabilising reagent also provides an opportunity to tune both the magnetic properties of the suspension so optimising its relaxivity, and to include chemical recognition sites which can be used to target the nanoparticle. Other properties which must be considered include the chemistry and charge of the chosen polyelectrolyte, which may play a critical role in the formation of nanoassemblies.

Surface modification of nanoparticles by polyelectrolytes has been extensively reported by Caruso[1-7] and Mohwald[8-11] whose groups have pioneered the layer-by-layer approach, whereby sequential adsorption of anionic and cationic polyelectrolytes onto oppositely charged surfaces produces coated particles by electrostatic attractions. The LBL technique has been used to produce polyelectrolyte coated gold nanorods which can then be selectively immobilised onto charged surfaces.[12] A similar method has been used to obtain magnetic-fluorescent nanocomposites comprising of magnetite nanoparticles which have been exposed to several cycles of the layering process before negatively charged CdTe quantum dots were finally added.[13]

Several researchers have found strong indications that the magnetic properties of the suspensions can be controlled by using synthetic polyelectrolytes which give finer control, due to their well-defined electrostatic charge and polymer length. Berret *et. al.*[14] have reported the use of a block copolymer as a stabiliser for magnetic nanoparticles, where one block is of opposite charge to the particles and the second

block is neutral. This type of block copolymer only self-assembles when there is an oppositely charged species present. When citrate-coated maghemite nanoparticles are mixed with the block copolymer, a stable suspension is formed. Two forms of the block copolymer are investigated, both with different charged monomer molecular weights. PCS measurements reveal the particles form aggregates with a size between 60 and 80 nm, while cryo-TEM shows a primary particle size of 6.3 nm. The relaxivity (r_1) at 20 MHz is reported as 24 and 17.5 s^{-1} mM^{-1} for the lower and higher molecular weight polymers respectively. The r_2 values are higher, at 74 and 162 s^{-1} mM^{-1} respectively, which could make these magnetic fluids potential T_2 contrast agents.

Polyelectrolytes have also been used to produce linear assemblies of magnetite nanoparticles. Sheparovych and co-workers[15] have used poly(2-vinyl *N*-methylpyridinium iodide) to align citrate-coated magnetite nanoparticles (Figure 7.1).

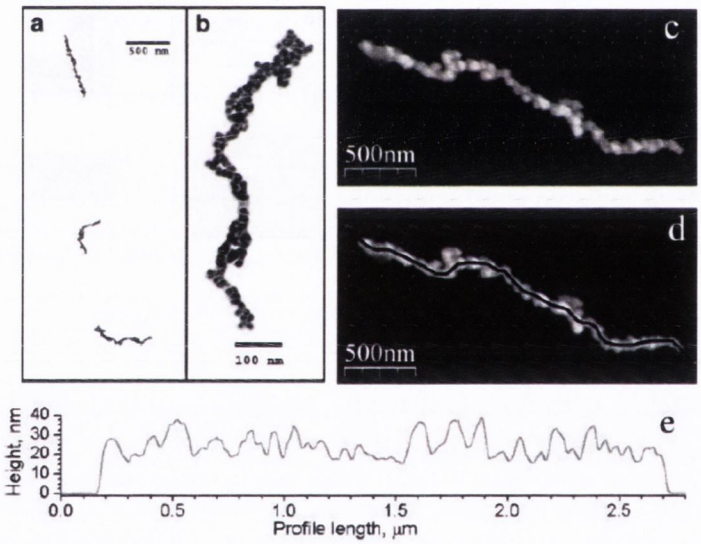

Figure 7.1 (a), (b) TEM images and **(c), (d)** AFM images of magnetic nanowires stabilised by poly(2-vinyl *N*-methylpyridinium iodide); **(e)** shows a cross section of a single nanowire

Lithographic techniques are traditionally used to produce assemblies of magnetic nanoparticles. Field directed assemblies could provide an inexpensive technique for producing the same effects with magnetic nanoparticles and nanowires.[16, 17] Sahoo *et. al.*[18] have found a correlation between finer structures and applied magnetic field strengths. Magnetic nanoparticles, prepared by

coprecipitation, were coated with oleic acid, drop-cast onto an GaAs wafer and dried in the presence of external magnetic fields of strengths 0.8, 6, 11, and 17 T. AFM measurements reveal irregularly shaped strands are formed at 0.8 T, while at 17 T smaller clusters are found (Figure 7.2). There are many effects at play here, including the coupling of each particles dipole moment to the applied field, magnetic dipole-dipole interactions and van der Waals interactions. The nanoparticles within each cluster will tend to align with the applied field. But their orientation will be influenced by dipole-dipole interactions with neighbouring particles. The overall effect is that the particles will tend to orient in a head-to-tail manner with their easy axes aligned with the magnetic field and with adjacent particles spacially staggered to minimise the local magnetostatic energy.

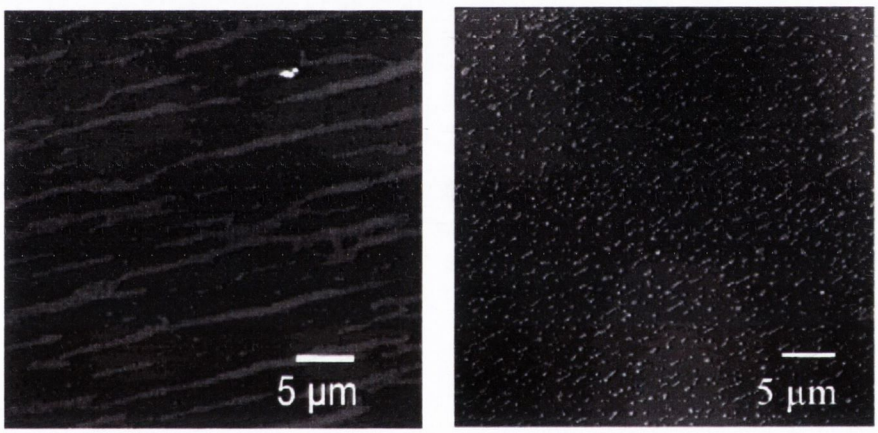

Figure 7.2 AFM images of magnetic nanoparticles aligned with a **(a)** 0.8 T and **(b)** 17 T external magnetic field[18]

Cheng *et. al.*[19] have studied the magnetic field assembly of Co nanoparticles with a 0.05 T magnetic field. The assemblies have been prepared in five stages. After sonication (stage I), linear chains are formed by the application of an external magnetic field (stage II). After the removal of the field, the chains aggregate and fall to the bottom of the reaction vessel (stage III). Upon agitation, the chains fold into coiled 3-D structures (stage IV) before forming closed loops (Stage V). The cyclable process is found to be repeatable. T. Alan Hatton and coworkers[20, 21] have synthesised polyelectrolyte adsorbed polystyrene beads coated with maghemite nanoparticles. The beads were linked to a polyelectrolyte patterned glass slide *via* an EDC coupling reaction between the carboxylated beads (the final polyelectrolyte coating is polyacrylic acid) and the amine terminated glass surface. Chain formation

was achieved by the addition of a cross-linker to form amide bonds between the beads. By applying an external magnetic field, the covalently linked beads formed chains. Variations of the applied field caused the chains to adopt different configurations, including hairpin and S-shaped loops.

The main aim of this part of our project was to develop a new family of magnetic fluids based on water soluble iron oxide or cobalt ferrite-polyelectrolyte nanocomposites and to demonstrate their utility for clinical MRI applications. We plan to use commercially available polyelectrolytes *in situ* for the preparation of magnetic nanoparticles by coprecipitation technique. In this case, polyelectrolytes are expected to serve both as nanoparticle stabilisers and chemical linkers for magnetic nanowires assembly. For this study, the negatively charged polyelectrolyte, polysodium-4-styrene sulfonate (PSS) (Figure 7.3), was used.

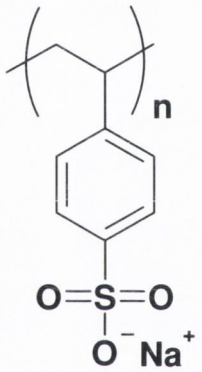

Figure 7.3 Structure of polyelectrolyte, polysodium-4-styrene sulfonate (PSS)

Thus the technical objectives of this part of the project are:

(i) To prepare new polyelectrolyte stabilised magnetic fluids.

(ii) To characterise and optimise the fluid using NMR methods (NMRD profiles for T_1 measurement).

(iii) To investigate new nanocomposites by transmission electron microscopy (TEM), Raman and FTIR spectroscopy and XRD patterns.

7.2. Initial feasibility studies

In order to evaluate the potential of PSS as a stabiliser for magnetite nanoparticles, two initial experiments were carried out, with varying PSS concentration (Table 7.1). The polyelectrolyte was dissolved in Millipore water and added to the iron solution in the desired concentrations before precipitation with ammonia solution. The final

washings of the particles were stable suspensions and were characterised by NMRD analysis to determine the suspensions relaxivity and, hence, contrast agent efficiency. The nanocomposites have also been studied by TEM.

Table 7.1: Initial PSS stabiliser experiments

Sample	Total iron conc (M)	PSS conc (M)
PE1	0.030	4.28×10^{-6}
PE2	0.030	7.57×10^{-5}

7.2.1. TEM analysis

TEM images were recorded of the samples (Figure 7.4) prepared with and without external magnetic field. It was found that both PE1 and PE2 form aggregates without magnetic treatment. However, upon drying in the presence of an external perpendicular magnetic field (0.5 T), networks of strings or "nanowires" were observed. The average particle size was found by measuring 100 particles of each sample. For PE1, the average size was 11.3 ± 1.6 nm and for PE2, 10.3 ± 1.8 nm.

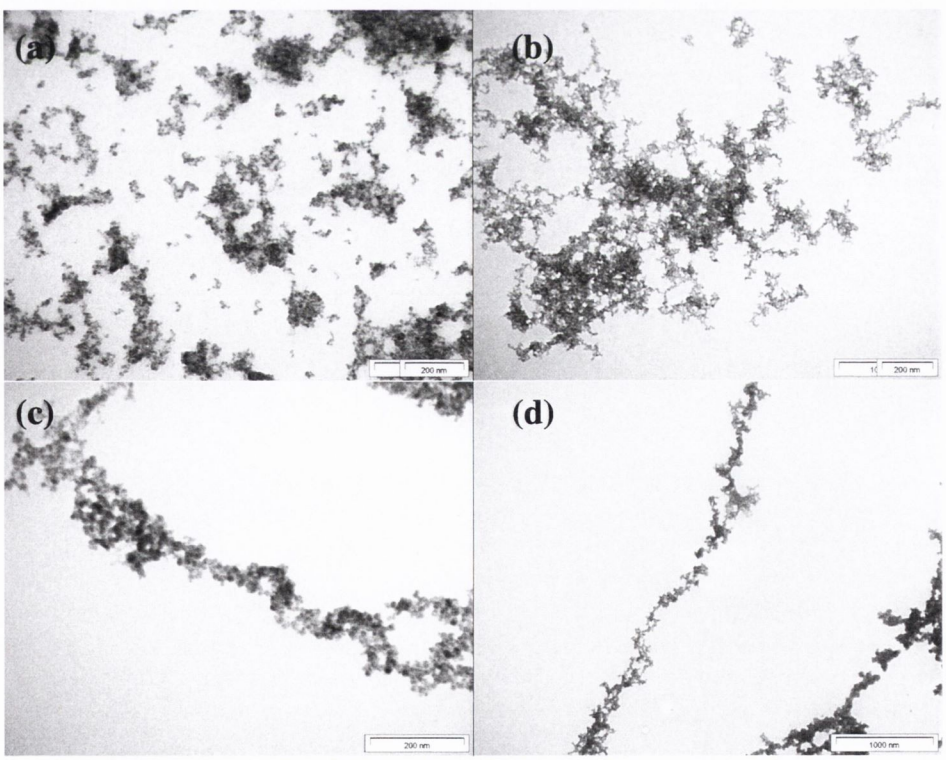

Figure 7.4 TEM images of **(a)** PE1 and **(b)** PE2; **(c)** PE1 and **(d)** PE2 dried in a 0.5 T external magnetic field

7.2.2. NMRD and PCS analysis

The final washings of PE1 and PE2 were analysed by NMRD to determine the relaxities of the magnetic fluids (Figure 7.5). It was found that PE1 had a higher relaxivity at low field compared to PE2, whose inversion point occurred at higher field. From the profiles obtained and in comparison with the current literature, it may be concluded that PE2 contains more superparamagnetic material than the PE1 sample. This is to be expected. The polyelectrolyte is added to the iron solution prior to particle formation. The particles are presumably formed along the negatively charged PSS chain. With experiments where there is a higher concentration of PSS, it is likely that the particles will be stabilised by the polyelectrolyte after nucleation. If there is a lower concentration of PSS initially, the particles should aggregate at the nucleation sites. PCS data agrees with this supposition, as the cluster size for PE1 is 41 nm larger than for PE2 (Table 7.2).

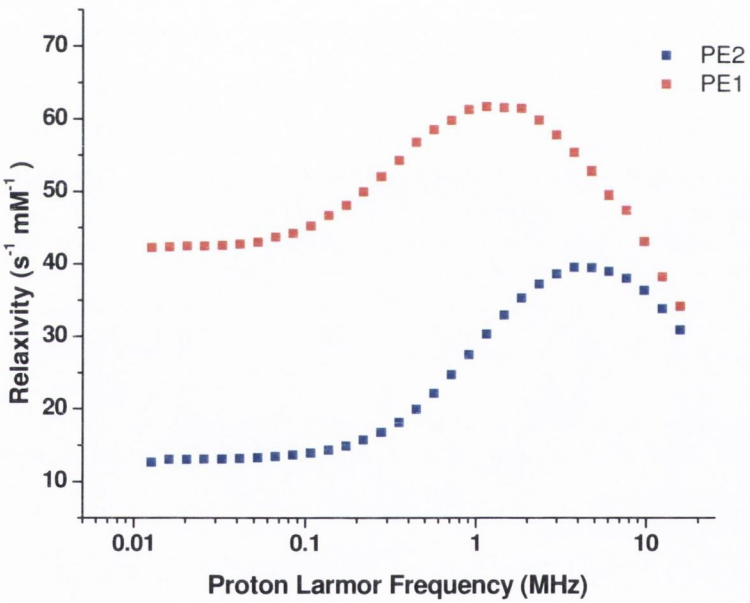

Figure 7.5 NMRD profiles of samples PE1 and PE2

Table 7.2: PCS results for PE1 and PE2

Sample	Z-average	PDI
PE1	216	0.219
PE2	175	0.203

Because the NMRD profiles for the two samples were markedly different, it was concluded that a systematic study would be beneficial to explore the variation of the profiles with PSS and total iron concentration.

7.3. Experimental design for synthesis and optimisation of polyelectrolyte stabilised nanoparticles

To develop and optimise synthesis of PSS-magnetite nanocomposites, we have performed a 2^2 factorial design experiment. The two factors to be varied at low and high levels are total iron and polyelectrolyte concentration. By systematically varying these two experimental conditions, it was hoped to study the variation in magnetic fluid relaxivity. The first design was set up as in Table 7.3. The factorial design is also graphically represented in Figure 7.6.

Table 7.3: Initial 2^2 study for polyelectrolyte stabilised particles

Sample	Total Fe conc (M)	PSS conc (M)	Fe/PSS ratio
R	0.020	1.9×10^{-5}	1053
S	0.030	1.43×10^{-5}	2098
T	0.026	1.22×10^{-5}	2131
U	0.030	7.14×10^{-6}	4260
V	0.006	1.29×10^{-5}	465
W	0.006	1.29×10^{-6}	4651
X	0.012	5.71×10^{-6}	2101
Y	0.020	9.52×10^{-6}	2100
Z	0.020	9.52×10^{-7}	21008

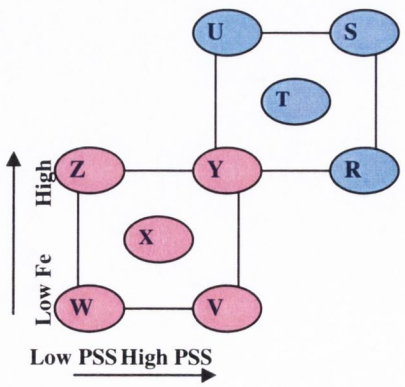

Figure 7.6 Graphical representation of 2^2 factorial design.

The experiments were carried out in random order at room temperature. All preparations were performed under argon to prevent any Fe^{2+} oxidation. Briefly, a known concentration of polyelectrolyte was added to a predetermined iron concentration under argon. To precipitate the magnetic nanoparticles, 0.88 ammonia solution (2 mL) was added with constant stirring. The suspension was stirred for 30 minutes and then allowed to settle. The magnetite nanoparticles were washed to neutral with Millipore water (18 MΩ.cm) (5 × 20 mL) and the final washings kept for TEM and NMRD analysis. The black precipitate was dried under vacuum and characterised via IR and Raman spectroscopy, and XRD analysis.

7.3.1. Characterisation of PSS-magnetite composites

7.3.1.1. Electron microscopy analysis

Transmission electron microscopy was carried out on the samples to determine the primary particle size (Figure 7.7). 10 μL of sample was dropped onto a formvar coated copper grid and dried overnight. In most images, a core-shell structure is observable. This is presumably made up of polyelectrolyte coating the nanoparticle surface. The average particle sizes, taken from 100 particles, are given in the table below.

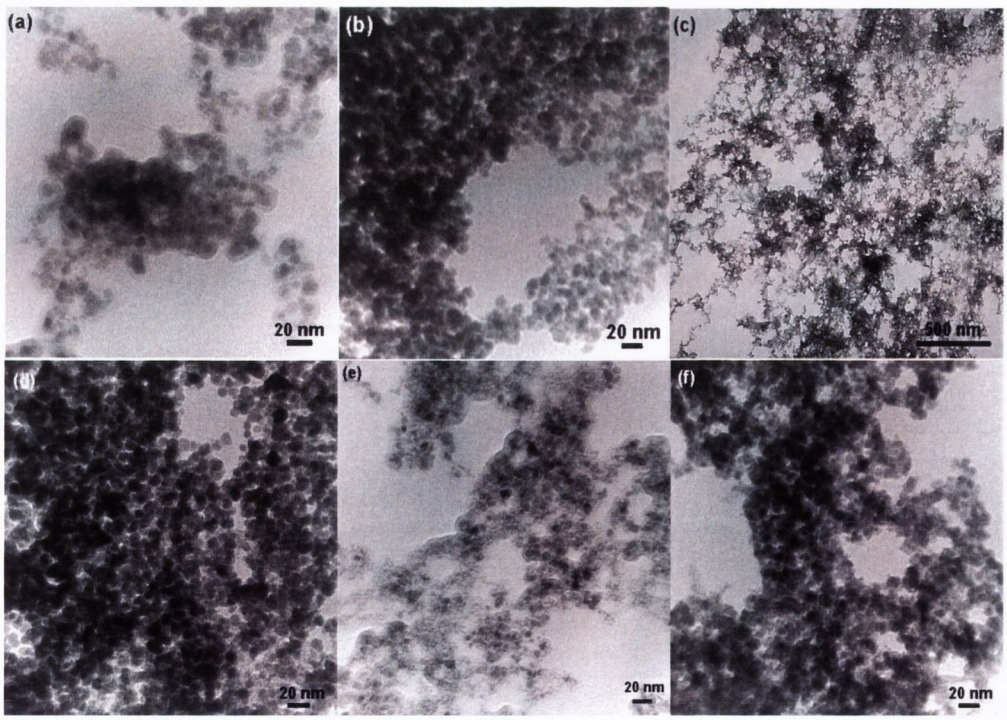

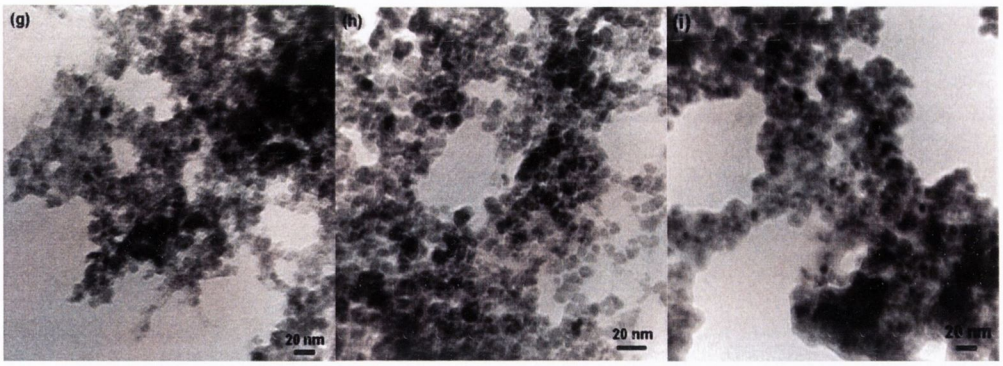

Figure 7.7 TEM images of samples **(a)** R, **(b)** S, **(c)** T, **(d)** U, **(e)** V, **(f)** W, **(g)** X, **(h)** Y and **(i)** Z

In order to check the effect of an external magnetic field on these samples, TEM images were taken of the magnetic fluids subjected to a 0.5 T perpendicular magnetic field (Figure 7.8). In each case, 10μL of the sample was deposited on a copper formvar grid, which was then placed in the centre of a 0.5 T perpendicular magnetic field.

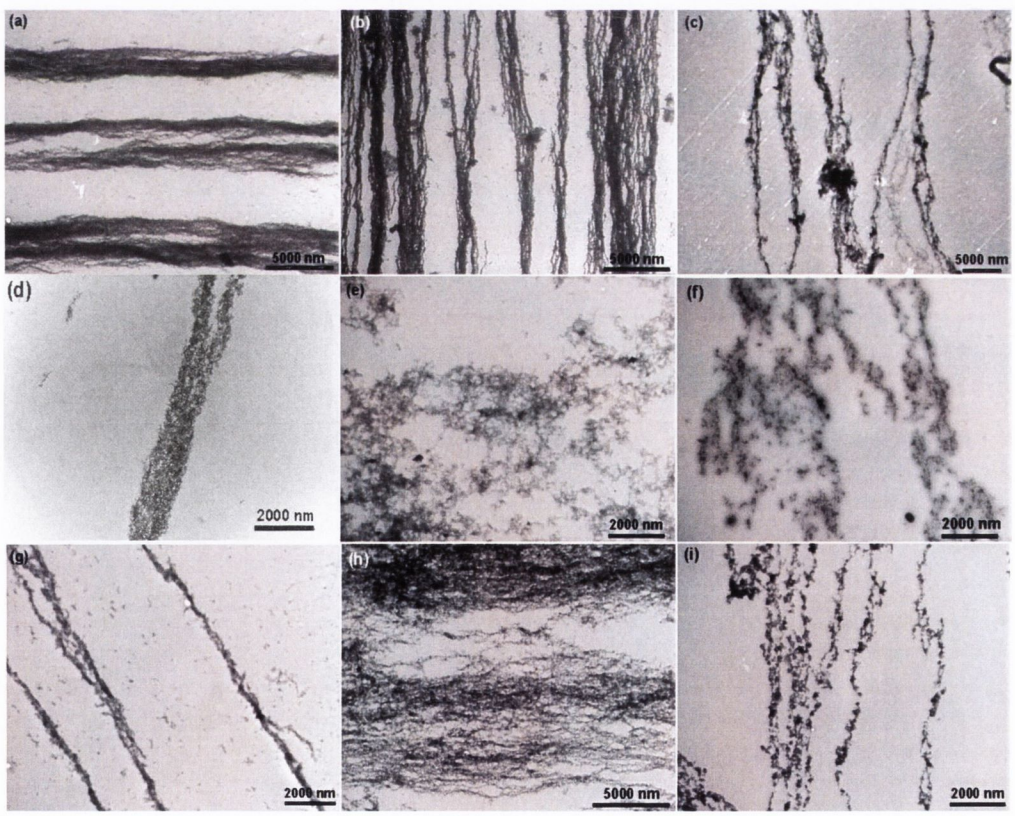

Figure 7.8 TEM images taken of sample **(a)** R, **(b)** S, **(c)** T, **(d)** U, **(e)** V, **(f)** W, **(g)** X, **(h)** Y and **(i)** Z, dried in perpendicular magnetic field (0.5 T)

It was found that, upon drying in the presence of the field, some of these samples formed ordered long-range nanowires. The length of these nanowires was only limited by the TEM grid size (~10 μm), while the width varied from sample to sample. In the case of samples V and W, there were no distinguishable wires formed when in the presence of a magnetic field. For samples R, S, T, U, X and Z, there is a clear formation of nanowires. In sample Y, the formation of high density nanowires was observed, formed by a cross-linking of smaller nanowires. TEM images were also taken of samples dried in a parallel magnetic field, but no nanowire formation was noted.

When compared to the Fe/PSS ratios (Table 7.3), it is found that the most uniform nanowires are formed in samples R, S and T, when the average ratio is 1750. However, the constituent concentrations alone also determine the wire formation. For the lowest PSS concentration (X, Y and Z), the thinnest nanowires are formed, with crosslinking occurring in sample Y. If the iron concentration is too low, then there is no observation of nanowires, as is the case in samples V and W. It is clear from this initial study that, while maintaining the iron and PSS concentrations as appreciable levels, a lower ratio of Fe/PSS will favour nanowire formation.

7.3.1.2. NMRD analysis

In order to investigate the magnetic properties of the dispersions from which the nanowires were formed, and to test their MRI potential, nuclear magnetic resonance dispersion (NMRD) and photon correlation spectroscopy (PCS) studies were undertaken.

For samples with the lowest iron concentration, there were no stable suspensions formed. However, in the cases of samples R, S, T, U and Y, stable suspensions were formed and their relaxivities were calculated from NMRD experiments (Figure 7.9). It is important to note that these samples also formed the most ordered nanowires under external magnetic field according to TEM results. In the case of suspensions of superparamagnetic nanoparticles, the relaxation rate enhancement is usually expressed as a concentration independent relaxivity, r_1, which has units s^{-1} mM^{-1} (of Fe). The r_1 values are critical as they measure the contrast efficacy of the suspension for T_1-weighted imaging applications.

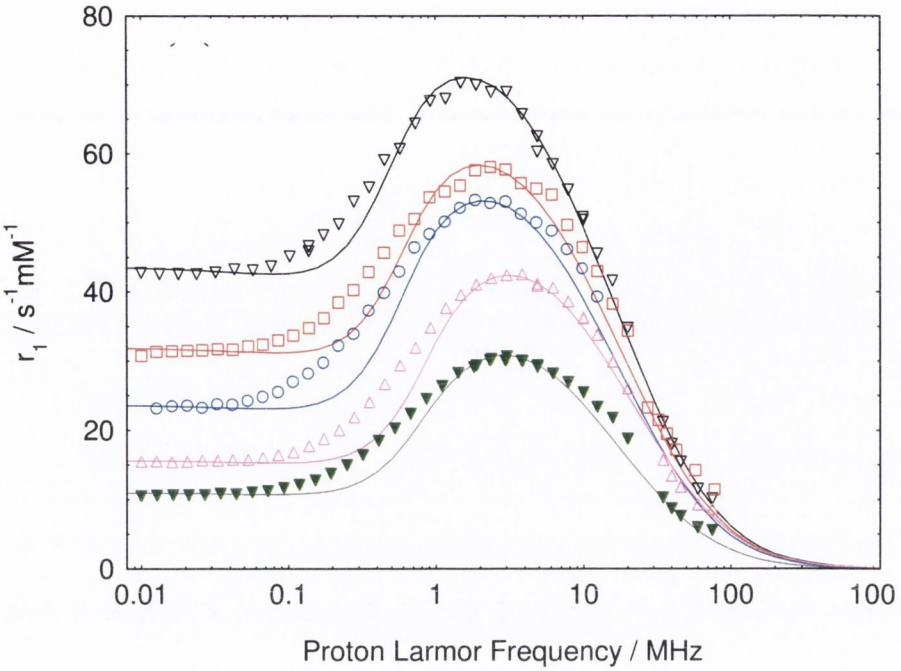

Figure 7.9 NMRD relaxation data for sample R (□), sample S (○), sample T (▼), sample U (▽) and sample Y (△). The solid curves are the fits to a monodisperse superparamagnetic model

The first observations are that the relaxivity values vary significantly from sample to sample. In all cases the relaxation enhancement is very significant and the profiles exhibit a r_1 maximum in the range of 1-3MHz. This demonstrates that the suspensions are predominantly superparamagnetic. PCS data confirms that the primary particles are aggregated into clusters of equivalent spherical size, about an order of magnitude greater than the primary particles. The cluster size distributions were all unimodal and the polydispersity indices were all relatively low. The NMRD data conforms acceptably to the theory developed by Muller and coworkers for relaxation by superparamagnetic nanoparticles. The theory is strictly applicable to suspensions of monodisperse, sub-20 nm, particles.

The highest relaxivities are found for samples U, R and S which formed the most uniform nanowires. The lowest relaxivity is found for the crosslinked sample Y. The NMRD results, along with the TEM data, reveal that for stable magnetic suspensions which form uniform nanowires, a Fe/PSS ratio of approximately 2000 is required while keeping the iron and PSS concentrations above 0.02 and 10^{-6} M respectively.

7.4. Full statistical study of PSS-magnetite system

With these observations in mind, the factorial study was extended to check for further changes in r_1 with varying iron and polyelectrolyte concentrations. The graphical representation is given in Figure 11, while details of the full study are given in Table 7.4. One sample was repeated to check for reproducibility (sample B_re).

Table 7.4: Total factorial design study for polyelectrolyte stabilised particles

Sample	Total Fe conc (M)	PSS conc (M)	Fe/PSS ratio	Sample	Total Fe conc (M)	PSS conc (M)	Fe/PSS ratio
A	0.043	4.08×10^{-4}	105	N	0.043	4.08×10^{-5}	1054
B	0.030	3.57×10^{-4}	84	O	0.030	3.57×10^{-5}	840
C	0.020	2.38×10^{-4}	84	P	0.043	2.04×10^{-5}	2108
D	0.043	2.04×10^{-4}	211	Q	0.043	8.16×10^{-6}	5270
E	0.030	1.78×10^{-4}	168	R	0.020	1.9×10^{-5}	1052
F	0.051	1.19×10^{-4}	429	S	0.030	1.43×10^{-5}	2098
G	0.043	1.02×10^{-4}	421	T	0.026	1.22×10^{-5}	2131
H	0.051	2.38×10^{-5}	2143	U	0.030	7.14×10^{-6}	4202
I	0.054	4.2×10^{-5}	1286	V	0.006	1.29×10^{-5}	465
J	0.020	9.52×10^{-5}	210	W	0.006	1.29×10^{-6}	4651
K	0.030	7.14×10^{-5}	420	X	0.012	5.71×10^{-6}	2101
L	0.006	6.49×10^{-5}	92	Y	0.020	9.52×10^{-6}	2100
M	0.020	4.76×10^{-5}	420	Z	0.020	9.52×10^{-7}	21008

The colour code denotes the design number. The pink and blue represent the first study, further extension of that study is in green and the final experiments carried out are given in orange (Figure 7.10).

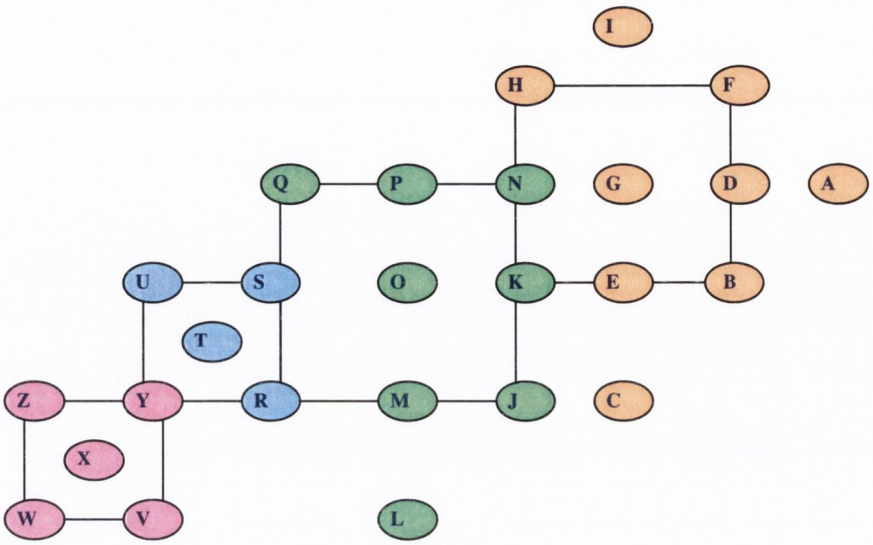

Figure 7.10 Graphical representation of full factorial polyelectrolyte-magnetite study

7.4.1. FTIR spectra

FTIR spectra of the samples were recorded in KBr (Figure 7.11).

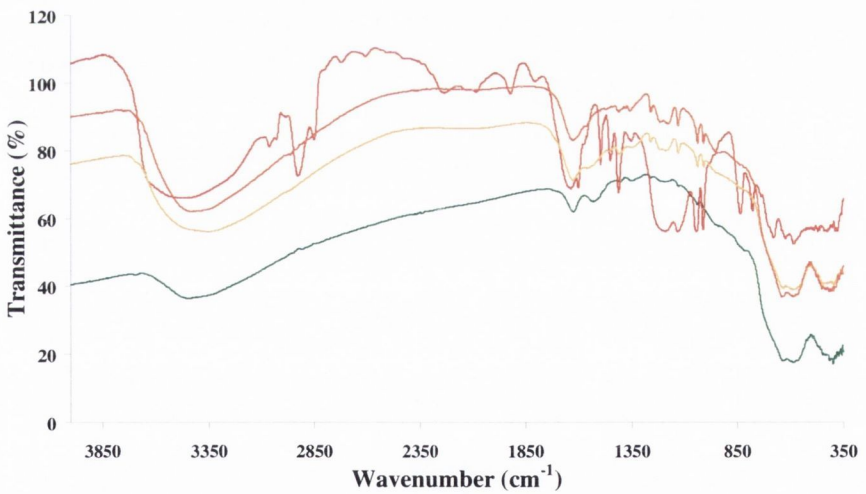

Figure 7.11 FTIR spectra of PSS-modified magnetite nanoparticles in KBr, showing PSS only (red) and samples D (yellow), H (green) and S (orange)

The spectrum of pure PSS reveals stretches for aromatic C-H bonds at 2921 cm^{-1} and out of plane C-H stretches at 1040 and 1009 cm^{-1}. Stretches for the CH_2 polymer backbone are found at 1495 and 1446 cm^{-1}, while aromatic C-C stretches are seen at 1633 cm^{-1}. The stretches for R-SO_2-OR are found at 1409 and 1188 cm^{-1} and

S-O stretches are seen at 828 and 773 cm^{-1}. For all PSS-functionalised nanoparticles, the stretches for aromatic C-C bonds, CH_2 bonds, sulfonate bonds and aromatic C-H bonds are still seen. The stretch at 580 cm^{-1} is attributed to Fe-O stretches, while the shoulder on this peak, at 631 cm^{-1}, could be a stretch for a Fe-O-S bond. These were typical spectra obtained for all samples.

7.4.2. Raman spectra

Raman spectra of the samples were carried out (Figure 7.12). The presence of magnetite was confirmed in all samples. Peaks found at 680 cm^{-1} and 496 cm^{-1} are in good agreement with the literature values for magnetite.[22, 23] Sharper peaks belonging to haematite are found at 222, 288, and 406 cm^{-1} for two samples only (samples Q and T).[24]

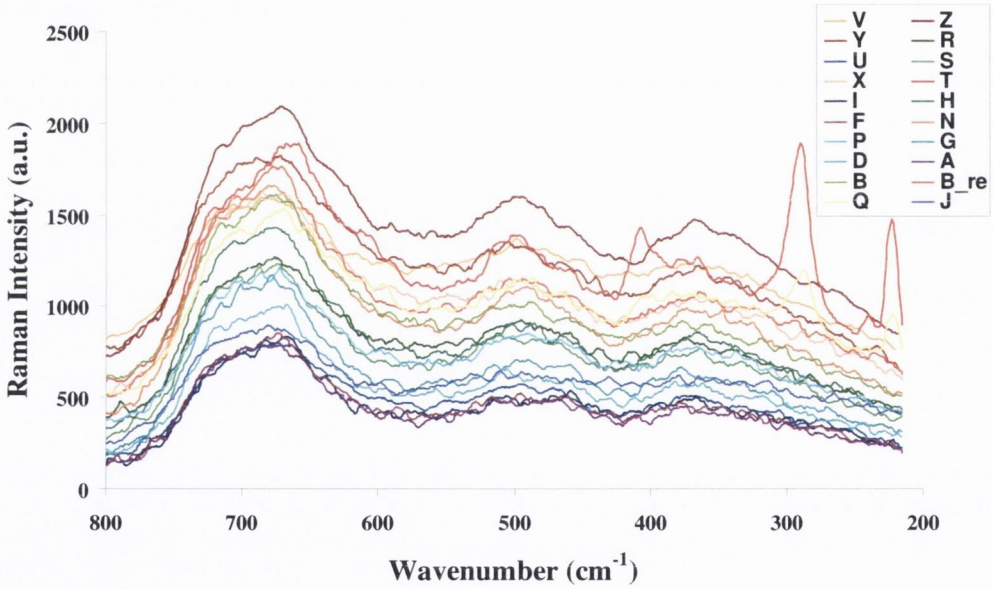

Figure 7.12 Raman spectra of PSS-modified magnetite nanoparticles

7.4.3. XRD patterns

XRD patterns were carried out on selected samples (Appendix 11). The peaks obtained are found to correspond to the JCPDS database for magnetite. All XRD patterns obtained show the same result, with the peaks all matched to the magnetite spectrum.

7.4.4. TEM analysis

TEM images for selected samples are given in Figure 7.13.

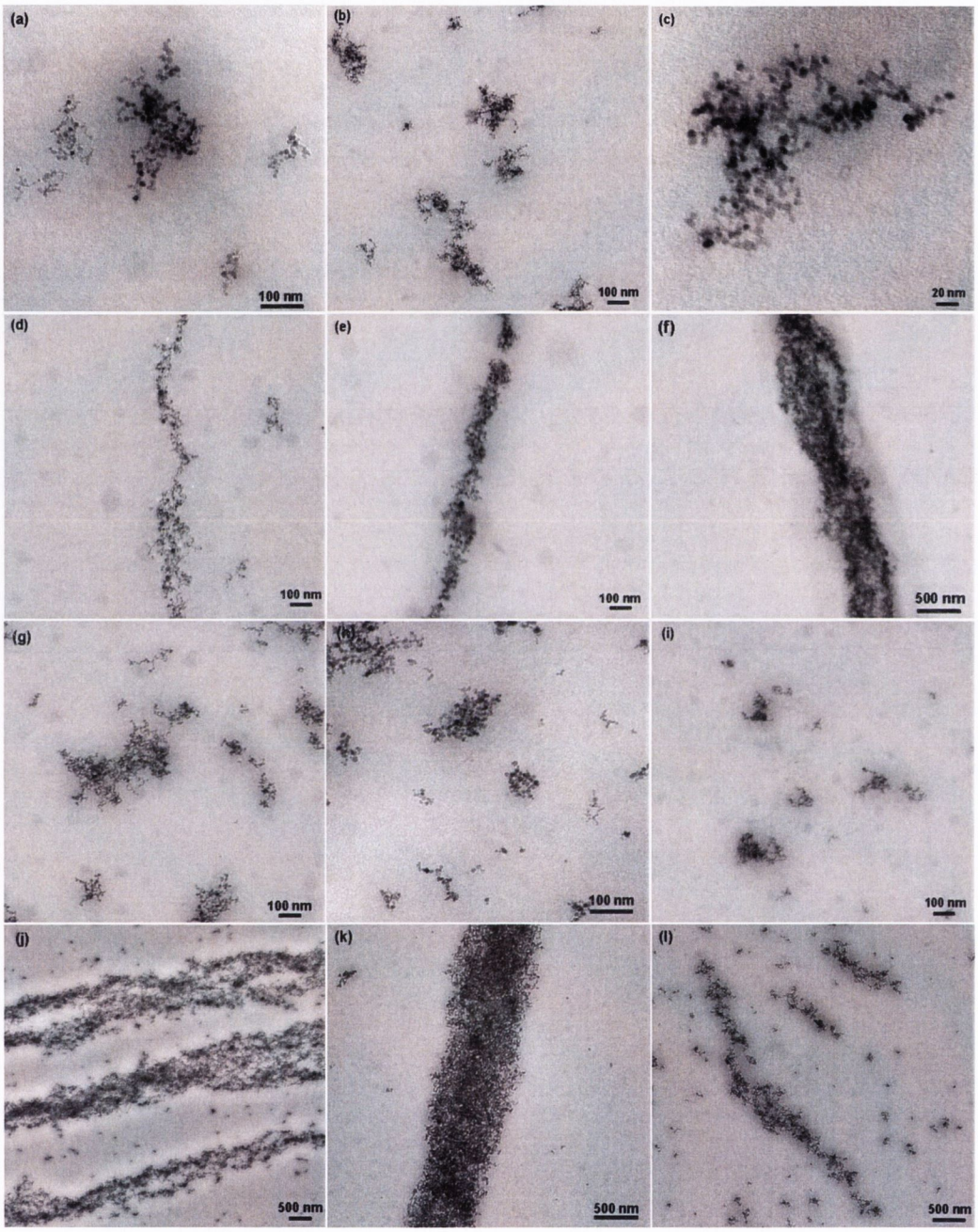

Figure 7.13 (a) I, **(b)** H, **(c)** F, **(d)** I mag field, **(e)** H mag field, **(f)** F mag field, **(g)** N, **(h)** P, **(i)** G, **(j)** N mag field, **(k)** P mag field, and **(l)** G mag field

A drop (5 μL) of each sample was dried on a copper formvar grid both without and with the presence of a magnetic field. For the samples alone, the particles are found to aggregate into clusters. Once subjected to an external magnetic field, the

particles are found to align in 1-D arrays. The analysis of average primary particle sizes and nanowire widths is summarised in Table 7.5.

Table 7.5 Analysis of average particle size and nanowire width for PSS -magnetite nanocomposites

Sample	Primary particle size (nm)	Nanowire width (nm)	Fe/PSS ratio	Sample	Primary particle size (nm)	Nanowire width (nm)	Fe/PSS ratio
A	6.5 ± 1	236 ± 50	105	N	11.2 ± 2	805 ± 200	1054
B	7.1 ± 1	930 ± 280	84	O	10.7 ± 1.6	420 ± 140	840
C	8.3 ± 1.4	108 ± 39	84	P	10.3 ± 1.7	986 ± 150	2108
D	6.1 ± 1	220 ± 30	211	Q	9.8 ± 1.7	103 ± 12	5270
E	7 ± 1.1	613 ± 150	168	R	10.2 ± 1.2	1464±450	1052
F	7.6 ± 1.2	382 ± 83	429	S	10.1 ± 2.2	213 ± 96	2098
G	6.1 ± 0.9	250 ± 80	421	T	9.4 ± 1.6	1272±280	2131
H	11.4 ± 2.4	111 ± 37	2143	U	9.9 ± 1	1040±120	4202
I	10.4 ± 2.1	200 ± 60	1286	V	10.2 ± 2.7	No wires	465
J	7.4 ± 1.4	197 ± 53	210	W	10.4 ± 1.9	No wires	4651
K	8.3 ± 1.3	540 ± 140	420	X	10.6 ± 1.9	1179±280	2101
L	9.3 ± 1.6	2987 ±340	92	Y	7.9 ± 1.2	Clustered	2100
M	10.5 ± 1	1966 ±260	420	Z	10.1 ± 2	300 ± 120	21008

It is noted that for high Fe/PSS ratios, there are a greater number of samples which form wider nanowires. In general, the narrowest wires are formed when the concentration of the polyelectrolyte is kept at 10^{-4} M.

7.4.5. NMRD and PCS analysis

PCS data was collected for all samples which formed stable suspensions (Table 7.6, Figure 7.14). The data obtained confirms the presence of clusters of particles in all samples. The polydispersity index for all samples is relatively low. The results also agree with TEM sizes obtained for the nanowires. Sample Q, for example, gives a z-average of 95 nm, while in TEM the average nanowire size is found to be 103 nm. In general, there is a good agreement between the cluster sizes reported by PCS and the average nanowire width obtained in TEM. Most of the TEM

results are larger than those found by PCS, which is due to clustering caused by the drying of the sample for TEM preparation.

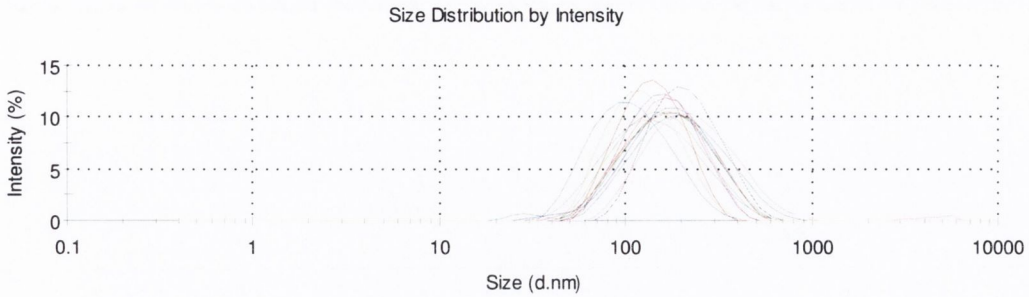

Figure 7.14 Combined PCS intensities for PSS-functionalised magnetite nanoparticles. Note the size distribution intensities do not vary hugely over all samples.

Table 7.6 PCS results for total factorial design study for polyelectrolyte stabilised magnetite particles

Sample	Z-average	PDI	Sample	Z-average	PDI
A	196	0.250	N	184	0.201
B	166	0.248	O	112	0.148
C	-	-	P	140	0.145
D	150	0.181	Q	95	0.198
E	136	0.209	R	203	0.191
F	150	0.155	S	154	0.151
G	122	0.166	T	137	0.178
H	134	0.194	U	97	0.169
I	150	0.187	V	-	-
J	-	-	W	-	-
K	-	-	X	-	-
L	-	-	Y	138	0.219
M	142	0.229	Z	215	0.349

All NMRD profiles for any stable suspensions formed in the study are shown in Figure 7.15. Note that the profile curves differ significantly between the samples. In order to discuss the results best, the profiles have been split in two, those with an r_1

maximum below 4 MHz (Figure 7.16) and those with an r_1 maximum above 4 MHz (Figure 7.17).

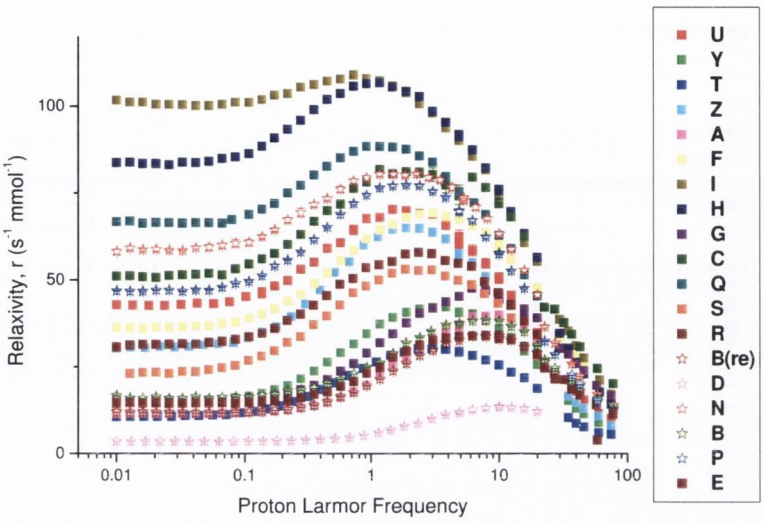

Figure 7.15 NMRD profiles for all stable suspensions from full factorial study

At lower frequencies (< 4MHz), the principle mechanism governing the relaxation process is the Néel process, i.e. the movement of the nanoparticles' internal magnetic moment. This means that the relaxation time (T_1) is shorter at lower frequencies. This in turn gives rise to a higher relaxation rate at lower frequency (since $R_1 = 1/T_1$).

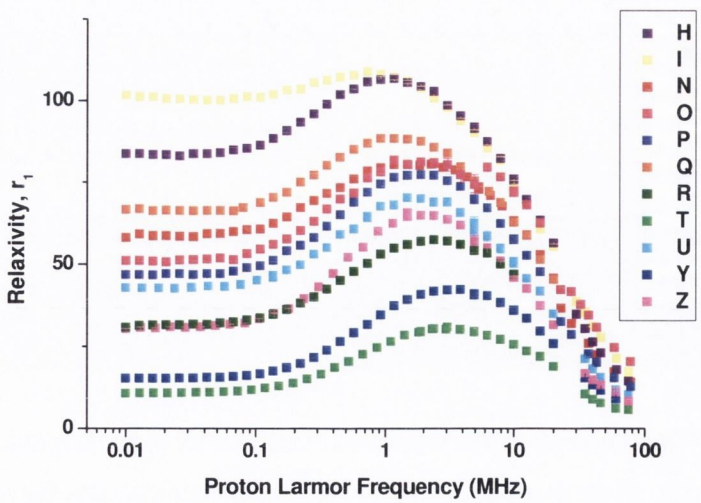

Figure 7.16 NMRD profiles for samples with r_1 maximum below 4 MHz

This type of behaviour is noted for more clustered material, where there are larger particles or aggregates. These samples exhibit a relaxation rate enhancement at lower frequency. As Figure 7.16 shows, the relaxivity is higher at lower frequency and then decreases. Above 4 MHz (Figure 7.17), the relaxivity is dependant on the diffusion of water molecules around the magnetic nanoparticles. This is a faster process than that of the particles diffusing in solution. The result is that the maximum relaxivity is found to occur at higher frequency. The smaller the nanoparticles, i.e. the more superparamagnetic, the higher the frequency r_1 occurs at.

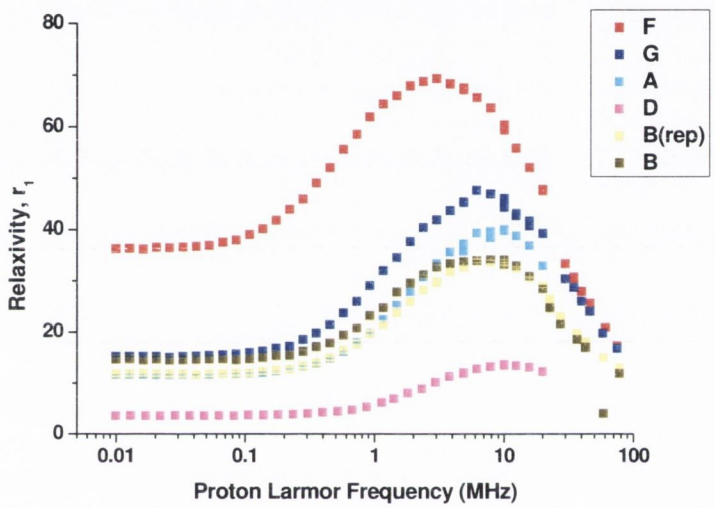

Figure 7.17 NMRD profiles for samples with r_1 maximum above 4 MHz

In order to find a correlation between the relaxation process and the constituent concentrations, it is necessary to consider the iron:polyelectrolyte concentration ratios (Table 7.7).

It can be seen that at lower Fe/PSS ratios, the profiles adopt more superparamagnetic type behaviour, while at higher ratios, there is a trend towards magnetically clustered behaviour. At lower Fe/PSS ratios, the excess PSS can act as both a nucleation site for initial particle formation and as a stabiliser once the particles are formed. This will act to reduce the primary particle size. Indeed, this is found to be the case for the six samples which have an r_1 maximum above 4 MHz. The primary particle sizes for samples A, B, D, E, F and G are all below 8 nm. However, it is important to maintain the optimal balance of the iron and PSS concentrations in order to keep the nanoparticles stable in solution.

In the case of those samples exhibiting NMRD profiles for clustered material, the relatively lower concentration of PSS. If there is less polyelectrolyte available for coating and stabilisation, the particles may grow into larger aggregates, thereby displaying mostly clustered behaviour in the NMRD profiles.

Table 7.7 Iron/PSS ratios for samples

Low Frequency samples		**High frequency samples**	
Sample	Fe/PSS ratio	Sample	Fe/PSS ratio
S	2100	F	430
N	1060	B	85
Q	5320	D	210
O	850	A	100
R	1070	G	420
H	2140		
I	1285		
Z	21320		
U	4260		
Y	2130		

7.5. Full statistical study of PSS-cobalt ferrite nanocomposites

It has been reported that the coercivities of iron oxides can be raised significantly, while retaining their practical benefits (like good chemical and physical stability) by modifying them with cobalt.[25] Cobalt-modified oxide particles are the predominant magnetic material used in video tapes today, but they are also used in audio tapes and in some tapes and disks for high-density digital recording. Therefore we decided to develop our polyelectrolyte approach above for the preparation of similar cobalt ferrite nanowires, which expect to have much higher coercivities and anisotropy energies than magnetic iron oxides. The particles were prepared using our modification of the method reported by Markovich and coworkers.[26] Briefly, the addition of ammonia solution to iron (II) chloride and cobalt (II) nitrate dissolved in Millipore water at 80 °C precipitated out cobalt ferrite nanoparticles. The addition of PSS to the solution before ammonia addition afforded stable magnetic suspensions for

some of the preparations. The primary particles formed in this manner are larger than those formed in the case of the magnetite reactions. For this reason, there were less stable suspensions formed, as the larger cobalt ferrite aggregates fell out of solution. Also, it was found that at lower metal concentrations, it was difficult to recover particles. For this reason, the study was carried out from sample A to U (i.e. experiments V to Z were not done). All cobalt ferrite - PSS nanocomposites have been characterised by IR and Raman spectroscopy, XRD patterns, TEM analysis and PCS and NMRD techniques.

7.5.1. FTIR spectra

FTIR spectra were carried out in KBr. Selected spectra are shown in Figure 7.18.

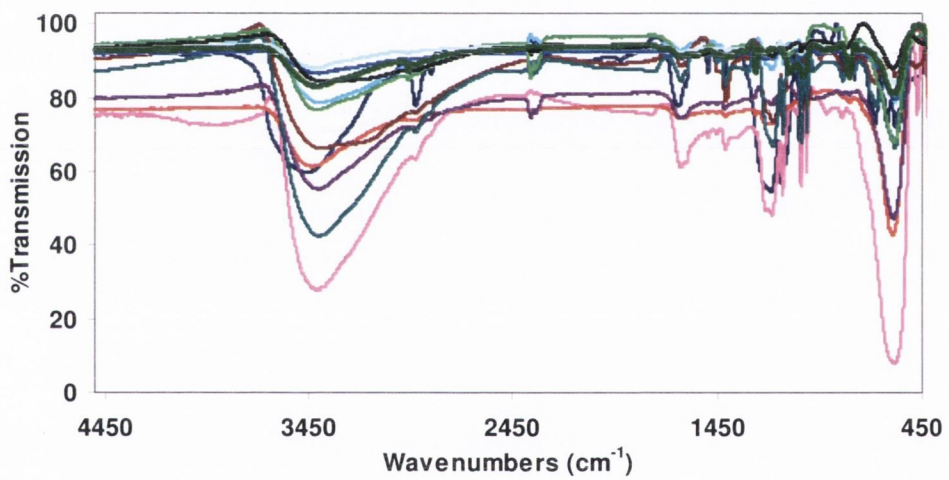

Figure 7.18 Selected FTIR spectra for PSS stabilised cobalt ferrite particles with PSS (navy), I (pink), H (red), F (light blue), N (purple), G (brown), D (teal), K (royal blue), B (light green), P (pale blue), A (black), C (green)

All samples reveal a stretch at 580 cm^{-1}, which is assigned to the Fe-O bonds. Co-O bonds are reported to have a stretch at 670 cm^{-1}. In the spectra shown, this peak appears as a shoulder on the Fe-O stretch. As with the magnetite samples, the PSS-functionalised cobalt ferrite nanoparticles show stretches for aromatic C-C bonds, CH_2 bonds, sulfonate bonds and aromatic C-H bonds.

7.5.2. Raman spectra

Raman spectra were recorded for all samples, with selected spectra shown in Figure 7.19 (remaining spectra may be found in Appendix 12). There are 5 active Raman modes in cobalt ferrite. The highest frequency Raman mode at 688cm^{-1} is assigned to the T-site mode, which reflects the local lattice effect in the tetrahedral sublattice, and the peak at 469cm^{-1} to the O-site mode, which reflects the local lattice effect in the octahedral sublattice[47]. The other peaks to be found in the spectrum occur at 615, 290 and 225cm^{-1} and are in very good agreement with the 5 optically active Raman modes ($A_{1g}+E_g+3F_{2g}$), characteristic of the cubic inverse-spinel structure O_h^7 (Fd3m) space group[48]. The intensity of the peaks at 290 and 225 cm^{-1} in sample B indicates that there is a degree of oxidation caused presumably by heating from the Raman laser.

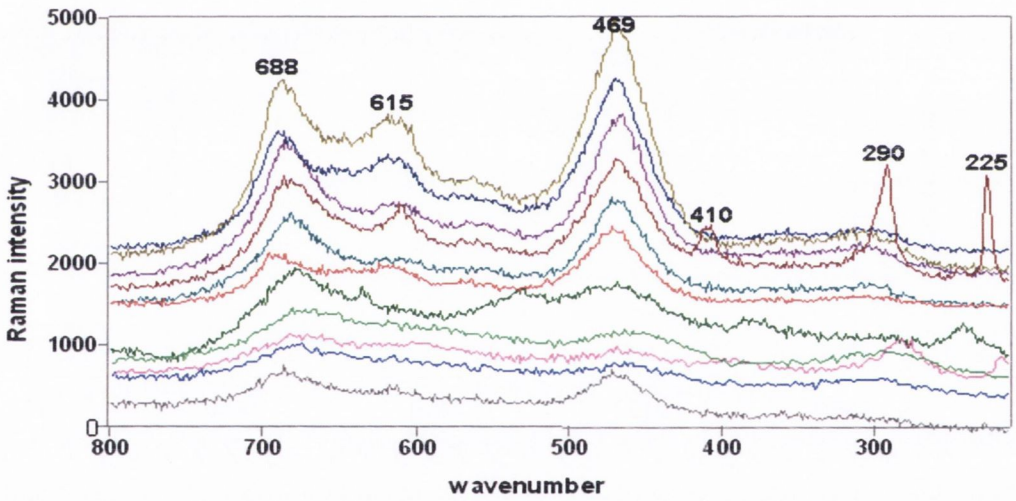

Figure 7.19 Selected Raman spectra for PSS stabilised cobalt ferrite particles. From top to bottom: D, N, H, B, I, K, G, P, A, C, and F.

7.5.3. XRD patterns

XRD patterns obtained for selected samples are shown in Figure 7.20. The patterns found were compared to the JCPDS database for cobalt ferrite and are shown in Figure 21 as red lines, which overlap with the patterns obtained for these samples. All samples measured gave the same XRD patterns which were matched with the standard for cobalt ferrite.

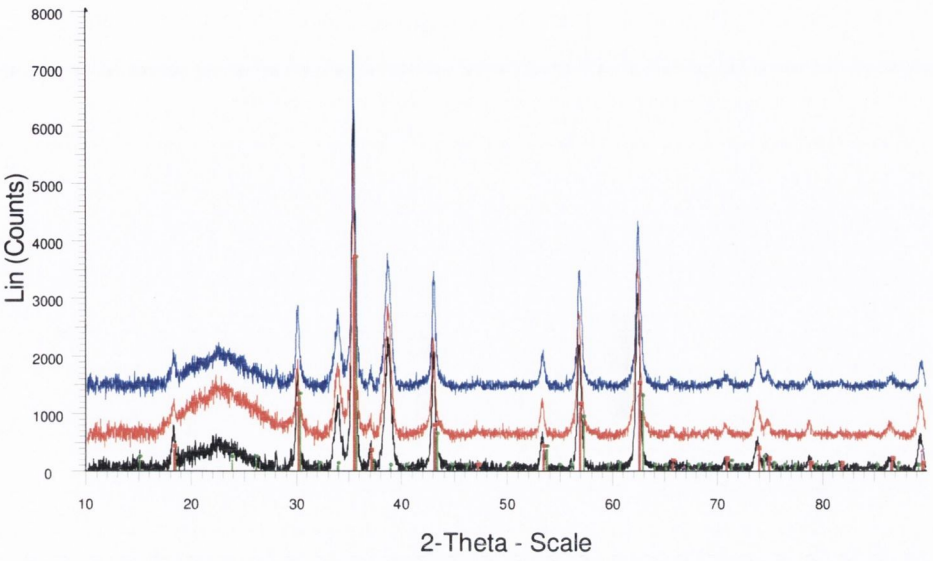

Figure 7.20 XRD patterns PSS stablised cobalt ferrite samples A (black), D (red) and F (blue)

7.5.4. TEM analysis

TEM images were taken of all of the nanocomposites. Selected images are shown in Figure 7.21. Other samples also gave aggregated assemblies of particles. The particle sizes are given in Table 6.

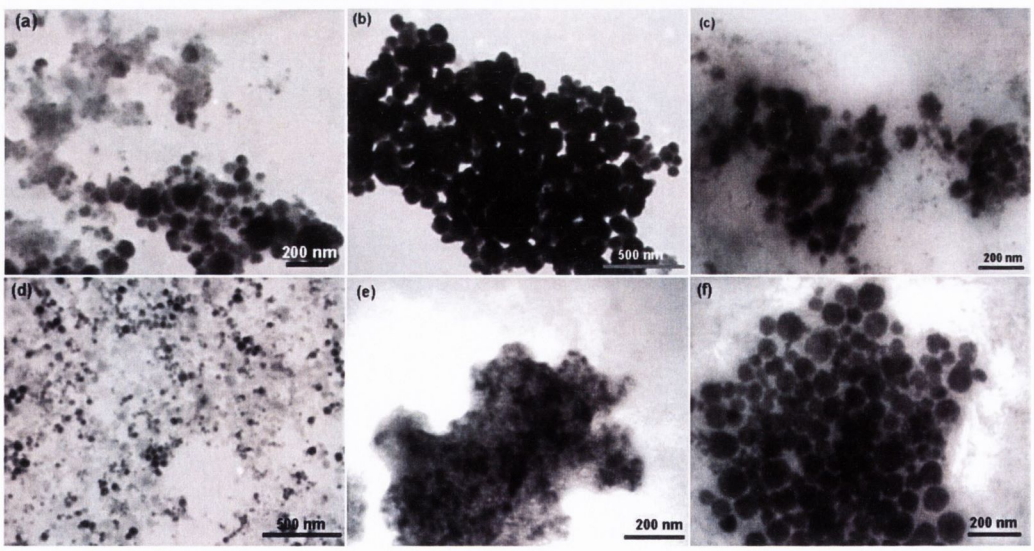

Figure 7.21 TEM images of samples (a) I, (b) F, (c) N, (d) D, (e) A and (f) P

Table 7.8 Factorial design for PSS stabilised nanoparticles and response (TEM size distribution)

Sample	Primary particle size (nm)	Metal/PSS ratio	Sample	Primary particle size (nm)	Metal/PSS ratio
A	62 ± 29	105	K	24 ± 10	420
B	62 ± 35	84	L	94 ± 27	92
C	57 ± 45	84	M	27 ± 16	420
D	32 ± 8	211	N	42 ± 11	1054
E	58 ± 33	168	O	22 ± 16	840
F	69 ± 28	429	P	72 ± 21	2108
G	23 ± 13	421	Q	137 ± 56	5270
H	133 ± 27	2143	R	24 ± 7	1052
I	73 ± 28	1286	S	45 ± 24	2098
J	131 ± 8	210	U	49 ± 18	4202

When compared to their magnetite counterparts, it is found that the cobalt ferrite particles are larger, some by an order of magnitude. Such variations in primary particle size are likely to have an effect on the relaxivities of any magnetic fluids formed. Also, because of such large sample sizes, there are fewer stable suspensions formed. For these samples, the formation of nanowires is again noted when dried under a perpendicular magnetic field (Figure 7.22).

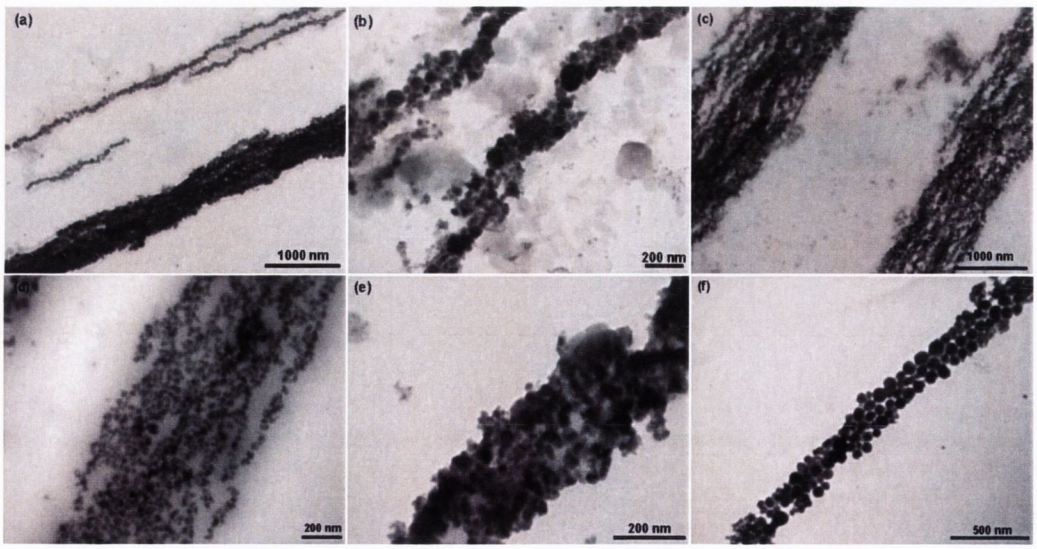

Figure 7.22 TEM images of samples (a) I, (b) F, (c) N, (d) D, (e) A and (f) P, measured at 100kV. Samples deposited on copper formvar grids which were dried in 0.5T perpendicular magnetic field.

Table 7.9 Size distribution study of wires formed in perpendicular magnetic field

Sample	Avg. width (nm)	Std. Dev. of width	Metal/PSS ratio
A	306	84	210
D	765	404	429
F	135	47	84
I	299	143	105
N	1176	616	211
P	217	107	420

Although no absolute pattern can be distinguished, there are indications that a high concentration of PSS gives rise to wires with a small width, and a low concentration of Co/Fe gives larger widths of wires. The larger the width of the wires, the more uniform they appear to be.

7.5.5. NMRD and PCS characterisation

NMRD analysis was carried out on the stable suspensions formed (Figure 23). Cobalt ferrite has higher magnetic anisotropy energy when compared to magnetite. This means that the direction of its magnetization is along a particular preferred crystallographic direction is favoured. This should have repercussions on the NMRD response. Indeed, it is noted that the magnetic fluids obtained have extremely high relaxivity at low field. The highest low-field relaxivity found previously was for single stranded Herring DNA-magnetite nanocomposites (~275 s^{-1} $mmol^{-1}$ at 0.01 MHz).[43] The PSS-functionalised cobalt ferrite has an even larger relaxivity, 400 s^{-1} $mmol^{-1}$ at 0.01 MHz for samples D and N.

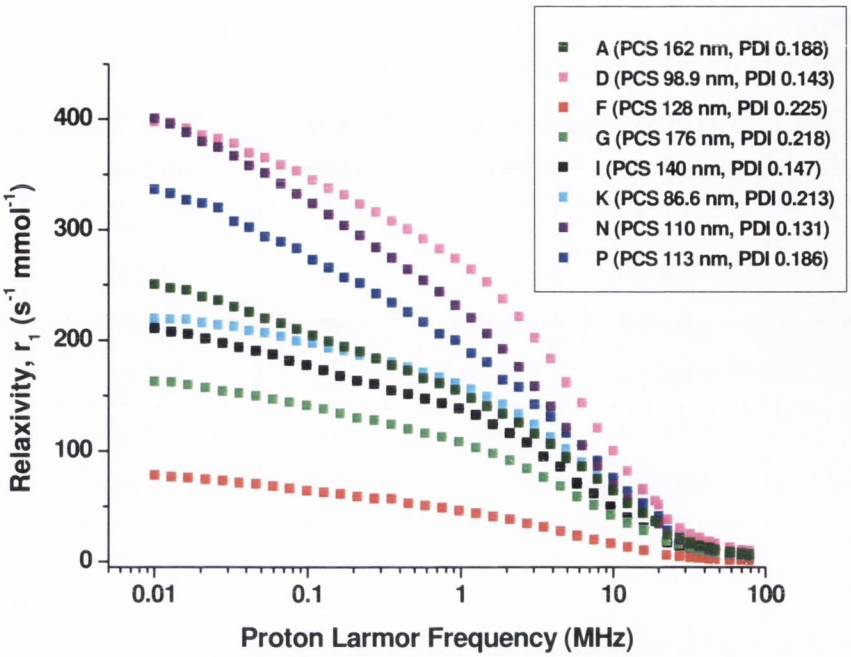

Figure 7.23 Relaxation rates for PSS stabilised cobalt ferrite samples

Samples D and N differ only in the concentration of PSS. Therefore, it is clear that the iron concentration has a big impact on the relaxivity profiles.

Photon Correlation Spectroscopy (PCS) was carried out on the five samples which formed water stable magnetic fluids (Table 7.10). PCS is a method of measuring particle size in water. This is useful to compare with TEM results, which give particle sizes on a dry medium.

Table 7.10 PCS results for total factorial design study for polyelectrolyte stabilised cobalt ferrite particles

Sample	Z-Average	PDI	Sample	Z-Average	PDI
A	162	0.188	H	-	-
B	-	-	I	140	0.147
C	-	-	J	-	-
D	99	0.143	K	87	0.213
E	-	-	L	-	-
F	128	0.225	N	110	0.131
G	176	0.218	P	113	0.186

In comparison with the PSS-functionalised nanoparticles, the PCS data is more varied (Figure 7.24). The highest relaxivity profiles also give the most uniform PCS data.

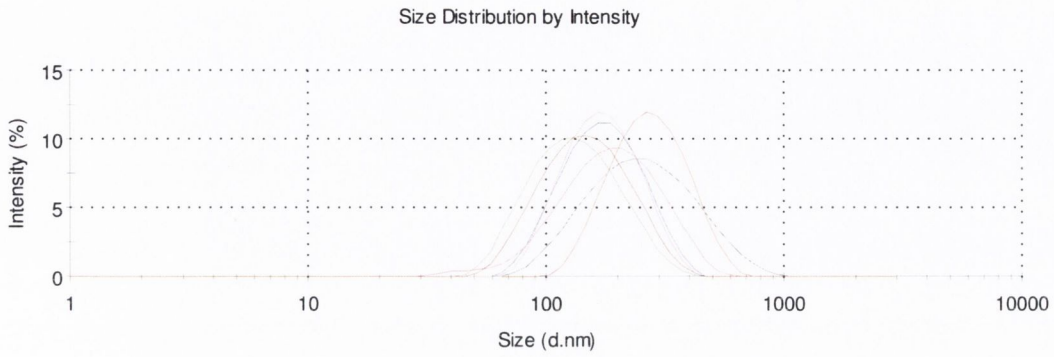

Figure 7.24 Combined PCS intensities for PSS-functionalised cobalt ferrite nanoparticles.

7.6. Conclusions

Using polyelectrolyte and in situ co-precipitation technique we have develop a new approach for the preparation of uniform nanowires of magnetic material and stable magnetic fluids with potential MRI capabilities. This method has several advantages over other existing procedures: it is a quick, inexpensive one step experiment which is reproducible and whose parameters can be varied to produce magnetic fluids with tuneable relaxivities. The reproducibility is confirmed by only a 6% difference in relaxivities between the repeat experiments (samples B and B_re). This is an exciting prospect as there is currently no reported method of a system which allows tuning of the contrast agent relaxivity. We have also demonstrated that by choosing an appropriate iron and polyelectrolyte concentrations and ratios we potentially can tune the frequency at which the highest relaxation is desired. Summary of the analysis on relaxivities of magnetite and cobalt ferrite - PSS nanocomposites are presented in Table 7.11.

Table 7.11 Relaxivity (r_1) values at 20 MHz for polyelectrolyte stabilised magnetic fluids

Sample	Fe_3O_4 fluids (r_1 at 20 MHz)	$CoFe_2O_4$ fluids (r_1 at 20 MHz)	Sample	Fe_3O_4 fluids (r_1 at 20 MHz)	$CoFe_2O_4$ fluids (r_1 at 20 MHz)
A	33.02	37.26	N	45.89	35.1
B	31.18		O	42.33	-
C	-	-	P	32.59	41.74
D	12.32	52.18	Q	45.53	-
E	28.57	-	R	34.39	-
F	47.84	6.5	S	31.25	-
G	39.29	18.77	T	18.95	-
H	55.56	-	U	34.94	
I	55.49	17.48	V	-	-
J	-	-	W	-	-
K	-	26.37	X	-	-
L	-	-	Y	25.85	-
M	-	-	Z	31.62	-

When compared to some of the commercially available iron oxide contrast agents, it is found that most of our magnetic fluids have a higher relaxivity at 20 MHz (Table 7.12). Therefore, these new magnetic fluids could have some very important applications in clinical MRI. Future work will include the testing *in vivo* of these fluids.

Table 7.12 Relaxivity values for commercial samples at 20 MHz

Commerically available magnetic fluids for MRI
Gd-DTPA, r_1=4.5
Ferumoxil, r_1=3.2
Ferumoxtran, r_1=22.7
Ferumoxide, r_1=23.7

From the statistical study, we have found that for PSS-magnetite systems, contrast agents with high relaxivities at clinical fields are produced when lower

iron:PSS ratios are used. For low field MRI contrast agents, increasing this ratio increases the relaxivity at lower field. For PSS-cobalt ferrite systems, we have observed the highest reported relaxivity for a particulate contrast agent at low field. We believe this research contribute to further development of new magnetic fluids for MRI and hyperthermia therapy. Magnetic nanowires might also find important applications in other areas such as information technology (e.g. magnetic storage) and nanoelectronics (e.g. nanowiring and nanointerconnects).

References

[1] K. S. Mayya, D. I. Gittins, A. M. Dibaj, F. Caruso, *Nano Letters* **2001**, *1*, 727.

[2] E. Blomberg, E. Poptoshev, P. M. Claesson, F. Caruso, *Langmuir* **2004**, *20*, 5432.

[3] K. S. Mayya, B. Schoeler, F. Caruso, *Advanced Functional Materials* **2003**, *13*, 183.

[4] V. Salgueirino-Maceira, F. Caruso, L. M. Liz-Marzan, *Journal of Physical Chemistry B* **2003**, *107*, 10990.

[5] F. Caruso, *Advanced Materials* **2001**, *13*, 11.

[6] J. H. Cho, J. F. Quinn, F. Caruso, *Journal of the American Chemical Society* **2004**, *126*, 2270.

[7] D. I. Gittins, F. Caruso, *Journal of Physical Chemistry B* **2001**, *105*, 6846.

[8] F. Caruso, R. A. Caruso, H. Mohwald, *Science* **1998**, *282*, 1111.

[9] A. A. Antipov, G. B. Sukhorukov, H. Mohwald, *Langmuir* **2003**, *19*, 2444.

[10] F. Caruso, H. Lichtenfeld, E. Donath, H. Mohwald, *Macromolecules* **1999**, *32*, 2317.

[11] E. Donath, G. B. Sukhorukov, F. Caruso, S. A. Davis, H. Mohwald, *Angewandte Chemie-International Edition* **1998**, *37*, 2202.

[12] A. Gole, C. J. Murphy, *Chemistry of Materials* **2005**, *17*, 1325.

[13] X. Hong, J. Li, M. J. Wang, J. J. Xu, W. Guo, J. H. Li, Y. B. Bai, T. J. Li, *Chemistry of Materials* **2004**, *16*, 4022.

[14] J. F. Berret, N. Schonbeck, F. Gazeau, D. ElKharrat, O. Sandre, A. Vacher, M. Airiau, *Journal of the American Chemical Society* **2006**, *128*, 1755.

[15] R. Sheparovych, Y. Sahoo, M. Motornov, S. M. Wang, H. Luo, P. N. Prasad, I. Sokolov, S. Minko, *Chemistry of Materials* **2006**, *18*, 591.

[16] M. Tanase, L. A. Bauer, A. Hultgren, D. M. Silevitch, L. Sun, D. H. Reich, P. C. Searson, G. J. Meyer, *Nano Letters* **2001**, *1*, 155.

[17] C. M. Hangarter, N. V. Myung, *Chemistry of Materials* **2005**, *17*, 1320.

[18] Y. Sahoo, M. Cheon, S. Wang, H. Luo, E. P. Furlani, P. N. Prasad, *Journal of Physical Chemistry B* **2004**, *108*, 3380.

[19] G. J. Cheng, D. Romero, G. T. Fraser, A. R. H. Walker, *Langmuir* **2005**, *21*, 12055.

[20] H. Singh, P. E. Laibinis, T. A. Hatton, *Nano Letters* **2005**, *5*, 2149.

[21] H. Singh, P. E. Laibinis, T. A. Hatton, *Langmuir* **2005**, *21*, 11500.

[22] O. N. Shebanova, P. Lazor, *Journal of Raman Spectroscopy* **2003**, *34*, 845.

[23] O. N. Shebanova, P. Lazor, *Journal of Solid State Chemistry* **2003**, *174*, 424.

[24] I. R. Beattie, T. R. Gilson, *Journal of the Chemical Society A -Inorganic Physical Theoretical* **1970**, 980.

[25] M. P. Sharrock, *IEEE Transactions on Magnetics* **1988**, *24*, 2856.

[26] T. Fried, G. Shemer, G. Markovich, *Advanced Materials* **2001**, *13*, 1158.

Chapter 8: Conclusions and Future Work

8.1. Conclusions

In this work, a number of new magnetic nanocomposite materials have been prepared and investigated, which could have a broad range of potential applications.

The use of a statistical study has been demonstrated as a good method for the optimisation of nanocrystal preparation by varying temperature and ultrasonic treatment conditions. These results enable the identification of the best conditions for nanocrystal formation with a narrow size distribution. It has been found that magnetite nanocrystals may be synthesised from the heterometallic precursor $[(THF)NaFe(O^tBu)_3]_2$ and to obtain the smallest particles with the narrowest size distribution, it is best to do the experiment at a temperature of 30 °C with 10 hours of ultrasound.

Extensive studies have also been performed on magnetic iron oxide–silica composites prepared from an organometallic Fe (II) alkoxide precursor, and TEOS. It was found that the particle size decreases with increasing silica concentration. These new materials exhibit superparamagnetic behaviour at room temperature. Nanorods are formed at an optimal level of 10at% silica.

This work has also shown that the octaaminopropylsilsesquioxane is an excellent stabilising agent for the formation of water-stable magnetic nanoparticle suspensions, which show promising results for use as novel MRI contrast agents. "Two in one" fluorescent–magnetic nanocomposites have also been prepared. These are based on magnetite–porphyrin ionically and covalently linked nanocomposites. These materials have been internalised by human THP-1 and osteoblast cells without any deleterious effects to the cells. This is an exciting outcome as these nanocomposites could provide a new method for biological imaging, medical diagnostic and therapy.

Stable suspensions of magnetite nanoparticles using DNA surfactants have been prepared and their NMRD responses studied. In aqueous suspension these materials undergo aggregation, the suspensions of single stranded Herring DNA-magnetite nanocomposites exhibit very high relaxivity at low field, which could be important with the advent of low field MRI. Intercalation studied have found that the double stranded DNA structure is not compromised during the preparation and readily intercalates with acridine orange to provide magnetic-fluorescent nanocomposites. There is a quenching of the fluorescence for the single stranded DNA-magnetite

nanocomposites. This is because, since the double helix is no longer intact, the acridine orange can only electrostatically bind to the DNA, leaving it more open to quenching by the magnetic particles.

Polyelectrolyte (PSS) stabilised magnetite and cobalt ferrite nanoparticles have afforded new magnetic fluids, whose efficacy as contrast agents has been demonstrated. These magnetic fluids, which arrange in chains in the presence of an external magnetic field, are found to have higher r_1 relaxivities when compared to the current nanoparticulate contrast agents available. This demonstrates the great potential of these fluids for MRI and possibly hyperthermia application. These composites have also been found to arrange in wires by external magnetic field, which makes them potentially useful for information technology (e.g. magnetic storage) and nanoelectronics (e.g. nanowiring and nanointerconnects) applications.

In conclusion, it is believed that this work will contribute to the further development of several important areas of nano and biotechnology.

8.2. Future Work

Future work will include further research and development on magnetic nanowires, magnetic-fluorescent nanocomposites, magnetic nanoparticle-drug conjugates and the immobilisation of organic catalysts on magnetic nanoparticles.

8.2.1. Development of magnetite- polyelectrolyte nanocomposites

The success of polysodium-4-styrene sulfonate as a stabiliser for the formation of water stable magnetic fluids has been encouraging. One future challenge will be to see if this can be extended to include a variety of commercially available polyelectrolytes. Some preliminary work has been carried out, using the polyelectrolytes polyallylamine hydrochloride, poly (diallyldimethylammonium chloride) and polyethylenimine. TEM images of samples prepared and dried in the presence of a 0.5 T external magnetic field are shown in Figure 8.1.

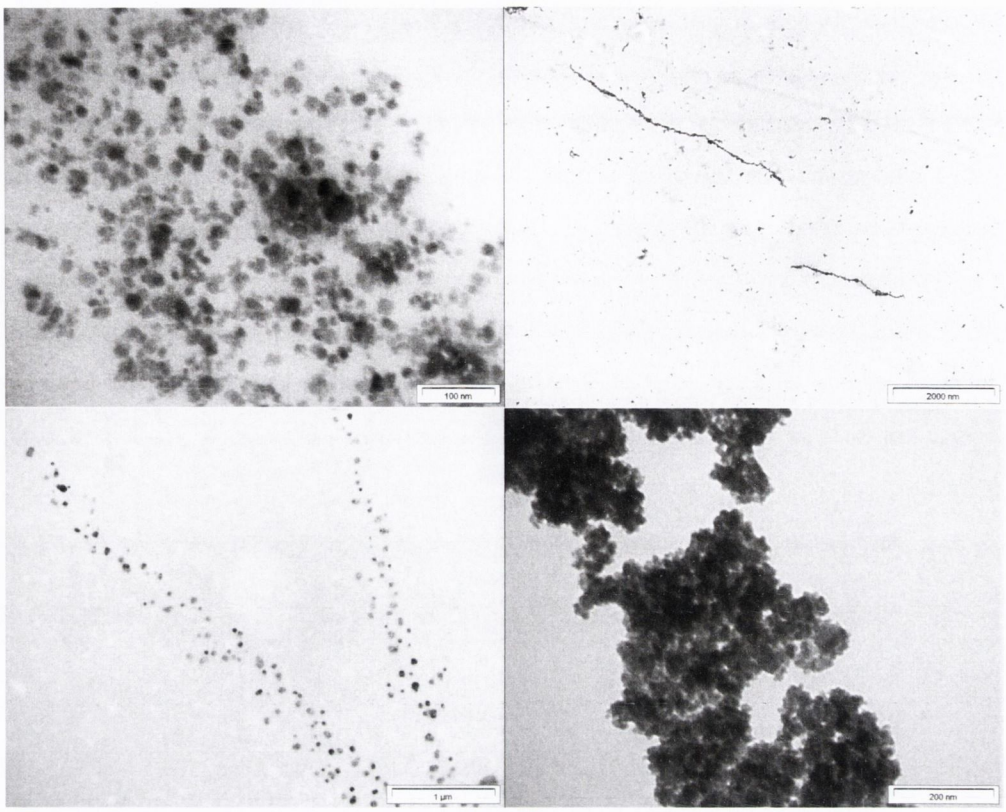

Figure 8.1 (a) Polyallylamine hydrochloride-functionalised nanoparticles and (b) subjected to external magnetic field; (c) polyethylenimine-functionalised nanoparticles and (d) poly (diallyldimethylammonium chloride) -functionalised nanoparticles

Preliminary MRI studies have also been carried out. MR images were obtained of the magnetite-PSS nanocomposite sample E after injection into a live mouse under anesthetic in order to study the effect of the contrast agent on the brain, specifically the hippocampus. Firstly, a coronal image, positioned at approximately 3.2 mm posterior to the bregma, was obtained using a localiser scan in order to contain a good cross-section through the hippocampus. Subsequently, two scans were acquired using the reference image – an Echo Planar Imaging (EPI) scan and a Fast Low Angle Shot (FLASH) scan. For the EPI scan (Figure 8.2 a, b), the coronal slice is imaged every 0.7 sec for a duration of 35 sec. Figure 8.2(a) shows an image of the brain immediately after injection of PSSS-Mag (0.4mL) in the tail vein. At this time point, none of the bolus has yet reached the brain. Figure 8.2(b) shows an image of the brain 11.2 sec after injection. There is significant darkening of the image as the bolus has now reached the brain. For the FLASH scan (Figures 8.2 c, d), the coronal

slice is imaged every 0.8 sec for a duration of 48.5 sec. Figure 8.2(c) shows an image of the brain of a second rat immediately after injection of PSSS-Mag (0.4mL), when none of the bolus has yet reached the brain. Figure 8.2(d) shows an image of the same brain 13.6 sec after injection. Again, a significant darkening of the brain is noted. Using the FLASH scan, the occlusion of the superior sinus sagittalis vein (SSS) can be clearly seen. Before the bolus arrives, the SSS appears white on this T1 weighted image and following occlusion of the vein, it appears black as it fills with PSSS-Mag. A third rat was injected with PSSS-Mag (0.4mL) and no visible signs of any adverse reaction were noted after monitoring for twenty-four hours.

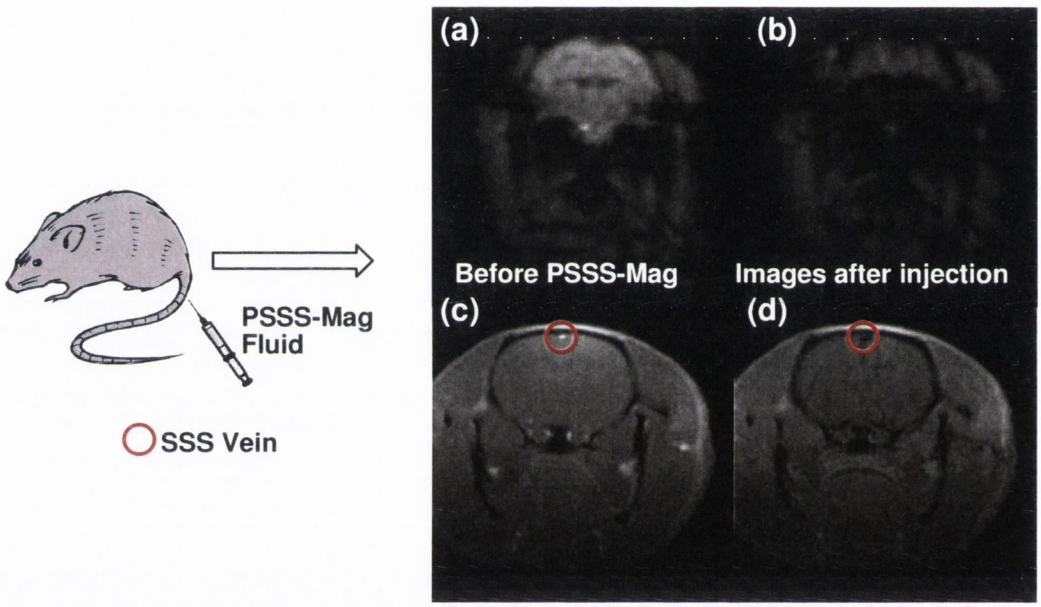

Figure 8.2 Echo planar image (EPI) of mouse brain (a) before and (b) as PSSS-Mag1 passes through; Fast Low Angle Shot (FLASH) image of mouse brain (c) before and (d) as PSSS-Mag1 passes through

These preliminary studies show that the magnetic fluid demonstrates good biocompatibility and potential for in vivo MRI diagnostic.

Finally, Figure 8.3 shows a preliminary study for the formation of grid nanoassemblies of overlying magnetic nanowires, which could have some potential applications in nano-pattering and nano-electronics.

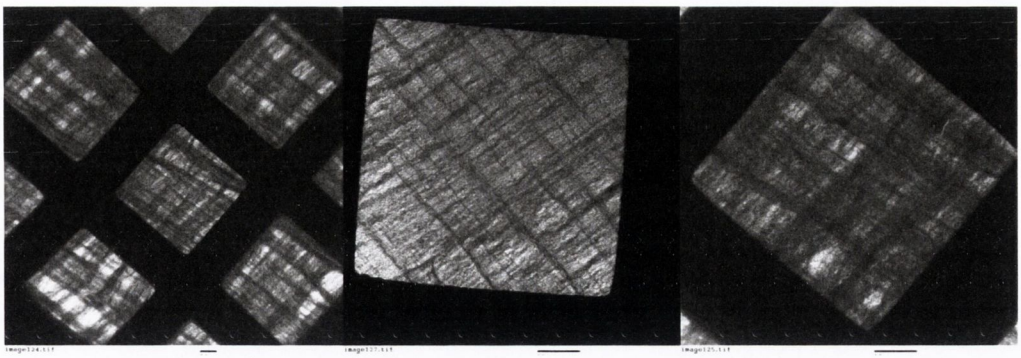

Figure 8.3 PSS functionalised magnetite nanoparticles arranged in grid assemblies by the application of an external magnetic field

8.2.2. DNA modified nanoparticles and intercalation studies

Initial intercalation studies have shown that the ruthenium complex $[Ru(phen)_2dppz]Cl_2$ is associated with the DNA functionalised magnetic nanowires. A confocal image of the DNA-magnetite nanocomposites linked to the $[Ru(phen)_2dppz]Cl_2$ complex is shown in Figure 8.4. The blue colour represents a lifetime of τ_{AV}= 21.5 ns, while the green colour respresents a lifetime of τ_{AV}= 41 ns.

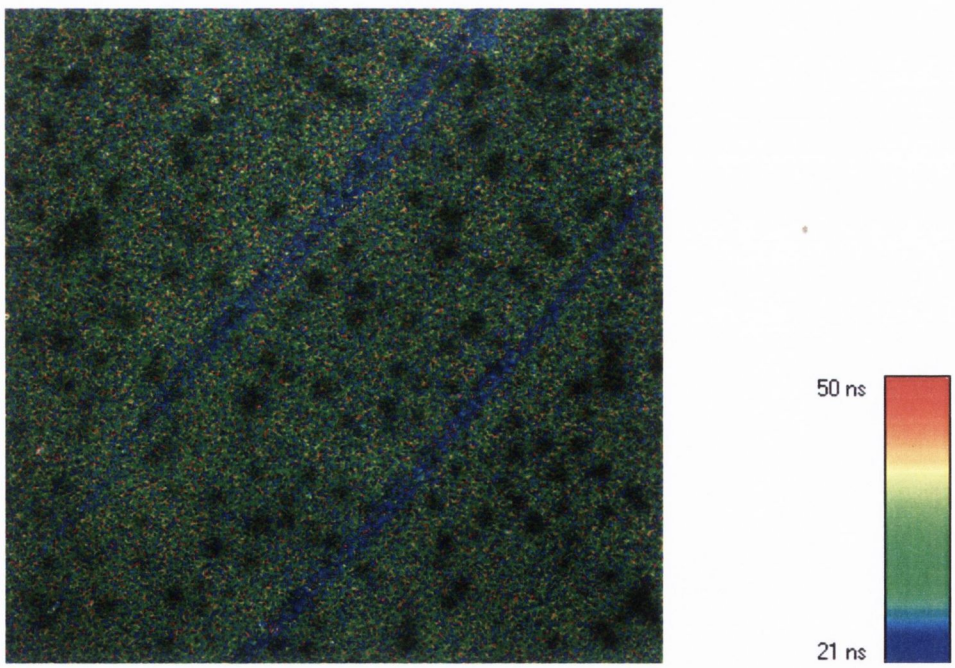

Figure 8.4 Confocal image of DNA-magnetite "decorated" with $[Ru(phen)2dppz]Cl_2$

8.2.3. Drug-functionalised magnetic nanoparticles

It has been demonstrated in this work that magnetic nanoparticles have some attractive potential applications, including conjugation with drugs to provide targeted drug delivery. Current chemotherapies have major disadvantages in that they are relatively non-specific and lead to negative side effects, where the active drug attacks normal healthy cells. The use of magnetic nanoparticles as drug carriers could provide a site-specific drug delivery system where an external magnetic field could be used to concentrate the bound drug to the target site. It is planned to develop the conjugation of anti-inflammatory, pro-apoptotic and anti-proliferative agents to magnetic nanoparticles to be used as novel modes for targeted drug delivery. One of the concepts is to develop the conjugation bioactive cyclopentenone molecules to magnetite (Fe_3O_4) nanoparticles (Scheme 8.1). It is expected that employing this type of approach would open up new possibilities in the administration of biologically active molecules and their targeted delivery to sites of disease may be achieved.

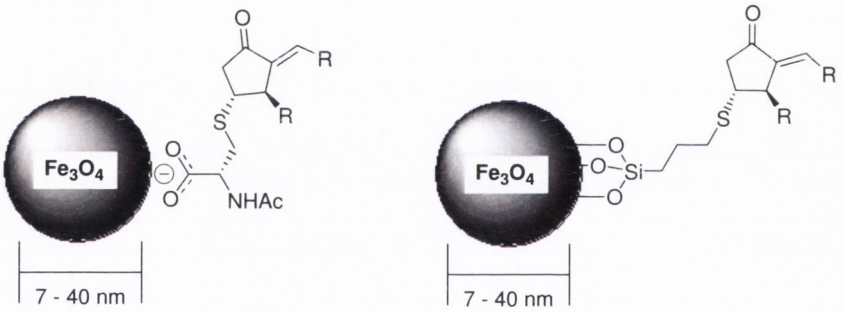

Scheme 8.1 Possible drug conjugation routes

8.2.4. Immobilization of organic catalyst onto magnetic nanoparticles

Initial studies have been carried out on the preparation and testing of catalyst-laden magnetic nanoparticles. One of the difficulties facing chemists employing organic catalysts is the removal of the catalyst after the reaction. We have proposed to resolve this problem by covalently binding the catalyst to magnetic nanoparticles (Figure 8.5). This work was performed in collaboration with Dr. Stephen Connon and his group, who have an expertise in organic synthesis and catalysis. Initially silica coated magnetite nanoparticles have been prepared. Then the catalyst to be used has

been modified with 3-chloropropyltriethoxysilane which can then react with the particle surface by a base catalysed reaction.

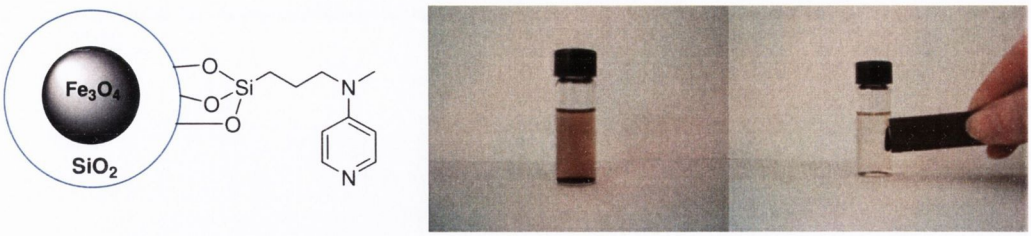

Figure 8.5 Schematic of catalyst immobilised onto the surface of silica coated magnetite nanoparticles, and demonstration of the recyclability of the catalyst-loaded particles

The catalyst coated particles have been tested and a 95% conversion rate has been found. The recyclability of the catalyst has also been investigated and after 20 cycles there is no noticeable reduction in the reactivity of the catalyst. Future work is needed to check the ability of the catalyst-functionalised nanoparticles to catalyse a variety of reactions without a decrease in reactivity.

Chapter 9: Appendices

Appendix 1: ^{1}H NMR of $[(THF)NaFe(^{t}BuO)_3]_2$ heterometallic precursor

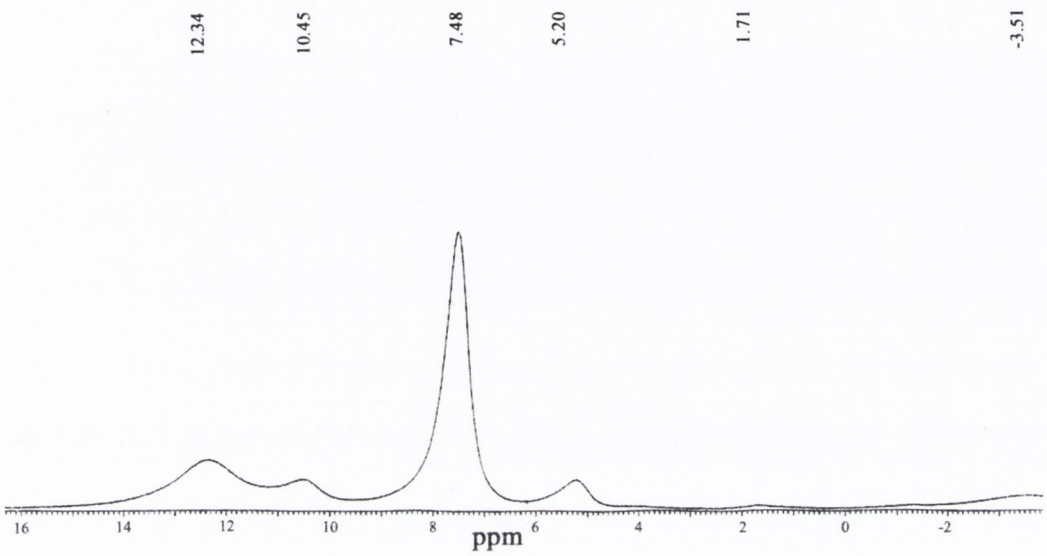

Appendix 2: IR spectrum of $[(THF)NaFe(^{t}BuO)_3]_2$ heterometallic precursor

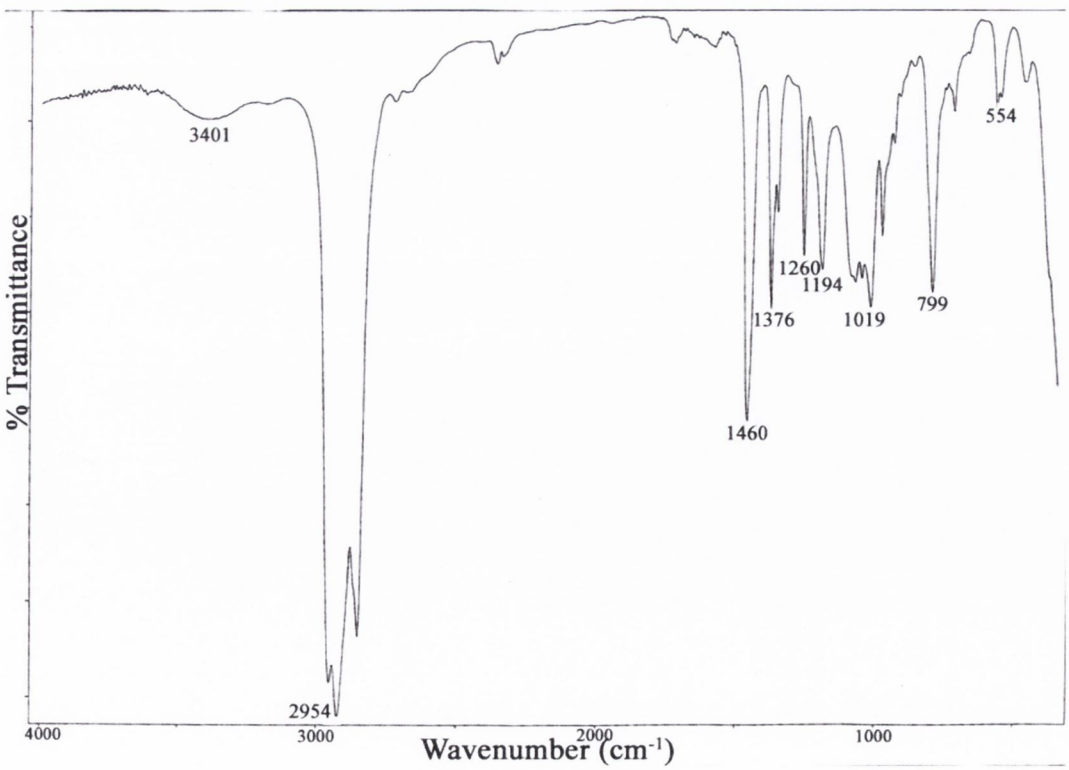

Appendix 3: Magnetisation measurements for samples S1 – S9

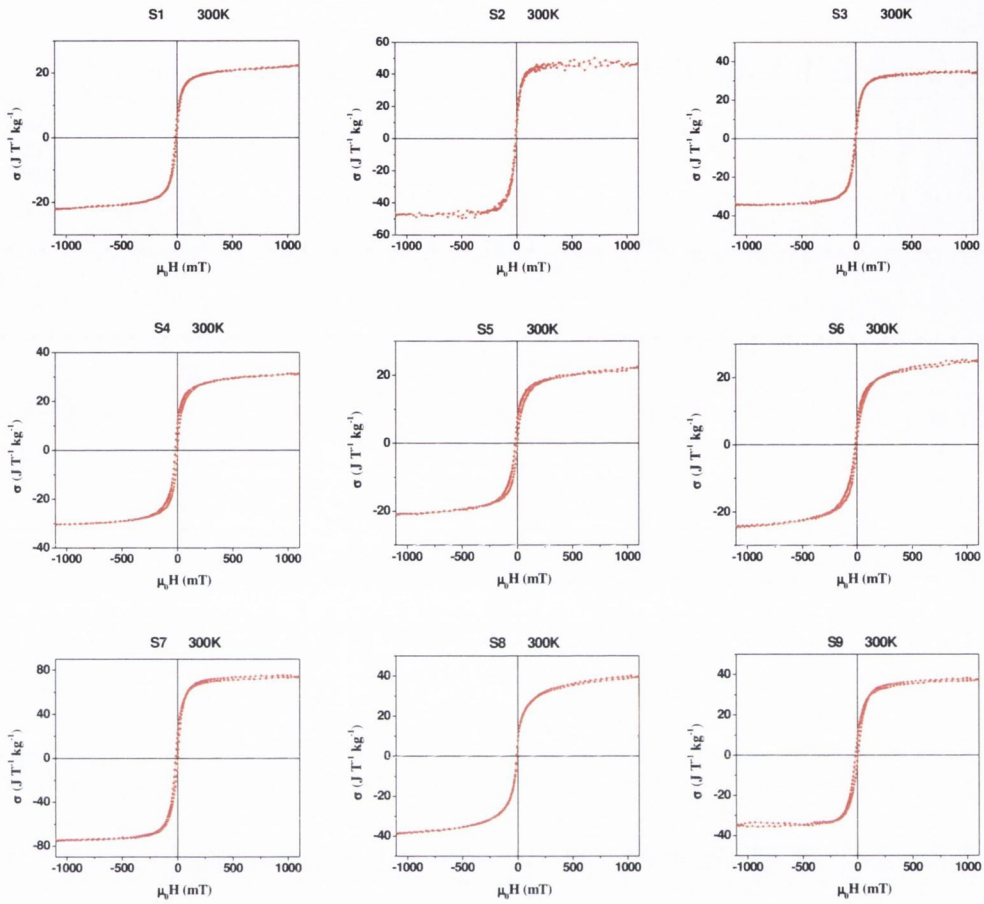

Appendix 4: ^{1}H NMR spectrum of $[Fe(OBu^{t})_2(THF)]_2$ precursor

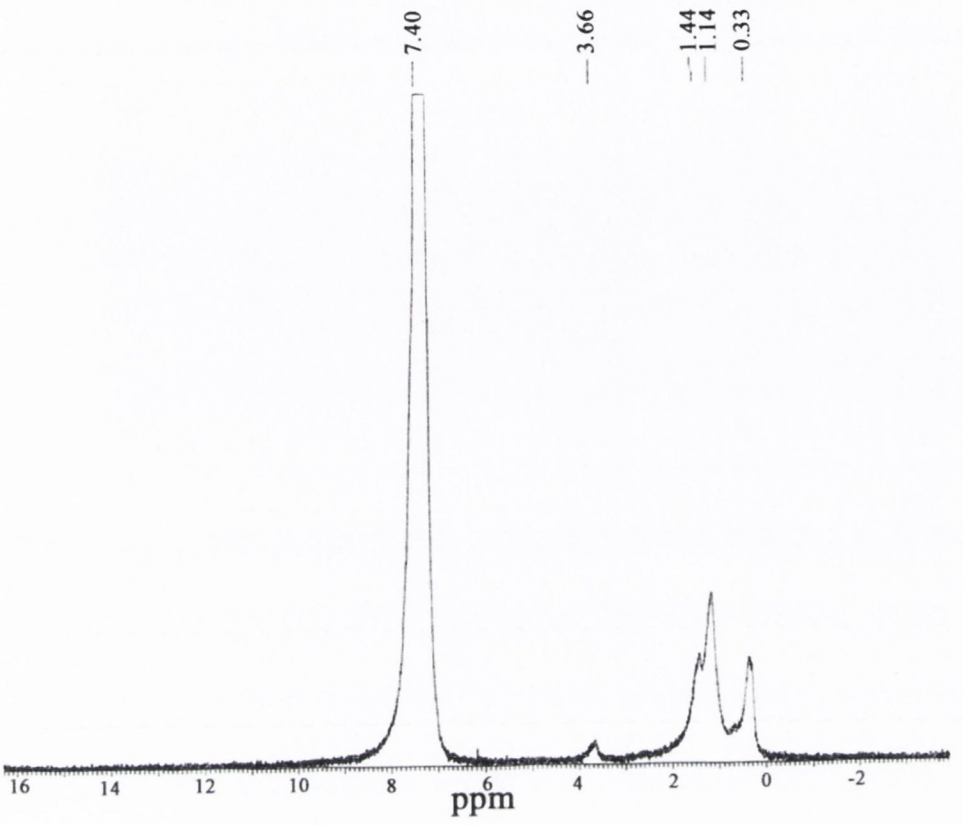

Appendix 5: IR spectrum of $[Fe(OBu^{t})_2(THF)]_2$ precursor

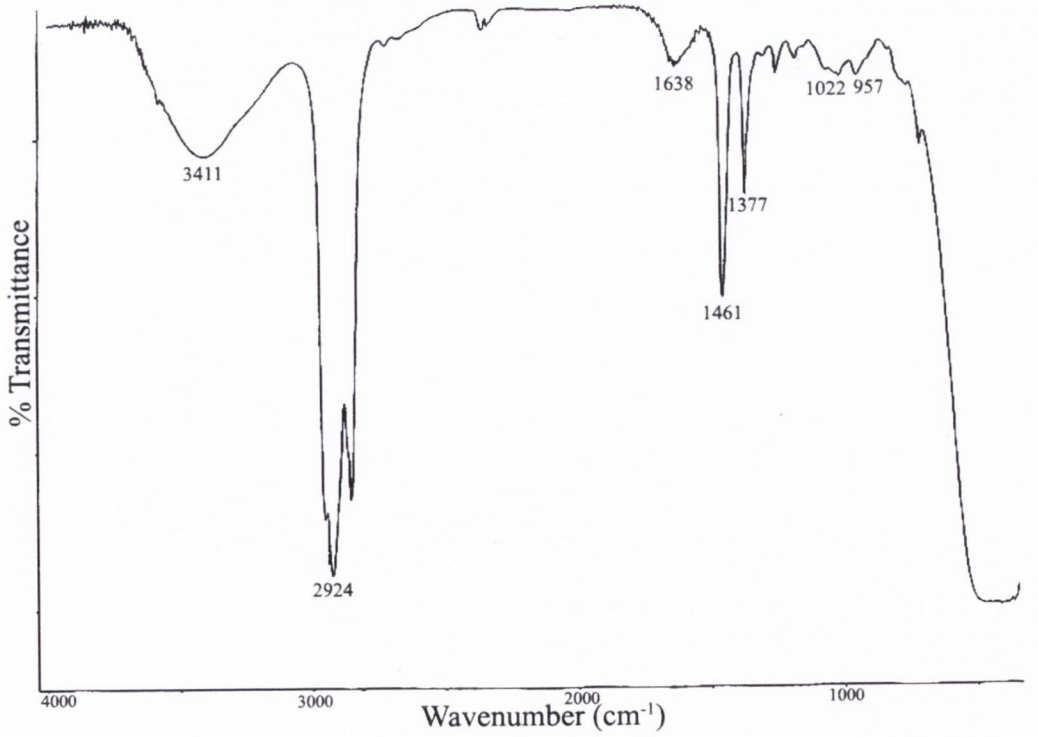

Appendix 6: Wavelengths for selected Raman bands of samples FS1 – FS9

Sample	Wavenumbers					
FS1	299	396	501	600	673	1304
FS2	286	394	-	599	654	1304
FS3	291	398	494	598	679	1312
FS4	287	397	489	602	685	1299
FS6	290	399	480	559	687	1283
FS8	297	401	500	-	686	1339
FS9	-	399	518	-	685	1308

Appendix 7: TGA derivative graphs for samples (a) FS1, (b)FS2, (c) FS3, (d) FS4, (e) FS5, (f) FS6, (g) FS7, (h) FS8 and (i) FS9

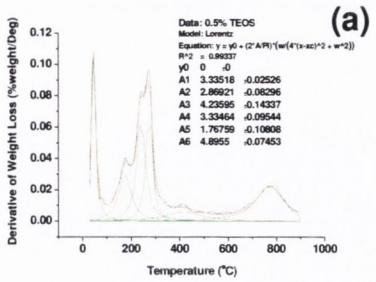

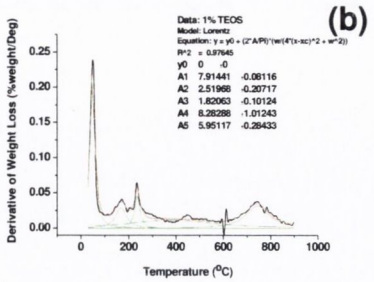

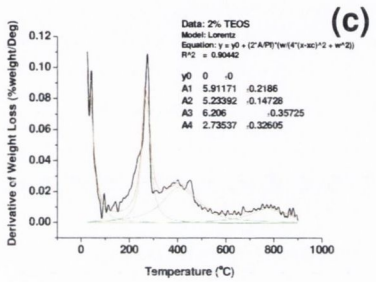

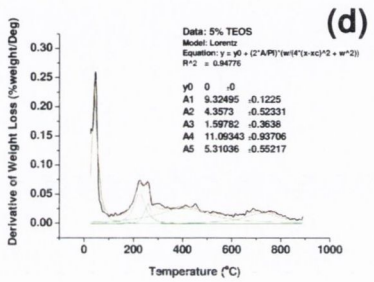

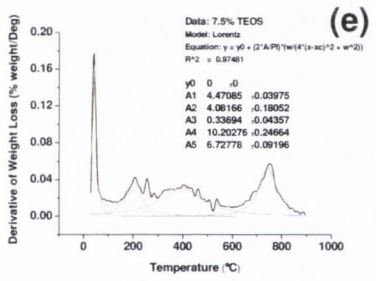

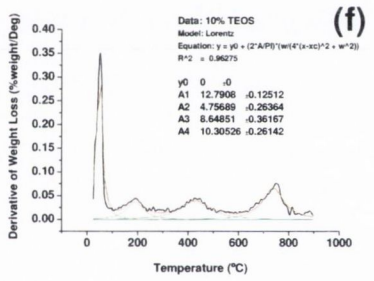

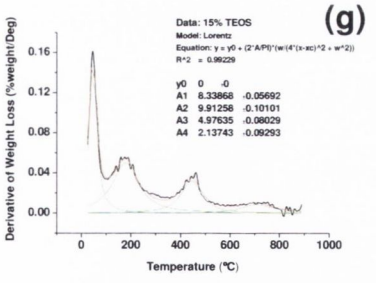

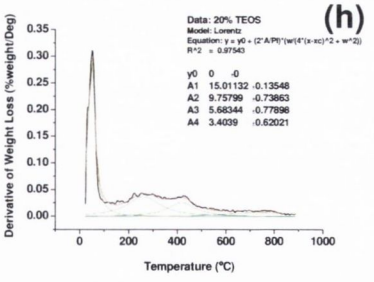

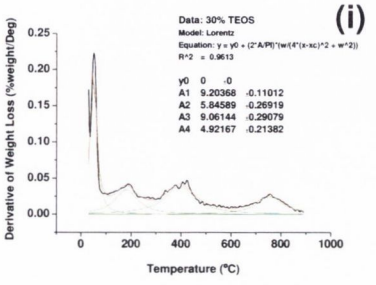

Appendix 8: Emission and excitation spectra and absorption spectrum (inset) of acridine orange in phosphate buffer

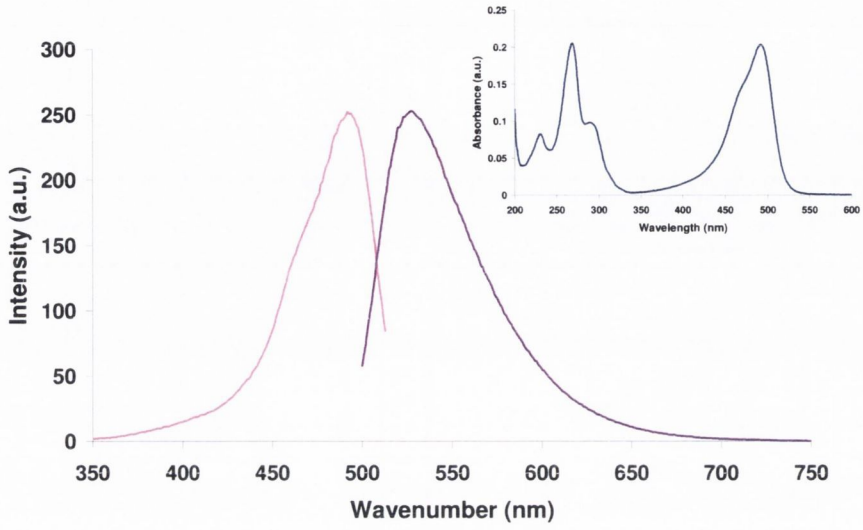

Appendix 9 (a): Absorption spectra showing the change observed when acridine dye only (9.2×10^{-7} M) is bound to double stranded Salmon DNA (9.2×10^{-5} M). Inset shows changes in 493 nm band. The red curve is the original acridine orange solution and the legend shows the curves as 200 µL DNA solution is added. The intrinsic binding constant has been determined by monitoring the absorbance at 493 nm after each addition of DNA and was found to be 2.6×10^{5} M^{-1}.

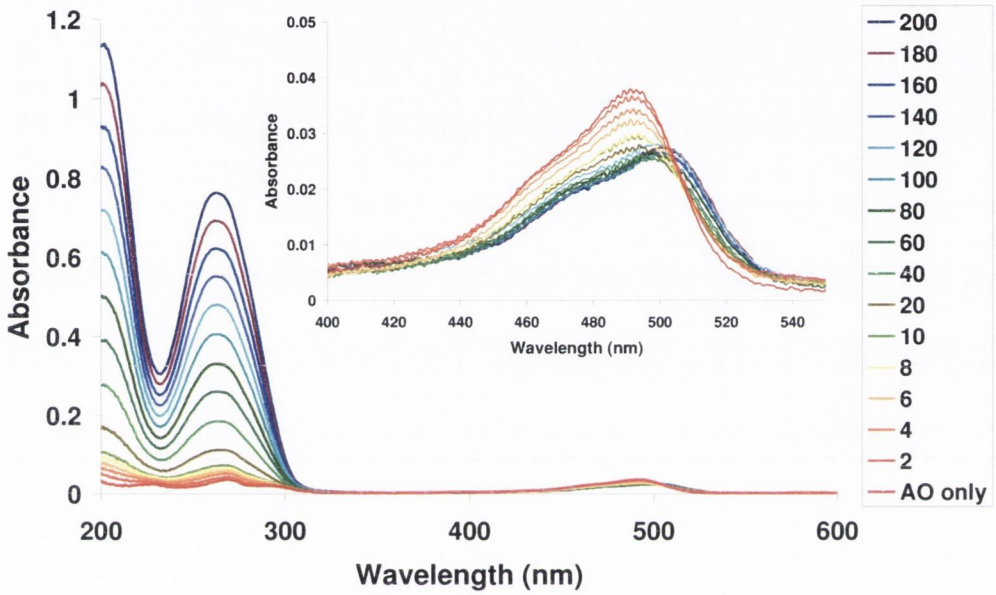

Appendix 9 (b): Absorption spectra showing the change observed when acridine dye only (9.2×10^{-7} M) is bound to single stranded Herring DNA (9.2×10^{-5} M). Inset shows changes in 493 nm band. The red curve is the original acridine orange solution and the legend shows the curves as 200 μL DNA solution is added. The intrinsic binding constant has been determined by monitoring the absorbance at 493 nm after each addition of DNA and was found to be 6.2×10^{5} M^{-1}.

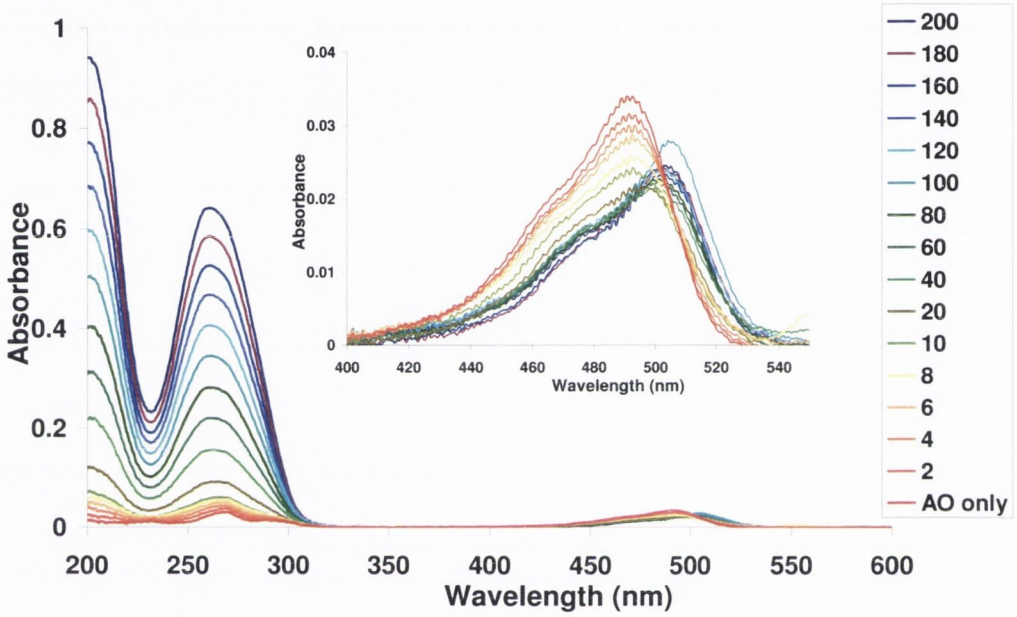

Appendix 9 (c): Absorption spectra showing the change observed when acridine dye only (9.2×10^{-7} M) is bound to single stranded Salmon DNA (9.2×10^{-5} M). Inset shows changes in 493 nm band. The red curve is the original acridine orange solution and the legend shows the curves as 200 μL DNA solution is added. The intrinsic binding constant has been determined by monitoring the absorbance at 493 nm after each addition of DNA and was found to be 1.3×10^{5} M^{-1}.

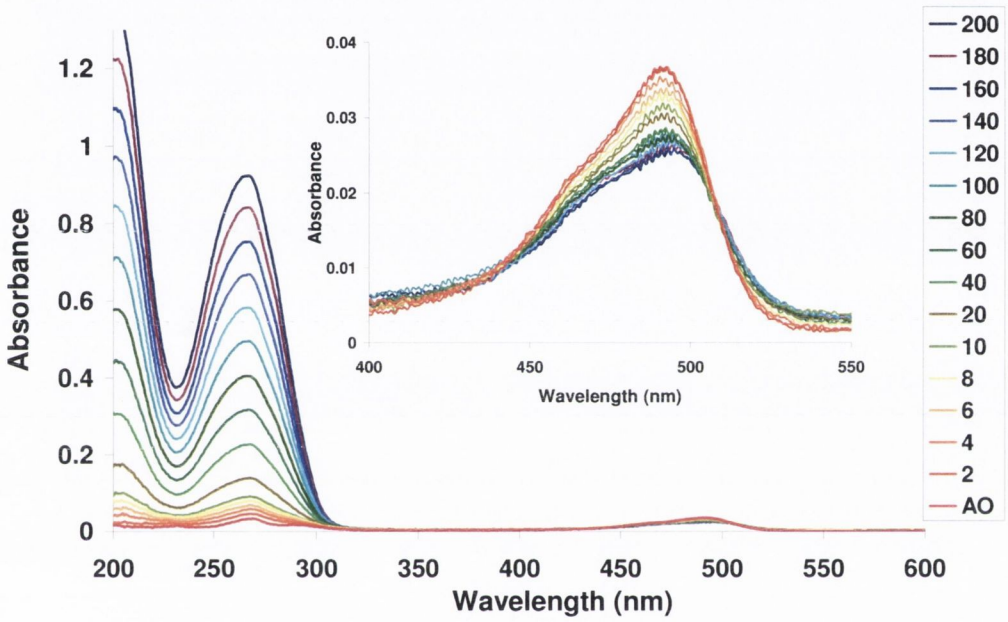

Appendix 10 (a): Fluorescence spectra of double stranded Herring DNA-magnetite composites intercalated with acridine orange (λ_{em} = 493 nm, λ_{ex} = 527 nm). The intensity decreases initially upon addition of DNA and then is found to increase. The red curve is the original acridine orange spectrum (9.2×10^{-7} M) and the legend shows the curves as aliquots of DNA solution (9.2×10^{-5} M) are added (up to 200 μL).

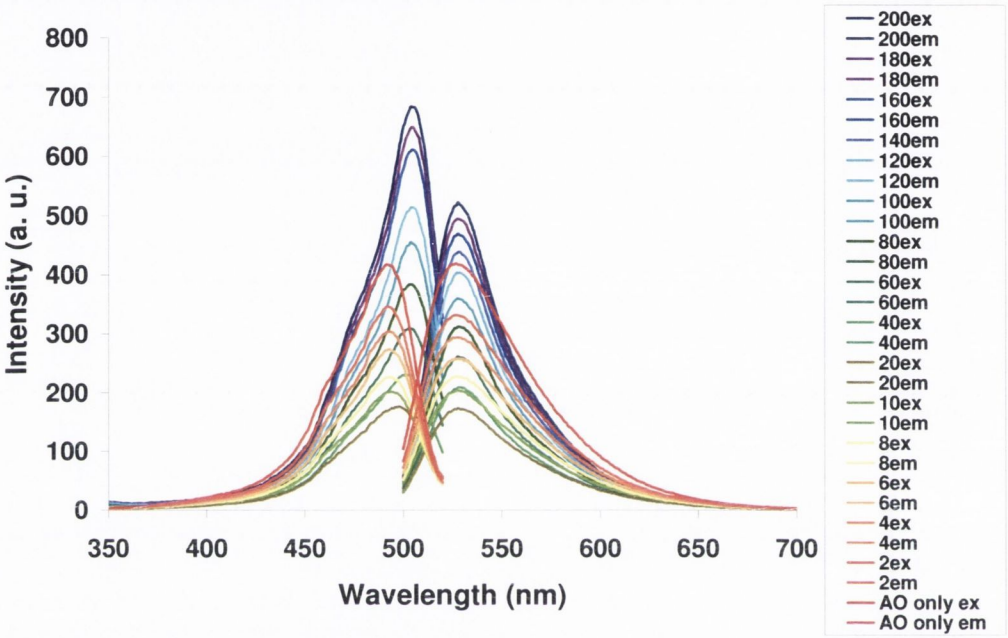

Appendix 10 (b): Fluorescence spectra of single stranded Herring DNA intercalated with acridine orange (λ_{em} = 493 nm, λ_{ex} = 527 nm). The intensity decreases initially upon addition of DNA and then is found to increase. The red curve is the original acridine orange spectrum (9.2×10^{-7} M) and the legend shows the curves as aliquots of DNA solution (9.2×10^{-5} M) are added (up to 200 μL).

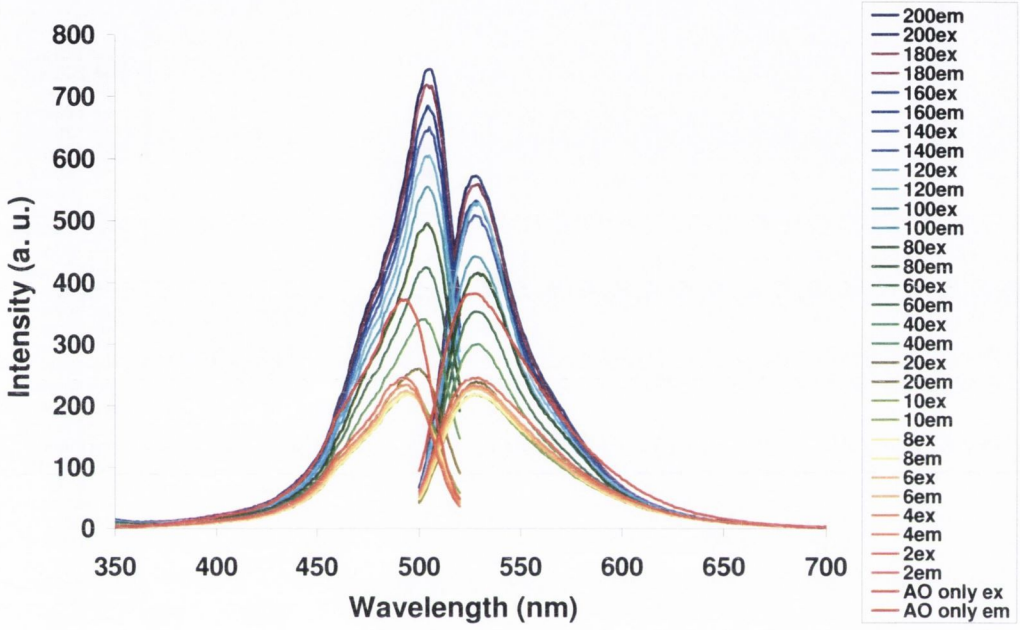

Appendix 10 (c): Fluorescence spectra of single stranded Salmon DNA intercalated with acridine orange (λ_{em} = 493 nm, λ_{ex} = 527 nm). The intensity decreases initially upon addition of DNA and then is found to increase. The red curve is the original acridine orange spectrum (9.2×10^{-7} M) and the legend shows the curves as aliquots of DNA solution (9.2×10^{-5} M) are added (up to 200 μL).

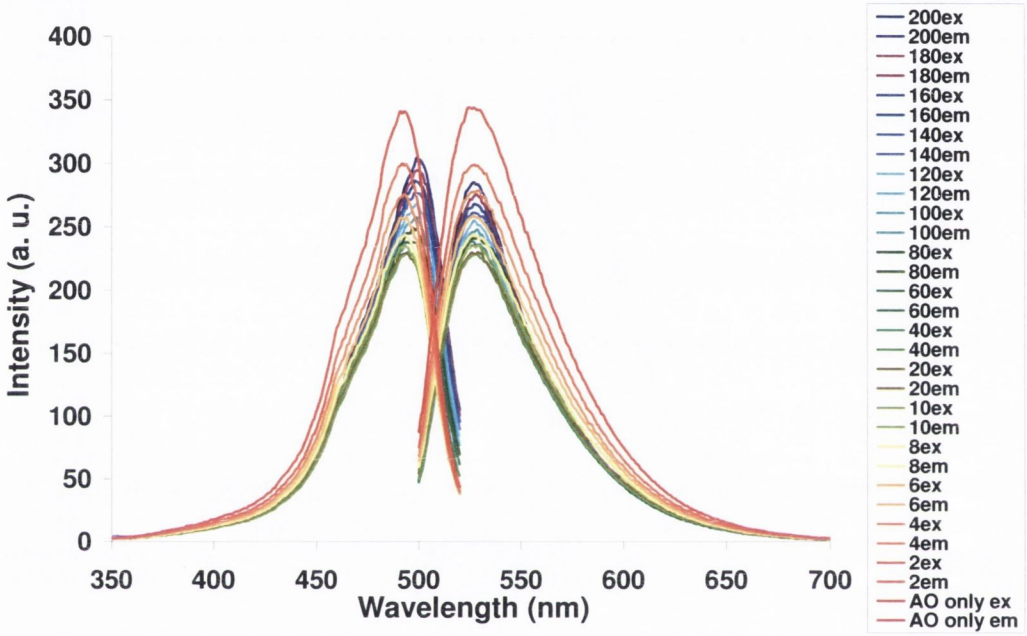

Appendix 11: XRD patterns for samples Z (red), Q (light green), B (blue), D (turquoise), G (pink), P (yellow), F (green), I (orange), T (purple), and S (grey).

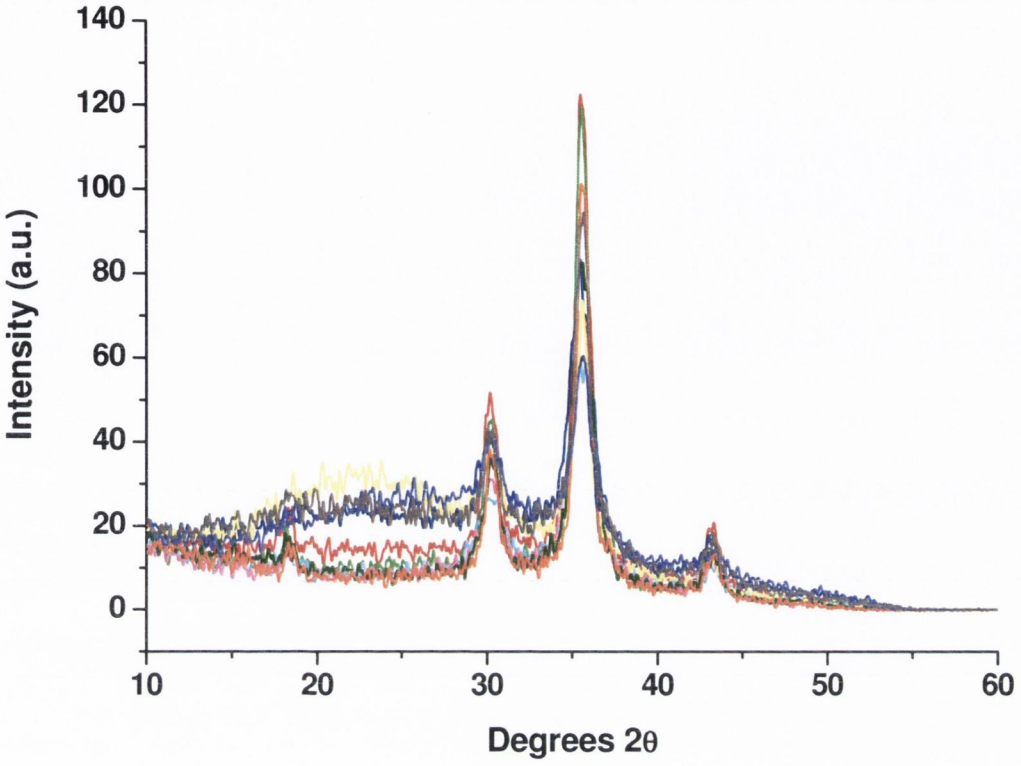

Appendix 12: Raman study for PSS-functionalised cobalt ferrite nanoparticles. From top to bottom: E, U, M, S, Q, R, O, and J

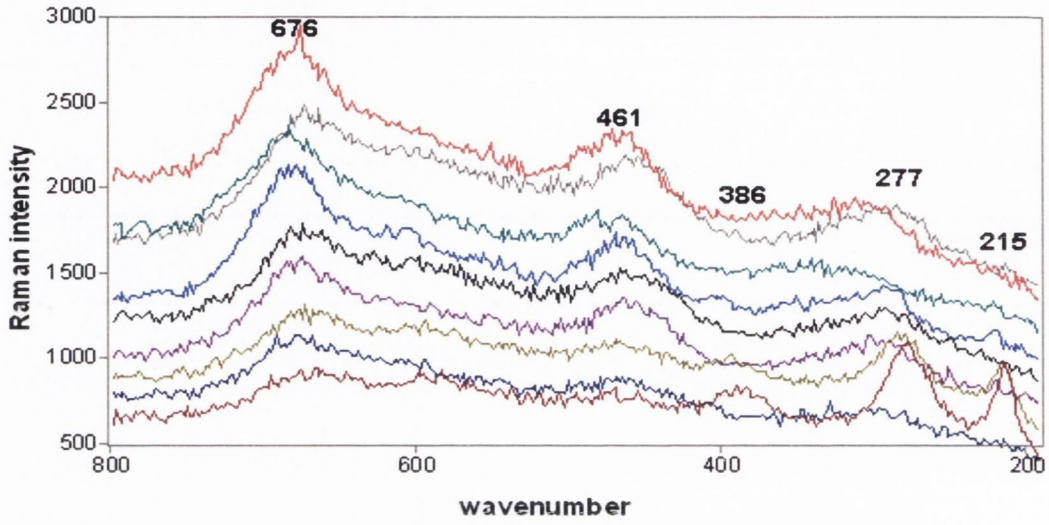

Publications, presentations and posters

1. A Magnetic-Nanoparticle-Supported 4-*N*,*N*-Dialkylaminopyridine Catalyst: Excellent Reactivity Combined with Facile Catalyst Recovery and Recyclability

C. O. Dálaigh, S. A. Corr, Y. Gun'ko, S. J. Connon, *Angew. Chem. Int. Ed.*, **2007,** 46 (23), 4329-4332

2. "Jelly Dots": Synthesis and Cytotoxicity Studies of CdTe Quantum Dot-Gelatin Nanocomposites

S. J. Byrne, Y. Williams, A. Davies, S. A. Corr, Y. K. Gun'ko, A. Rakovich, Y. P. Rakovich, J. F. Donegan, Y. Volkov, *Small*, **2007**, DOI: 10.1002/smll.200700090

3. Synthesis, Characterisation, and Biological Studies of CdTe Quantum Dot-Naproxen Conjugates

S. J. Byrne, B. le Bon, S. A. Corr, M. Stefanko, C. O'Connor, Y. K. Gun'ko, Y. P. Rakovich, J. F. Donegan, Y. Williams, Y. Volkov, P. Evans, *ChemMedChem*, **2007**, 2, 183 – 186.

4. Magnetic-fluorescent nanocomposites for biomedical multitasking

Serena A. Corr, Aisling O' Byrne, Yurii K. Gun'ko, Swapankumar Ghosh, Dermot F. Brougham, Siobhan Mitchell, Yuri Volkov, Adriele Prina-Mello, Chem. Commun., **2006**, (43), 4474-4476 (*Chem Commun Inside Cover*)

5. Optimisation of the synthesis and modification of CdTe quantum dots for enhanced live cell imaging

Stephen J. Byrne, Serena A. Corr, Tatsiana Y. Rakovich, Yurii K. Gun'ko, Yury P. Rakovich, John F. Donegan, Siobhan Mitchell, Yuri Volkov, J. Mater. Chem., **2006**, (28), 2896-2902

6. Emission properties of colloidal quantum dots on polyelectrolyte multilayers

Vamsi K. Komarala, Yury P. Rakovich, A. Louise Bradly, Stephen J. Byrne, Serena A. Corr, Yurii K. Gun'ko, Nanotechnology, **2006**, 17(16), 4117-4122

7. New two in one magnetic fluorescent nanocomposites

Serena A. Corr, Yurii K. Gun'ko, Stephen J. Byrne, Alexios P. Douvalis, Munuswamy Venkatesan, and Robert D. Gunning, Proc. SPIE, **2005**, 5824, 51-78

8. Preparation and biological investigation of luminescent water soluble CdTe nanoparticles

Stephen J. Byrne, Ciara M. O'Driscoll, Serena A. Corr, Yurii K. Gun'ko, Siobhan Mitchell and Yuri Volkov, Proc. SPIE, **2005**, 5824, 129-137.

9. Magnetic nanoparticle assemblies on denatured DNA show unusual magnetic relaxivity and potential applications for MRI

Stephen J. Byrne, Serena A. Corr, Yurii K. Gun'ko, John M. Kelly, Dermot F. Brougham, Swapankumar Ghosh, Chem. Commun., **2004**, (22),2560-2561

10. Magnetite nanocrystals from a single source metallorganic precursor: metallorganic chemistry vs. biogeneric bacteria

Serena A. Corr, Yurii K. Gun'ko, Alexios P. Douvalis, Munuswamy Venkatesan, Robert D. Gunning, J. Mater. Chem., **2004**, (6),944-946

Conference presentations

- "Magnetic Nanowires from Nanoparticle assemblies", COST Meeting, Leuven, Belgium, 10th November 2006
- "The Development of New Magnetic Nanocomposites and Magnetic Fluids". Departmental Seminar, 14th April 2005
- "Development of New Two-in-One Magnetic-Fluorescent Nanocomposite Materials". SPIE Conference, 4th April 2005
- "Development of New Two-in-One Magnetic-Fluorescent Nanocomposite Materials". Nanoparticle Research Day, 1st April 2005
- "The Development of New Magnetic Nanocomposites and Magnetic Fluids". 28th Annual MSI Meeting, 1st September 2004
- "Magnetic nanoparticles and magnetic fluids for MRI". Biomedical Imaging Symposium, 9th June 2004

- "Development of New Magnetic Nanocomposites and Magnetic Fluids for Biomedical Applications". Centre for Microscopy and Analysis Open Day, 24th March 2004

Conference Posters

- Magnetic nanoparticle assemblies on DNA, ICSM Conference, Dublin, July 2006.
- Development of New Two-in-One Magnetic-Fluorescent Nanocomposite Materials, Materials Research Society Spring Meeting, San Francisco, April 2006.
- New Two-in-One Magnetic-Fluorescent Nanocomposite Materials, Bioinspired Nanomaterials for Medicine and Technologies, Marl, Germany, 2005.
- New Two-in-One Magnetic-Fluorescent Nanocomposite Materials, BioNano 3, University of Sussex, UK, September 2005
- Maghemite-Silica Nanorods from Single Source Metallorganic Precursor, Nano 2004, Wiesbaden, Germany, June 2004.
- Sol-gel synthesis of first maghemite-silica nanotubes from single source metallorganic precursor MSI 2005
- Preparation of magnetite nanocrystals from a single source metallorganic precursor, 1st Annual Nanotechnology Symposium, University College Cork, September 2003
- Investigation of porphyrin functionalised magnetic nanoparticles, 27th Annual MSI Meeting, University College Cork, September 2003